

Molecular Magnetic Architectures: From Mononuclear to Polynuclear Complexes

Zur Erlangung des akademischen Grades eines
DOKTORS DER NATURWISSENSCHAFTEN

(Dr. rer. nat)

von der KIT-Fakultät für Chemie und Biowissenschaften
des Karlsruher Instituts für Technologie (KIT)



genehmigte

Dissertation

von

Nithin Suryadevara

aus

Warangal, India

Präsident: Prof. Dr. Burkhard Luy

Referent: Prof. Dr. Mario Ruben

Korreferent: Prof. Dr. Annie Powell

Prüfer: Prof. Dr. Stephan Bräse

Prüfer: Prof. Dr. Manfred Kappes

Tag der mündlichen Prüfung: 08.12.2020

Declaration

I, Nithin Suryadevara, declare that this thesis entitled “*Molecular Magnetic Architectures – From Mononuclear to Polynuclear Complexes*” and the work presented in it are my own and the work was undertaken under the supervision of Prof. Mario Ruben at the Institute of Nanotechnology (INT), at the Karlsruhe Institute of Technology (KIT). I confirm that:

- This work was done wholly while in candidature for a research degree at KIT.
- The whole thesis was written by me and no other sources other than the specified were used.
- The rules for ensuring good scientific practice of the Karlsruhe Institute of Technology (KIT) have been used and the submission and archiving of the primary data, in accordance with section A(6) of the rules for ensuring good scientific practice of KIT, has been ensured.
- The electronic version of the work is consistent with the written version.
- Where I have consulted the published work of others, this is always clearly attributed.
- I have acknowledged all main sources of help.
- Where the thesis is based on work done by myself jointly with others, I have made clear exactly what was done by other and what I have contributed myself.
- Furthermore, I declare that I did not undertake any previous doctoral studies and that I am currently not enrolled in any other ongoing doctoral procedure.

Signature:

Date:

Deklaration

Ich, Nithin Suryadevara, erkläre, dass diese Arbeit mit dem Titel “*Molecular Magnetic Architectures – From Mononuclear to Polynuclear Complexes*” und die darin vorgestellten Ergebnisse meine eigenen sind. Die Arbeit wurde unter der Leitung von Prof. Dr. Mario Ruben am Institut für Nanotechnologie (INT), am Karlsruher Institut für Technologie (KIT) angefertigt. Ich bestätige:

- Diese Arbeit wurde vollständig während der Kandidatur für ein Forschungsstudium am KIT durchgeführt.
- Die gesamte Arbeit wurde von mir verfasst und es wurden keine anderen Quellen als die angegebenen verwendet.
- Es wurden Maßnahmen zur Sicherstellung einer guten wissenschaftlichen Praxis des Karlsruher Instituts für Technologie (KIT) angewendet und die Übermittlung und Archivierung der Primärdaten gemäß Abschnitt A(6) der Regeln zur Sicherstellung einer guten wissenschaftlichen Praxis des KIT sichergestellt.
- Die elektronische Fassung des Werkes entspricht der schriftlichen Fassung.
- Im Fall, dass ich die veröffentlichten Arbeiten anderer konsultiert habe, wird dies immer eindeutig zugeordnet.
- Ich habe alle wichtigen Hilfsquellen zur Kenntnis genommen.
- Wenn die Arbeit auf Arbeiten basiert, die ich gemeinsam mit anderen geleistet habe, habe ich kenntlich gemacht, was von anderen geleistet wurde und was ich selbst beigesteuert habe.
- Des Weiteren erkläre ich, dass ich kein vorheriges Promotionsstudium absolviert habe und mich derzeit nicht in einem anderen laufenden Promotionsverfahren befinde.

Unterschrift:

Datum:

Table of Content

Chapter 1 Introduction	1
1.1 Challenges in Information Technology.....	1
1.2 Basics in Magnetism	1
1.3 Areas in Magnetochemistry	3
1.3.1 Introduction to Spin-Crossover	4
1.3.2 Introduction to Single Molecule magnetism	13
1.3.3 Aims of the thesis	18
Chapter 2 Iron(II) bis(pyrazolyl)pyridine (<i>bpp</i>)-based molecules – From surface to bulk	17
2.1 Introduction	17
2.2 Surface characterization techniques	20
2.3 Objectives.....	24
2.3.1 Objective 1: Self-assembly of carboxylic acid derivative of 2,6-di(1H-pyrazol-1-yl)isonicotinic acid on Ag(111).....	24
2.3.2 Objective 2: Hysteresis engineering of <i>bpp</i> -based SCO complexes	29
2.4 Conclusion.....	43
Chapter 3 Chiral Resolution of SCO active Iron(II) Grid complexes	45
3.1 Chiral Systems.....	45
3.1.1 Introduction to Chirality	45
3.1.2 Characterization Methods: Circular Dichroism.....	46
3.1.3 Chirality and Molecular Electronics	48
3.2 Supramolecular chemistry and grid complexes	50
3.2.1 Introduction to Grid complex system	50
3.2.2 Introduction to Homoditopic ligand system	52
3.3 Objectives.....	53
3.3.1 Objective 1: Separation of TRANS and CIS – isomers of ligand L.....	54
3.3.2 Objective 2: Chiral resolution of Λ and Δ – enantiomers in S-type conformers	58
3.4 Conclusions	71

Chapter 4 Terbium(III) Single-molecule magnets based on tetra-pyrrole ligands	73
4.1 Introduction	73
4.1.1 Lanthanide Chemistry.....	73
4.1.2 Magnetism in lanthanides	73
4.1.3 Lanthanide based SMMs	75
4.1.4 Phthalocyanine-type ligands and [LnPc ₂] structure.....	76
4.2 Objectives.....	78
4.2.1 Objective 1: Synthesis and Characterization of Tb (Porphyrinato) (Phthalocyaninato) sandwich complexes	78
4.2.2 Objective 2: Synthesis and Characterization of poly-nuclear Tb (Porphyrinato) (Phthalocyaninato) sandwich complexes.....	96
4.3 Conclusion.....	114
Chapter 5 Experimental Section.....	115
5.1 Materials and Equipment	115
5.2 Iron(II) bis(pyrazolyl)pyridine (<i>bpp</i>) based molecules – From surface to bulk.....	116
5.2.1 Preparation of ligands and complexes	116
5.2.2 Preparation of substrates, samples; STM and XPS studies	118
5.2.3 DSC and TGA experiments.....	119
5.3 Chiral resolution of SCO active Iron(II) Grid complexes.....	119
5.3.1 Preparation of ligands for Grid complexes.....	119
5.3.2 Preparation of Fe(II) Grid complexes.....	124
5.3.3 Other Techniques.....	127
5.4 Mononuclear and polynuclear SMM complexes	128
5.4.1 Synthesis of Porphyrin Ligands.....	128
5.4.2 Synthesis of Tb Phtalocyanato Porphinato double deckers.....	132
5.4.3 Polynuclear Double-decker complexes	135
5.4.4 Other Techniques.....	138
5.5 Crystal Structures	139
Conclusion and Outlook.....	145
Bibliography.....	147
Appendix	157

List of Figures

Figure 1.1: Magnetic ordering in A) paramagnetic, B) ferromagnetic, C) antiferromagnetic and D) ferrimagnetic materials (where χ is the magnetic susceptibility).....	2
Figure 1.2: Schematic representation of the SCO phenomena in a Fe(II) complex with d^6 electronic configuration.	4
Figure 1.3: Simplified Tanabe-Sugano (TS) diagram of d^6 metal ions in an octahedral environment. (Reproduced from Ref. 15).....	5
Figure 1.4: Schematic representation of the HS (red) and LS(blue) potential wells for an octahedral iron(II) complexes. (Reproduced from Ref. 8)	6
Figure 1.5: Changes in physical properties accompanied by SCO phenomenon: A) change in a magnetic moment; B) change in structural properties, C) thermochromism, and D) change in heat capacity.	7
Figure 1.6: Various types of ST curves: A) gradual, B) abrupt, C) with thermal hysteresis, D) two-step, and E) incomplete ST. γ_{HS} on Y-axis represents the fraction of HS content (Reproduced from Ref. 16).....	8
Figure 1.7: The mechanisms of LIESST and reverse-LIESST in iron(II) SCO compounds (Reproduced from Ref. 8).	9
Figure 1.8: Schematic diagram of the SQUID magnetometer (reproduced from SQUID manual).	11
Figure 1.9: A) Molecular structure of the Mn_{12} complex. Purple (Mn^{3+}), dark green (Mn^{4+}), red (O), and grey (C). B) Magnetisation hysteresis curve was measured on a single-crystal of Mn_{12} at 2.2 K (\circ) and 2.8 K (\bullet) (Reproduced from Ref. 26).	14
Figure 1.10: The energy barrier U_{eff} for the reversal of the spins between the spin 'up' ($M_s = 10$) and 'down' ($M_s = -10$) state for Mn_{12} complex (Reproduced from Ref. 30).	15
Figure 1.11: χ_M'' signals for a microcrystalline sample of $[Mn_{12}O_{12}(O_2CCH_2Br)_{16}(H_2O)_4]$ and shift in peaks can be observed on increasing the frequency. (Reproduced from Ref. 33).....	17
Figure 2.1: A) Structural view of $[Fe(bpp)_2]^{2+}$ complex and types of bpp ligands in the literature. B) Angles used in the definitions of the distortion parameters Σ and Θ . C) Distortion parameters ϕ , θ and ψ in $[Fe(bpp)_2]^{2+}$ derivatives (Reproduced from Ref. 60).	18
Figure 2.2: Schematic representation of the Top-Down and Bottom-Up approaches.....	20
Figure 2.3: Schematic representation of the working principle of STM (Source: Wikipedia)....	21
Figure 2.4: Schematic representations of (A) constant current mode and (b) constant height mode of the STM.	22
Figure 2.5: A) Schematic representation of the photoelectric effect and B) energy level diagram representing the photoelectric effect.	23
Figure 2.6: Low Temperature (LT)-STM images of bpp-COOH. (A) Overview image (1.0 V, 50 pA) of the porous structure. (B) Molecular model overlaid on a close-up image (-0.25 V, 50 pA). (C) Schematic representation of the motif and the resulting pattern on the surface. (D) Pattern overlaid on STM image (-0.25 V, 50 pA).....	26
Figure 2.7: XPS spectra of bpp-COOH on Ag(111). (A-B) C 1s and O 1s regions for submonolayer coverage, (C-D) C 1s and O 1s regions after annealing to 100 °C, (E) O 1s region after dosing Fe on a submonolayer coverage of L1 , (F) model of ligand L1	27

Figure 2.8: LT-STM images (-0.5 V, 50 pA) of <i>bpp</i> -COOH annealed at 373 K. (A) Mesh indicated by yellow lines. (B) The molecules in the pore are shown in green color.	28
Figure 2.9: STM images of coordination polymer formed by <i>bpp</i> -COOH and Fe. (A) Overview image from LT-STM (-0.5 V, 100 pA). (B and C) Close-up of coordinated molecules (0.25 V, 50 pA). Brighter protrusions are assigned to the Fe coordination of the tail. (D) RT-STM image (0.4 V, 80 pA) showing the stability of the coordination polymer at RT. (E) Schematic representation of head to head coordination and (F) representation of head to tail coordination.	29
Figure 2.10: A) Crystal structure of complex C1 at 150 K. Displacement ellipsoids are at the 50% level, and B) crystal packing of complex C1 . Hydrogen atoms and disordered atoms were omitted for clarity.	31
Figure 2.11: Intermolecular contacts (denoted in blue dotted lines and circled) within the unit cell in complex C1	33
Figure 2.12: χ_T vs. T plot for complex C1 (on the left) and the table with parameters associated with SCO behaviour of complex C1 (on the right). A scan-rate of 3 K/min was used in settle mode.	33
Figure 2.13: A) TGA curve for complex C1 , B) powder XRD patterns of crushed C1 crystals at 293 K, compared to pattern calculated from the single-crystal structure at 150 K (an inverted trace in green colour) and C) powder XRD patterns of crushed crystals of C1 in pristine state at 330 K and 293 K (red colour).	34
Figure 2.14: A) Crystal structure of low spin complex C2 at 150 K. Displacement ellipsoids are at the 50% level, and B) crystal packing of complex C2 . Hydrogen atoms and disordered atoms were omitted for clarity.	35
Figure 2.15: Intermolecular contacts (denoted in blue dotted lines) within the unit cell of the LS state of complex C2	36
Figure 2.16: SCO behaviour of complex C2 A) 4 cycles at 3 K/min showing $\Delta T = \sim 65$ K and B) reproducibility check with 3 K/min and 1 K/min scan rates in settle mode.	37
Figure 2.17: A) Crystal structure of di-cation complex C2 at 300 K (HS). Displacement ellipsoids are at the 50% level, and B) crystal packing of complex C2 . H-atoms and disorders were omitted for clarity.	39
Figure 2.18: Intermolecular contacts in the unit cell of complex C2 (high-spin) at 300 K.	40
Figure 2.19: Images of the red-colored single crystal at different temperatures while cooling. The cracks occurred due to distortion were circled.	41
Figure 2.20: DSC analysis of complex C2 at a scan rate of 2 K/min.	41
Figure 3.1: Representation of A) (R)- and (S)-enantiomers, B) enantiomers & diastereomers, C) left and right-handed helical structures, and D) examples of enantiomers in coordination complexes - Λ and Δ isomers of $[\text{Ru}(\text{bpy})_3]^{2+}$	46
Figure 3.2: Representation of linearly polarized light (red), as a summation of LCP (blue) and RCP (green), (A) before and (B) after passing through a sample. (C) representation of ellipticity (θ) (D) Representation of positive and negative Cotton effects.	47
Figure 3.3: A) Schematic representation of Natural optical activity, Magnetically induced optical activity and Magneto-chiral anisotropy, B) representation of Magneto-Chiral Dichroism effect.	49
Figure 3.4: Pictorial representation of A) second harmonic generation and B) CISS effect.	49

Figure 3.5: Schematic representation of [n x n] grids complex architectures forming from ‘n’ metal centers and ‘n’ ligands.	51
Figure 3.6: A) The conformational isomerism and tautomerism in ligand L . B) L_{Trans} and L_{Cis} conformers of L in solution. C) Divergent coordination chemistry of ligand L (black bar) on coordination with Fe ²⁺ metal ions (grey balls). D) Λ and Δ -isomers of the S-grid complex.	53
Figure 3.7: ¹ H NMR spectra of L_T and L_C in CDCl ₃	55
Figure 3.8: (A) Crystal structure of S-form of grid complex, (B) unit cell containing both the Λ and Δ -isomers (anions, hydrogen, and solvent molecules were omitted for clarity), [Fe(II)-orange, O-red, C- carbon, N- blue].	57
Figure 3.9: χ T vs. T plots of C (left) and S (right) forms of complexes in the temperature region of 5-370 K.	58
Figure 3.10: Scheme for the synthesis of enantiomeric grid complexes representing the pairs of diastereomers and enantiomers.	60
Figure 3.11: ESI spectra showing the formation of grid complex (inset: experimental in blue and simulated spectra in green and table showing the assignment of the peaks). Here Tf stands for triflate anion (CF ₃ SO ₃).	61
Figure 3.12: IMS data of crude samples A) P_a and B) P_i showing two diastereomers in both the samples. The mass spectrum extracted from the two peaks of P_a is shown in inset C.	62
Figure 3.13: Crystal structures of (all S, Λ) and (all R, Δ)– enantiomeric Fe(II) grid complexes at 180 K (H atoms, counter anions, and solvent molecules were omitted for clarity).	63
Figure 3.14: CD spectra of single crystals grown in a crystallization vial by vapor diffusion of THF into complex in acetonitrile.	64
Figure 3.15: CD spectra over 4 recrystallization steps, each recrystallization step by vapour diffusion of THF into complex dissolved in acetonitrile.	65
Figure 3.16: UV-Vis and CD of (all S, Λ) and (all R, Δ) - Fe(II) grid complexes measured in acetonitrile as solvent.	66
Figure 3.17: Comparison of experimental CD (top) and simulated CD spectra (bottom) of (all S, Λ) - Fe(II) grid complex.	67
Figure 3.18: Simulated line spectra of A) Low-spin and B) High-spin (all S, Λ) - Fe(II) grid complexes.	67
Figure 3.19: χ T vs. T plots and photo-magnetic characteristics of (all S, Λ)- and (all R, Δ)- complexes.	68
Figure 3.20: Mössbauer spectra for ⁵⁷ Fe enriched (all S, Λ) and (all R, Δ) complexes at 77 K and 300 K, green represents LS, and red represents HS states.	70
Figure 4.1: Level scheme of the electronic structures of the Ln ³⁺ ion obtained after the electronic repulsion, spin-orbit coupling, crystal field splitting, and hyperfine coupling.	74
Figure 4.2: Quadrupole approximations of the 4f-shell electron distribution for the Ln(III) ions. (Reproduced from Ref. 166)	76
Figure 4.3: Energy diagram for the ground-state multiplets of [Pc ₂ Ln] ⁻ (Ln: Tb, Dy, Ho, Er, Tm, or Yb). (Reproduced from Ref. 167)	77
Figure 4.4: AC susceptibility data of A) Mn ₁₂ complex and B) [TbPc ₂] ⁻ TBA ⁺ . (Reproduced from Ref. 26, 31). Here χ'' represents the out-of-phase magnetic susceptibility.	77

Figure 4.5: UV-Vis spectra of porphyrins P1-P4 measured in CHCl ₃ , showing both Soret bands and Q-bands in the 250-800 nm region.....	79
Figure 4.6: ESI-MS characterization of the double-deckers DD1a-DD4a in negative mode (experimental data in blue, and simulated in red).....	81
Figure 4.7: ¹ H NMR spectrum of [Y ^{III} (Pc)(P1)] in CDCl ₃ : DMSO-d ₆ (1:1) in the presence of ca. 10% (by volume) hydrazine hydrate.....	82
Figure 4.8: Simplified molecular orbital diagram for neutral complex [Tb(Porphyrin)(Pc)] (Reproduced from Ref. 184).....	83
Figure 4.9: UV-Vis-NIR absorption spectra of DD1a-DD4a in CHCl ₃ . The peak positions from these spectra were presented in Table 4.1 for comparison.	84
Figure 4.10: UV-Vis-NIR absorption spectra of neutral and anionic forms of DD1a in CDCl ₃ (on left) The figure in inset represents the scheme for conversion neutral to reduced double-decker complex. Clear visualization of colours difference between neutral (brown) and reduced (green) forms of DD1a in CDCl ₃ (on the right).....	84
Figure 4.11: Cyclic voltammogram (left) and differential pulse voltammogram (right) of DD1a-DD4a in CH ₂ Cl ₂ containing 0.1 M [Bu ₄ N][PF ₆] at a scan rate of 50 and 10 mV/s, respectively.	85
Figure 4.12: Top and side views of the molecular structure of neutral complex DD1a , obtained from single crystal showing the SAP coordination, hydrogen atoms are omitted for clarity [Tb(III)-green, C-grey, N-blue, Br-light brown].	86
Figure 4.13: Top and side views of the molecular structure of A) DD2a and B) DD4a complex, obtained from single crystals, showing the SAP coordination, hydrogen atoms are omitted for clarity [Tb(III)-green, C-grey, N-blue, O-red, I-violet].	87
Figure 4.14: A) DC magnetic data for complexes DD1a-DD4a and B) frequency dependence of the out-of-phase (χ'') AC susceptibility of DD1a-DD4a in zero field at 15 K.	88
Figure 4.15: Out of phase AC susceptibilities for neutral sandwich complexes DD1a-DD4a in respective OFs.....	89
Figure 4.16: ln(τ) vs. 1/T plots for neutral double-decker complexes DD1a-DD4a . The continuous line corresponds to the best fit for the Arrhenius equation to determine the activation energy (U_{eff}) and pre-exponential factor (τ_0).	90
Figure 4.17: Top and side views of the molecular structure of A) DD1b and B) DD4b complex obtained from single crystals, showing the SAP coordination, hydrogen atoms are omitted for clarity [Tb(III)-green, C-grey, N-blue, O-red, Br-light brown].	92
Figure 4.18: A) DC magnetic data for compounds DD1b-DD4b and B) frequency-dependent of the out-of-phase (χ'') AC susceptibility of DD1b-DD4b in zero field measured at 15 K.	93
Figure 4.19: Out-of-phase ac susceptibilities for reduced sandwich complexes DD1b-DD4b at zero field.	94
Figure 4.20: ln(τ) vs. 1/T plots for anionic double-decker complexes DD1b-DD4b . The continuous line corresponds to the best fit for the Arrhenius equation to determine the activation energy (U_{eff}) and pre-exponential factor (τ_0).	95
Figure 4.21: Schematic representation of the building blocks and their planned stepwise assembly. The magnetic building blocks are represented in green, and the linking groups in blue.	97
Figure 4.22: Retrosynthesis of heteroleptic binuclear double-decker complexes.	97

Figure 4.23: A) ESI-MS characterization of the neutral complex DD5a in negative mode (experimental data in blue, and simulated in red). B) UV-Vis-NIR absorption spectra of neutral and anionic forms of DD5 in CDCl ₃	99
Figure 4.24: A) DC magnetic data for compounds DD5a and DD5b and B) frequency-dependent of the out-of-phase (χ'') AC susceptibility of DD5a and DD5b in zero field at 15 K.	100
Figure 4.25: A) Out-of-phase ac susceptibilities for reduced sandwich complex DD5b at zero field, and B) $\ln(\tau)$ vs. $1/T$ plot for anionic double-decker complexes DD5b . The continuous line corresponds to the best fit for the Arrhenius equation to determine the activation energy (U_{eff}) and pre-exponential factor (τ_0).	100
Figure 4.26: EPR spectra of Y analogs of DD5a (i.e., Y-DD5a complex in red).	102
Figure 4.27: Temperature-dependent EPR spectra of A) Y-DD5a in solid state. B) Y-DD5a in frozen solution (CD ₂ Cl ₂ :CDCl ₃ in 4:1 ratio) and C) Tb-DD5a in frozen solution state (CD ₂ Cl ₂ :CDCl ₃ in 4:1 ratio).....	102
Figure 4.28: Concentration-dependent EPR spectra of Tb-DD5a ($c = 5$ mM (on left) and $c = 28$ mM (on right) in 4:1 CD ₂ Cl ₂ :CDCl ₃)	103
Figure 4.29: Plot of IT vs. T where I is the double integral of EPR signal proportional to magnetic susceptibility.....	103
Figure 4.30: A) Power dependent EPR spectra of Y-DD5a at constant temperature of 4.2 K. and B) Temperature dependent EPR spectra of Y-DD5a at constant power $P = 8.64 \mu\text{W}$ and at concentration $c = 12.7$ mM.	104
Figure 4.31: Power-dependent EPR spectra of monomeric complex Y-DD5a at 4.2 K at various concentrations of A) 12.7 mM, B) 1.0 mM and C) 0.1 mM.	105
Figure 4.32: ESI-MS of neutral dimeric complexes C1a-C3a in positive mode.	106
Figure 4.33: MALDI-TOF spectra for neutral dimeric complexes C1a-C3a in positive mode.	107
Figure 4.34: ¹ H NMR spectra of Yttrium analogs of dimeric complexes in CDCl ₃ :DMSO-d ₆ (1:1) in the presence of ca. 10% (by volume) hydrazine. The yellow stripe highlights the presence of proton peaks from the linker in the dimers Y-C2 and Y-C3 and its absence in dimer Y-C1	107
Figure 4.35: A) UV-Vis-NIR absorption spectra of C1a-C3a in CHCl ₃ , and B) UV-Vis-NIR absorption spectra of neutral and anionic forms of C3 in CDCl ₃	108
Figure 4.36: Proposed models for neutral dimeric complexes C1a-C3a , respectively obtained by structural optimization. Hydrogen atoms are omitted for clarity [Tb(III)-green, C-grey, N-blue, and O-red].	109
Figure 4.37: A) DC magnetic data for compounds C1b – C3b and B) frequency-dependent of the out-of-phase (χ'') AC susceptibility of C1b , C2b and C3b in zero field at 2 K.	110
Figure 4.38: Out-of-phase ac susceptibilities plots at zero field (on left), and $\ln(\tau)$ vs. $1/T$ plot (on right) for anionic dimeric complexes A) C1b , B) C2b , and C) C3b	111
Figure 4.39: A) ESI-MS analysis and B) MALDI-TOF analysis for neutral trimeric complexes C4 in positive modes.	112
Figure 4.40: A) EPR spectra of Y analog of DD5a (i.e., Y-DD5a complex in red) and Tb-C3a (in blue) and B) the EPR spectra of dimeric complex Tb-C3a dissolved in 4:1 CDCl ₂ :CDCl ₃ (with $c=12$ mM and as frozen sample).	113

List of Schemes

Scheme 2.1: Synthesis of ligand L1 (<i>bpp</i> -COOH).	25
Scheme 2.2: Synthesis of ligand L2 and complexes C1 and C2	31
Scheme 3.1: Synthetic scheme for the preparation of ligand L	54
Scheme 3.2: Synthetic scheme for separation of TRANS (L_T) and CIS (L_C) forms of ligands.	55
Scheme 3.3: Synthesis of S and C grid complexes from TRANS(L_T) and CIS(L_C) ligands, respectively.	56
Scheme 3.4: Scheme for the synthesis of chiral ligands L_a and L_l	59
Scheme 4.1: Synthesis of porphyrins P1-P4 (TMS stands for trimethylsilyl).	79
Scheme 4.2: Synthesis of neutral Tb-double deckers complexes DD1a-DD4a	80
Scheme 4.3: Synthesis of reduced complexes (DD1b-DD4b) from neutral complexes (DD1a-DD4a).	91
Scheme 4.4: Synthesis of porphyrin P5	98
Scheme 4.5: Synthesis of neutral double-decker complex DD5a	98
Scheme 4.6: Synthesis of coupled di-nuclear sandwich complexes C1a-C3a	106
Scheme 4.7: Synthesis of coupled tri-nuclear sandwich complex C4	112

Abstract

The broad field of molecular magnetic materials has potential applications in the storage and processing of the information. Despite of the enormous applications of these materials, till now, there are no suitable candidates ready for the real application. So, over the decades, plenty of research has been progressing to develop suitable candidates in the field of Spin-crossover (SCO) and single molecule magnetism (SMM). In SCO, there are several reports with large hysteresis but found to be not suitable for applications since they do not satisfy many other criteria, which include the stability of the hysteresis that should be around room temperature. At the same time, for the development of the molecular devices, the bottom-up fabrication of these functional molecules is needed. Even though most of the SCO complexes are mononuclear, significant progress has been seen towards polynuclear complexes due to their tunable properties. Molecular chirality is an additional concept that plays a key role in magnetism, particularly in spintronic applications. So introducing the concept of chirality into these polynuclear SCO complexes may result in novel magneto-optical hybrid complexes. On the other hand, in the field of SMMs, lanthanide complexes have risen as attractive materials due to extremely large anisotropy in lanthanide ions. However, most of these complexes show characteristic SMM behaviour at liquid helium temperatures; there is a need for designing newer SMMs with higher blocking temperatures.

In the present thesis, in the first chapter, a brief introduction to fields - SCO and SMM, and their importance to the present technological world is provided. Moreover, the methods for characterization used for these complexes are presented.

The second chapter deals with the studies of bis(pyrazolyl)pyridine (*bpp*) derivatives in bulk and surface. The ligand (*bpp*-COOH) was deposited on Ag(111) surface and was found to form a Kagome lattice structure on annealing, and the ligand showing two types of coordination modes with Fe on Ag(111). STM and XPS were used to study the self-assembled structures formed on the surface. On the other hand, the bulk SCO Fe(II) complexes were prepared using a derivative of *bpp* ligand by varying the counter anions. The structural and SCO properties of the complexes were investigated by various techniques like X-ray diffraction (XRD), Superconducting Quantum Interference Device (SQUID) magnetometry, and differential scanning calorimetry (DSC). Interestingly, our magnetic studies on the complex synthesized with perchlorate anion showed a stable hysteresis of 60 K around room temperature.

The third chapter deals with the chiral resolution of tetra-nuclear Fe(II) SCO grid complexes. For this deconvolution of grid complexes, we designed and synthesized a novel chiral ligand. The complexation of these ligands with Fe(II) resulted in enantiomerically pure grid complexes which were elucidated by XRD and Circular Dichroism (CD) studies. These enantiomeric complexes showed gradual SCO and photo-induced SCO properties.

The CD spectra calculated using TDDFT showed good agreement with experimental results obtained from Mössbauer spectroscopy and SQUID magnetometry.

The fourth chapter deals with mononuclear, binuclear and tri-nuclear Tb-sandwich SMM complexes. We explored and characterized the series of complexes of mixed porphyrin and phthalocyanine mono Tb SMM sandwich complexes by tuning the periphery of porphyrin ligand and redox properties. Moreover, a series of binuclear complexes were synthesized by varying the length of the linker, and their magnetic properties were characterized. Besides, preliminary electron paramagnetic resonance (EPR) studies were performed in the neutral complexes to study the radical.

In summary, various kinds of molecular magnetic architectures were synthesized and characterized in this thesis as below - (i) surface and bulk studies of *bpp* based Fe(II) complexes, (ii) tetranuclear enantiomeric Fe(II) SCO grid complexes, and (iii) mononuclear, binuclear and trinuclear Tb- SMM complexes based on porphyrins and phthalocyanine. Such design and studies of these magnetic materials are key for future devices based on a bottom-up approach.

Zusammenfassung

Das breite Feld molekularer, magnetischer Materialien hat potentielle Anwendungen in der Datenspeicherung und -verarbeitung. Trotz der vielen Anwendungsmöglichkeiten dieser Materialien, gibt es bis heute keine geeigneten Kandidaten für reale Anwendungen. Innerhalb der letzten Jahrzehnte wurden einige Versuche unternommen, geeignete Materialien im Bereich der „Spin-Crossover“ Verbindungen (SCO) und „Single-Molecule Magnets“ (SMM) zu finden. In der Literatur lassen sich einige SCO Verbindungen mit großer Hysterese finden, allerdings waren diese für Anwendungen ungeeignet, da sie nicht in allen Bereichen die erforderlichen Kriterien erfüllten. Zu den Kriterien gehört z.B. die Stabilität der Hysterese bei Raumtemperatur. Ebenfalls werden für die Entwicklung molekularer Maschinen, bottom-up Herstellungsmethoden für die funktionellen Moleküle benötigt. Auch wenn die meisten SCO-Komplexe mononuklear sind, konnte ein erheblicher Fortschritt für polynukleare Komplexe und ihre variablen Eigenschaften beobachtet werden. Molekulare Chiralität ist ein weiteres Konzept, welches entscheidend für den Magnetismus ist, speziell bei spintronischen Anwendungen. Die Einführung des Konzepts der Chiralität in mehrkernigen SCO-Komplexen kann daher zu neuartigen magneto-optischen Hybridkomplexen führen. Andererseits gelten, auf dem Gebiet der SMMs, Lanthanoid-Komplexe aufgrund ihrer sehr großen Anisotropie als attraktive Materialien. Die meisten dieser Komplexe zeigen jedoch ihr charakteristisches SMM-Verhalten erst bei flüssigen Heliumtemperaturen; Es ist notwendig, neue SMMs mit höherer „blocking temperature“ zu entwickeln.

In der vorliegenden Arbeit wird im ersten Kapitel eine kurze Einführung in SCO und SMMs und ihre Bedeutung für die gegenwärtige technologische Welt gegeben. Darüber hinaus werden die für diese Komplexe verwendeten Charakterisierungsmethoden beschrieben.

Das zweite Kapitel befasst sich mit den Untersuchungen von Bis(pyrazolyl)pyridin (*bpp*)-Derivaten als Reinstoff und auf Oberflächen. Der Ligand (*bpp*-COOH) wurde auf einer Ag(111)-Oberfläche abgeschieden und bildete nach dem Tempern eine Kagome-Gitterstruktur. Außerdem koordiniert der Ligand zu Fe auf zwei unterschiedliche Arten auf Ag(111). Mittels STM und XPS Messungen, wurden die auf der Oberfläche gebildeten selbstorganisierten Strukturen untersucht. Die reinen SCO-Fe(II)-Komplexe wurden mit einem Derivat des *bpp*-Liganden, unter Variation der Gegenionen, hergestellt. Die Struktur- und SCO-Eigenschaften der Komplexe wurden mit verschiedenen Methoden wie Röntgendiffraktometrie (XRD), SQUID-Magnetometrie und dynamische Differenzkalorimetrie (DSC) untersucht. Interessanterweise zeigten unsere magnetischen Untersuchungen des mit Perchlorat-Anionen synthetisierten Komplexes eine stabile Hysterese von 60 K bei Raumtemperatur.

Das dritte Kapitel befasst sich mit der Trennung chiraler, tetra-nuklearer Fe(II)-SCO-Gitterkomplexe. Für die Dekonvolution von Gitterkomplexen haben wir einen neuen

chiralen Liganden entworfen und synthetisiert. Die Komplexierung der Liganden mit Fe(II) führte zu enantiomerenreinen Gitterkomplexen, die mittels XRD und Circular dichroismus (CD) nachgewiesen wurden. Diese Enantiomer-Komplexe zeigten sukzessiven SCO sowie photoinduzierte SCO-Eigenschaften. Die mittels TDDFT berechneten CD-Spektren zeigten eine gute Übereinstimmung mit den experimentellen Ergebnissen, die aus Mössbauer-Messungen und SQUID-Magnetometrie erhalten wurden.

Das vierte Kapitel befasst sich mit mononuklearen, binuklearen und trinuklearen Tb-Sandwich-SMM-Komplexen. Wir untersuchten und charakterisierten eine Reihe von Komplexen gemischter Porphyrin- und Phthalocyanin-Mono-Tb-SMM-Sandwichkomplexe, indem wir die Peripherie der Porphyrin-Liganden und die Redox Eigenschaften abstimmten. Darüber hinaus wurde eine Reihe von binuklearen Komplexen, durch Einbringen eines Linkers variabler Länge, synthetisiert und ihre magnetischen Eigenschaften charakterisiert. Außerdem wurden Elektronenspinresonanz-Messungen (EPR) an den neutralen Komplexen durchgeführt, um das Radikal zu untersuchen.

Zusammenfassend wurden im Rahmen dieser Thesis unterschiedliche molekulare und magnetische Gebilde synthetisiert und charakterisiert: (i) Oberflächen- sowie Reinstoffuntersuchungen von *bpp*-basierten Fe(II) Komplexen, (ii) tetranukleare, enantiomere Fe(II) SCO Gitterkomplexe, und (iii) mono-, bi- und trinukleare Tb SMM-Komplexe, basierend auf Porphyrin- und Phthalocyaninliganden. Untersuchungen und das Design solcher magnetischer Materialien sind der Schlüssel um zukünftige Geräte von Grund auf herstellen zu können.

Acknowledgments

First of all, I would like to thank Prof. Mario Ruben for giving me the opportunity to conduct this Ph.D. work in his group and for his continuous support throughout my Ph.D. journey.

I would also like to thank Dr. Eufemio Moreno Pineda, Dr. Svetlana Klyatskaya, Dr. Senthil Kumar Kuppusamy, and Dr. Asato Mizuno for their help and guidance in my work.

I would also like to thank all my labmates – Dr. Conchi, Shirin Shakouri, Sören Schlittenhardt, TingTing Ruan, Dr. Bernhard Schäfer, Dr. Zhi Chen, Sai Prasanna Kumar, Nico Balzer, Michal Valasek, and Liang Xu for the help and creating the friendly atmosphere in the workplace. I never felt away from home because of you guys.

I also would like to thank Mr. Hagen Sparrenberger for being helpful and providing the lab supplies.

I would like to thank Dr. Joachim Burck for helping me with Circular Dichroism (CD) concepts and instrumentation. I would also like to thank Mr. Ansgar Pausch from Prof. Wim Klopper's group, IPC, for performing TDDFT calculations. I also thank Dr. Ananya Baksi from Prof. M. Kappes group for helping and providing valuable suggestions with Ion-Mobility mass spectrometry.

I also thank Mr. Tim Hochdörffer from Prof. Volker Schünemann's group from TU Kaiserslautern for helping with Mössbauer experiments. I also thank Dr. Ivan Salitros for helping with LIEEST experiments.

I would also like to thank our collaborators - Prof. Johannes V. Barth group from TU-Munich, especially Mr. Peter Knecht and Dr. Anthoula Papageorgiou, for performing STM and XPS experiments with our samples provided. I also thank Dr. Benoit Heinrich from IPCMS, Strasbourg for performing DSC, TGA and SWAXS experiments.

I also thank Dr. Jorge Enrique Olivares Pena from Prof. Wolfgang Wenzel group for performing the structural optimizations. I would also like to thank Dr. Athanassios K. Boudalis for performing EPR spectroscopy and helping me to understand them.

I also thank Dr. Eufemio, Dr. Asato and Dr. Olaf for measuring the crystal for single crystal XRD measurements.

I thank my friends, Surya Abhishek, Syamal Praneeth, Sahana, Mridula, Sree Harsha for their company, friendship, and their support during my low times. I also thank my friends Vamsi, Haritha, Raghu, Debalina, Sukeert, Sahithi, Vaishnavi and Bhargavi who are away from me, but always available to talk and support.

I cannot complete this without acknowledging my family, who are everything to me. They support all the time, irrespective of the problem. I thank my parents, Venkateswarlu and Madhavi, and my sister, Niteesha, and brother-in-law, Abhinay Sama for their love and support.

Nithin Suryadevara

To

Amma and Nanna

&

My little nephew Pradyum.

Chapter 1

Introduction

1.1 Challenges in Information Technology

In the current age of electronics and technology, our life revolves around the internet, computers, mobile phones, and other devices, which involve storage and transmission of information. The field of information technology deals with the multidisciplinary approach of applying physics, chemistry, mathematics, and logics for the development of methods for dealing with data. In the last decades, we have advanced from floppy disks and CD-ROMs to hard disks. Today, commercially available hard drives have a storage density up to 1Tbit/in².¹

In recent years, due to the development of high-speed computers and miniaturization of devices, the data density of the hard drive has been increasing at a very high rate, doubling every 12 months, which is much faster than Moore's law predictions.² However, with the extensive use of social networks, the internet, and high-end computing devices, a huge volume of data is being produced every second. Hence, one of the major concerns for today's technology is storing and sustaining rapidly growing data.

To increase the data storage capacity, scientists are trying to miniaturize the size of silicon chips, but this is an expensive method. Alternatively, researchers are studying magnetic molecules opening to the field of “magnetochemistry” to resolve the issues by storing information in a single molecule.³

1.2 Basics in Magnetism

All materials exhibit some kind of magnetism. The origin of magnetism in the materials depends on the orbital and spin motion of the electrons and how these electrons interact with each other. Depending on how the materials respond in the magnetic field at different temperatures, it is classified into five major types: diamagnetic, paramagnetic, ferromagnetic, ferrimagnetic, and antiferromagnetic materials (Figure 1.1).

Diamagnetism: These materials are composed of molecules which have no net magnetic moment (i.e., all the orbital shells are filled with no unpaired electrons). However, when the material is exposed to a magnetic field, a negative magnetization is generated, and thus the magnetic susceptibility of diamagnetic materials is negative. Diamagnetism is a fundamental property of all matter. All materials exhibit some diamagnetic behaviour because of some paired electrons, i.e., ferromagnetic and paramagnetic materials also show diamagnetic behaviour to some extent.

Paramagnetism: The paramagnetic materials possess the magnetic moment due to unpaired electrons in the orbitals of the molecule. In the presence of magnetic field, the magnetic

moments in the material align in the direction of the field, resulting in positive magnetization (M) and thus show positive susceptibility. They do not retain their magnetization on the removal of the magnetic field (Figure 1.1 A).

Ferromagnetism: In ferromagnetic materials, the magnetic moments of atoms or molecules are aligned parallel, in the presence of a magnetic field, but unlike paramagnetic materials, they remain aligned even after removing the field. However, above a certain temperature called Curie's temperature, this material loses its behaviour and becomes paramagnetic materials (Figure 1.1 B).

Anti-ferromagnetism: In these materials, the magnetic moments of the neighboring atoms or molecules are aligned in opposite directions, and thus it has zero net magnetic moments. Like ferromagnetic materials, above a certain temperature, called Neel's temperature, these materials turn into paramagnetic materials since the materials lose their ordering due to thermal agitation (Figure 1.1 C).

Ferrimagnetism: The interaction between the spins in ferrimagnetism is similar to anti-ferromagnetism, but the net magnetic moment is different from zero. It happens in cases where the lattice contains different materials or ions with different magnetic moments in anti-parallel directions (Figure 1.1 D).

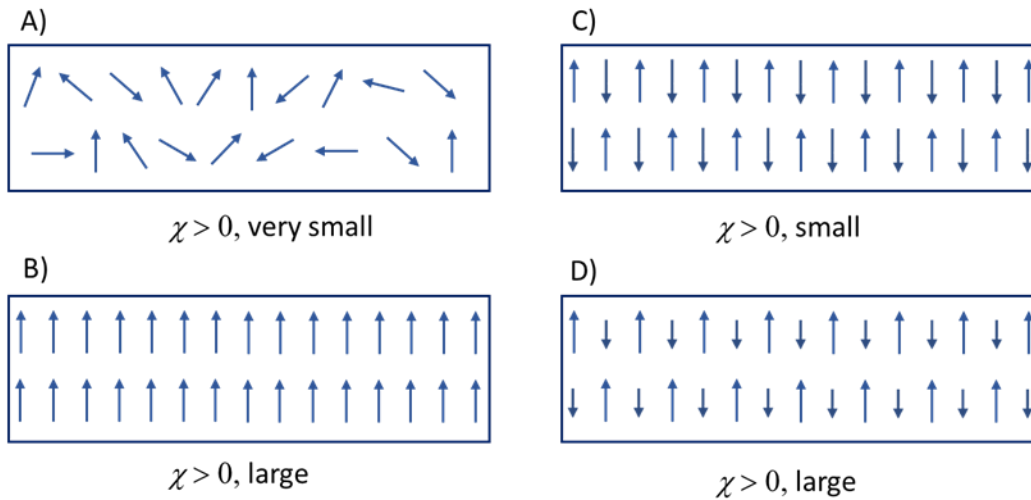


Figure 1.1: Magnetic ordering in A) paramagnetic, B) ferromagnetic, C) antiferromagnetic and D) ferrimagnetic materials (where χ is the magnetic susceptibility).

When a material is placed in a magnetic field H , the net magnetic field inside the material is the sum of the magnetic field applied and the magnetic field generated by the material. The net magnetic field, called magnetic induction, represented by B , is given by

$$B = H + 4\pi M \quad (1.1)$$

$$\frac{B}{H} = 1 + 4\pi\left(\frac{M}{H}\right) \quad (1.2)$$

$$\frac{B}{H} = 1 + 4\pi\chi_v \quad (1.3)$$

Where M is the magnetization (property of the material) and χ_v is the volume magnetic susceptibility. Magnetic susceptibility is defined as a degree of magnetization of a sample in an external magnetic field. The above term is named as volume susceptibility since B , H , and M are defined per unit volume. Susceptibility is independent of the magnetic field; hence, it is convenient to use. For most studies, the molar magnetic susceptibility χ_M is used. It has units of $\text{cm}^3 \text{mol}^{-1}$. All the magnetic measurements in this thesis are presented as $\chi_M T$ in units of $\text{cm}^3 \text{K mol}^{-1}$. The molar magnetic susceptibility of paramagnetic materials is given by Curie's law as

$$\chi_M = C/T \quad (1.4)$$

Where C is the Curie's constant, which depends on the spin multiplicity of the ground state and T is the temperature. It is given by

$$C = N_A \mu_B^2 g^2 S(S + 1)/3k_B \quad (1.5)$$

Where N_A is the Avogadro's number, k_B is the Boltzmann constant, S is the spin quantum number, μ_B is Bohr magneton, and g represents the Landé factor. In most of the paramagnetic compounds, this inverse relationship between T and χ is observed. However, a deviation on extrapolation to zero Kelvin is also observed. This is called Curie-Weiss law and is given by

$$\chi_M = \frac{C}{T - \theta} \quad (1.6)$$

Where θ is the Weiss constant, a positive θ indicates ferromagnetic interaction, whereas a negative θ indicates antiferromagnetic interaction.

1.3 Areas in Magnetochemistry

Magnetochemistry is the field that deals with the relationship between magnetic properties and the structure of a molecule. Spin crossover (SCO) and single-molecule magnetism (SMM) are some of the interesting concepts of research in the field of magnetochemistry. The work presented in this thesis is related to both the fields – SCO and SMMs. In order to use the molecules for real application in electronics and storage devices, magnetic bistability is required. SCO and SMM complexes can exhibit this behaviour. In the following sections, these two topics will be discussed briefly.

1.3.1 Introduction to Spin-Crossover

Background

Spin-Crossover (SCO), also known as spin transition (ST) behaviour is a phenomenon that occurs in 3d metal complexes where the spin state of the metal center changes with the application of external perturbation such as a change in temperature, pressure, light, or influence of the external magnetic or electric field.^{4,5,6,7,8} This phenomenon was observed for the first time in the 1930s by Cambi and Szego on magnetic studies on iron(III) dithiocarbamates by varying the substituents. They observed that some complexes exhibited magnetic susceptibilities corresponding to five unpaired electrons, while some other complexes showed magnetic moments corresponding to one unpaired electron.⁹ Three decades later, in 1964, the first interpretations based on ligand field theory were provided on the Fe(II) system of $[\text{Fe}(\text{phen})_2(\text{NCS})_2]$.¹⁰ Since then, SCO has been observed in iron(II), iron(III), cobalt(II) along with cobalt(III), chromium(II), manganese(II), and manganese(III) complexes to a small extent.^{6,8,11,12,13,14} In the following pages, the brief explanation of the SCO phenomenon is given with a special focus on iron(II), since it is commonly observed and the SCO compounds discussed in this thesis are Fe(II) complexes.

The octahedrally coordinated first-row transition metal complexes with the configuration of d^4 - d^7 can exist in two states. According to crystal field theory, in the presence of an octahedral field, the five d -orbitals lose their degeneracy and split into two sets: e_g ($d_{x^2-y^2}$, d_{z^2}) and t_{2g} (d_{xy} , d_{yz} , d_{xz}) with a different energy. The value of the crystal field energy (Δ_o) depends on the types of ligands, and if the Δ_o is larger than pairing energy P , ($\Delta_o \gg P$), then the electrons occupy in low-spin fashion. In the other case, $\Delta_o \ll P$, the electrons obey Hund's first rule and takes the high-spin state in which spin multiplicity is high. In the case where the difference between Δ_o and P is small, transitions can occur between HS and LS as a result of external stimuli (Figure 1.2).

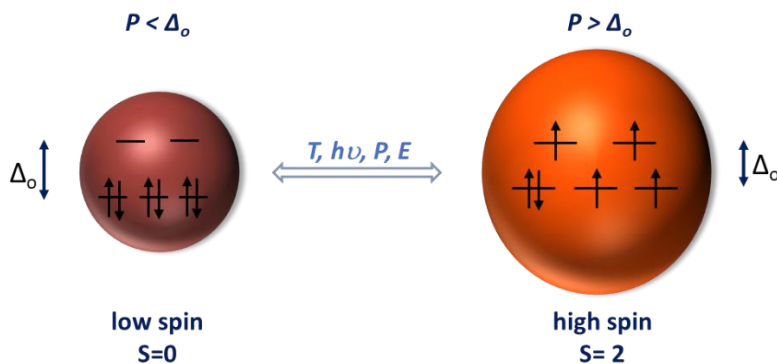


Figure 1.2: Schematic representation of the SCO phenomena in a Fe(II) complex with d^6 electronic configuration.

Whether the complexes show SCO or not depends conclusively on the ligand field strength. Tanabe-Sugano (TS) diagrams illustrate the energy splitting of orbitals of a free ion (d^n) as a function of an octahedral ligand field.¹⁵ The TS diagram for iron(II) with $3d^6$ configuration is shown in Figure 1.3. According to this diagram, at $\Delta=0$, the metal is a free ion, and in the presence of the ligand field, the 5D free ion state splits into $^5T_{2g}$ as ground state and 5E_g as an excited state. On increasing the field strength, over critical value Δ_c (i.e., at $\Delta = P$), $^1A_{1g}$ becomes the stable ground state. In general, Δ depends on the type of ligand and metal used in the complexes. Among various Iron(II) complexes, the two with contrasting behaviour are $[\text{Fe}(\text{H}_2\text{O})_6]^{2+}$ and $[\text{Fe}(\text{CN})_6]^{4-}$, which adopt HS and LS, respectively. ST complexes are those which has a ligand field near the crossing point Δ_c , where the difference between the HS and LS is within the magnitudes of $k_B T$. As discussed before, this small difference in energy can be fulfilled by a change in temperature, pressure, on irradiation of light, or with electric or magnetic fields.

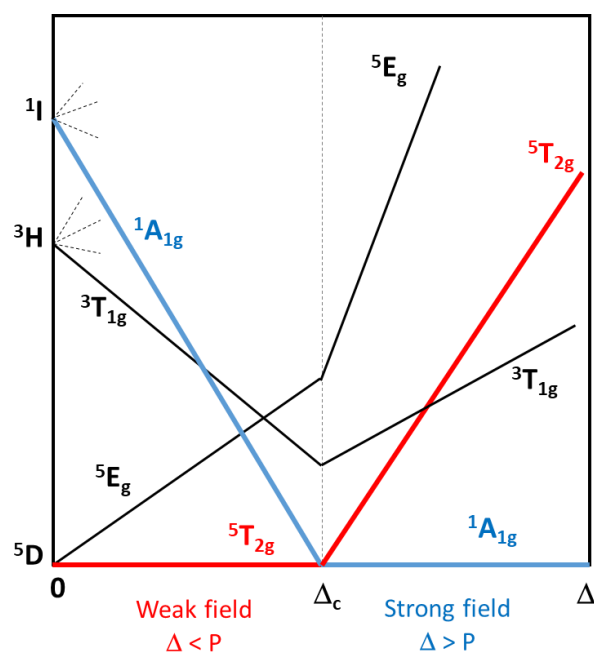


Figure 1.3: Simplified Tanabe-Sugano (TS) diagram of d^6 metal ions in an octahedral environment. (Reproduced from Ref. 15)

The first direct consequence of this change in electronic configuration from LS to HS is an increase in metal-ligand bond length by 10% and, thus, an increase in the volume of the octahedral complex by 25%.^{15,16} This is because e_g orbitals have an anti-bonding character, with increasing population of electrons, the metal-ligand bond length increases. On the contrary, an increase in the number of electrons in t_{2g} , influences the electron back donation between the metal ion and the empty π^* orbital of the ligands and thus decreases the bond length.

However, the ligand field splitting depends not only on the type of ligands but also on the metal-ligand distance, r , with $\Delta \sim 1/r^n$ ($n = 5 - 6$). In order to understand the SCO and Δ_c in detail, Figure 1.4 shows the configurational coordinate diagrams (electronic energies) of particular spin states (LS and HS) as a function of distance r . The E vs. r plot shows two parabolas. The horizontal displacement of the potential wells corresponds to $\Delta r = r_{HS} - r_{LS} = 0.2 \text{ \AA}$, while the vertical displacement indicates that the LS state is stabilized over HS by ΔE_o .¹⁷

The parabolic curvature for LS is larger, and the number of vibrational levels per unit energy is larger for the HS state. In order for SCO to occur, the zero-point energy (ZPE) $\Delta E_o = \Delta E_{HS} - \Delta E_{LS}$ should be in the range of accessible energies $k_B T$. At low temperatures, even SCO complexes are in LS state. As the temperature increases, the thermal energy is transformed into vibrational energy by populating the excited vibrational levels at the crossing points of both the HS and LS states. According to the Franck-Condon principle, it is the place where LS \leftrightarrow HS transition takes place, and this point corresponds to Δ_c , which was explained in the TS diagram. The enthalpy loss by a transition from LS to HS states is balanced by gaining entropy in the HS state since HS has a higher density of vibrational states and larger spin multiplicity.¹⁷

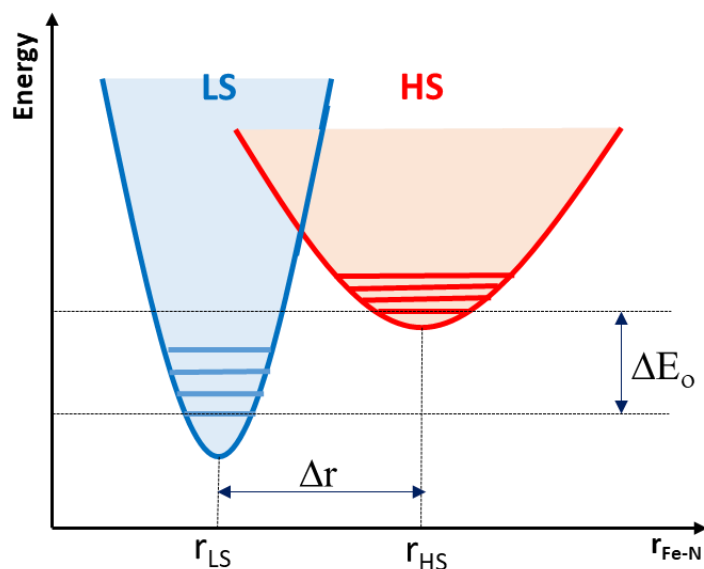


Figure 1.4: Schematic representation of the HS (red) and LS (blue) potential wells for an octahedral iron(II) complexes. (Reproduced from Ref. 8)

In addition to the above changes, several other reversible changes in physical properties in SCO materials can be observed on ST, which include¹⁶ (Figure 1.5),

(a) change in the magnetic moment due to change in the number of unpaired electrons, Fe(II) in LS has no unpaired electrons, i.e., diamagnetic (with $S=0$), and Fe(II) in HS has four unpaired electrons, i.e., paramagnetic (with $S=2$). (b) change in structural properties like unit cell parameters (a , b , c , α , β , γ , V) and bond lengths (Fe(II)-N), (c) change in colour (thermochromism), (d) heat is evolved on SCO from HS to LS and is taken up while going back to HS, thus changes in thermodynamical quantities (ΔS , ΔH , C_p), (e) change in dielectric constant ϵ , (f) electron density at nucleus differs for both HS and LS; thus, isomer shift and quadrupole splitting are very different.

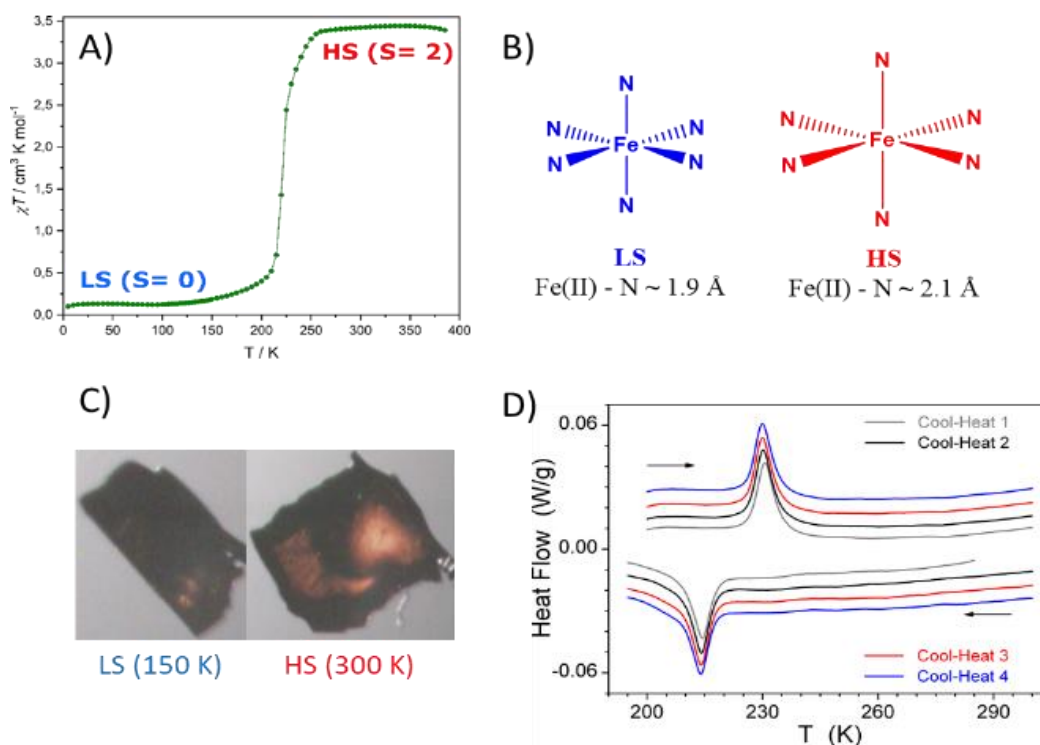


Figure 1.5: Changes in physical properties accompanied by SCO phenomenon: A) change in a magnetic moment; B) change in structural properties, C) thermochromism, and D) change in heat capacity.

Types of SCO behaviour and cooperativity

One of the most significant consequences of the spin-transition phenomenon is a change in magnetic properties. The change from LS to HS can increase the magnetic moment of the system, and measuring the change is the most convenient way for monitoring spin transitions. An ST curve is usually obtained by plotting the fraction of high spin content (γ_{HS}) vs. temperature (T). This curve shows a crucial characteristic feature $T_{1/2}$, which is defined as the temperature at which both LS and HS are in a 1:1 ratio. Moreover, these curves provide a lot more information through investigation of the shape of the curve, as shown in Figure 1.6. Although SCO is a purely molecular phenomenon, the shape of the transition curves

depends on the cooperative interaction between the molecules, i.e., it strongly depends on the intermolecular interactions.

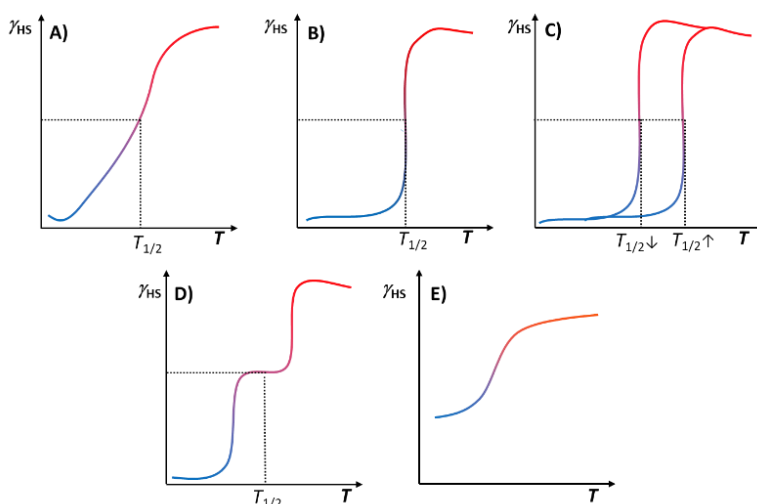


Figure 1.6: Various types of ST curves: A) gradual, B) abrupt, C) with thermal hysteresis, D) two-step, and E) incomplete ST. γ_{HS} on Y-axis represents the fraction of HS content (Reproduced from Ref. 16).

Cooperativity describes the interaction between the switching molecules and describes how the change in the structure of one molecule affects the structure of the neighboring molecule in the same material. Depending on the nature of the material, the curves can adopt several forms that include gradual, abrupt, hysteric, incomplete, or multi-step SCO (Figure 1.6).

LIESST measurements

Along with a change in temperature as a standard perturbation, light is another common external stimulus to induce ST from LS to HS. Irradiation of light into the SCO complex at low temperature could induce LS-HS conversion, with metastable HS state with a very long life.^{18,19} This photo-physical phenomenon is called the Light-Induced Excited Spin State Trapping (LIESST) effect. This method was firstly observed for Fe(II) SCO complexes by Decurtins and coworkers in 1984.¹⁸ Later on, the reverse LIESST effect was also observed, which indicates the possibility of switching back from HS to LS through irradiation of light of higher wavelengths. Figure 1.7 shows a simple illustration of the LIESST effect using a Jablonski diagram.²⁰ Irradiation of laser light excites the LS state (1A_1) to spin allowed parity forbidden 1T_1 or 1T_2 (triplet) ligand field states. These decay fast via two consecutive intersystem crossing (ISC) processes, to spin-triplet 3T_1 or 3T_2 , and finally to 5T_2 (HS state). The decay of 5T_2 to 1A_1 is highly spin forbidden and parity forbidden.⁸ Thus, this metastable HS state has a long lifetime at low temperatures.

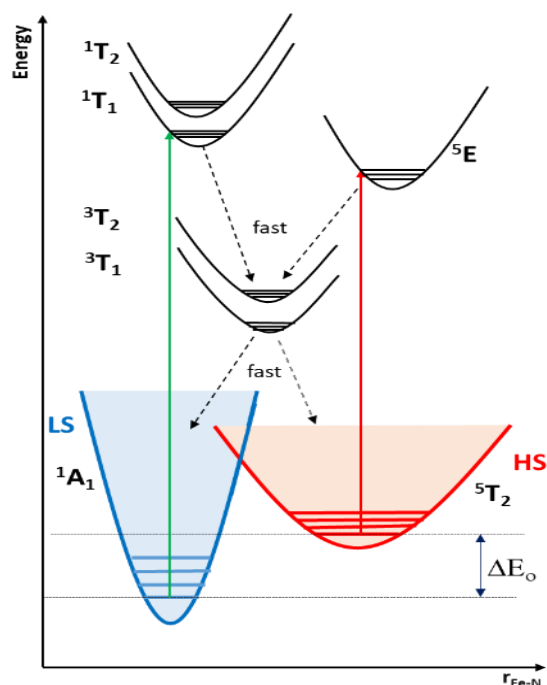


Figure 1.7: The mechanisms of LIESST and reverse-LIESST in iron(II) SCO compounds (Reproduced from Ref. 8).

Several techniques can be used to detect the LIESST effect, such as Raman, Mössbauer, and optical reflectivity spectroscopies. Even so, the SQUID magnetometer, coupled with an optical source, is used widely nowadays for these experiments. The LIESST effect is characterized by the conversion efficiency from LS to metastable HS state and critical LIESST temperature (T_{LIESST}). T_{LIESST} is defined as the temperature above which the light-induced HS information is erased. This is obtained from the minimum of the $\frac{\partial}{\partial T} \chi_M T$ vs. T curve. It was also observed that the higher the thermally induced spin transition temperature, the lower is T_{LIESST} , and this is referred to as the inverse energy gap law.

Detection of Spin-Crossover

As mentioned earlier, the rearrangement of spins that occur during SCO can lead to various changes in physical properties that depend on electronic distribution. The major ones among them are variation in bond lengths and crystal lattice dimensions, magnetic properties, and colours. With the help of these changes in properties, there are various techniques to monitor the ST behaviour. Table 1.1 below shows a list of analytical methods that can be used. Some of these methods used in this thesis are briefly explained in the following sections.

Table 1.1: Various analytical methods for monitoring SCO behaviour.

Analytical Method	Characteristic Value
Magnetic Measurements	Magnetic susceptibility
Mössbauer Spectroscopy	Isomeric shift and Quadrupole splitting
X-Ray Diffraction	Metal-Bond distances
NMR Spectroscopy	Paramagnetic chemical shifts and magnetic susceptibility
Calorimetry	Heat capacity
UV-Vis spectroscopy	d-d/CT excitation energy
Vibrational Spectroscopy	Metal-ligand vibrational energies

Magnetic susceptibility measurements

As shown before, $3d^6$ metal complexes can exist in two different states - paramagnetic in HS state whereas diamagnetic in LS states; thus, magnetic susceptibility measurements at various temperatures is a primary technique to investigate the Fe(II) SCO complexes. These methods use the techniques of using measuring magnetic susceptibility measurements at various temperatures, and thus one can extract the spin state at a particular temperature. Among these magnetic susceptibility measurements, Faraday-balance and Gouy-balance are the oldest examples, but they became less important since they can operate mostly only at room temperatures. Among the modern methods, SQUID magnetometers (Superconducting QUantum Interference Device) are a powerful tool for finding the magnetic susceptibility of the given complexes.

A SQUID is a very sensitive magnetometer to detect incredibly small magnetic fields. It uses the properties of electron pair wave coherence and Josephson junctions to detect the very small magnetic fields. Josephson junctions are junctions where two superconductors are separated by an insulating material, through which electrons tunnel from one conductor to the other without an applied voltage. The current passing through this Josephson junction is modulated by the samples' magnetic flux, and this is detected by the system.

A commercial SQUID magnetometer (Figure 1.8) consists of four main components – (a) a superconducting magnet, (b) one or more superconducting detection coils coupled inductively to the sample, (c) the SQUID connected to the detection coil and (d) a superconducting magnetic shield. When a sample is moved up and down, it produces changes in magnetic flux in the pickup coils. The above change in magnetic flux changes the current in the detection system and thus produces variations in the SQUID output voltage, which is proportional to the magnetic moment of the sample. Typically, the input coils and SQUID are maintained in liquid helium to maintain them in a superconducting state.

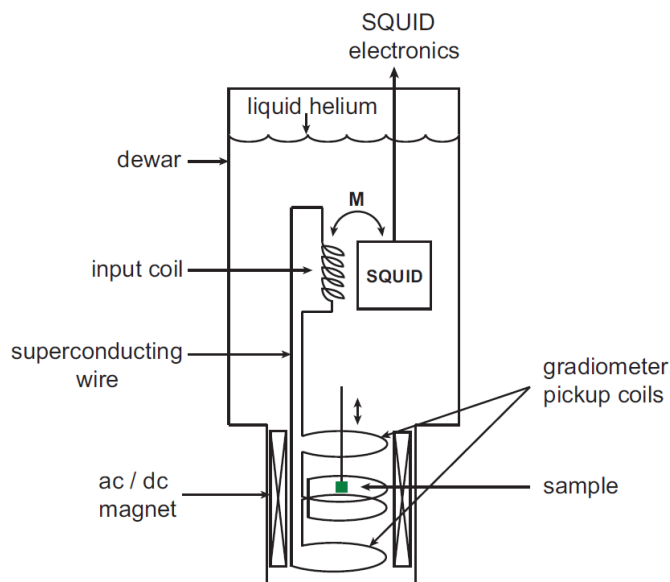


Figure 1.8: Schematic diagram of the SQUID magnetometer (reproduced from SQUID manual).

If the sample does not have a permanent magnetic moment, an external magnetic field (DC field) can be applied to magnetize it. When the sample is placed in the region of the detection coils, the change in detected magnetisation is proportional to the magnetic moment of the sample. With this magnetisation, molar magnetic susceptibility (χ_M) can be measured, which is a measure of the degree of the extent to which magnetic dipoles align in the external magnetic field (DC field) per unit mole of the sample. Using the data (longitudinal moment) from SQUID measurements, χ_M of the material can be calculated with the following equation –

$$\chi_M = \frac{\text{Longitudinal Moment}}{\text{External Field}} \times \frac{\text{Molecular Weight}}{\text{Weight of Sample}} \quad (1.7)$$

For studying the SCO complexes, the magnetic data from SQUID is processed and plotted as $\chi_M T$ vs. T with $\chi_M T$ on Y-axis and T on X-axis. In Fe(II) SCO complexes, the HS state is paramagnetic with four unpaired electrons ($S=2$), and LS state is diamagnetic with no unpaired electrons ($S=0$). These two states can be distinguished since the number of unpaired electrons is different, which is related to $\chi_M T$, calculated from the following equation.

$$\chi_M T = 0.12505 g^2 S(S + 1) \quad (1.8)$$

$$\mu_{\text{eff}} = g\sqrt{S(S + 1)} \quad (1.9)$$

Employing these equations, Table 1.2 shows the values of $\chi_M T$ corresponding to the number of unpaired electrons.

Table 1.2: Values of $\chi_M T$ and μ_{eff} calculated for the number of unpaired electrons.

No. of Unpaired Electrons	S	$\chi_M T$ ($\text{cm}^3 \text{K mol}^{-1}$)	μ_{eff} (B.M)
0	0	0	0
1	0.5	0.375	1.73
2	1	1.000	2.83
3	1.5	1.876	3.87
4	2	3.001	4.89
5	2.5	4.377	5.92

X-Ray Diffraction

Single crystal X-ray diffraction study of the complex is one of the most valuable methods of analysis for SCO complexes. It gives not only the structure of the complex but also several other structural parameters of the complex, which are highly useful for the analysis of the spin state of the system. This vital information includes bond length, unit cell parameters, distortion parameters, and these parameters can also reveal intermolecular interactions. Upon ST from LS to HS, the metal-ligand bond lengths increase typically from *ca.* 1.9 Å in LS to *ca.* 2.1 Å in HS.^{8,16} This can be studied using variable temperature crystal structure determination to help in understanding the SCO process and the effect of the molecular interactions. Along with this, the transition from LS to HS results in changes in parameters of unit-cell and volume of the complex. The ST from LS to HS also produces deformation in Fe(II)N₆ octahedral geometry. This deviation from the octahedral geometry is indicated by the distortion parameter Σ and Θ which will be discussed in Chapter 2.

Differential Scanning Calorimetry

Differential scanning calorimetry (DSC) technique is used to identify the presence and nature of the phase transition of a material. This experiment monitors the change in the heat capacity of the sample by varying the temperature. This method measures the difference in heat required to increase the temperature of the sample and reference as a function of temperature. This heat flow can be either positive for endothermic transitions or negative for exothermic ones. Therefore, DSC has been widely used in the field of SCO to study the details of phase transitions.⁸

DSC measurements give the information of thermodynamic quantities like entropy and enthalpy change during the spin transition. SCO can be considered as a phase change process; thus, the Gibbs energy change is given by $\Delta G = \Delta H - T\Delta S$. Generally, the enthalpy change ($\Delta H = H_{\text{HS}} - H_{\text{LS}}$) is around 10-20 kJ mol⁻¹, whereas the entropy change ($\Delta S = S_{\text{HS}} -$

S_{LS}) is around 50-80 kJ mol⁻¹ K⁻¹. ST is an entropy-driven process since the degree of freedom of the HS complex is higher than that of the LS complex. Out of this, approximately 25% (13 kJ mol⁻¹ K⁻¹) is due to change in spin multiplicity from LS to HS, whereas the significant part originates from changes in intra-molecular and inter-molecular vibrations.

Spin-Crossover applications

Due to the presence of bistability between the LS and HS in SCO complexes, these classes of magnetic materials have high potential applications, for example, in high-capacity memory devices for information storage and temperature sensors and as an active element of the display.^{21,22} Although it has been several decades that SCO complexes have been introduced, it is still a great challenge to use them in information technology. Kahn and coworkers have reported several requirements to be fulfilled in SCO compounds in order to use them in the devices.²¹ But most of them reported till now have not fulfilled all the requirements.⁷

- The transitions for both the cooling and heating modes should be abrupt.
- Thermal hysteresis must be present with a hysteresis width of around 50 K.
- The transition temperatures ($T_{1/2\downarrow}$ and $T_{1/2\uparrow}$) should be around room temperature, ideally with room temperature as the center of the hysteresis.
- The ST should cause a change in the colour, which can be easily detectable.
- More importantly, the complex should show stable hysteresis even after several thermal cycles.

1.3.2 Introduction to Single Molecule magnetism

Background

Single-molecule magnets are a class of metal-organic compounds that, below a blocking temperature, show super-paramagnetic behaviour, and hysteresis, that is purely of molecular origin. Since its discovery, this field has become a prominent area of research due to its enormously rich physical properties— and thus, for two decades, numerous amount of SMMs were produced and studied.^{23,24} The study of SMM started in the 1990s with the first-ever reported SMM [Mn₁₂O₁₂(CH₃COO)₁₆(H₂O)₄]·2CH₃COOH·4H₂O. Even though its synthesis was reported in the 1980s,²⁵ the SMM nature was investigated in 1993 by Gatteschi and coworkers, with it showing magnetic hysteresis at 4 K, which was a major breakthrough in the field of molecular materials.²⁶

Traditional magnets consist of a large number of magnetic domains. They show hysteresis in M vs. H plots. However, in the case of SMMs, each molecule is considered to be a magnetic domain. Each molecular magnetic domain can be magnetized upon the application of an external field and can slowly relax on the removal of the external field. This ability of a single-molecule to work as a magnet can be highly important because of its

application in high-density memory devices, spintronics, etc. However, up to date, they were only at low temperatures i.e., blocking temperature (T_B , *vide infra*) is low.

After the observation of SMM behaviour in the polynuclear Mn_{12} complex, the following few years, research was mainly focused on the synthesis/studies of polynuclear complexes with different 3d-metals. But before we go any further, it is important to get into details of few quantification terms for an SMM: blocking temperature (T_B) and the effective energy barrier (U_{eff}). The former is defined as the temperature below which hysteresis of the magnetization curve is observed. It can also be defined as the temperature at which a peak is observed in the out of phase susceptibility (χ'') at a given frequency. The latter one, the effective energy barrier, is referred to as anisotropy or relaxation barrier. This is determined by relaxation times from AC susceptibility measurements using out-of-phase and in-phase components.

The Mn_{12} complex consists of four Mn(IV) ($S = 3/2$) and eight Mn(III) ($S = 2$) ions that are coupled antiferromagnetically to yield a complex with a spin $S = 10$. The spin ground state is characterized by a large negative zero-field splitting (ZFS) term D . The combined effect of spin multiplicity with negative ZFS (D) results in a large U_{eff} , which is given by $S^2|D|$ or $(S^2-1/4)|D|$ for integer spin and half-integer spin, respectively.

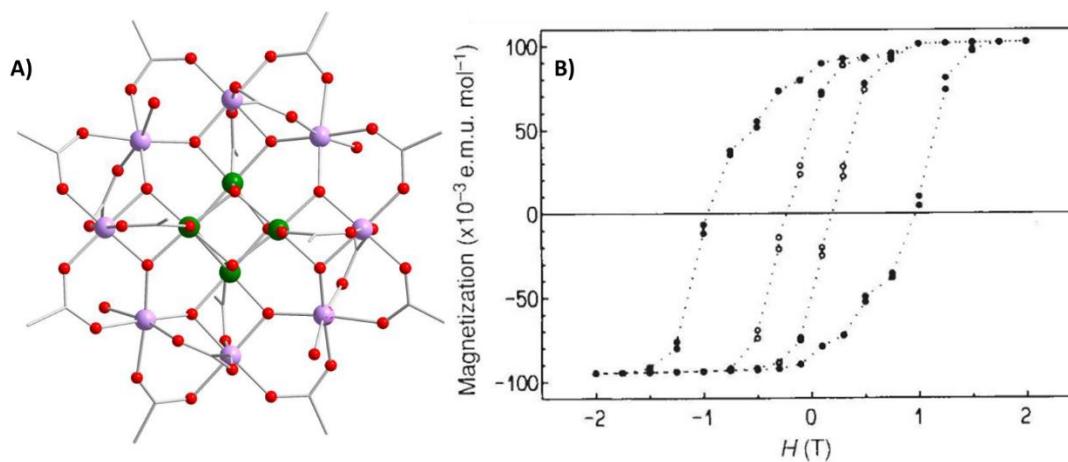


Figure 1.9: A) Molecular structure of the Mn_{12} complex. Purple (Mn^{3+}), dark green (Mn^{4+}), red (O), and grey (C). B) Magnetisation hysteresis curve was measured on a single-crystal of Mn_{12} at 2.2 K (\circ) and 2.8 K (\bullet) (Reproduced from Ref. 26).

In 3d SMMs, the barrier can be described by a double-well scheme with a negative value of the ZFS parameter, stabilizing the spin state with large $M_s=10$ and $M_s=-10$ in the lowest energy (Figure 1.10). So, from this, further studies were focused on improving the ground state of upcoming new complexes to increase the energy barrier. It became apparent that to improve the SMM properties, the anisotropy parameters, and the spin parameters have to be enhanced. Research has been focused on increasing the spin (S) of the complexes, but for a long period of time, the $Mn_{12}Ac$ complex possessed the highest known anisotropy

barrier of $U_{\text{eff}} = 61 \text{ cm}^{-1}$ (71 K). Despite a tremendous amount of research on polynuclear transition metal-based SMMs with high nuclearity,²⁷ and spin (S),²⁸ the highest energy barrier achieved over two decades is 86 K,²⁹ which is only 15 K above the first-ever observed. For all these, it was understood that lack of anisotropy had made them inefficient SMMs, and the importance of magnetic anisotropy was realized.

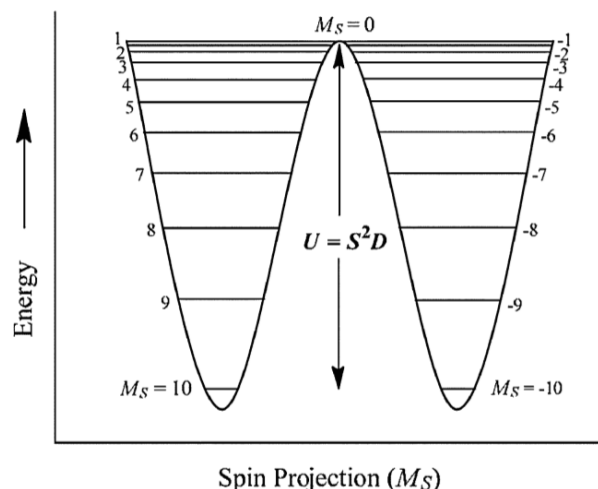


Figure 1.10: The energy barrier U_{eff} for the reversal of the spins between the spin 'up' ($M_S = 10$) and 'down' ($M_S = -10$) state for Mn_{12} complex (Reproduced from Ref. 30).

When in 2003, Ishikawa and coworkers showed that lanthanide ions show strong anisotropy, they turned out to be the best and most promising candidates for SMMs with high energy barriers. The $[\text{TbPc}_2]^-$ complex exhibited slow relaxation of magnetization at 50 K and showed a barrier U_{eff} of 230 cm^{-1} (331 K).³¹ The high energy barrier resulted in large unquenched orbital moments and strong spin-orbit coupling, leading to strong anisotropy in lanthanides. The magnetism of Lanthanides will be briefly introduced in Chapter 4.

SMM Measurements

The important parameter for evaluating the performance of an SMM is the blocking temperature T_B . This can be obtained from either (a) AC susceptibility measurements, (b) hysteresis loop measurements, or (c) zero-field cooling (ZFC) and field cooling (FC) magnetization curves. Usually, the second method, the hysteresis loop measurement, is adapted, but one has to be careful while comparing the temperature since the hysteresis depends on the field sweep. Nowadays, the most efficient method for identifying SMM behaviour is AC magnetic measurements. For the characterization of SMMs in this thesis, AC susceptibility measurements were performed using a conventional SQUID magnetometer.

In these measurements, the sample is placed in between the two coils, where a small oscillating field ($< 10 \text{ Oe}$) is generated inside the coils. This AC field induces the magnetic

moment in the sample and is detected by the secondary coils. This AC field frequency is varied during the measurements between 0.1 – 1500 Hz, and this results in in-phase (χ') and out-of-phase (χ'') signals. When the frequency of the AC field is in resonance with the flipping (reversal) rate of the magnetic moment, a peak is observed in χ'' vs. ν plots. This is the rate at which the spin flips between the two potential wells. The AC susceptibility is given as

$$\chi(\omega) = \chi_s + \frac{\chi_T + \chi_s}{1 + i\omega\tau} \quad (1.10)$$

Where τ is the relaxation time, which is the time required for the thermal equilibrium to be established. The measured susceptibility is the isothermal susceptibility, χ_T when the angular frequency ω of the ac field is very low ($\omega\tau \ll 1$) and is the adiabatic susceptibility, χ_s when the angular frequency ω of the ac field is very high ($\omega\tau \gg 1$). The real and imaginary components of the susceptibility are given by

$$\chi'(\omega) = \chi_s + \frac{\chi_T - \chi_s}{1 + (\omega\tau)^2} \quad (1.11)$$

$$\chi''(\omega) = (\chi_T - \chi_s) \frac{\omega\tau}{1 + (\omega\tau)^2} \quad (1.12)$$

When the relaxation process is not characterized by a single τ , the ac susceptibility is given by³²

$$\chi(\omega) = \chi_s + \frac{\chi_T + \chi_s}{(1 + i\omega\tau)^{(1-\alpha)}} \quad (1.13)$$

Then, the real and imaginary components of the susceptibility are given by

$$\chi'(\omega) = \chi_s + \frac{(\chi_T - \chi_s)[1 + \omega\tau^{1-\alpha} \sin(\alpha\pi/2)]}{1 + 2(\omega\tau)^{1-\alpha} \sin(\alpha\pi/2) + (\omega\tau)^{2(1-\alpha)}} \quad (1.14)$$

$$\chi''(\omega) = (\chi_T - \chi_s) \frac{(\omega\tau)^{1-\alpha} \cos(\alpha\pi/2)}{1 + 2(\omega\tau)^{1-\alpha} \sin(\alpha\pi/2) + (\omega\tau)^{2(1-\alpha)}} \quad (1.15)$$

with the α factor describing the distribution of the relaxation times in a sample. When α is zero, the equation 1.14 and 1.15 transforms into 1.11 and 1.12, respectively, and indicates the presence of only one relaxation process in the molecule.

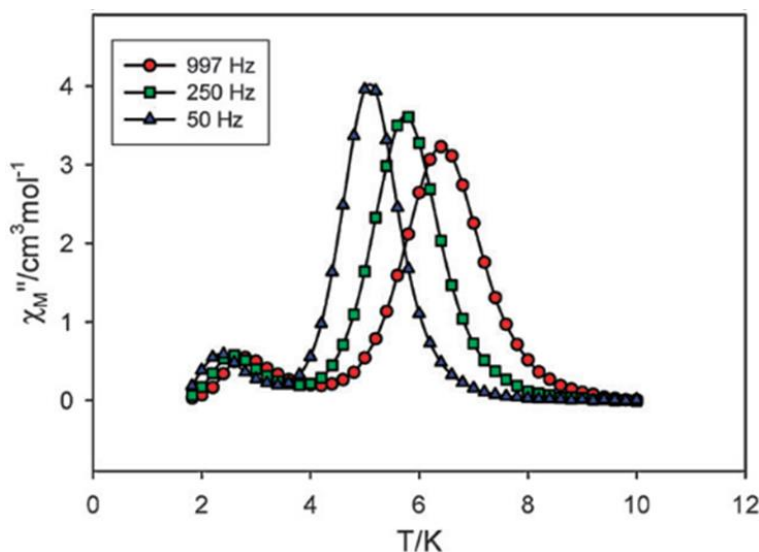


Figure 1.11: χ_M'' signals for a microcrystalline sample of $[\text{Mn}_{12}\text{O}_{12}(\text{O}_2\text{CCH}_2\text{Br})_{16}(\text{H}_2\text{O})_4]$ and shift in peaks can be observed on increasing the frequency. (Reproduced from Ref. 33)

The shift in the peaks in χ'' vs. T or χ'' vs. ν , is the characteristic of the SMM behaviour, as shown in Figure 1.11. The maximum of χ'' will be observed when the frequency satisfies the relation $\omega\tau=1$. Thus the relaxation time is calculated using the following equation

$$\tau = \omega^{-1} = \frac{1}{2\pi\nu} \quad (1.16)$$

Once all the χ' vs. ν and χ'' vs. ν isotherms are employed, relaxation time from each temperature is determined, it is used to determine the U_{eff} using Arrhenius law

$$\tau = \tau_o \exp\left(\frac{U_{\text{eff}}}{k_B T}\right) \quad (1.17)$$

$$\ln\tau = \ln\tau_o + \frac{U_{\text{eff}}}{k_B T} \quad (1.18)$$

Where τ_o is a pre-exponential factor and has a value in the range of $10^{-7} - 10^{-10}$ s. On plotting $\ln(\tau)$ vs. $1/T$, U_{eff} can be extracted from the slope, and the plot also offers details about the relaxation pathways.

Applications

SMM complexes have extremely long magnetization relaxation times (even in years), and this combined with their molecular-scale, makes them attractive towards high-density information storage. Moreover, their inbuilt rich quantum phenomena, which include quantum tunneling effects and quantum interference, make them applicable for quantum computing and molecular spintronics.^{34,35} Till now, the SMMs reported were showing

magnetic bistability at very low temperatures. To make them applicable for devices, researchers are exploiting new complexes to find magnetic bistability around room temperature.

1.3.3 Aims of the thesis

Magnetic molecules are the key components that help in reducing the size of data storage devices. The aim of the present work is to examine several aspects of the above-mentioned fields of magnetochemistry.

Aim 1 – To study the self-assembly of bis(pyrazolyl)pyridine (*bpp*) based ligand and their surface coordination with Fe- atoms on Ag(111) and to engineer the hysteresis in $[\text{Fe}(\text{bpp})_2]^{2+}$ family SCO complexes.

Aim 2 – To separate the enantiomeric tetra-nuclear Fe(II) SCO grid complexes, with the aim to synthesize new multifunctional materials.

Aim 3 – To synthesize and characterize a new class of Tb(III) SMM complexes based on porphyrin and phthalocyanine ligands. Further, to synthesize and characterize new polynuclear magnetic architectures by using various bridging molecules.

Chapter 2

Iron(II) bis(pyrazolyl)pyridine (*bpp*)-based molecules – From surface to bulk

2.1 Introduction

The field of SCO research has shown continuous attraction, because of its vast potential applications in several fields, for example, in the fabrication of high capacity memory devices for information storage, display technologies, magnetic resonance imaging contrast agents, molecular sensors, etc.^{4,7,11,16,22,36} To use these materials for practical applications, they should fulfill some requirements like – abrupt transition, wide thermal hysteresis near room temperature with stability and reproducibility, and chemical stability.^{16,36,37,38}

In the literature, a few of the requirements mentioned above were satisfied by various families of compounds. One of them is the family of triazoles ligands. The 1D-triazole-based iron(II) complexes exhibit cooperativity with wide thermal hysteresis width of 15-80 K.^{9,10,11,12,13,39-44} Hoffman type frameworks are another class of complexes that exhibit RT transition and wide hysteresis loops. These are 3D hetero-metallic networks with the general formula of $[\text{Fe}^{\text{II}}(\text{pz})\text{M}^{\text{II}}(\text{CN})]_n \cdot x\text{H}_2\text{O}$ (pz= pyrazine, CN=cyano, and M=Pd, Pt, Ni).^{15,16,17,18} Recently, a new Fe(II) SCO framework was reported based on bicyclic ligands 1,6-naphthalene, which has shown stable thermal hysteresis of 19 K around RT.⁴⁹ Along with this, bis(pyrazolyl)pyridine (*bpp*) (Figure 2.1 A) based mononuclear Fe(II) compounds have become attractive since Halcrow and coworkers reported an iron(II) complex on *bpp* showing abrupt spin transition behaviour around room temperature with 3 K hysteresis.⁵⁰ Compared to the other two systems, this *bpp* systems are mononuclear and thus have molecular character.

Since the report on *bpp* based Fe(II) complexes by Halcrow and coworkers, it has become a popular family of compounds in the field of SCO research.⁵⁰ This is the result of the flexibility of appending the functional groups on the skeleton of the ligand, which can tune the ligand field and thus affect the spin state of the coordinating Fe(II) ion. Till now, more than 100 reports have been published on Fe(II) complexes of *bpp* molecules, in which around half of them are SCO active.⁵¹ Since many reports on these complexes were available, and more than half of them show SCO, the structure-property relationships were deduced from the available crystal structures.^{21,22,23,24,25,26,27} The primary and basic structural parameter is the average Fe-N bond distance, which varies from ~2.1 Å in HS complexes to ~1.9 Å in LS complexes. Other structural indices used for the quantification of SCO behaviour are angular parameters Σ and Θ which are defined as follows –

$$\Sigma = \sum_{i=1}^{12} |90 - \beta_i| \quad (2.1)$$

$$\Theta = \sum_{j=1}^{24} |60 - \gamma_j| \quad (2.2)$$

Here β_i are the 12 cis N-Fe-N angles about the Fe(II) atom, and γ_j are the 24 unique N-Fe-N angles measured on the projection of two triangular faces of the octahedron (Figure 2.1 B). Σ is a general measure of the deviation of the metal ion from the ideal octahedral geometry, whereas Θ specifically indicates the distortion towards the trigonal prismatic structure. For a perfectly octahedral LS complex, both the parameters are zero. Σ and Θ are usually larger in a HS complex. Hence the change in Σ and Θ between the spin states reflects the angular rearrangement of the coordination sphere during ST.

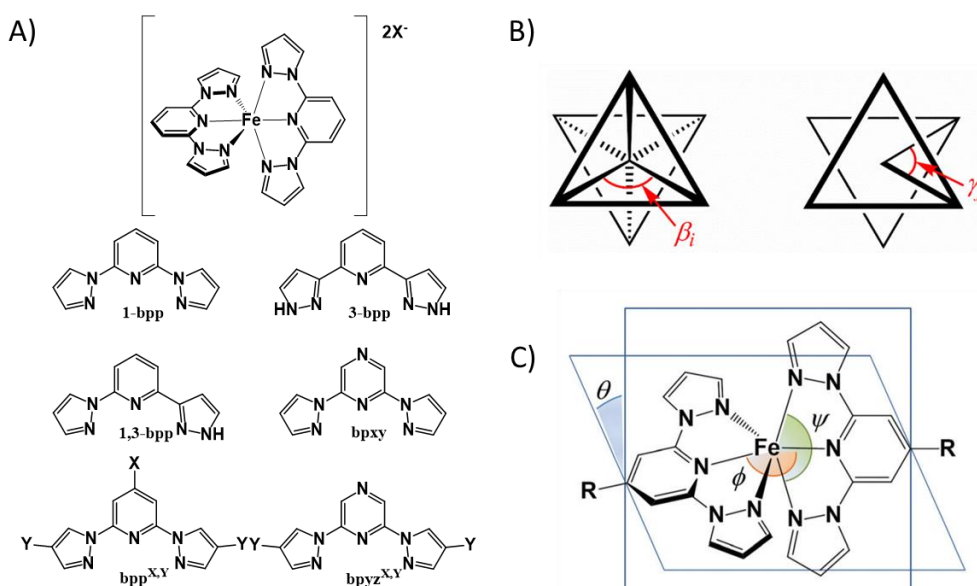


Figure 2.1: A) Structural view of $[\text{Fe}(\text{bpp})_2]^{2+}$ complex and types of *bpp* ligands in the literature. B) Angles used in the definitions of the distortion parameters Σ and Θ . C) Distortion parameters ϕ , θ and ψ in $[\text{Fe}(\text{bpp})_2]^{2+}$ derivatives (Reproduced from Ref. 59).

The angular parameters, ϕ and θ are the two more structural indices that are often used to describe structural variations upon SCO iron(II) complexes. ϕ indicates the trans-N_{pyridyl}-Fe-N_{pyridyl} angle, and θ indicates the dihedral angle between the planes of two ligands (Figure 2.1 C). They reflect the relative disposition of the ligands and therefore describe the shape of a complex. Larger deviations of these angles from their ideal values, $\phi = 180^\circ$ and $\theta = 90^\circ$, indicate the HS-state of a complex. A strong deviation of the angles

from the ideal values tend to stabilize the HS-state and thus often inhibit the SCO in solid-state.⁶⁰ Clamp angles and bite angles are the other useful indicators for SCO studies. The trans N_{pyrazole}-Fe-N_{pyrazole} clamp angle is given by ψ , whereas α is the average of 4 cis N_{pyridine}-Fe-N_{pyrazole} angles. Jahn-Teller (JT) Distortion in HS complexes causes a large deviation from ideal octahedral geometry, and therefore, ψ ranges around 140-150° and α ranges between 72-74°. Whereas in LS complexes, due to the absence of JT distortion, their values are near to ideal octahedral values— $\alpha = 79-81^\circ$ and $\psi = 155-163^\circ$.⁵¹

The above discussed angular parameters play a vital role in controlling the SCO behaviour of iron(II) complexes along with several other factors such as lattice solvent, counter-ions, and the nature of intermolecular interactions.⁶⁰ In addition to these factors, ligand design also plays a crucial role in tuning the SCO property of a complex.^{52,61,62,63} Ligand field strength around a central iron(II) ion can be tuned by introducing electron-donating or -withdrawing substituent on the ligand skeleton. Some reports have already shown the effects of σ - donating and π - accepting properties of the ligands on the SCO properties of the iron(II) complexes derived from them.⁶⁴ Apart from electronic effects, the substituents can also influence the SCO properties by affecting the intermolecular attractions or repulsions, resulting in structural changes accompanying the transition.⁵¹ Chemists are dedicating their efforts to design SCO complexes with stable hysteresis around RT, using the ligand field engineering approach.

However, the task is not just limited to the development of the new functional materials but also to bring them into the device application. Once the SCO complex with the mentioned requirements is obtained, the next step is to make them applicable as devices. For the production of the macroscopic systems and devices possible, in the microstructure industries, there is a need for the development of fabrication of functional molecular assemblies. This could be achieved by the autonomous ordering of atoms, i.e., self-assembly, on various surfaces (metallic, semiconductor, or molecular materials). This fabrication by nano ordering can be achieved by the bottom-up approach, which helps to assemble the atomic and molecular constituents to an organized structure on the surface, using specific interactions between the molecules like hydrogen bonding, electrostatic forces, Van der Waals forces (Figure 2.2).^{65,66}

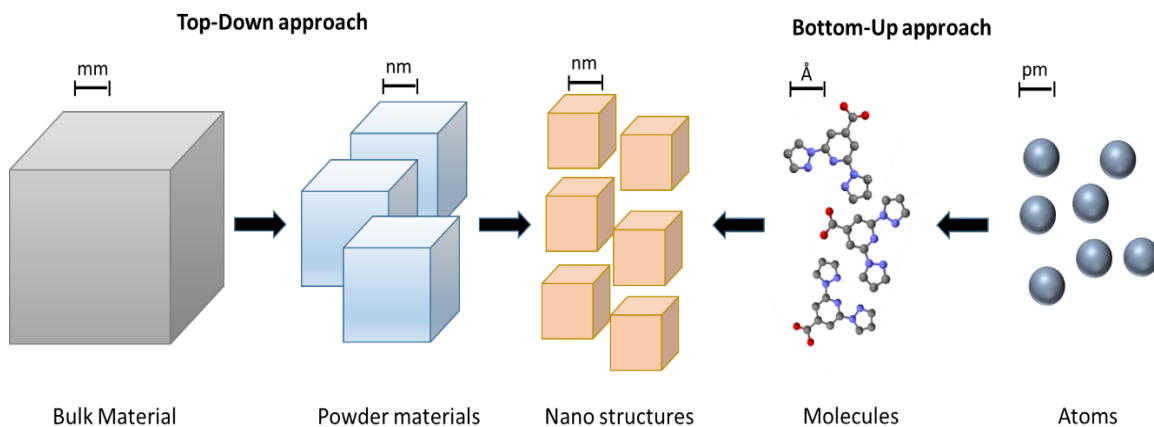


Figure 2.2: Schematic representation of the Top-Down and Bottom-Up approaches.

2.2 Surface characterization techniques

To understand the shape, chemical and physical properties of the surface, some characterization techniques are required especially to study at the nano level. Scanning tunneling microscopy (STM) is an outstanding technique to have an insight into the on-surface self-assembly with a resolution up to the nanometer region. STM can provide an excellent characterization of the ligand + metal phases. However, it cannot directly characterize the charge state of the local chemical environment of the components of the network. To study the local environment in the network, X-ray photoelectron spectroscopy (XPS) is an exceptional technique. This method can present the measurements of electron core level binding energies of the metal center and chelating atoms of the ligands. The resolution of a shift in the core level binding energies due to change in the chemical environment is the strong feature of the XPS technique, which helps in the characterization of the self-assembled pattern. These two different structure characterization techniques used for the studies in this chapter are briefly explained below.

a) Scanning Tunneling Microscopy (STM)

STM is an advanced microscope that allows us to visualize the material at an atomic scale. A proper resolution is one with 0.1 nm in lateral and 0.01 nm in-depth resolution. It consists of a scanning tip that images the surface, depending on the tunneling current. The STM, not only provides the three-dimensional interpretation about the topography of the surface but also yields information on spectroscopic properties. Thus the STM became a valuable tool in various fields of research.

Gerd Binnig and Heinrich Rohrer developed STM at IBM in 1982, for which they were awarded Nobel prize in 1986. Earlier, the STM used to deal only with high vacuum

conditions, but due to advancements in science, now it can work even in the air, water, or other liquids as a medium with various ranges of temperatures. The STM consists of several components – atomically-sharp probing tip, a flat atomic sample, a piezoelectric tube, controlling the digital circuit system, and a computing system (Figure 2.3). The tips are either mechanically formed Pt/Ir (4:1) alloy tips or electrochemically etched Pt/Ir or W-tips. The surface samples consist typically of single crystals of Au, Ag, Cu, Ni, Pd, Ru, and HOPG.⁶⁷

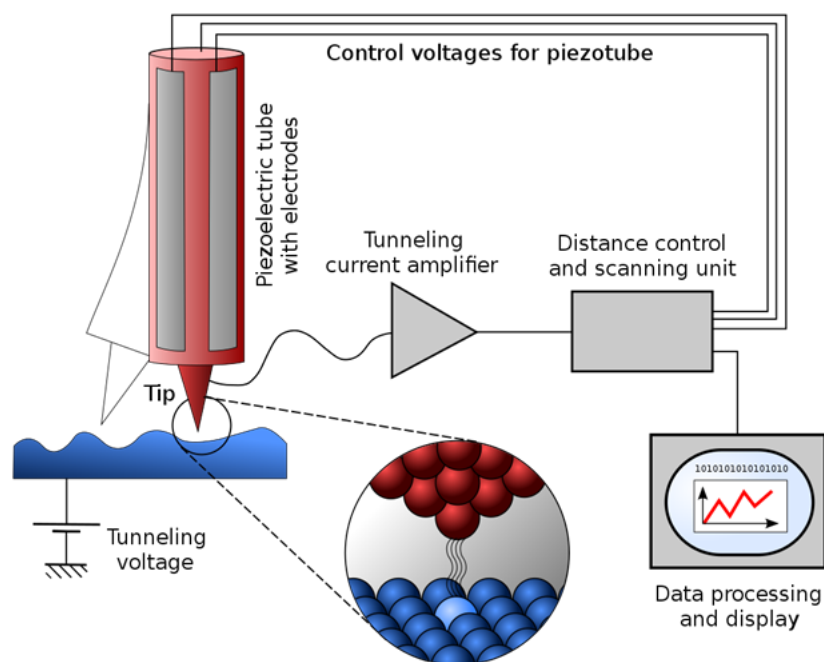


Figure 2.3: Schematic representation of the working principle of STM (Source: Wikipedia).

In general, when two electrodes are separated by an insulator, it forms a barrier for electron transport. If the barrier is very small, then the electron can travel through the barrier from one electrode to another by a quantum mechanical mechanism called quantum tunneling. The same concept is used in STM, where the electrodes here are scanning tip (probe) and the surface of the sample. When the tip is close enough to sample (5-10 Å), the tunneling current flows between surface and probe, which depends exponentially on the distance between the scanning tip and surface. Thus, a change in a few Angstrom (Å) in the distance can affect the current by a factor of ten. The vertical and horizontal movements of the tip can be precisely controlled by changing the voltages applied to the piezoelectric tube.

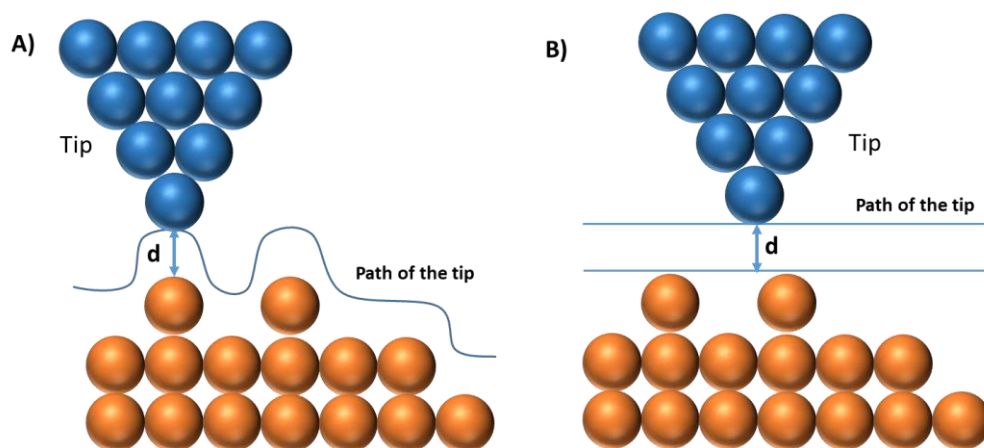


Figure 2.4: Schematic representations of (A) constant current mode and (B) constant height mode of the STM.

There are two types of scanning modes in STM: constant height mode and constant current mode. In the constant current mode, by using a feedback loop, the tip is vertically adjusted to keep the current constant (Figure 2.4 A). The topographic image of the surface is generated by using the recorded vertical position of the tip. Whereas, in constant height mode (Figure 2.4 B), the vertical position of the tip is not changed, and the current measured at the lateral position is used to produce the image. However, this mode is useful only for flat surfaces; if not, it could crash the tip with the surface.

b) X-Ray Photoelectron Spectroscopy (XPS)

When a photon strikes the substrate, its energy can be transferred to the electron in the substance, leading to electron emission. This effect is known as the photoelectric effect, and the electron released in this way is called a photoelectron. The energy measurement of the emitted electron is called photoelectron spectroscopy (PES).

Along with STM, the other essential method used in this thesis for surface characterization is XPS. In XPS, X-ray photons are used to irradiate the surface under study, and the technique is also called ESCA (electron spectroscopy for chemical analysis). XPS is one of the widely used techniques for surface analysis.

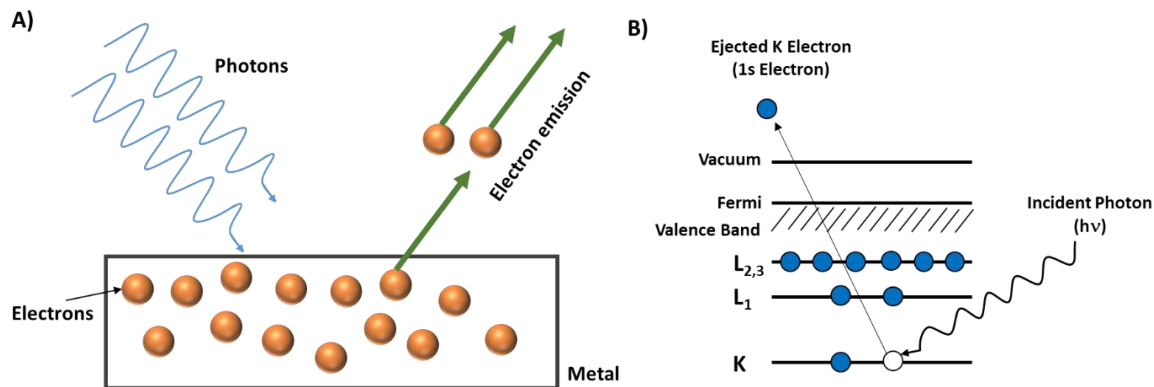


Figure 2.5: A) Schematic representation of the photoelectric effect and B) energy level diagram representing the photoelectric effect.

When X-rays hit the surface, the core level electrons of surface atoms absorb the X-Rays photon energy $h\nu$, overcome their binding energy E_b , and emit from the surface with KE (Figure 2.5). This can be explained as the following equation-

$$h\nu = KE + \Phi + E_b \quad (2.3)$$

Where $h\nu$ represents the energy of the X-ray source. In general, $MgK\alpha$ and $AlK\alpha$ are the two sources used because of their high energy and narrow width. Φ is the work function of the instrument. KE represents the kinetic energy of the photoelectron emitted and will be measured by the analyzer. Thus, the binding energy of the core level electron can be calculated from the above Equation 2.3.

The binding energy spectrum can be used to detect the elements in the substance. Every element has its unique electronic structure, and thus unique spectra can be observed. Furthermore, the binding energy (BE) of the specific core electron depends not only just on the element but also on the chemical environment and also on the oxidation state of the element. In other words, when the same electron is bonded to different chemical species, the binding energy of the electron is different in both cases. This variation in BE causes a shift in corresponding XPS peaks, and this is termed as a chemical shift.

The phenomenon that can be seen in XPS is an effect of electronegativity. The electronegative atom attracts the electrons and thus requires high energy to remove the electron. Thus, binding energy can be enhanced with the presence of an electronegative atom. Splitting of binding energy peaks is an additional phenomenon that can be observed in XPS. This can be formed in electrons of higher than s -orbital, and this is called spin-orbital coupling. In p , d , and f orbital shells (i.e., shells with $l > 0$), two configurations are possible with $J = (L + S)$. Since S can be $+1/2$ or $-1/2$, J can attain two values corresponding to two

states. The peaks generated from this spectrum can help in the quantification of the elements in the sample, depending on the intensities of the peaks.

2.3 Objectives

To harness SCO-based applications, SCO complexes with stable hysteresis around room-temperature and thermal stability need to be realized. Crucially, on surface SCO characteristics of such complexes should also be studied to progress towards the realization of SCO-based device architectures such as switching and memory elements. The following objectives are pursued in this chapter of the thesis to progress towards the realization of SCO-based device architectures.

Objective 1: Studies on the self-assembly of a novel tridentate bis(pyrazolyl)pyridine (*bpp*) ligand on the Ag(111) surface and its on-surface coordination with Fe atoms.

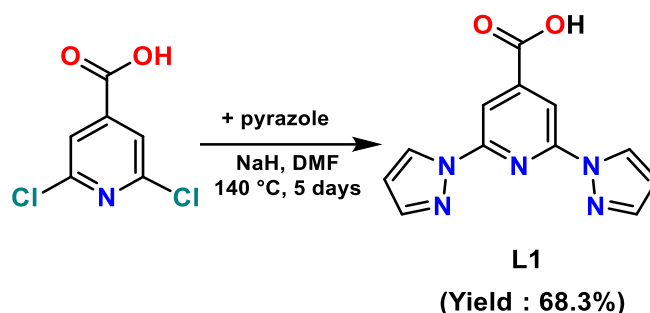
Objective 2: Hysteresis engineering of Fe(II)-SCO complexes based on a *bpp* ligand by varying the solvent and counter anions.

2.3.1 Objective 1: Self-assembly of carboxylic acid derivative of 2,6-di(1H-pyrazol-1-yl)isonicotinic acid on Ag(111)

The results reported in this part of this chapter were produced in collaboration with the group of Prof. Johannes Barth from TU Munich.

One of the most studied families of SCO complexes is iron (II) complexes of tridentate ligand 2,6 bis(pyrazolyl)pyridine (*bpp*) because of their propensity to show abrupt transition around room temperature. For the on-surface self-assembly and coordination studies, the simplest *bpp*-COOH molecule was selected because of its extra coordination site of the carboxylic acid group on the pyridine moiety. Thus, this molecule can coordinate through tridentate chelating nitrogens and carboxylate groups on the pyridine ring.

The ligand (**L1**) was prepared by treating 2,6-dichloro-isonicotinic acid with pyrazole in DMF and stirring the reaction mixture at 140 °C for five days (Scheme 2.1). The expected ligand was obtained as a colorless product with a 68% yield.⁶⁸ The analytical purity of the ligand was established by performing ¹H-NMR, ¹³C-NMR, and ESI-MS.



Scheme 2.1: Synthesis of ligand **L1** (*bpp*-COOH).

Self-assembly of *bpp*-COOH (**L1**) on Ag(111)

The deposition of the ligand **L1** molecules was successfully achieved by the organic molecular beam epitaxy from quartz crucible held at 170 °C onto a previously cleaned Ag(111) surface. Figure 2.6 A shows the high-resolution STM image of *bpp*-COOH molecules deposited on the Ag(111) surface. From the image, a porous structure can be observed, which consists of a motif with 17 molecules in it. A unit cell can be visualized using six motifs, rotated by multiples of 60°. The resulting pattern has a porosity of ~0.2, with pores of triangular, rectangular, and hexagonal shapes, with most of the hexagonal pores containing excess molecules. In a hexagonal motif, a two-fold symmetric and three-fold symmetric part can be observed and represented with green and red colours, respectively, in Figure 2.6 C. Similarly, a triangular pattern can be visualized using three sets of four molecules represented by blue colour. The molecules in the pore show different orientations and favoring hydrogen bonding with the carboxylic group.⁴³ The clear hydrogen-oxygen interaction can be visualized between the oxygen of the carboxylic group and hydrogens on pyridine or pyrazole rings (Figure 2.6 B).

XPS, one of the best tools to study surface molecules, helps in confirming the deposition of molecules on the surface. From XPS data, two different oxygen species of carboxylic acid groups can be distinguished from O 1s spectra (Figure 2.7 B) (-OH at 533 eV and C=O at 531.2 eV). Whereas C 1s spectra were deconvoluted into five components, differentiating the carboxylic C, two different carbons in pyridine ring, and two types of carbon in pyrazole ring.^{69,70} The binding energy values of these different carbon atoms are tabulated in Table 2.1. On annealing to 100 °C, deprotonation of the majority of the carboxylic groups was observed. This resulted in the minimization of the intensity of carboxylic 'C' peak, which is compensated by the evolution of an additional peak at 288.3 eV. This new peak is attributed to carbon atoms of carboxylates. Besides, O 1s spectra also

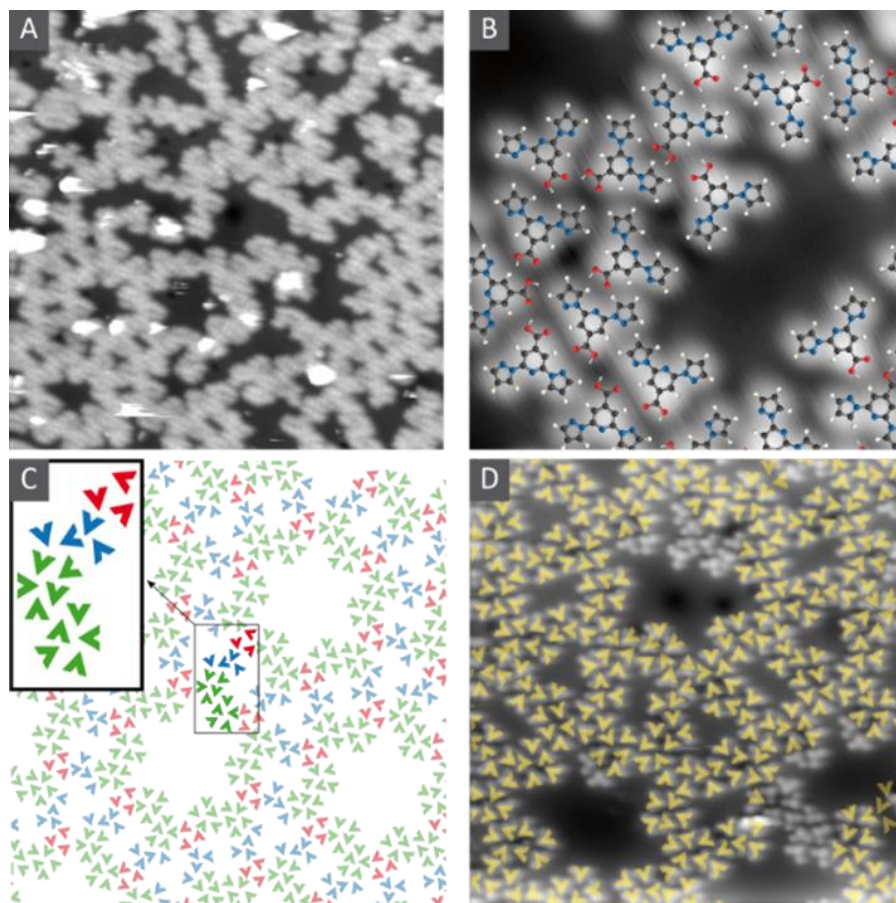


Figure 2.6: Low Temperature (LT)-STM images of *bpp*-COOH. (A) Overview image (1.0 V, 50 pA) of the porous structure. (B) Molecular model overlaid on a close-up image (-0.25 V, 50 pA). (C) Schematic representation of the motif and the resulting pattern on the surface. (D) Pattern overlaid on STM image (-0.25 V, 50 pA).

revealed a reduction in the intensity of the original peaks and showed a new peak at 530.7 eV, which is attributed to the newly formed carboxylate.^{70,71} Being a quantity method of spectroscopy, the relative amounts of functional groups are deduced from the area below the XPS peaks. So the ratio of the peak areas of the O 1s spectra (Figure 2.7 D) indicates the presence of 70% of deprotonated carboxylic acid groups (carboxylate ions) and 30% of intact carboxylic acid groups in total.

The following Figure 2.7 and shows the XPS spectra of the different components in C and O in the molecules, and Table 2.1 shows the types of carbon and oxygen atoms present in the molecules along with their corresponding binding energies from the XPS spectra.

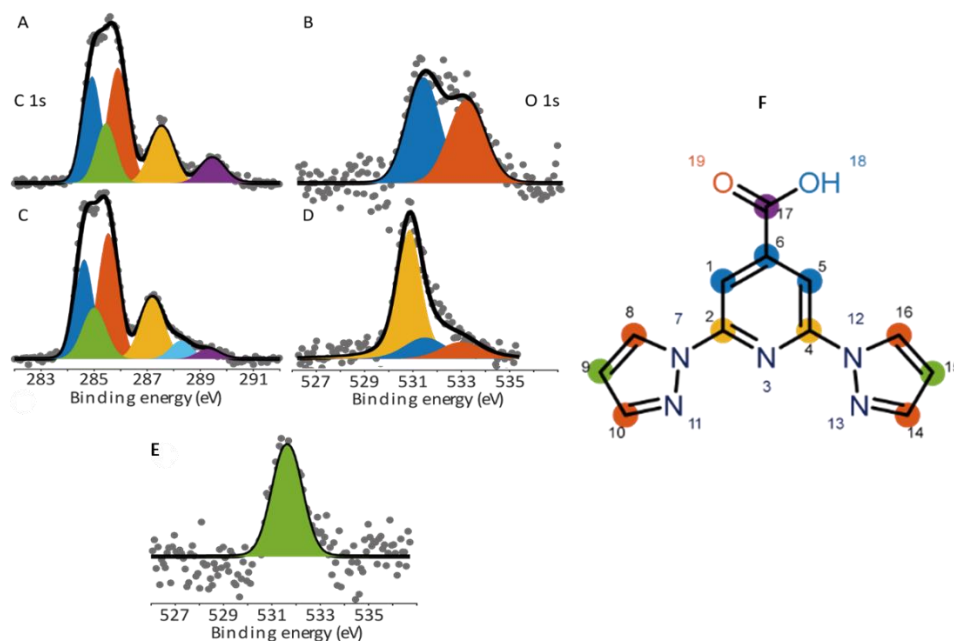


Figure 2.7: XPS spectra of *bpp*-COOH on Ag(111). (A-B) C 1s and O 1s regions for submonolayer coverage, (C-D) C 1s and O 1s regions after annealing to 100 °C, (E) O 1s region after dosing Fe on a submonolayer coverage of **L1**, (F) model of ligand **L1**.

The annealed sample on Ag(111) was subjected to LT STM, and a densely packed phase was observed, forming a Kagome lattice, with a pore occupation factor of 1 (Figure 2.8 A). Each pore accommodates one additional molecule (Figure 2.8 B). A unit cell [6 -2 8 6] can be imagined with respect to the underlying Ag(111) lattice, consisting of three molecules building up the lattice and one molecule filling up the pore. The lattice is formed by using hydrogen bonding interactions between the carboxylate group and hydrogens of C9 and C15 of the pyrazole group of the neighboring molecule.

Table 2.1: Binding energies of the respective atoms extracted from XPS data.

	Atomic position	Before Annealing / eV	After Annealing / eV
C 1s	1,5,6	284.8	284.8
	9,15	285.3	285.3
	8,10,14,16	285.7	285.7
	2,4	287.4	287.4
	17	289.5	288.3, 289.5
O 1s	18	533	533, 530.7
	19	531.2	531.2, 530.7

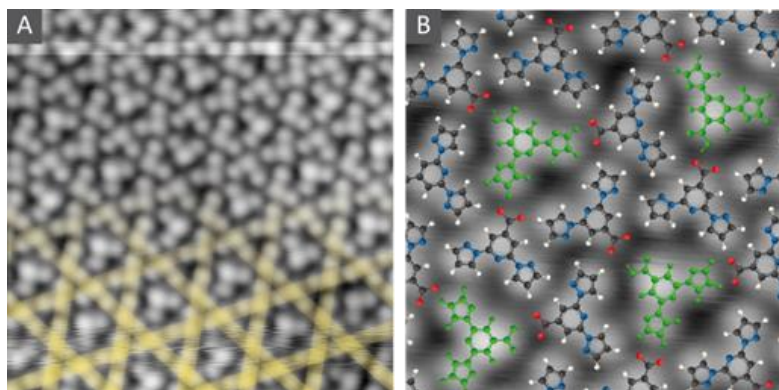


Figure 2.8: LT-STM images (-0.5 V, 50 pA) of *bpp*-COOH annealed at 373 K. (A) Mesh indicated by yellow lines. (B) The molecules in the pore are shown in green color.

Metal-organic coordination oligomers of *bpp*-COOH and Fe on Ag(111)

Iron(Fe) was evaporated from home built metal evaporator by wrapping Fe around a tungsten wire, which is heated up using applied current. After subsequent deposition of Fe on the surface containing *bpp*-COOH, coordination with Fe atoms was observed as in Figure 2.9. Two different modes of coordination between Fe atoms and *bpp*-COOH ligands were noticed. The first mode is head to tail bonding between the molecules forming a 1D chain, i.e., each Fe atom is coordinated to the carboxylic acid of one molecule and three nitrogen atoms in the chelating pocket of the other molecule.^{72,73} The second mode of coordination is knots, where the carboxylic groups of 4 molecules face each other and are together coordinated to two Fe atoms.⁷⁴ The other molecules are attached to these chains through the carboxylic group through hydrogen bonding.

XPS measurements have shown a single O 1s peak at 531.6 eV (Figure 2.7 F), and this chemical shift is consistent with Fe coordinated to carboxylate group in the literature.⁷¹ This shows that the deposition of iron at RT enhances the deprotonation of carboxylic acid and enable Fe coordination with carboxylates.

Annealing to 100 °C showed an increase in the formation of 1D chains and knots (Figure 2.9). STM images showed an enhancement in the amount of Fe coordination molecules, thus increasing the length of the chains. Due to this annealing, 50% of the molecules have shown Fe-N coordination, forming oligomers, with an average length of 3 molecules and with a maximum length of 8 molecules.

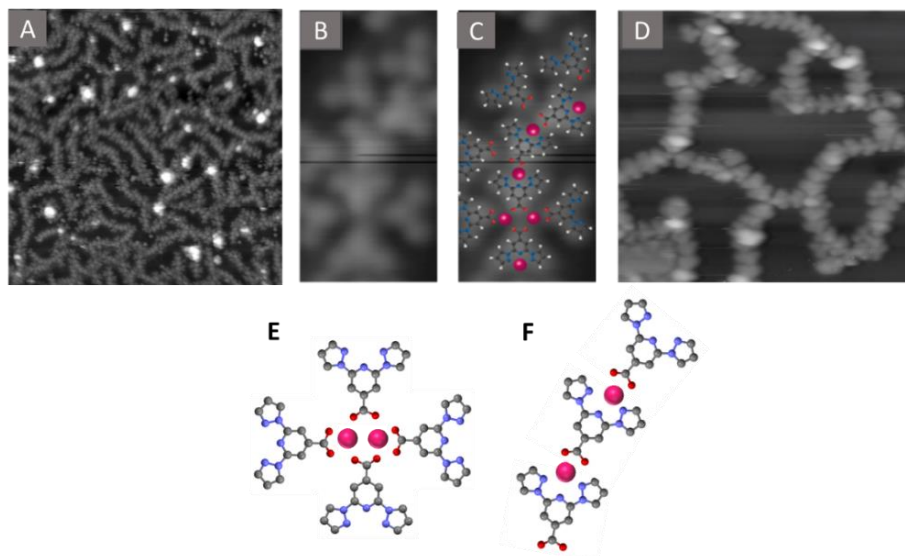


Figure 2.9: STM images of coordination polymer formed by *bpp*-COOH and Fe. (A) Overview image from LT-STM (-0.5 V, 100 pA). (B and C) Close-up of coordinated molecules (0.25 V, 50 pA). Brighter protrusions are assigned to the Fe coordination of the tail. (D) RT-STM image (0.4 V, 80 pA) showing the stability of the coordination polymer at RT. (E) Schematic representation of head to head coordination and (F) representation of head to tail coordination.

Unlike the several SCO system, here tail to tail coordination by Fe atoms was not found on this surface. However, the head to tail coordination motif is similar to that single-crystal structure reported with Co(II).⁷⁵ The planar coordination motif presumably further promoted on Ag(111) surface.

2.3.2 Objective 2: Hysteresis engineering of *bpp*-based SCO complexes

DSC, SWAXS and TGA measurements were performed in collaboration with Dr. Benoit Heinrich, IPCMS, Strasbourg.

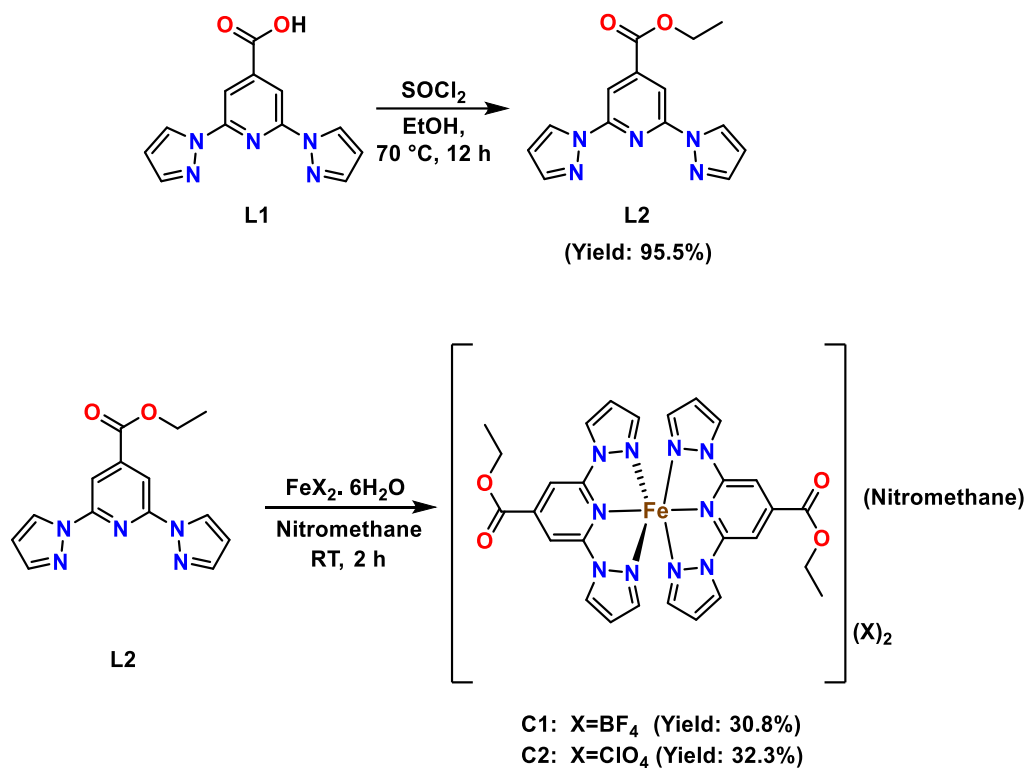
The bulk-scale anion dependent SCO properties of $[\text{Fe}(\text{bpp-COOH})_2](\text{X})_2$ ($\text{X} = \text{BF}_4^-$, ClO_4^- , CF_3SO_3^- , SbF_6^- , and AsF_6^-) complex composed of *bpp*-COOH ligand discussed in the foregoing section was already reported by Coronado and coworkers.⁷⁶ The complexes with BF_4^- and ClO_4^- showed abrupt and reversible spin transition with a small hysteresis. In contrast, the others showed irreversible spin-state switching characteristics. From the synthetic point of view, it is possible to synthesize a range of novel *bpp*-COOR ligand architectures for SCO research, starting from *bpp*-COOH ligand as a precursor. Several reports detailing SCO characteristics of $[\text{Fe}(\text{bpp-COOR})_2](\text{X})_2$ complexes have appeared in the literature.^{68,77–80} Among them, Ruben and coworkers have recently reported a 100 K

thermal hysteresis loop associated with an iron(II) complex—[Fe(*bpp*-COOC₂H₅)₂](ClO₄)₂·CH₃CN. However, the SCO of the complex is not stable upon repeated cycling, and a reduction in hysteresis width and χT value was observed in each subsequent cycle starting from the first cycle. In addition, it was also showed that complete removal of the solvent by heating to 400 K had trapped the complex in LS state.

On the other hand, [Fe(*bpp*-COOC₂H₅)₂](ClO₄)₂·(CH₃COCH₃) complex reported by Coronado and coworkers showed a LS to HS spin transition around 330 K. However, due to loss of solvent at this temperature, the complex remained in HS state during the cooling cycle. These both are some of the best examples showing the importance of solvent in the lattice, and the loss of solvent could destroy the SCO behaviour of the complex. However, there is no rule or theory in general explaining how the lattice solvent molecule affects the SCO behaviour, and every time the effect of solvent is independent of the other. Besides, these lattice solvent could involve in appropriate intermolecular contact and play a significant role in SCO behaviour. Consequently, we have attempted to tune the SCO properties of [Fe(*bpp*-COOC₂H₅)₂](ClO₄)₂ system by preparing it as a nitromethane (CH₃NO₂) solvate—[Fe(*bpp*-COOC₂H₅)₂](ClO₄)₂·CH₃NO₂. The rationale behind the approach is nitromethane is one of the commonly used solvents for the preparation of Fe(II) complexes, and it has a higher boiling point (101 °C) than that of acetonitrile (82 °C) and acetone (56 °C).

The ligand **L1**, used in the previous task, was used as the starting material for the synthesis of the ligand **L2**. The ligand **L2** was prepared by treating **L1** with thionyl chloride in the presence of ethanol (Scheme 2.2).⁸¹ The ligands were completely characterized by ¹H-NMR, ¹³C-NMR, and ESI-MS.

Fe(II) complexes were prepared by treating the equimolar amount of ligand with respective iron salts like Fe(BF₄)₂·6H₂O and Fe(ClO₄)₂·6H₂O by stirring in nitromethane for 2 h at RT, as depicted in scheme 2.2. The filtered compound was concentrated, and with slow diffusion of diethyl ether (DEE), respective complexes were obtained in crystalline form.



Scheme 2.2: Synthesis of ligand **L2** and complexes **C1** and **C2**.

[Fe(L2)₂][BF₄]₂·(CH₃NO₂) - Complex C1

The crystallographic analysis of the black colored single crystals of complex **C1** was performed at 150 K. It has revealed that the complex has crystallized in the monoclinic space group $P2_1/n$ with cell volume 3594.42(10) Å³. In complex **C1**, the Fe(II) center is coordinated octahedrally by two tridentate **L2** ligands (Figure 2.10 A).

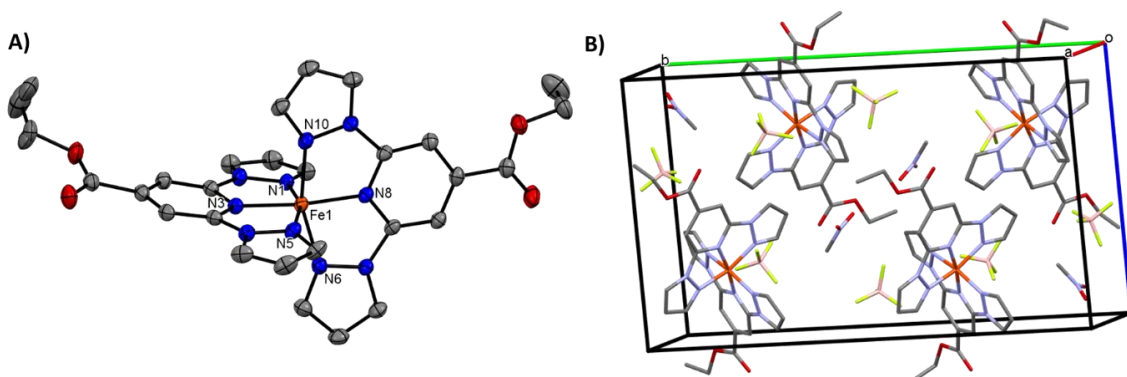


Figure 2.10: A) Crystal structure of complex **C1** at 150 K. Displacement ellipsoids are at the 50% level, and B) crystal packing of complex **C1**. Hydrogen atoms and disordered atoms were omitted for clarity.

A single unit-cell contains four $[\text{Fe}(\mathbf{L2})_2][\text{BF}_4]_2$ units with four nitromethane molecules in the crystal lattice (Figure 2.10 B). The asymmetric unit contains a full complex with one solvent molecule. The average Fe(II)-N bond length of 1.926(5) Å and the angular parameters listed in Table 2.2 indicate the low-spin state of the complex at 150 K.

Table 2.2: Selected bond lengths (Å), angles, and distortion indices (°) of complex **C1** at 150 K.

Parameter	Value	Parameter	Value
Temperature / K	150	rFe–N (average)	1.926(5)
Fe ₁ -N ₁ (pyrazolyl)	1.954(2)	N ₃ -Fe ₁ -N ₈ (ϕ)	172.50(8)
Fe ₁ -N ₃ (pyridyl)	1.888(2)	N ₆ -Fe ₁ -N ₁₀ (ψ)	160.67(8)
Fe ₁ -N ₅ (pyrazolyl)	1.973(2)	N ₁ -Fe ₁ -N ₅ (ψ)	160.60(8)
Fe ₁ -N ₆ (pyrazolyl)	1.974(2)	Σ	83.62
Fe ₁ -N ₈ (pyridyl)	1.893(2)	Θ	89.39(6)
Fe ₁ -N ₁₀ (pyrazolyl)	1.962(2)	α	80.39(16)

Intermolecular interactions play a significant role in inducing cooperative SCO behaviour in SCO complexes. Crystal structure analysis of the complex revealed the absence of classical hydrogen bonds in the crystal lattice of the complex. Few short interactions were observed (Figure 2.11), which include i) the hydrogen of the pyrazole ring and the oxygen atom of the carbonyl group of the neighboring cation (O1-H11, $d = 2.50$ Å), ii) the hydrogen atom of the nitromethane solvent and the fluorine atom of the counter anion (H29A-F2A, $d = 2.31$ Å), iii) the fluorine atom of the counter anion with the hydrogen atom of the pyridine ring (H21-F3A, $d = 2.44$ Å) and with the hydrogen atom of the pyrazole moieties (H23-F4A, $d = 2.84$ Å).

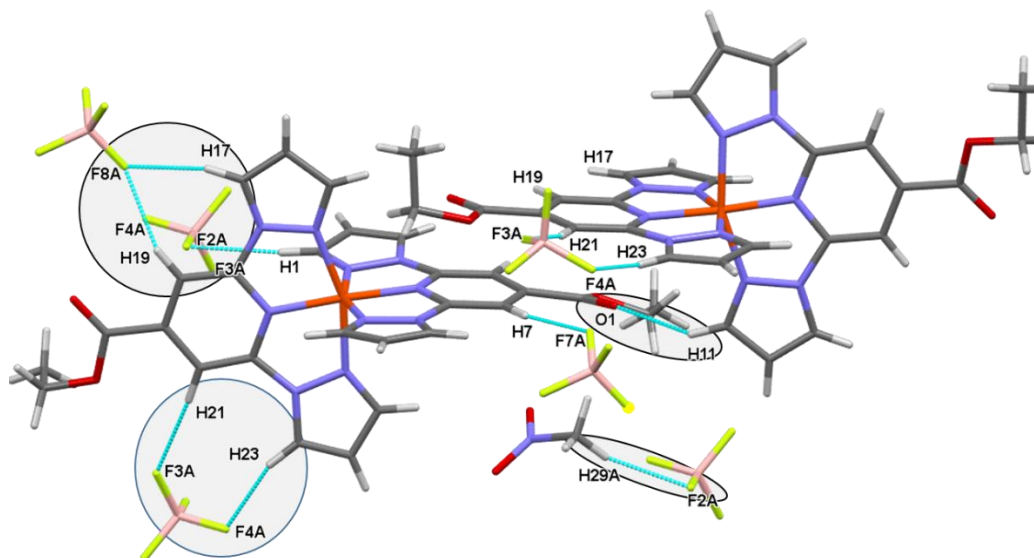


Figure 2.11: Intermolecular contacts (denoted in blue dotted lines and circled) within the unit cell in complex **C1**.

The variable temperature magnetic measurements of the complex **C1** (Figure 2.12) revealed SCO active nature of the complex. In the first heating curve, a χT value of $3.45 \text{ cm}^3 \text{ mol}^{-1} \text{ K}$ was observed at 370 K, indicating a pure HS-state of the complex at that temperature. In the subsequent cooling step, the HS to LS transition is observed with $T_{1/2} = 307 \text{ K}$, and a complete diamagnetic LS-state was reached around 280 K, which is in agreement with the crystallographic data collected at 150 K. Overall, a hysteresis width of $\sim 43 \text{ K}$ was observed for the first heat-cool cycle. In the subsequent cycles, a decrease of the χT values and hysteresis widths were observed. This could be attributed to the loss of solvent during the SCO process, as reported for $[\text{Fe}(\text{bpp}\text{-COOC}_2\text{H}_5)_2](\text{ClO}_4)_2 \cdot \text{CH}_3\text{CN}$.⁶⁸

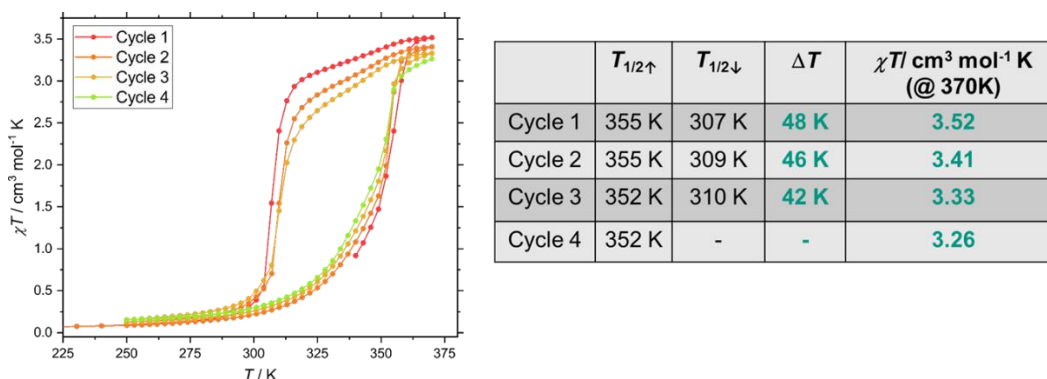


Figure 2.12: χT vs. T plot for complex **C1** (on the left) and the table with parameters associated with SCO behaviour of complex **C1** (on the right). A scan-rate of 3 K/min was used in settle mode.

Thermogravimetric analysis (TGA) (Figure 2.13 A) shows the slow release of solvent at 350 K, and this shows the possibility of a loss of a slight amount of lattice solvent during the magnetic measurements. Figure 2.13 shows the loss of solvent *ca.* 1.5% in weight around 370 K.

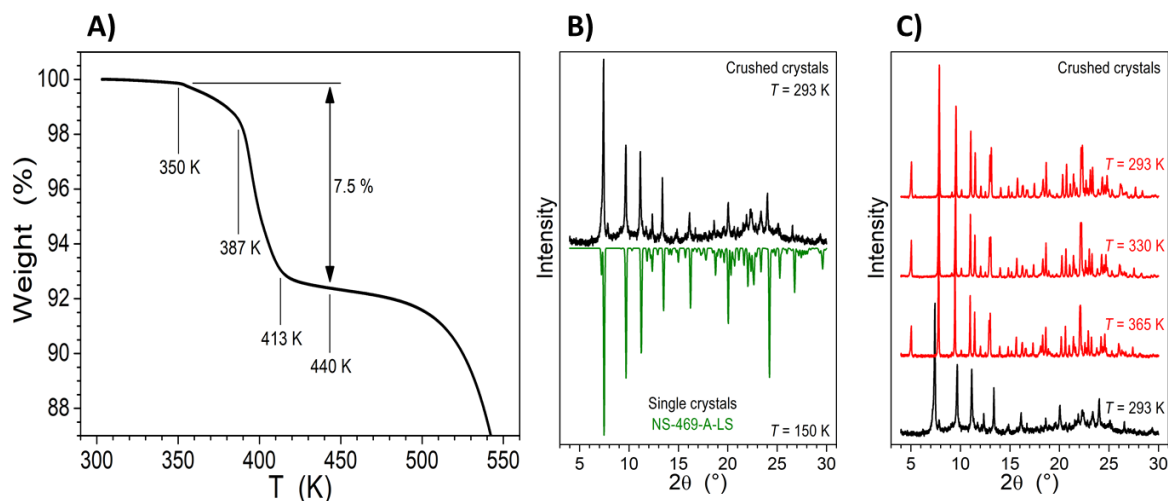


Figure 2.13: A) TGA curve for complex **C1**, B) powder XRD patterns of crushed **C1** crystals at 293 K, compared to pattern calculated from the single-crystal structure at 150 K (an inverted trace in green colour) and C) powder XRD patterns of crushed crystals of **C1** in pristine state at 330 K and 293 K (red colour).

To further investigate the structural reorganization associated with SCO, the Small and Wide Angle X-ray Scattering (SWAXS) studies were performed on **C1**. Figure 2.13 B shows that the pattern revealed from the crystals is identical to the pattern simulated from the single-crystal structure. Upon heating to 365 K, the phase change is clearly observed, which is in agreement with magnetic measurements. However, the reverse transition was not observed on cooling back to 293 K, which is not in agreement with the magnetic measurements (Figure 2.13 C). This could be due to the difference in the time scales since the powder XRD measurements are prone to longer acquisition times. Also, due to high ST temperature ($T_{1/2\uparrow} = 355$ K), we couldn't obtain the crystal structure of the HS state.

[Fe(L2)₂][ClO₄]₂·(CH₃NO₂) - Complex **C2**

Crystallization of **C2** by diffusing DEE into a concentrated solution of the complex in nitromethane yielded orange and wine red colored crystals. The crystallographic analysis of the wine-red colored single crystals of complex **C2** was performed at 150 K. It has revealed that the complex has crystallized in the monoclinic space group $P2_1/n$ with cell volume 3650.70(8) Å³. The complex **C2** of the formula [Fe(L2)₂][ClO₄]₂ contains a complex

cation where the Fe(II) center is coordinated octahedrally by two tridentate ligands **L2** (Figure 2.14).

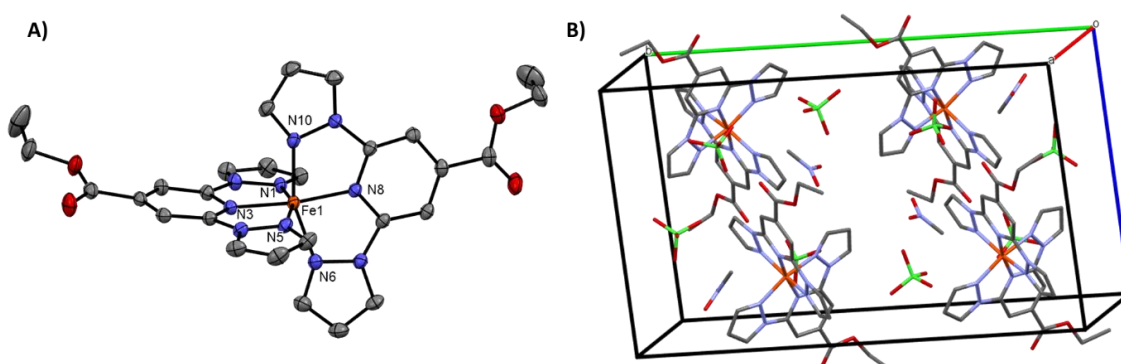


Figure 2.14: A) Crystal structure of low spin complex **C2** at 150 K. Displacement ellipsoids are at the 50% level, and B) crystal packing of complex **C2**. Hydrogen atoms and disordered atoms were omitted for clarity.

A single unit-cell contains four $[\text{Fe}(\mathbf{L2})_2][\text{ClO}_4]_2$ units with two nitromethane molecules in the crystal lattice. The perchlorate anions were found to be highly disordered in the crystal lattice. The asymmetric unit contains a full complex with one solvent molecule. The crystal structure at 150 K reveals the average Fe(II)-N bond length of 1.941(5) Å, which indicates the low-spin state. The dihedral angle (θ) of 87.00(2)°, the trans- $\text{N}_{\text{pyridine}}\text{-Fe-}\text{N}_{\text{pyridine}}$ angle (ψ) = 171.80(7)°, and the distortion parameter (Σ) = 83.95 further confirm the LS state of the complex at 150 K. Moreover, the list of the structural parameters collected in Table 2.4 elucidates the near-ideal octahedral coordination environment around the central metal ion.

In the crystal lattice, the complex cations are arranged in a linear fashion mediated by short intermolecular contacts involving the complex cations and counter anions (Figure 2.15). No direct interactions between the complex cations were observed. The short contacts involve (i) the hydrogen atom of the pyrazole and pyridine moieties of the cationic complex and the oxygen atom of the perchlorate anion (H7–O11B, $d = 2.40$ Å, H9–O11B, $d = 2.08$ Å), (ii) the oxygen atom of the perchlorate anion and the hydrogen atom of the ethyl group of the complex cation (O5A–H27B, $d = 2.50$ Å), (iii) the oxygen atom of the counter anion and the hydrogen atom of the pyridine ring (O12B–H19, $d = 2.47$ Å).

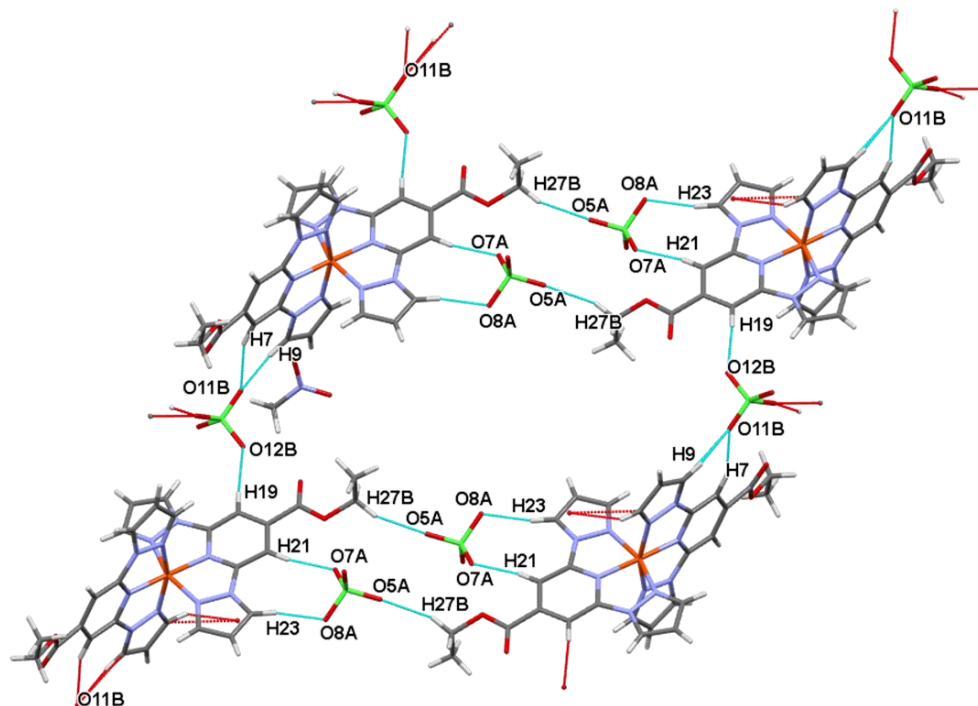


Figure 2.15: Intermolecular contacts (denoted in blue dotted lines) within the unit cell of the LS state of complex **C2**.

The first cooling of the sample was performed after heating the complex (red wine crystals of **C2**) to 330 K. Upon cooling, a complete HS to LS switching was observed with $T_{1/2\downarrow} = 257$ K; the χT value of $0.05 \text{ cm}^3 \text{ mol}^{-1} \text{ K}$ at 200 K confirms the LS state of the complex at that temperature. Subsequent heating induced LS to HS switching with $T_{1/2\uparrow} = 319$ K; χT value of $3.45 \text{ cm}^3 \text{ mol}^{-1} \text{ K}$ indicates the 100% HS-state of the complex. Overall, $\Delta T = 62$ K and $T_{1/2} = 288$ K were observed for the first heat-cool cycle, as shown in Figure 2.16. Such centering of the $T_{1/2}$ at RT and the associated hysteresis width of 62 K renders the complex suitable for SCO-based applications, especially in memory architectures. Moreover, the complex **C2** is one of the rare examples of SCO complexes capable of undergoing bistable SCO with switching temperature centered at RT. Similar hysteresis widths were observed in the subsequent cool-heat cycles. Importantly, χT values remained similar in each scan, indicating the stable nature of spin-state switching in **C2** with respect to cool-heat cycling. This result is remarkable in view of the unstable SCO characteristics reported for $[\text{Fe}(\text{bpp}-\text{COOC}_2\text{H}_5)_2][\text{ClO}_4]_2$ series of complexes featuring different lattice solvents such as acetone and acetonitrile. The elemental analysis (see Experimental Section) of the sample after magnetic measurements showed the presence of nitromethane in it. Thus the role of nitromethane contributing to the occurrence of bistable SCO in **C2** is validated.

It is also well known that the scan rate can affect the hysteresis width of SCO complexes. So, to investigate the scan rate dependence of SCO in **C2**, a fresh batch of crystals were prepared and were subjected to magnetic measurements at 3 K/min for two cycles and then one thermal cycle at 1 K/min. From Figure 2.16 B, it can be seen that the 60 K hysteresis was maintained at 1 K/min.

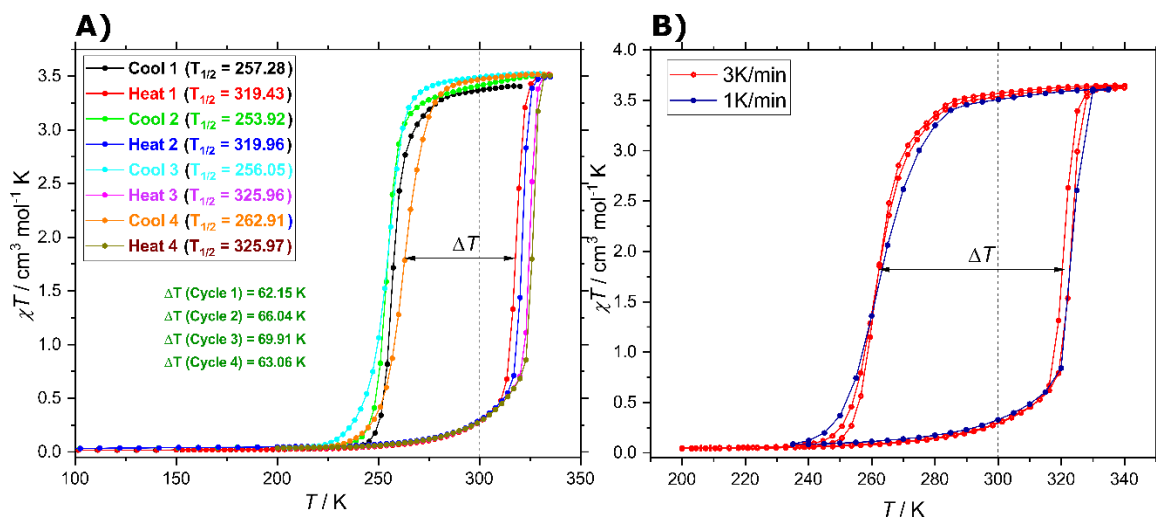


Figure 2.16: SCO behaviour of complex **C2** A) 4 cycles at 3 K/min showing $\Delta T = \sim 65$ K and B) reproducibility check with 3 K/min and 1 K/min scan rates in settle mode.

To characterize the HS form of **C2** and to gain insights into the structural variations associated with the LS to HS switching of **C2**, the wine-red LS crystal of the complex was heated at a rate of 1 K/min to 335 K. An apparent colour change from wine-red to orange has been observed upon heating the sample from 300 K to 335 K, indicating an in-situ LS to HS switching. First, crystallographic analysis of the wine-red crystals at room temperature (300 K) revealed that the structure is the same as that of the structure obtained at 150 K. This indicates the stable nature of LS-state of **C2** at RT as inferred from the magnetic studies. Second, the XRD structure determination of the in-situ switched single crystal of **C2** revealed the HS-state of it at 335 K. The HS form of **C2** maintained the monoclinic $P2_1/n$, the space group as that of the LS complex. Remarkably, a 4% increase in unit cell volume was observed upon LS to HS switching, that is, the unit cell volume of the HS complex is larger than the LS complex. A single unit cell of HS **C2** is composed of four $[\text{Fe}(\text{L2})_2][\text{ClO}_4]_2$ units with four nitromethane molecules in the crystal lattice. The asymmetric unit contains a full complex with one solvent (nitromethane) molecule, which is similar to that of the LS crystal structure. Moreover, the presence of nitromethane was confirmed from the crystal structure, and its stable existence has to be noticed. The average Fe(II)-N bond length of 2.16(2) Å and angular parameters further confirms the HS state of the orange-coloured crystals measured at 335 K. The high R value associated with the HS structure of **C2** could

be due to prolonged exposure to X-rays and the distortion associated with the LS to HS switching process.

Table 2.3: Crystal parameters of complex **C2** crystals (red-wine and orange) at various temperatures.

Parameter	HS (335 K) ^a	HS (300 K) ^a	HS (335 K) ^b	LS (300 K) ^b	LS (150 K) ^c
Crystal System (space group)	Monoclinic ($P2_1/c$)				
a/ Å	9.7805(2)	9.7181(2)	9.8065(8)	10.7048(2)	10.5596(1)
b/ Å	25.8234(5)	25.7973(4)	25.936(2)	24.2312(4)	23.9540(3)
c/ Å	15.2337(2)	15.1984(2)	15.2891(12)	14.7020(3)	14.6034(7)
$\beta/^\circ$	96.159(2)	95.980(2)	96.268(7)	98.509(2)	98.774(1)
$V/ \text{Å}^3$	3825.30(12)	3789.52(8)	3865.5(5)	3771.58(2)	3650.70(2)
Colour	orange	orange	orange	Red-wine	Red-wine
Spin state	HS	HS	HS	LS	LS

^a Orange block crystal (crystal 1). ^b redwine block crystal (crystal 2). ^c red-wine block crystal (crystal 3)

The center of the hysteresis loop at RT indicates the stable nature of HS and LS forms at 298 K. This is indeed the case because X-ray structure determination of the orange crystals of **C2** revealed the HS-state of it. Due to the small amount of orange **C2** crystals obtained from the crystallization process, we could not characterize the spin-state switching characteristics of the complex. However, cooling of the sample by immersing it in a dry-ice bath revealed a color change from orange to wine-red characteristic of HS to LS switching. At 300 K, and the structure obtained has revealed that the complex has crystallized in a monoclinic lattice with $P2_1/n$ space group. Moreover, the unit cell parameters are the same as that of the in-situ generated HS crystals at 335 K. This crystal structure of HS bright orange crystal reveals the avg. Fe-N bond length of 2.156(5) Å. The distorted nature of the HS complex can be clearly seen from Φ angle (trans N-Fe-N) as 158.45°, where it is around 171° in LS. The same conclusion can be drawn from the other parameters like clamp angle (ψ) = 145.45(8)° and 145.77(8)° and distortion index (Σ) = 156.78°, and this is in agreement with the χT vs. T plots. The same red bright crystals were subjected to X-Ray analysis at 335 K (Figure 2.17), and it reveals the HS structure the same as that of 300 K. Moreover, Table 2.3 shows unit cell parameters of red-wine and orange crystals at various temperatures. It shows that the parameters of HS structure obtained from red-wine crystals on slow heating to 335 K, are similar to that of HS structure obtained from orange crystals at 300 K. This

shows that both crystals are same, and thus we performed the magnetic measurements with mixture of orange and red-wine crystals and this produced the same results.

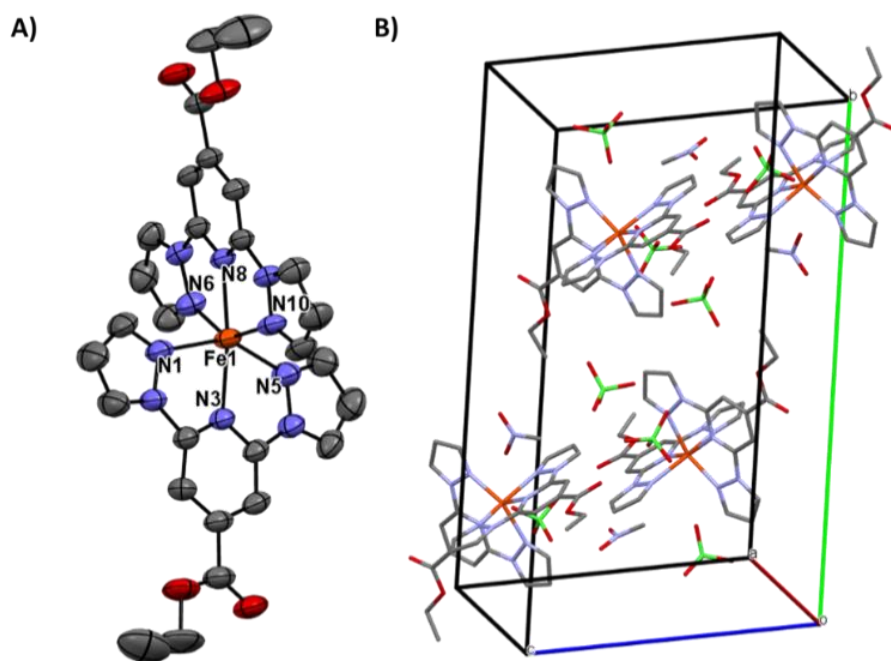


Figure 2.17: A) Crystal structure of di-cation complex **C2** at 300 K (HS). Displacement ellipsoids are at the 50% level, and B) crystal packing of complex **C2**. H-atoms and disorders were omitted for clarity.

The crystal packing of the HS complex **C2** contains the arrangement of the complex cations along the *c*-axis mediated by short contacts involving the complex cations and counter anions (Figure 2.18). No direct interactions between the complex cations were observed. The short contacts involve (i) the hydrogen atom of the pyrazole moieties of the cationic complex and the oxygen atom of the perchlorate anion (H2–O5, $d = 2.51$ Å, H9–O10, $d = 2.3$ Å), (ii) the oxygen atom of the perchlorate anion and the hydrogen atom of the pyridine ring of the complex cation (O9–H19, $d = 2.38$ Å), (iii) the oxygen atom of the carbonyl group of the cationic complex and the hydrogen atom of the solvent (O1–H29B, $d = 2.49$ Å).

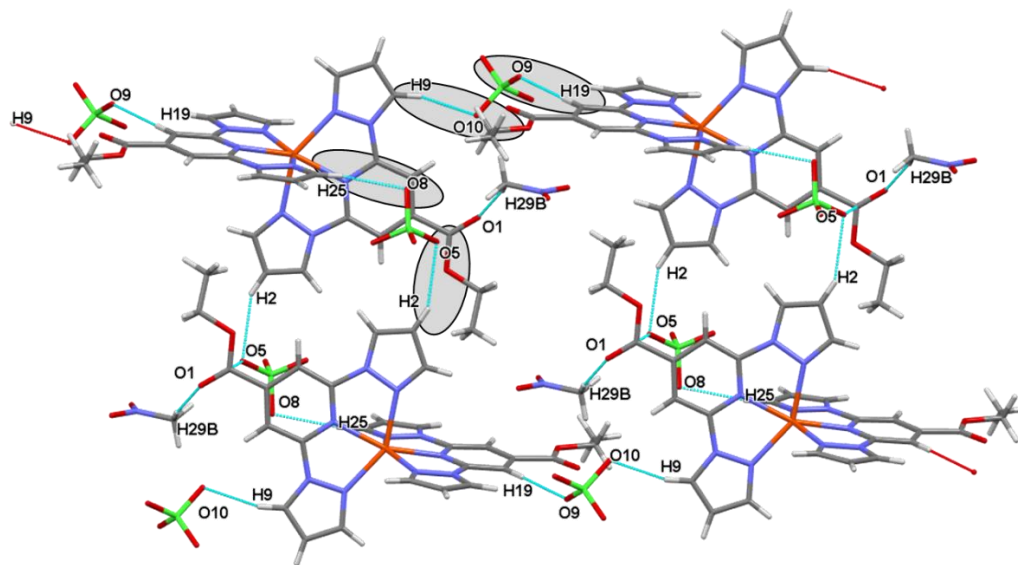


Figure 2.18: Intermolecular contacts in the unit cell of complex **C2** (high-spin) at 300 K.

Table 2.4: Selected Bond lengths (Å), angles (°), and distortion indices of the complex **C2** crystals structures at various temperatures.

Parameter	HS (335 K) ^a	HS (300K) ^a	LS (300 K) ^b	LS (150 K) ^c
Fe ₁ -N ₁ (pyrazolyl)	2.185(3)	2.187(2)	1.962(2)	1.953(1)
Fe ₁ -N ₃ (pyridyl)	2.134(3)	2.138(2)	1.911(2)	1.891(2)
Fe ₁ -N ₅ (pyrazolyl)	2.168(3)	2.155(2)	1.984(2)	1.972(2)
Fe ₁ -N ₆ (pyrazolyl)	2.197(3)	2.164(2)	1.973(2)	1.973(2)
Fe ₁ -N ₈ (pyridyl)	2.141(3)	2.132(2)	1.906(2)	1.893(2)
Fe ₁ -N ₁₀ (pyrazolyl)	2.159(3)	2.183(2)	1.979(2)	1.961(2)
rFe-N (average)	2.164(7)	2.156(5)	1.953(5)	1.941(5)
N ₃ -Fe ₁ -N ₈ (ϕ)	158.6(1)	158.45(7)	171.3(1)	171.80(7)
N ₆ -Fe ₁ -N ₁₀ (ψ)	145.3(1)	145.77(8)	159.7(1)	160.52(7)
N ₁ -Fe ₁ -N ₅ (ψ)	145.4(1)	145.45(8)	159.4(1)	160.59(7)
Σ	157.2	156.78	88.54	83.95
θ	81.34(3)	80.48(3)	87.96(3)	87.00(2)
α	73.10(10)	73.22(11)	79.87(18)	80.36(13)

(^a Orange block crystal (crystal 1), ^b black block crystal (crystal 2), ^c black block crystal (crystal 3))

Our attempts to determine the in-situ generated LS form of **C2** by cooling the orange crystals of the complex were not successful due to the cracking of the crystals, as shown in Figure 2.19. This cracking of the crystals can also be seen in the sample used for magnetic measurements. The crystals which were subjected to heating-cooling modes were turned into a fine powder, which is due to heavy distortion.

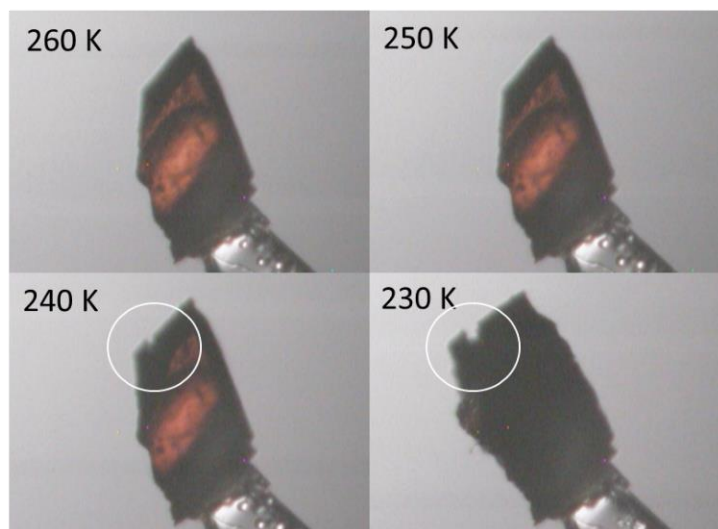


Figure 2.19: Images of the red-colored single crystal at different temperatures while cooling. The cracks occurred due to distortion were circled.

Differential scanning calorimetry (DSC) measurements were also performed on the crystalline materials to get insights into phase, enthalpy (ΔH), and entropy (ΔS) changes associated with the SCO of the complex. Four heat-cool cycles were performed at 2 K/min scan rate, and the results reproduced the trend that was observed from the magnetic measurements.

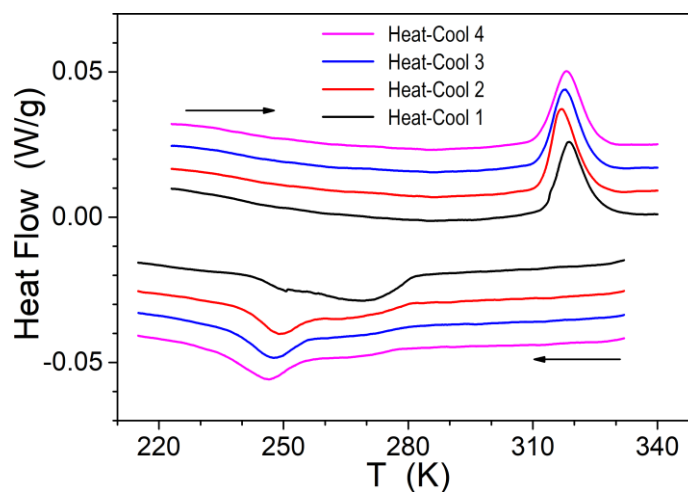


Figure 2.20: DSC analysis of complex **C2** at a scan rate of 2 K/min.

Relatively sharp transitions peaks were observed, whereas broadened peaks were observed in the cooling cycles. Figure 2.20 shows sharp SCO on heating, whose $T_{1/2\uparrow}$ coincides with $T_{1/2\uparrow}$ of magnetic measurements. Whereas SCO on cooling spreads over *ca.* 45 K, most probably because crossing from HS to LS structure goes through an intermediate phase and gives rise to two partially overlapping transitional peaks. The apparent discrepancy of $T_{1/2}$ between cooling cycle 1 and cycles 2,3,4 is explained by the variation of phase proportions: the first transition is more intense in cycle one and determines $T_{1/2}$, contrarily to cycles 2,3 and 4 for which the more intense transition is the second one. The phase coexistence further explains the discrepancies with $T_{1/2}$ values from SQUID. The $T_{1/2} = 283$ K and $\Delta T = 70$ K (for cycle 3) obtained from the DSC measurements are in close agreement with the SCO parameters ($T_{1/2} = 288$ K and $\Delta T = 69$ K, for 3rd cycle) obtained from the magnetic measurements. The change in enthalpy associated with SCO was found to be around 12.5 kJ mol⁻¹. The relation $\Delta S = \Delta H / T_{1/2}$ is used in the literature to describe the change in entropy associated with SCO of the complex. It is calculated and found to be 44.2 J K⁻¹mol⁻¹. Usually, the entropy values are greater than 13.4 J K⁻¹mol⁻¹, which is expected solely from a change in spin multiplicity from $S = 0$ to $S = 2$, upon SCO.⁸² Whereas, the excess entropy can be attributed primarily due to vibrational entropy change between LS and HS states.⁸³ Overall, the $T_{1/2}$ and ΔT values obtained from the DSC measurements are comparable with the values obtained from the magnetic measurements.

So hereby, we report two mononuclear iron(II) *bpp* based complexes with BF₄ (**C1**) and ClO₄ (**C2**) as anions and nitromethane as lattice solvent. The single-crystal XRD experiments at 150 K reveal the isostructural molecular architectures within the respective complexes. Both BF₄⁻ and ClO₄⁻ analogs crystallize in the same system and with same symmetry. The cell parameters at 150 K indicate that **C2** has higher cell parameters *a*, *b*, *c* and *V*, which could be due to a slightly larger size and additional disorderedness in perchlorate anion. The transition temperatures ($T_{1/2}$) for complexes **C1** and **C2** are 331 K and 288 K, respectively, with wide hysteresis. However, in the case of **C1**, the complex loses its hysteresis over the cycles and reduces the value of χT , and could be attributed to the loss of solvent, whereas it is not observed in case of **C2**.

The complex **C2** is one of the rare examples of *bpp*-complexes that has crystallized in both LS and HS forms during crystallization. The crystal structure investigations have shown a highly distorted structure at 300 K. In general, the Jahn-Teller distorted complexes exhibit HS behaviour, and they tend to show no SCO and traps in HS over the temperature range.^{84,85,86} However the recent reports of Halcrow and coworkers on ([Fe(Lig)₂][ClO₄]₂ (Lig= 4-methyl-2,6-di(pyrazol-1-yl)pyridine)); and Ruben and coworkers on [Fe(*bpp*-COOEt)₂][ClO₄]₂·CH₃CN are some exceptional cases of highly distorted complex to undergo SCO.^{68,87} Now, the reported complex **C2** is an additional complex that joins into the same family of complexes that show high distortion with SCO behaviour. Therefore, this complex **C2** is an example with an insufficient steric hindrance to block the HS state over the temperature range and thus leads to hysteresis. The insufficient steric hindrance could be a result of packing the distorted complex along with the solvent molecule, which not only

improves the cooperativity but also provides the space between the molecules that helps in undergoing the switching. Moreover, from the crystal structure provided, the complex **C2** remains always in $P2_1/n$ space group and doesn't undergo any symmetry breaking on ST. It can also be seen that solvent molecules have very few short contacts, which leads to the conclusion that free volume provided by solvent plays a major role. Similar examples in the literature can be found with an example of $[\text{Fe}(\text{bpp-COOEt})_2][\text{ClO}_4]_2 \cdot \text{CH}_3\text{COCH}_3$, where the complex showed an abrupt transition from LS to HS at 330 K, but due to loss of solvent, the molecule gets trapped in HS.⁷⁶ Similarly, the other complex $([\text{Fe}(\text{bpp-COOMe})_2][\text{ClO}_4]_2$ was crystallized without solvent and thus trapped in HS over the temperature range.⁵⁹ So, the complex **C2**, reported in this section, becomes important as the molecule is crystallized with nitromethane, which has a higher boiling point and requires a comparatively higher temperature to remove it, as it is not seen till 335 K and thus produces stable hysteresis.

2.4 Conclusion

In conclusion, we have applied XPS and STM to study the self-assembled metal-organic networks at surfaces. Our finding shows the formation of Kagome lattice by deprotonation of **L1** ligand. Each pore of the lattice was filled with an additional molecule, which was immobilized due to limited space within a pore. Whereas, sublimation of ligand **L1** and Fe subsequently resulted in coordination oligomers, with two different binding modes. We observed the formation of 1D chains by head-to-tail binding of the deprotonated **L1** ligand molecules coordinated by a Fe atom; and 2D knots, having 4 molecules in a cross-like orientation coordinated by two Fe atoms. These surface-confined self-assembled architectures open the way to engineer the complex nano-architectures as they could exhibit electronic, catalytic, magnetic, and other properties.

In addition, we also obtained a new *bpp* based SCO complexes **C1** and **C2** using a low volatile solvent (nitromethane) as a solvent. Both the complexes were structurally characterized by single-crystal XRD, and it is also noteworthy that both the LS and HS structures were obtained at 300 K (RT) in the case of complex **C2**. Moreover, the magnetic measurements on the complex **C1** showed above RT spin transition, whereas complex **C2** showed ST around room temperature with stable hysteresis of 60 K.

So in the quest for suitable candidates for SCO for future technological purposes with relevant thermal hysteresis centered around room temperature, now the complex **C2** stands ahead over all the previously reported complexes as it satisfies all the conditions stated by Kahn and coworkers. The presented complex **C2** shows the high reproducibility of ST over successive thermal cycles. This presence of the hysteresis around RT and the ability of the complex to be stable in both the states at RT makes them suitable for molecule-based switching and memory architectures for future device applications.

Chapter 3

Chiral Resolution of SCO active Iron(II) Grid complexes

3.1 Chiral Systems

3.1.1 Introduction to Chirality

Chirality is a fundamental characteristic property of living matter and nature. An object is referred to be chiral when it is non-superimposable with its mirror image. Chirality is universal, and it could be observed at various levels of hierarchy from subatomic and molecular to supramolecular, macroscopic scales.⁸⁸ Most of the biologically active molecules, such as amino acids, sugar, double-helical DNA, and peptides, are chiral in nature. As an outcome, chirality also plays a vital role in drug-biocomponent interaction. Consequently, chirality is of pharmaceutical industrial significance.⁸⁹ Not only in chemistry and biology, but it also has crucial importance in physics, materials, and nano-science.^{90,91}

In the view of molecular systems, chirality arises from chiral centers or chiral axis. The chiral molecules lack a plane of symmetry. A simple organic molecule is said to be chiral if it has a chiral center, i.e., an asymmetric carbon atom in the molecule. An asymmetric carbon atom is an sp^3 carbon atom attached to four different types of atoms. Each chiral center can have two different absolute configurations, which is nothing but the difference in the spatial arrangement of atoms at the chiral center. These two configurations are called enantiomers. For naming these enantiomers, (*R*) and (*S*) system is mostly used (Figure 3.1A). They come from the words Rectus (Latin word for right) and Sinister (Latin word for left), and they indicate the clockwise (*R*) and anti-clockwise (*S*) turning sense of substituents, according to Cahn-Ingold-Prelog rules (CIP).^{92,93} The presence of more than one chiral center in a molecule can give rise to diastereomers, for example, as shown in Figure 3.1.

The molecule can also be chiral, without an asymmetric carbon atom, by having an axial chirality. The chiral axis is an imaginary line in the molecule, which holds four groups placed in non-planar arrangement resulting in a non-superimposable mirror image. Allenes, spiro-compounds and biphenyls are some typical examples of these axial chiral compounds. A special case of axial chirality is present in helical molecules. This helicity is very common in supramolecular systems and can be right-handed or left-handed, giving rise to two enantiomers. These enantiomers are named as (*P*) or (*M*) for the clockwise or anti-clockwise rotation, respectively. The Λ and Δ chirality terms are used for defining coordination compounds, and these enantiomers can be referred to as Λ for a left-handed twist and Δ for a right-handed twist. More details on the supra-molecular chirality will be discussed further in the later sections.

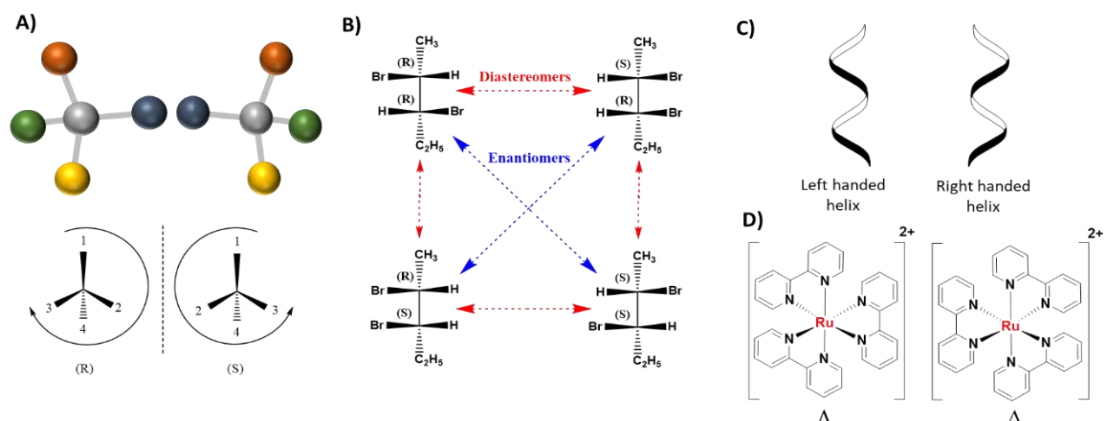


Figure 3.1: Representation of A) (*R*)- and (*S*)-enantiomers, B) enantiomers & diastereomers, C) left and right-handed helical structures, and D) examples of enantiomers in coordination complexes - Λ and Δ isomers of $[\text{Ru}(\text{bpy})_3]^{2+}$.

3.1.2 Characterization Methods: Circular Dichroism

An important step in research while working with chiral molecules is their characterization for chirality. X-ray structural analysis is one of the best methods of characterization, but it requires samples in crystal form, which could not be possible for all types of samples. The other prime methods for characterizations are spectroscopic techniques. These include circular dichroism (CD), vibrational CD (VCD), and Raman optical activity (ROA) spectroscopy. Among the spectroscopic methods, the CD is the most commonly used method for characterization. Even though CD gives less information compared to NMR or X-ray crystallography, it is a very quick method that requires a tiny amount of sample in the solution state.

Light is an electromagnetic wave composed of electric and magnetic fields, which oscillates perpendicular to each other. Light passing through a rotating polarized plane is considered as a circularly polarized light. A linearly polarized light is a summation of both right and left circularly polarized light, which are of the same amplitude and wavelength. When this linearly polarized light passes through a chiral media, it turns into elliptically polarized light due to the difference in absorbance between right and left circularly polarized light with chiral media (Figure 3.2). This phenomenon is called CD.^{94,95,96}

The CD spectrum is experimentally obtained by measuring the difference in absorption of left and right circular polarized light at each wavelength, and the equation is given as below

$$CD = A_l - A_r \quad (3.1)$$

By using Beer-Lambert's law, $\Delta\varepsilon$ is given as

$$\Delta\varepsilon = \varepsilon_l - \varepsilon_r = \frac{CD}{c \times d} \quad (3.2)$$

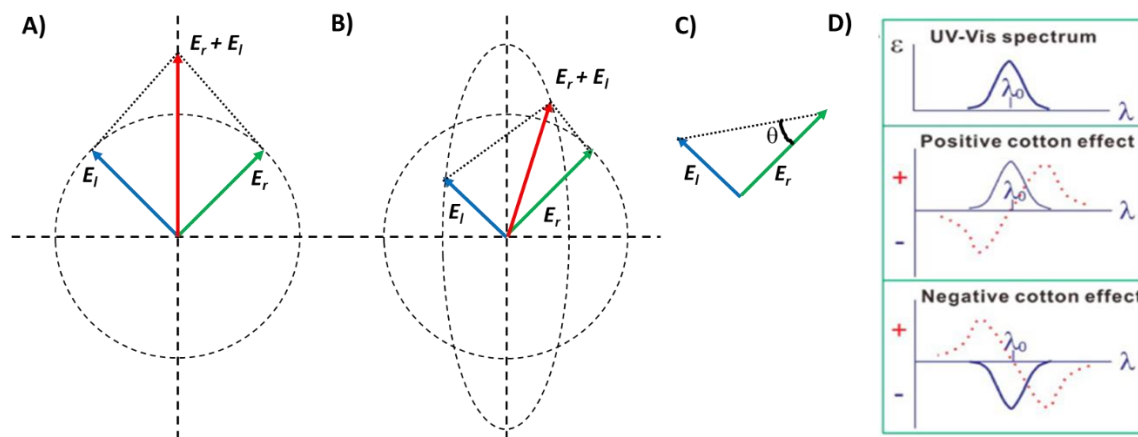


Figure 3.2: Representation of linearly polarized light (red), as a summation of LCP (blue) and RCP (green), (A) before and (B) after passing through a sample. (C) representation of ellipticity (θ) (D) Representation of positive and negative Cotton effects.

Here, A_l and A_r are the absorptions of left circularly polarized (LCP) and right circularly polarized (RCP) lights, respectively; and c and d are the sample concentrations (mol l^{-1}) and path length (cm), respectively. In general, the CD measurements are expressed in terms of ellipticity (θ), which is in terms of ‘*mdeg*’ at a particular wavelength. The degree of ellipticity (θ) is defined as the tangent of the ratio of the minor to major elliptical axis and ellipticity is related with CD by the following equation-

$$\theta(\text{mdeg}) = 32980 \times CD \quad (3.3)$$

Using the above equations, the net equation can be written as

$$\Delta\varepsilon = \frac{\theta}{32980 \times c \times d} \quad (3.4)$$

CD signals (bands) are signed ones and could be positive or negative, and these bands appear as mirror images for enantiomers. The peaks (+ve / -ve sign) in the CD spectra are referred to as the ‘Cotton effect’, which is a characteristic change in circular dichroism in the wavelength region of the absorption band of the chiral substance. It is said to be a positive cotton effect if the CD signal first increases by decreasing the wavelength and vice-versa (Figure 3.2 D).⁹⁶

3.1.3 Chirality and Molecular Electronics

It is not an exaggeration to say that ‘chirality’ has become one of the most crucial concepts in molecular sciences, linking to problems in many areas of sciences in everyday life. Initially, the interest in chiral compounds was focused on organic molecules, drugs, and biological molecules like sugars and carbohydrates. Gradually, due to their unique properties, the interest has moved towards other fields in chemistry like organometallic and coordination chemistry, molecular materials, and supramolecular chemistry.^{96,97} However, not limited to the above applications, chirality has also been playing an essential role in several features in molecular electronics, which could help in designing molecular devices. These properties include magneto-chiral dichroism (MChD), second harmonic generation (SHG), chiral induced spin selectivity (CISS) effects, and many more. These generally occur in non-centrosymmetric crystals. They can be explained as below –

- **Magneto-chiral dichroism (MChD)**

Magneto-chiral dichroism is an interaction between chirality, light, and magnetism with fascinating research challenges in various fields. It is a magneto-optical effect in which the absorption coefficient of the chiral molecule in an unpolarized light depends on the direction of the magnetic field applied. In simple words, magnetic fields can be used to modify the absorption of light in chiral media.

In the 19th century, Arago and Faraday discovered natural optical activity (NOA) and magnetically induced optical activity (MOA), respectively. Both these effects result in the rotation of the polarization of light. NOA occurs in chiral media, and due to spatial symmetry breaking, there is a difference between refractive indices of left and right circularly polarized light, which causes rotation of linearly polarized light. In contrast, MOA occurs in all materials under the applied magnetic field. Due to time-reversal symmetry breaking, the material presents different absorption coefficients depending on the direction of the magnetic field with respect to light (Figure 3.3 A).

The simultaneous breaking of spatial and time-reversal symmetries has opened up a new effect called magneto-chiral anisotropy (MChA) (Figure 3.3 A). This was first observed in 1997 by Rikken and Raupach.⁹⁸ They observed that on applying a static magnetic field parallel to propagation of light could produce a small shift in the value of the absorption of a chiral molecule. Moreover, this sign of the small shift changes by changing the direction of the magnetic field or by changing the other enantiomer (Figure 3.3 B).⁹⁹

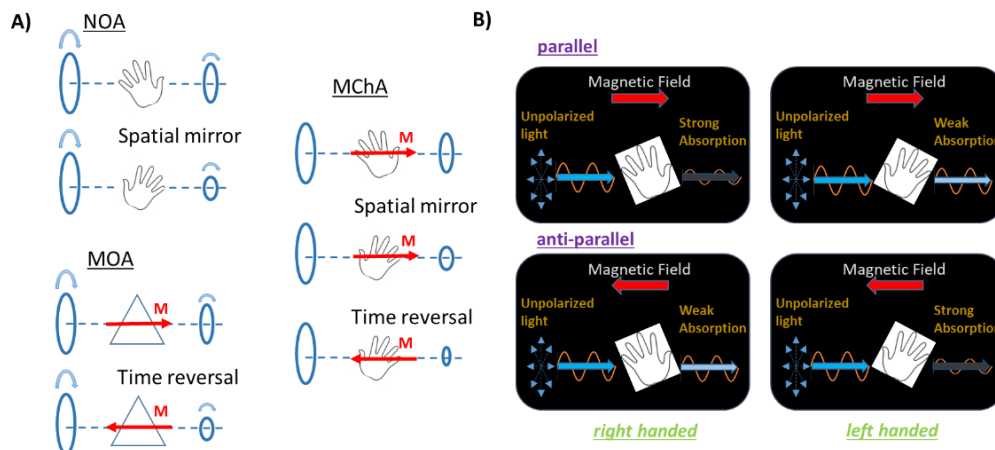


Figure 3.3: A) Schematic representation of Natural optical activity, Magnetically induced optical activity and Magneto-chiral anisotropy, B) representation of Magneto-Chiral Dichroism effect.

- **Second Harmonic Generation (SHG)**

Second-harmonic generation (SHG) is a phenomenon observed in non-linear optics. It is also called frequency doubling. In brief, SHG is a phenomenon in which the photons interacting with non-linear optical (NLO) materials are effectively combined to generate new photons with twice the frequency and so doubled energy. This has typical applications in microscopy, lasers, and many more (Figure 3.4 A).

These second-order non-linear effects are usually observed only from non-centrosymmetric materials.¹⁰⁰ Generally, such types of materials are prepared by incorporating donor-acceptor-substituted molecules that have polarizability into non-centrosymmetric structures such as crystals, self-assembled films, or polymer films. However, one other way is to use directly the chiral molecules, which are generally non-centrosymmetric. Thus, their second-order NLO response will be non-zero.

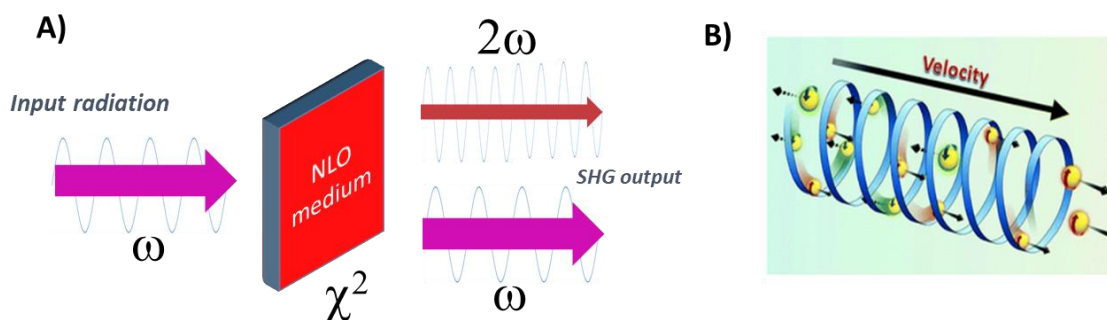


Figure 3.4: Pictorial representation of A) second harmonic generation and B) CISS effect.

- **Chiral-induced spin selectivity (CISS)**

The chiral-induced spin selectivity (CISS) effect was first observed by Prof. Ron Naaman in 1999. It says that the probability of electron transmission through chiral molecules depends on the spin of the electron. In this CISS process, the electrons of a certain spin can pass through the molecule more easily in one direction than the other, and the preferred spin depends on the chirality of the molecule. This observation was surprising since spin filtering is an ability usually associated with magnetic materials. This CISS effect can be applied in many ways, and one of the most important ways is spin filtering for spintronics. This can replace the ferromagnets in spintronics and could help in the miniaturization of electronic devices.¹⁰¹

3.2 Supramolecular chemistry and grid complexes

3.2.1 Introduction to Grid complex system

Supramolecular chemistry is defined by phrases such as “Chemistry beyond the molecule”, “chemistry of molecular assemblies and intermolecular bond” by Jean-Marie Lehn, who is the recipient of the Nobel Prize for his work in this field in 1987.¹⁰² The main objective of supramolecular chemistry is to design and synthesize multifunctional systems from multiple components, using non-covalent interactions to hold the components. These non-covalent interactions include (a) electrostatic (ion-ion, ion-dipole and dipole-dipole), (b) hydrogen bonding, (c) π - π stacking interactions, and (d) van der Waals forces.¹⁰³ Due to the interaction between molecular components, creating new functional architectures, supramolecular chemistry has emerged as an interdisciplinary field with a wide range of applications in electronics, catalysis, medicine, to name a few.^{104,105,106,107}

Self-assembly is a process where the components either separate or link to form ordered aggregates. It acts as a driving force that combines all the non-covalent interactions to construct a supramolecular system.^{108,109} Nature is the best example that uses self-assembly to form complex structures with high precision. Biological systems have highly functional complex structures formed from self-assembly. These include the formation of a DNA double-helical structure from the complementary nucleic acid strands and the formation of proteins from peptides.^{110,111}

Metallo-supramolecular chemistry is an actively pursued area of research in supramolecular chemistry, which uses the interaction between the ligands and metal centers for the construction of coordination networks. This allows combining the properties of ligands and metal centers into a defined structure with the generation of new properties. In the last few decades, several metallo-supramolecular architectures, such as helicates, racks, grid, cages, were synthesized.^{112,113,114,115} In such metallo-supramolecular structures, the

concept of chirality could arise from the spatial arrangement of the chelating ligands around the metal ions, or as a consequence of helical twist in the ligands.

Grid complexes are a family of supramolecular structures that are formed from a set of organic ligands and metal ions, depending on the structural information stored in the ligands and the coordination geometry of metal centers. It requires the perpendicular arrangement of ligands at the metal centers. So the nuclearity of the complexes entirely depends on the polytopic nature of the ligand and the ability of the metal ions to coordinate. It was also showed that the same ligand had yielded different architectures with different metal ions. On account of this reason, there is interest in generating different architectures depending on ligands and metal ions. In the literature, the two-dimensional grid complexes show a well-defined arrangement (Figure 3.5) of metal centers, with square $[n \times n]$ and rectangular $[n \times m]$ grids with $n, m \leq 4$.

The simplest and the most commonly occurring case in grid complexes is $[2 \times 2]$ array. Many reports were produced on synthesis and characterization of $[2 \times 2]$ grid-like complexes with Mn(II), Cu(II), Zn(II), Fe(II). The metal ions coordinate to ditopic ligands containing tridentate or bidentate coordination pockets arranged in a linear fashion. Depending on the transition metal used in the system, interesting optical, electrochemical, photo-physical, and magnetic properties can be accessed. Also, these properties can be varied by chemical functionalization of ligands. Thus the design of the ligands plays a crucial

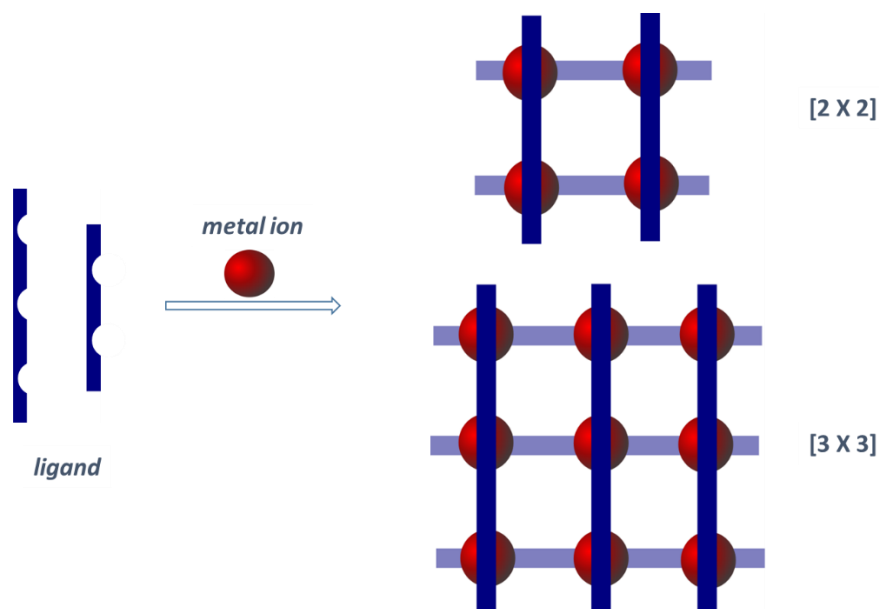


Figure 3.5: Schematic representation of $[n \times n]$ grids complex architectures forming from 'n' metal centers and 'n' ligands.

role in designing grid-type metallo-supramolecular architectures. Assembling ligands containing bidentate or tridentate subunits with ions leads to grids featuring tetrahedral (bidentate) or octahedral (tridentate) coordination geometry around the metal ions. Nitrogen donor ligands such as pyrazole, pyridine, pyrimidine, or imidazole are commonly used to construct metallo-supramolecular grids.^{104,116,117}

Since the prime focus of the work in this thesis is related to magnetism, we will be discussing the application of these grid complexes in spin-crossover systems. These systems have moved to the focus of scientific interest due to their potential application in molecular devices.^{114,118,119} As mentioned in the previous chapter, to obtain functional devices based on SCO complexes, requirements such as abruptness, wide hysteresis at room temperature along with robustness and stability needs to be achieved. Consequently, ligands design plays an important role in achieving device suitable grid complexes.

3.2.2 Introduction to Homoditopic ligand system

Our group recently reported on a homoditopic ligand **L**, which consists of two tridentate 2-(1H-imidazol-2-yl)-6-(pyrazol-1-yl)pyridine units interlinked *via* a central benzo[1,2-d:4,5-d']diimidazole bridge (Figure 3.6 A). The bridging unit can simultaneously undergo two tautomerization processes between the secondary amine and imine functional groups. In addition to this, the ligand can undergo conformational isomerism, which is due to the rotation of the single bond between the aromatic ring systems in the ligand. These two tautomerism and conformational isomerism lead the parent ligand to be available in two different conformations, namely CIS-conformation and TRANS-conformation (Figure 3.6 B). The names of these isomers were termed depending on their apparent shape of the conformer molecules. These two conformations are stabilized by the interaction between the N-based lone pair electrons and the H atoms of the neighboring aromatic rings. The ¹H NMR investigation of the solution sample of the ligand **L** has shown the presence of the two tauto conformers is in the ratio of 1:1.¹²⁰

This ligand system has two tridentate chelating units. Because of the two different modes of an arrangement of these chelating units in these tauto-conformers, coordination with transition metal ion leads to the formation of two different coordination products (S and C isomers; Figure 3.6 C) having different structure and properties. These two complexes were separated by fractional crystallization and have shown distinct SCO properties.¹²⁰

Dissolving of the S-form of isomer in nitromethane and heating the solution at 100 °C in a microwave oven for 30 min yielded C- isomer, as confirmed using ¹H-NMR spectroscopy.¹²⁰ This shows that the S-type of isomers is highly unstable in the solution phase.

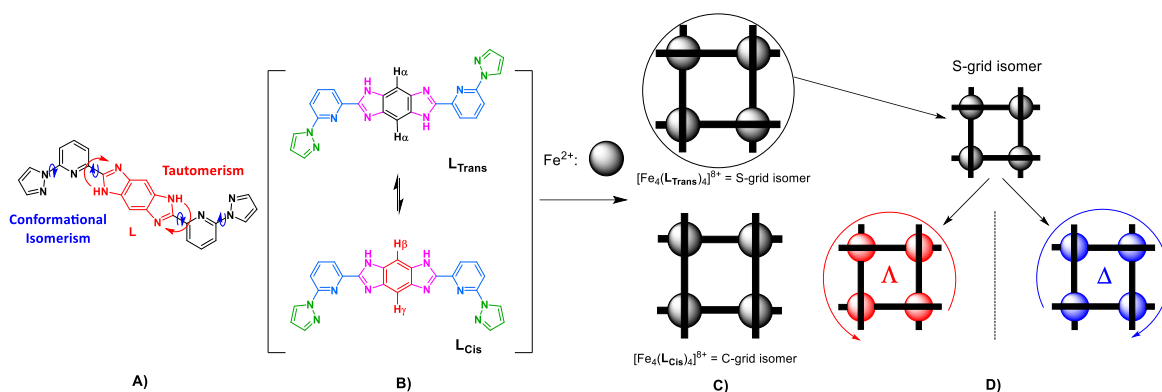


Figure 3.6: A) The conformational isomerism and tautomerism in ligand **L**. B) **L**_{Trans} and **L**_{Cis} conformers of **L** in solution. C) Divergent coordination chemistry of ligand **L** (black bar) on coordination with Fe $^{2+}$ metal ions (grey balls). D) Λ and Δ -isomers of the S-grid complex.

Magnetic studies revealed gradual SCO behavior of S-grid contrast to the C-grid trapped in the HS-state. Thus the S-form of complexes is of interest, not only because of its SCO active nature but also due to the chiral nature of the grids. In S-grid complexes, four trans ligands wrap the coordinating metal center in an inter-woven style, endowing the grid with chiral character—that is, they are present in both Δ and Λ forms (Figure 3.6 D) and are generally obtained as a racemic mixture. The separation of these enantiomers could offer an opportunity to study the enantiomer-dependent nature of spin-state switching in the S-grids.

The above type of chiral complexes can be separated into enantiopure forms, for example, by spontaneous resolution or by using some other methods like HPLC with chiral stationary media. In some other convenient cases, the enantiopure form can be separated by obtaining the diastereoselective synthesis using non-racemic ligands as building blocks. This strategy of using chiral ligands is successful in producing thermodynamically favored diastereomers.

3.3 Objectives

In order to produce chiral spin-crossover complexes, here in this chapter, we aim to have the following tasks as mentioned:

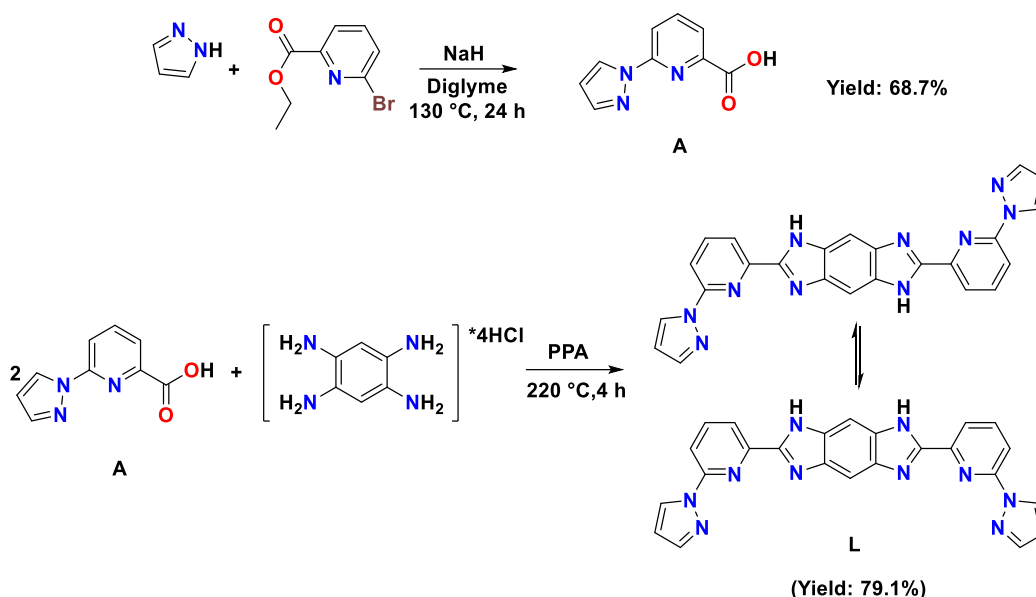
Objective 1: To separate the TRANS- and CIS- forms of the ligands prior to complexation to achieve the pure conformers of C and S isomers of Fe(II) grid complexes.

Objective 2: Once the S-form isomer of the grid complex is obtained, the next task is to resolve the enantiomers present in it and study them.

3.3.1 Objective 1: Separation of TRANS and CIS – isomers of ligand L

The syntheses and structural characterization of the ligands and complexes and magnetic characterization of the complexes were performed in INT.

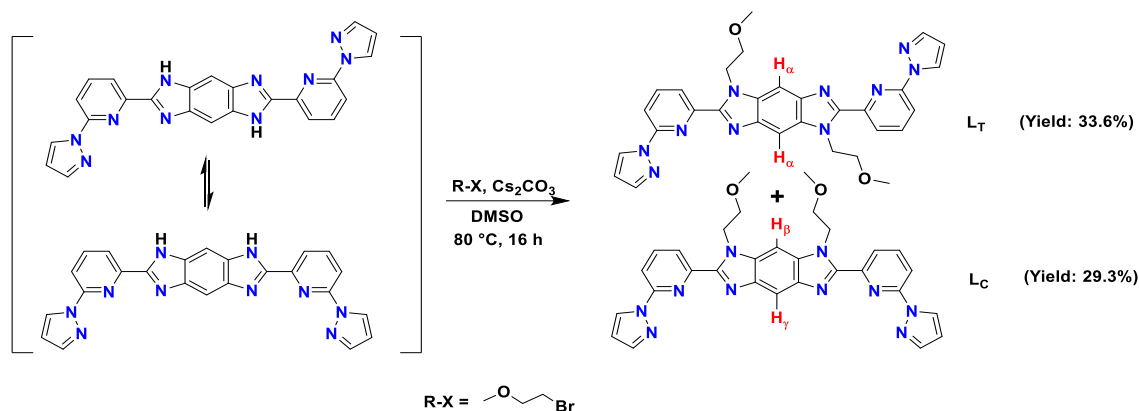
The parent ligand (**L**) was synthesized by the condensation reaction between the 6-(1*H*-pyrazol-1-yl)picolinic acid and 1,2,4,5- benzene-tetraamine in polyphosphoric acid (PPA), as shown in Scheme 3.1. The synthesized parent ligand was completely characterized and was confirmed by ¹H-NMR and ¹³C-NMR spectroscopy and mass spectrometry. NMR studies showed that both the tauto-conformers (TRANS and CIS) are present in solution in a 1:1 ratio. This was determined by the integration of singlet resonances of protons H_α, H_β and H_γ of benzene moieties of the ligand backbone.¹²⁰ This tautomerization of the ligand is an interesting property that gives access to different modes of coordination to metal ions leading to different products. However, to study the individual ligand or product formed, it is advantageous to block the tauto isomerization equilibrium.



Scheme 3.1: Synthetic scheme for the preparation of ligand **L**.

In ligand **L**, the tautomerization arises from the secondary imine group present on the imidazole ring of the ligand's backbone. The tautomerization can be blocked by performing a chemical substitution at this secondary amine function to form a tertiary amine. The resulting functionalized ligands could be obtained either in CIS or TRANS type conformation, which are conformationally locked from tautomerization. Due to the different structural conformations, the CIS- and TRANS- type of ligands show a difference in their polarity, which facilitates in the separation of the CIS- and TRANS- ligands by simple

column chromatography. Thus, the formation of parallel products upon coordination to metal ions can be achieved using these separated ligands.



Scheme 3.2: Synthetic scheme for separation of TRANS (L_T) and CIS (L_C) forms of ligands.

In order to prevent the tautomerization, the parent ligand system can be reacted with alkyl or benzyl bromide in DMSO as a solvent in the presence of Cs_2CO_3 as a base. As shown in Scheme 3.2, here, 3-bromoethoxy methane was used as an alkyl halide and treated with the parent ligand in basic media at 110 °C under inert conditions. After a workup and column chromatography on silica gel, two products - TRANS type and CIS type products were obtained. These compounds were entirely characterized by standard methods like 1H & ^{13}C -NMR spectroscopy and mass spectrometry. This substitution on the secondary amine group of imidazole has also improved the solubility of the ligands in common solvents—for example, chloroform, methanol, and DCM. The following proton NMR spectra (Figure 3.7) confirm the successful separation of the CIS and TRANS isomers and their purity.

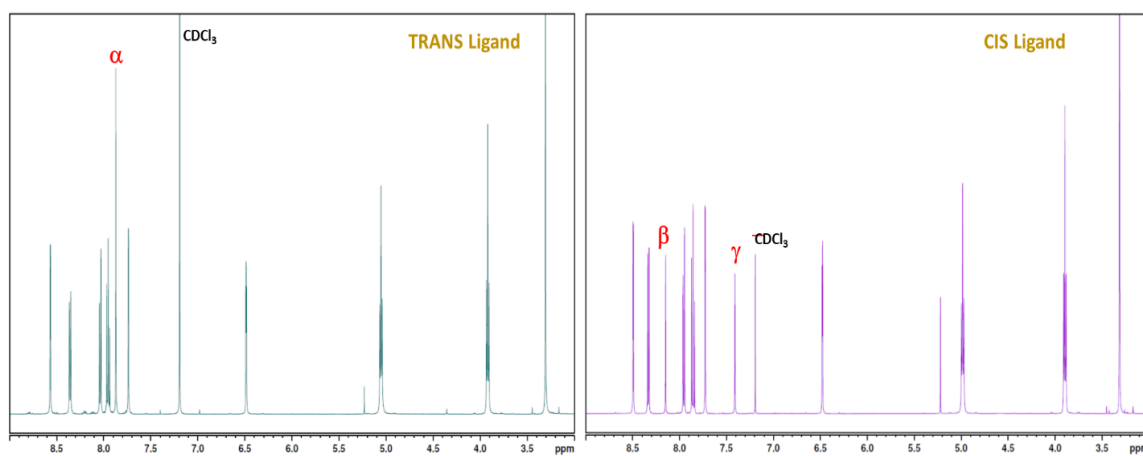
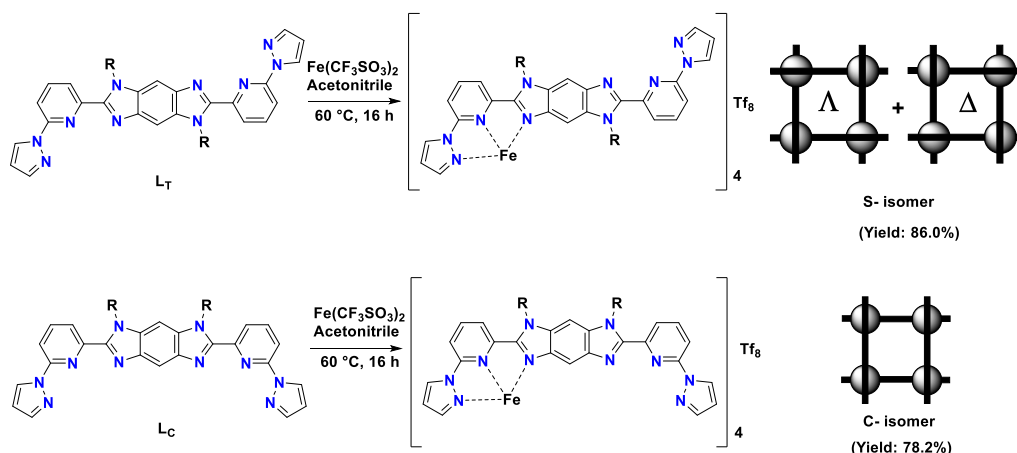


Figure 3.7: 1H -NMR spectra of L_T and L_C in $CDCl_3$ showing different peak positions for proton on central benzene ring.

This separation of the ligands helps in studying the required complexes individually and reduces the steps for recrystallization steps of purification. The pure conformers of grid-complexes could be obtained by treating the respective ligands with Fe(II) salt, as shown in Scheme 3.3. Treating the TRANS ligand with an equimolar amount of Fe(Tf)₂ in acetonitrile yielded the S-form of the complex. The formation of the tetra-nuclear compound was confirmed by single-crystal XRD and also mass spectrometry studies.



Scheme 3.3: Synthesis of S and C grid complexes from TRANS(L_T) and CIS(L_C) ligands, respectively.

The block-shaped crystals of S-grid were obtained by diffusing diethyl ether into the solution of the grid complex in acetonitrile. The single-crystal XRD studies at 220 K has confirmed the square-shaped grid complex with ligands in interwoven pattern and with four Fe(II) situated in corners. Each Fe(II) was coordinated by six nitrogen atoms from the ligands with a dihedral angle (Figure 3.8 A) of 85.51°. The compound was crystallized in an orthorhombic *P*2₁2₁2 space group with a cell volume of 19142.8(11) Å³ (*a*=32.5873(10), *b*=23.6689(10), *c*=24.8187(7)) and *Z*=4. The XRD studies reveal the charge of the square-shaped complex cation is balanced by eight triflate anions. The structure also contains seven acetonitrile molecules and two diethyl ether. Both the possible enantiomeric isomers can be observed in a single unit cell of the complex (Figure 3.8 B). The asymmetric unit consists of the two Fe₂(L)₂ units along with solvent and counter anion units. Among the two Fe₂(L_T)₂ units, one shows delta chirality, and the other one showing lambda chirality.

At 220 K, the avg. Fe-N bond length is around 1.942 Å, which corresponds to LS state of the complex, which is further supported by the N_{pyrazole}-Fe-N_{imidazole} angle (Φ) - 173.74° and Σ is around 87.367°.

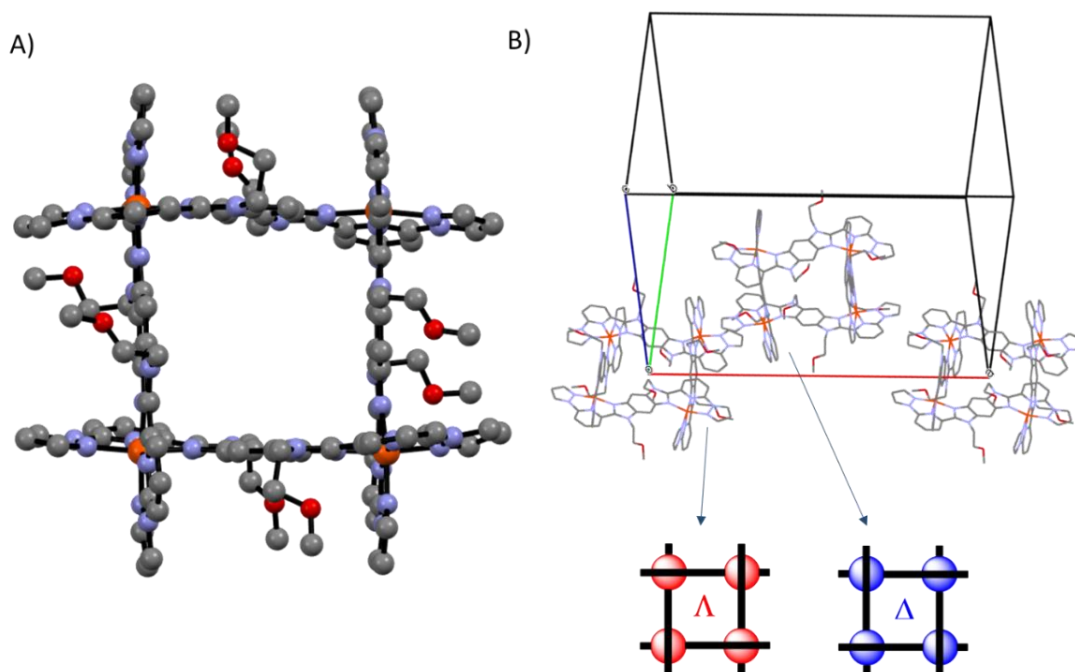


Figure 3.8: (A) Crystal structure of S-form of grid complex, (B) unit cell containing both the Λ and Δ -isomers (anions, hydrogen, and solvent molecules were omitted for clarity), [Fe(II)- orange, O-red, C- carbon, N- blue].

Similarly, the treatment of CIS type ligand with an equimolar amount of $\text{Fe}(\text{Tf})_2$ yielded solely C-type of grid complex. The formation of the tetra-nuclear grid complex was confirmed by mass spectrometry. The block-shaped crystals were obtained by diffusing diethyl ether into the solution complex in acetonitrile. However, the trials to solve the structure failed due to the poor quality of the crystals produced.

The magnetic investigation in the range of 5-375 K was performed for both the C and S isomer grid complexes synthesized above. The magnetic curves presented as χT vs. T for C and S complexes indicate HS and gradual SCO behaviour, respectively (Figure 3.9). The χT value at RT for C-complex is about $13 \text{ cm}^3 \text{ mol}^{-1} \text{ K}$ that corresponds to the HS-state of the complex at RT. The observed decrease in χT value below 50 K corresponds to zero-field splitting in HS complex.

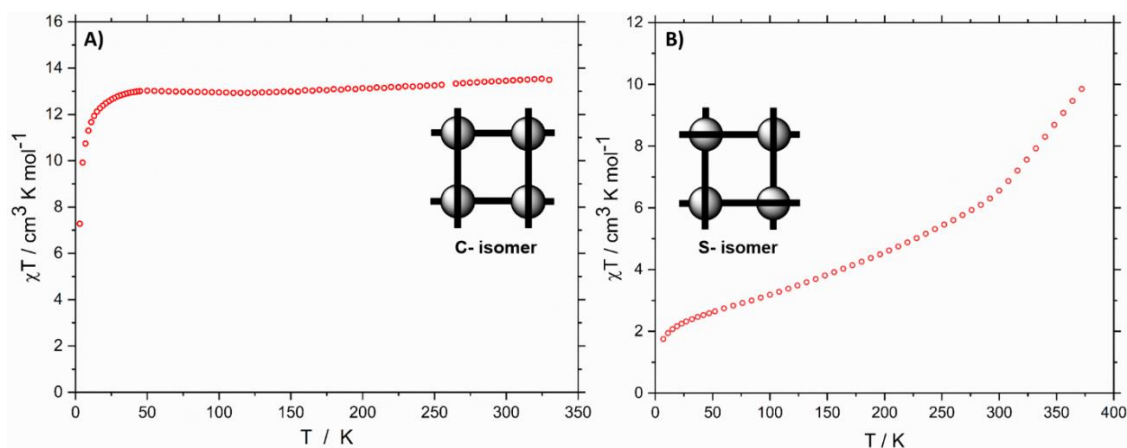


Figure 3.9: χT vs. T plots of C (left) and S (right) forms of complexes in the temperature region of 5-370 K.

In S-complex, a $\chi T = \sim 6.1 \text{ cm}^3 \text{ mol}^{-1} \text{ K}$ was obtained at RT, corresponding to about 45% of the complex in the HS. Below 220 K, the χT value is close $\sim 4.1 \text{ cm}^3 \text{ mol}^{-1} \text{ K}$, which shows most of the metal centers are in the LS state, in agreement with the crystallographic data.

Thus, the derivatives (**L_T** and **L_C**) obtained by alkyl substitution on secondary amino groups do not tautomerize anymore and can give access to only one [2x2] grid complex, either S or C. In this way, it helped to study the properties of isomeric coordination complexes and their SCO properties of the obtained [2x2] grid complexes. Furthermore, it is important to remember that grid complexes build from S form of such ligands show two chiral enantiomers. So, this separation of the S-form of the complex could help in the deconvolution of the enantiomers.

3.3.2 Objective 2: Chiral resolution of Λ and Δ – enantiomers in S-type conformers

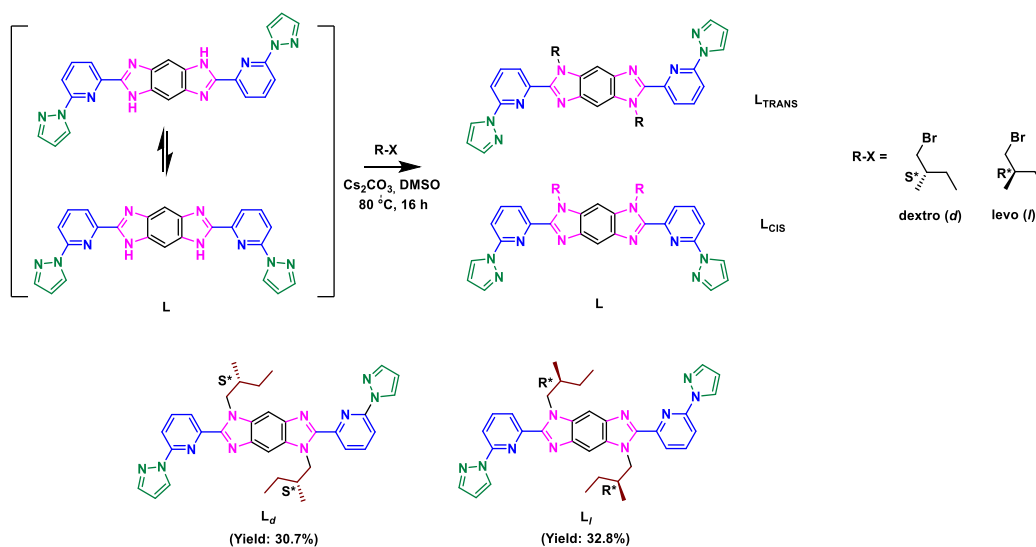
The results presented in this section were obtained in collaboration with the groups of Prof. Manfred M. Kappes in INT and Prof. Wim Klopper at IPC for IMMS measurements and TDDFT calculations, respectively. CD measurements were performed at IBG-1 and LIESST measurements by Dr. Ivan Salitros from the Slovak University of Technology in Bratislava, Slovakia. Mössbauer measurements were performed in collaboration with Prof. Volker Schünemann, TU Kaiserslautern.

As mentioned before, among both C-conformer and the S-conformers, the S- type conformers are interesting, not only just because of its SCO behavior but due to the presence of chirality in them. In the S- form of grid complex, the four TRANS form of the ligands wrap around the metals in an interwoven style, and this makes the complexes to be chiral.

So, the complexes are present in both Δ and Λ forms, and the separation of these SCO complexes might be helpful to investigate further the relationship between the cooperativity parameters in SCO and inbuilt chiral information

Till now, the majority of the chiral SCO complexes reported were obtained by spontaneous resolution, i.e., generation of crystals simultaneously in the mixture instead of racemic crystals. However, this method cannot be used to produce chiral materials in larger quantities. So far, different strategies were developed to solve the problem of isomeric deconvolution, such as using chiral counter anions,¹²¹ or by introducing chirality in the ligand.¹²² To the best of our knowledge, the resolution and the studies of two enantiomers of Fe(II) SCO grid complexes have not been reported yet. Our trials of chiral separation began with the famous method of using chiral counter ions to transform enantiomers into diastereomers and thus separate. In general, one of them should crystallize due to the difference in solubility between the diastereomers. Therefore, we applied the same separation method of using several counter anions like dibenzoyl tartrate, antimonyl tartrate and TRISPHAT. However, our trials were unsuccessful to replace triflate with any of the above anions. Thus, we chose the alternative way of appending the chirality on the parent ligand for the large scale separation of the two enantiomers of Fe(II) S-grids.

As reported in the previous task, we can separate the TRANS and CIS isomers by using some alkyl or benzyl bromides or iodides. However, for the present task of the chiral resolution, there is a need for chiral moiety to be added. So we selected the chiral bromides, (*S*)-3-methyl-1-bromobutane, and (*R*)-3-methyl-1-bromobutane to react with the parent ligand **L** to prepare a newly modified chiralized version of ligands.



Scheme 3.4: Scheme for the synthesis of chiral ligands **L_d** and **L_f**.

This chiral substitution on the secondary amine helps in two ways in just a single step – to get the TRANS- isomer for helping to get rid of the C- form of grid complex; and for introducing chiral moiety to help in chiral resolution. So the treatment of parent ligand **L** with chiral (*R*)- and (*S*)- alkyl bromides in DMSO in the presence of Cs_2CO_3 as a base produced two sets of enantiomerically pure CIS (R-CIS and S-CIS) and TRANS (R- TRANS and S- TRANS) isomers. Thus, tautomerism is prevented on the ligand **L** (Scheme 3.4). $^1\text{H-NMR}$ measurements confirmed the formation of CIS and TRANS ligands, as they show different shifts for protons on benzene rings, as described in the previous section. Due to symmetry in the TRANS ligands, and both the α -protons in the same chemical environment, they show a single peak.

Since our interest is on the S-type grid complex, we primarily focus here on TRANS type ligand. Based on the specific rotation of the chiral moiety affixed, we denoted the new trans ligands by \mathbf{L}_d and \mathbf{L}_l (Scheme 3.4). The reaction of the newly formed trans ligands (\mathbf{L}_d and \mathbf{L}_l) with equimolar amounts of $\text{Fe}(\text{CF}_3\text{SO}_3)_2$ in acetonitrile yielded two sets of four diastereomeric products \mathbf{P}_d ((all *S*, Λ) and (all *S*, Δ)) and \mathbf{P}_l ((all *R*, Λ) and (all *R*, Δ)) (Figure 3.10). Several strategies, such as using chiral solvents and chiral counter anions (for crystallization), and recrystallization with different solvents, were adopted to produce pure diastereomers. Among these, repeated recrystallization of the reaction products from acetonitrile helped the separation of pure diastereomers. The pure diastereoisomers were analyzed with ion mobility mass spectrometry (IMMS), and the presence of pure diastereomers was confirmed. Further, the isomeric purity of the complexes was also unambiguously elucidated by performing XRD and CD spectroscopic studies.

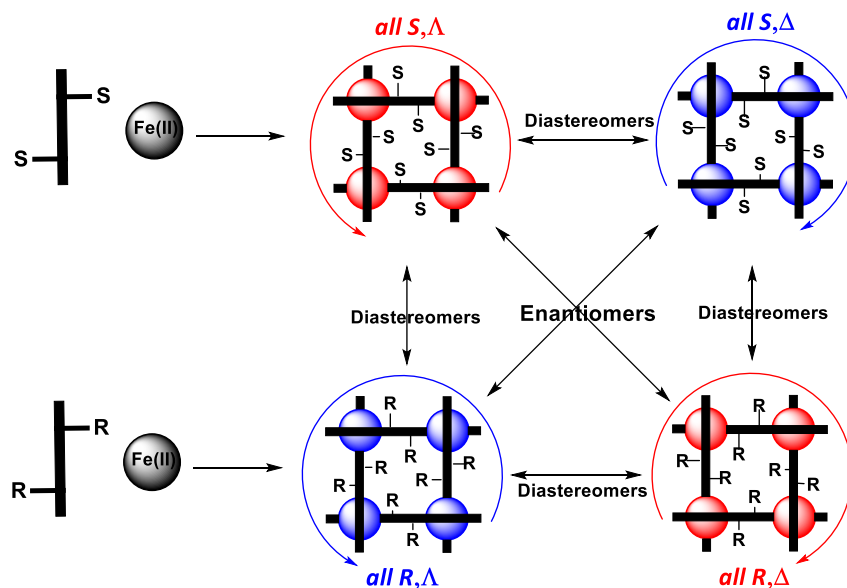


Figure 3.10: Scheme for the synthesis of enantiomeric grid complexes representing the pairs of diastereomers and enantiomers.

Electrospray ionization (ESI) and Ion mobility mass spectrometric (IMMS) studies

Electrospray ionization-mass spectrometry (ESI-MS) was employed for the identification of the complex. Briefly, about 10 $\mu\text{g/mL}$ concentrated solution of each sample in acetonitrile was electro-sprayed. The doubly charged ion peak was found in positive ion mode at m/z 1728 with other fragments (Figure 3.11).

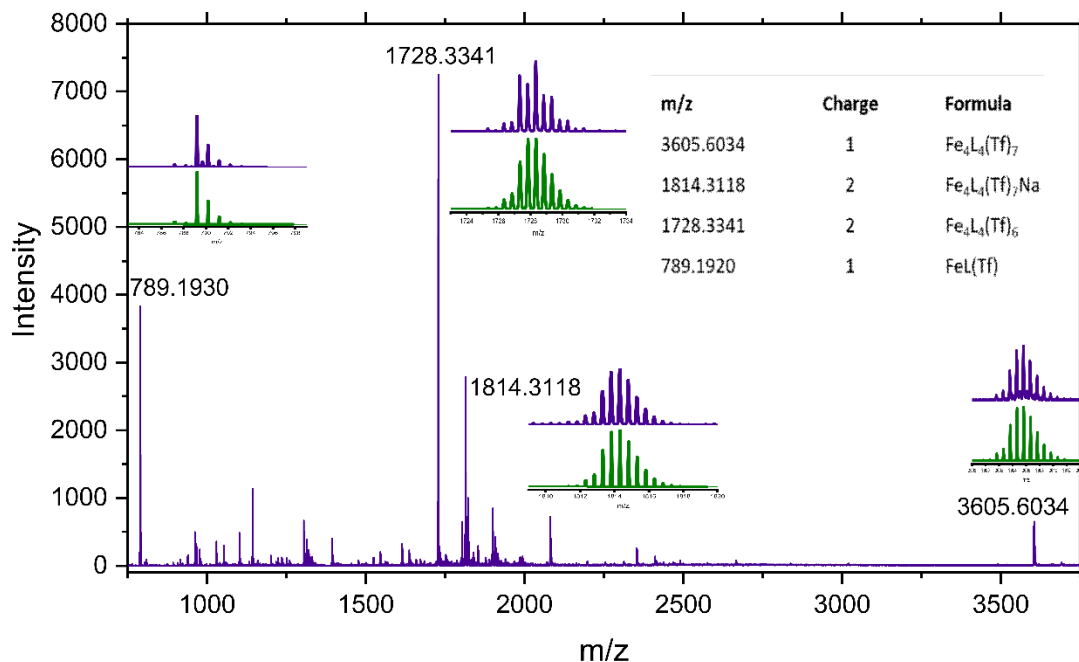


Figure 3.11: ESI spectra showing the formation of grid complex (inset: experimental in blue and simulated spectra in green and table showing the assignment of the peaks). Here Tf stands for triflate anion (CF_3SO_3).

To understand the structural details and to find the presence of diastereomers in the samples, ion mobility spectrometry (IMMS) experiments were performed. Extracted ion mobilogram for the peak m/z 1728 from \mathbf{P}_d and \mathbf{P}_l are shown in Figure 3.12 A and Figure 3.12 B, respectively. The obtained ion mobilogram of each \mathbf{P}_d and \mathbf{P}_l for the peak at 1728 m/z showed two peaks, suggesting the presence of two diastereomers. The intense peak for \mathbf{P}_d appeared at 4.86 ms, while the next peak was found at 5.26 ms. From the area under the peaks, the abundance of the \mathbf{P}_d and \mathbf{P}_l isomers was calculated as 73% and 27%, respectively (Table 3.1). Collision cross-section (CCS) of the ions was calculated using polyalanine dication as a calibrant. The CCS of \mathbf{P}_d1 and \mathbf{P}_d2 were 551 \AA^2 and 583 \AA^2 , respectively. The respective mass spectrum extracted from each of the peaks is shown in inset C. While the arrival time difference between the two diastereomers was 0.4 ms for \mathbf{P}_d , it was 0.34 ms for \mathbf{P}_l (Figure 3.12). The experimental CCS areas for diastereomers from the other crude product \mathbf{P}_l1 and \mathbf{P}_l2 were 559 \AA^2 (drift time (dt): 4.92 ms) and 583 \AA^2 (dt: 5.26 ms), respectively.

The major products of both crude samples show approximately the same CSS values, which is expected for enantiomers.

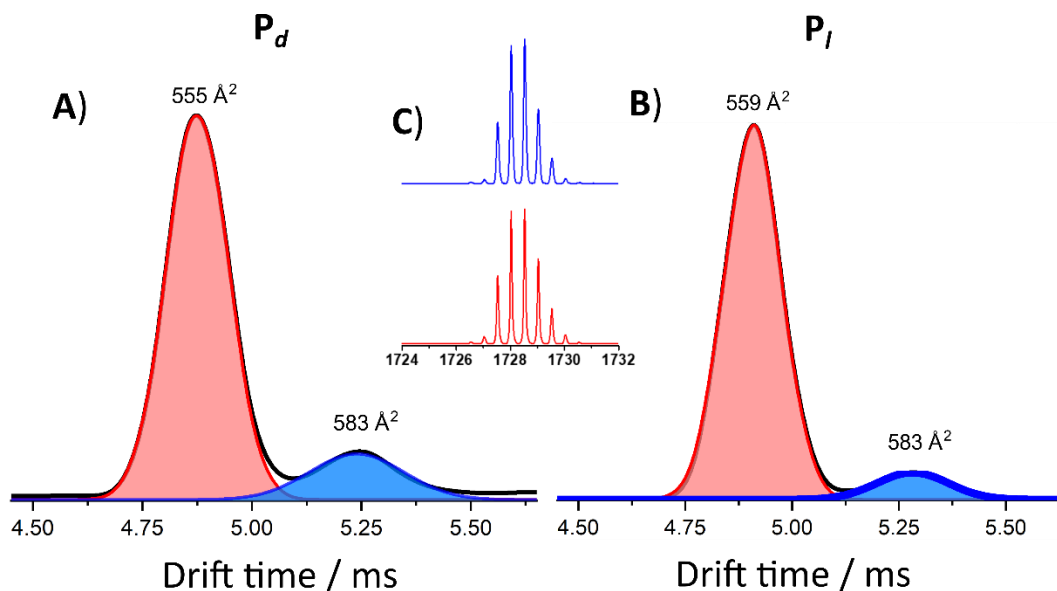


Figure 3.12: IMS data of crude samples A) P_d and B) P_i showing two diastereomers in both the samples. The mass spectrum extracted from the two peaks of P_d is shown in inset C.

Peak	Arrival time (ms)	CCS (\AA^2)	Area (%)
P_d1	4.86	555	73
P_d2	5.26	583	27
P_i1	4.92	559	81
P_i2	5.26	583	19

Table 3.1: CCS and Arrival times of different isomers formed were extracted from the above Figure 3.12.

Single Crystal X-Ray Diffraction studies

It is essential to elucidate the crystal structure of the above-synthesized complexes, to study their stereochemistry in detail. The crystalline forms of grids P_i and P_d were obtained by slow vapor diffusion of THF into the solutions of the complexes in acetonitrile. The single-crystal X-ray investigations of the crystals carried out at 150 K revealed the expected [2x2] grid type molecular structures. Both isomers were crystallized in a non-centrosymmetric $I4$ space group, and they are isostructural and isomorphous to each other. Depending on the orientation of ligands around the Fe(II) centers, the configuration of

crystals from the P_1 complex is (all S, Λ) and similarly (all R, Δ) from the P_d complex, and they were enantiomers to each other (Figure 3.13). All the ligands and metal centers in the structure are crystallographically equivalent with fourfold symmetry. Each unit cell has one grid complex, with the asymmetric unit consists of the $\text{FeL}_d/\text{FeL}_l$ moiety and one triflate anion. Due to the weak diffraction of the crystals and the poor quality of the data, other anions could not be located. However, the confirmation of eight triflates in the structure was confirmed by elemental analysis (see Experimental Section). The four Fe(II) ions are located at the corners of the square with an adjacent Fe-Fe distance of 8.978(5) Å, whereas diagonal Fe ions are separated by 12.696(4) Å. Each Fe(II) ion was coordinated by six nitrogen atoms from nearly perpendicularly oriented ligands with a dihedral angle of 87.86°. At 180 K, the average Fe-N bond lengths of the (all S, Λ) and (all R, Δ) complexes are 1.941(16) Å and 1.955(16) Å, respectively, which corresponds to the LS state.¹²³ The spin state of Fe(II)-bis(pyrazol-1-yl)pyridine complexes can be confirmed from angular components—for example, the $\text{N}_{\text{pyrazole}}\text{-Fe-N}_{\text{pyrazole}}$ angles (ϕ), which is about 160° for LS and 145° for HS—and the distortion indices Σ ($\Sigma = \sum_{i=1}^{12} |90 - \alpha_i|$, $\alpha = 12$ cis N-Fe-N angles, which is ca. 90° for LS and 160° for HS).^{60,124,125} From the crystal structures, the calculated average values of $\text{N}_{\text{pyrazole}}\text{-Fe-N}_{\text{imidazole}}$ angles (ϕ) are 159.4(4)° and 160.7(6)° for (all S, Λ) and (all R, Δ), respectively, confirming the LS for both structures. The bond lengths and the angular parameters are collected in Table 3.2.

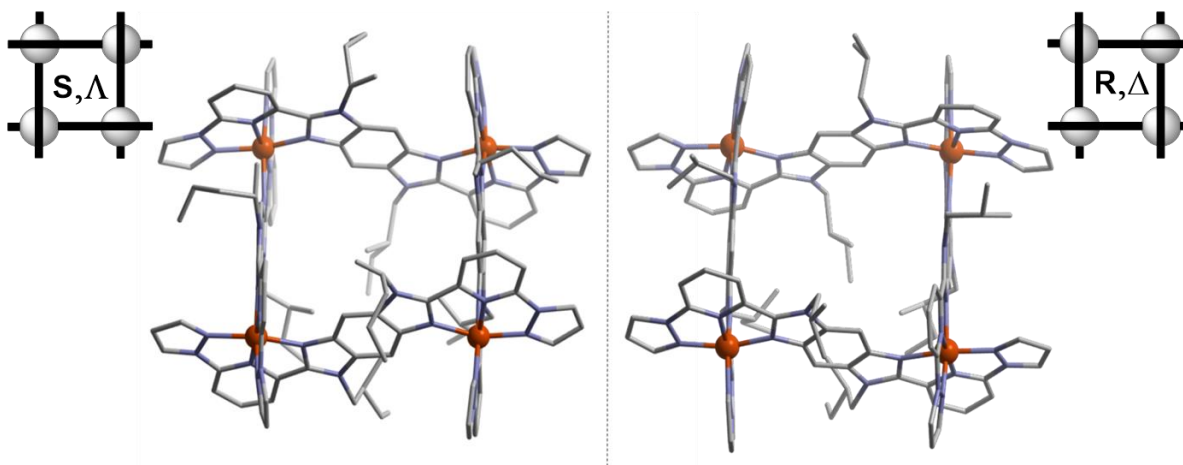


Figure 3.13: Crystal structures of (all S, Λ) and (all R, Δ)– enantiomeric Fe(II) grid complexes at 180 K (H atoms, counter anions, and solvent molecules were omitted for clarity).

Parameters	all <i>S</i> , Λ - isomer	all <i>R</i> , Δ - isomer
Temperature/ K	180	180
Avg. Fe-N bond length/ Å	1.941(5)	1.951(5)
N_{py} -Fe- N_{py} (Φ)/ °	175.25(3)	175.14(7)
Σ / °	91.67(9)	89.55(5)
θ / °	98.46(8)	98.13(9)
$a=b$ / Å	20.0596(6)	20.0874(7)
c / Å	24.4391(9)	24.6612(6)
Flack Parameter	0.056	0.12

Table 3.2: Bond lengths and angular parameters of the enantiomeric grid complexes.

UV-Vis and Circular Dichroism studies

Circular dichroism (CD) is a well-established technique for studying chiral molecules. Thus, to further analyze the stereochemistry of the complexes, the CD spectra of the complexes were studied in the solution-state.^{126,127} The crude sample from each reaction used for IMMS was dissolved in acetonitrile and subjected to CD measurements. The experiments showed weak signals, confirming a small diastereomeric excess in the crude samples (Figure 3.15), which is in agreement with the IMMS studies. However, this is in contrast to the XRD measurements, where the prepared samples were enantiopure.

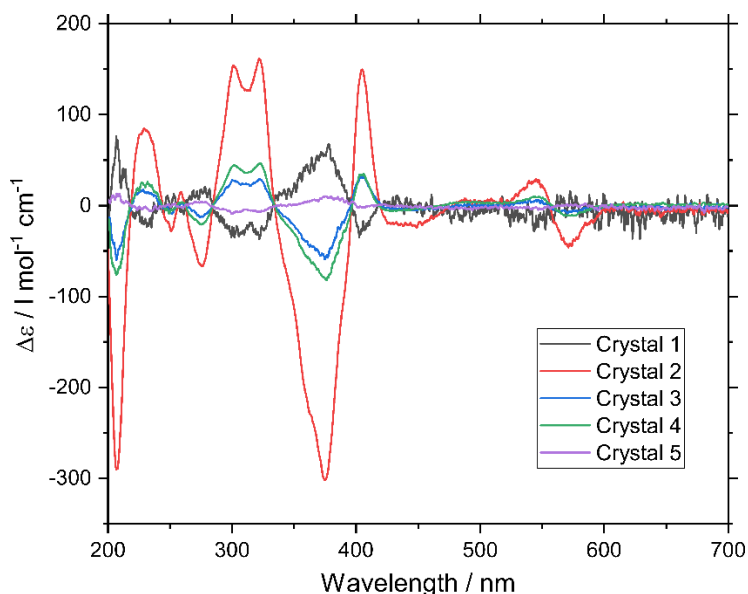


Figure 3.14: CD spectra of single crystals grown in a crystallization vial by vapor diffusion of THF into complex in acetonitrile.

To understand this problem, CD measurements were performed for several single crystals selected manually out of the crystal mixture by dissolving them in acetonitrile. Some of the crystals showed pronounced peaks with $\Delta\epsilon$ values of about $\pm 300 \text{ l mol}^{-1} \text{ cm}^{-1}$ at 383 nm, whereas some other crystals showed a major difference in terms of $\Delta\epsilon$ signal, which is smaller than $300 \text{ l mol}^{-1} \text{ cm}^{-1}$ (Figure 3.14). From this observation, it was clear that, on crystallization, only a few crystals formed were pure diastereomers, whereas the majority were not. Therefore, to achieve pure diastereomers in each case, several recrystallizations were performed, and over every recrystallization cycle, an improvement of signals for the bulk sample was found (Figure 3.14). After four recrystallizations, $\Delta\epsilon$ intensities of the complexes, which were the same as that of the corresponding single crystal was achieved, and this remained the same even on further recrystallizations. Thus, several steps of recrystallizations have provided a new strategy to produce pure diastereomers in each case.

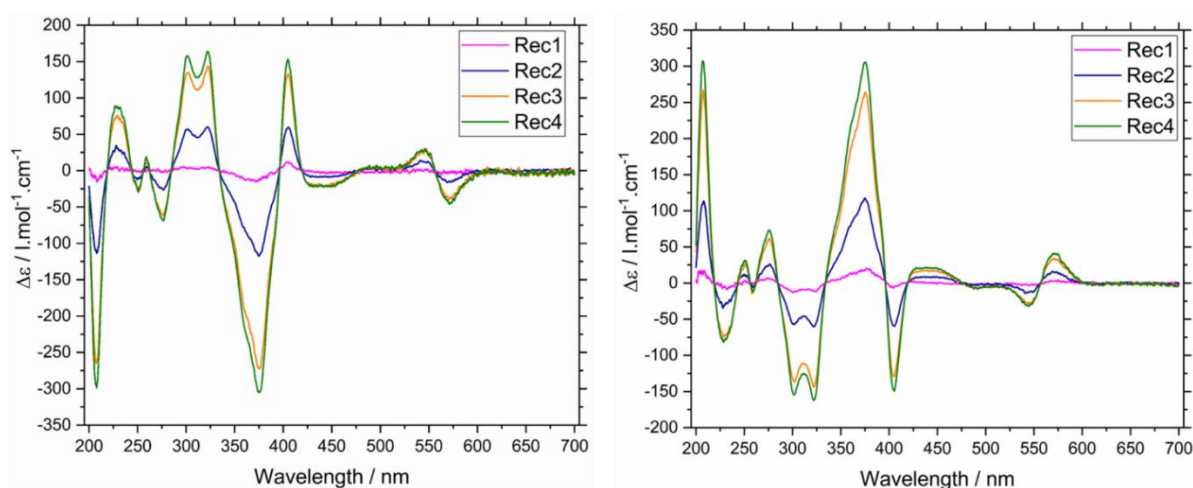


Figure 3.15: CD spectra over 4 recrystallization steps, each recrystallization step by vapour diffusion of THF into complex dissolved in acetonitrile.

Figure 3.16 shows the CD and UV-Vis spectra of the fully resolved enantiomers recorded in acetonitrile solution at 25°C. The two intense bands at 270 nm and 370 nm are due to ligand-centered (LC) $\pi \rightarrow \pi^*$ transitions.¹²⁸ The band at 550 nm corresponds to the metal to ligand charge transfer (MLCT) transition, which is observed in LS complexes.¹²⁸ All these bands showed strong CD activities for the pure (all *S*, Λ) and (all *R*, Δ)-enantiomers. Moreover, the CD signals were found to be exact mirror images with opposite sign of the bands. The most prominent feature in the spectra is the bisignate Cotton effect due to exciton coupling around 370 nm, which has a negative band for the (all *S*, Λ)-complex and a positive band for the (all *R*, Δ)-complex.

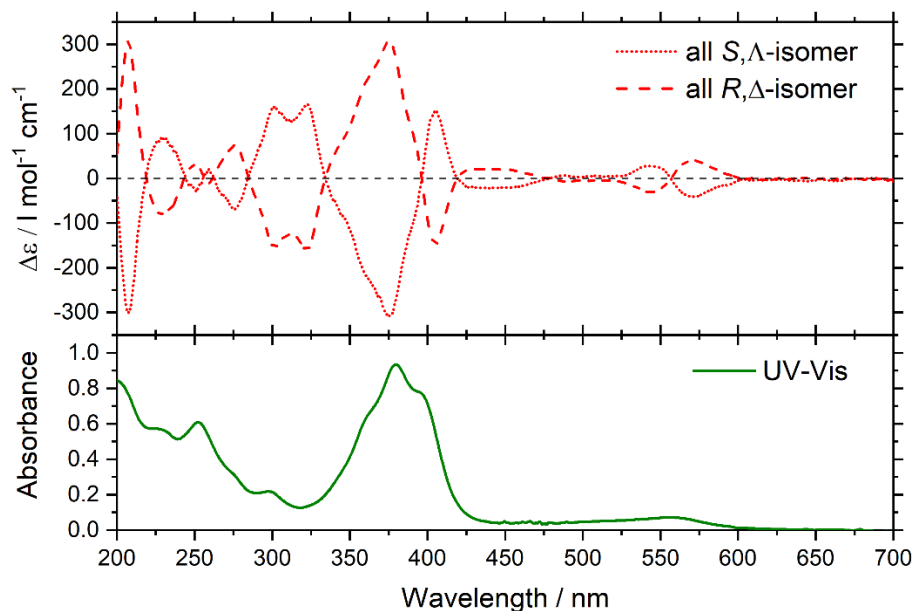


Figure 3.16: UV-Vis and CD of (all *S*, Λ) and (all *R*, Δ) - Fe(II) grid complexes measured in acetonitrile as solvent.

Time-dependent density functional theory (TDDFT) calculations on (all *S*, Λ) - Fe(II) grid complex and its comparison

Since its formal introduction in 1984 by Runge and Gross,¹²⁹ time-dependent density functional theory (TDDFT) has become a standard tool in the evaluation of excited-state properties.^{130–132} For the simulation of CD spectra, in particular, TDDFT has been proven to be an accurate and reliable method capable of handling molecules with up to hundreds of atoms.^{133–137} Calculations were performed on the low-spin and high-spin complexes. Before calculating their respective TDDFT spectra, the geometries of the complexes were optimized using TURBOMOLE.^{138,139,140} The different spectra are shown in Figure 3.17.

From the magnetic measurements, it was inferred that around 25% and 75% of the molecules are in the HS and LS states, respectively, at RT (*vide infra*). To mimic the RT situation in the calculations, a weighted average of the LS and HS spectra, which was compared to the experimental one was included. Overall, the calculated and the experimental spectra showed good agreement both qualitatively and quantitatively. The MLCT bands at around 550 nm, however, are significantly smaller in the calculated spectrum. This could be explained by the fact that hybrid functionals are known to underestimate charge-transfer (CT) excitations. We additionally performed calculations using the CAM-B3LYP functional,¹⁴¹ which was designed to capture the effects of CT excitations better. The results of the CAM-B3LYP calculations did not systematically improve upon the PBE0 calculations: the intensity of the MLCT bands was even smaller than the intensities obtained from the PBE0 functional.

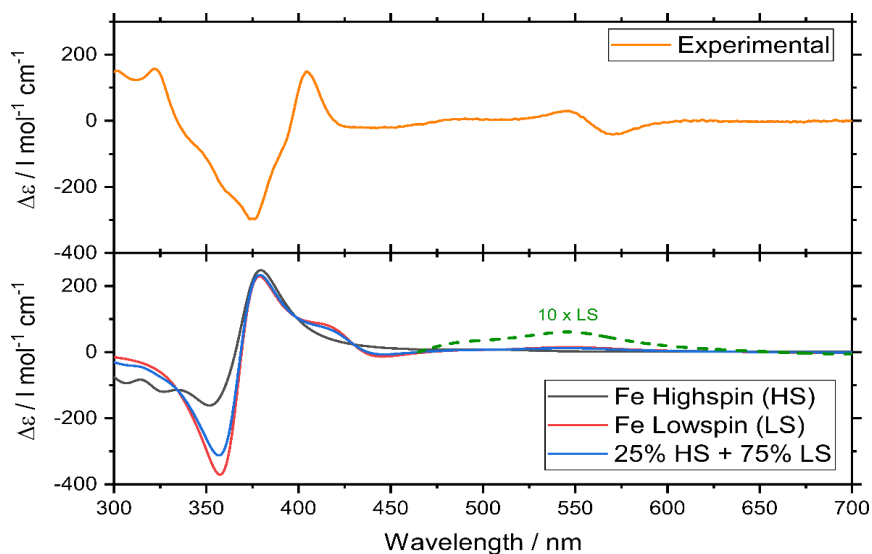


Figure 3.17: Comparison of experimental CD (top) and simulated CD spectra (bottom) of (all *S*, Λ) - Fe(II) grid complex.

One feature which is visible in the simulated spectra is the presence of the MLCT bands in the spectrum of the LS complex, whereas they are absent in the spectrum of the HS complex, as shown in Figure 3.18.

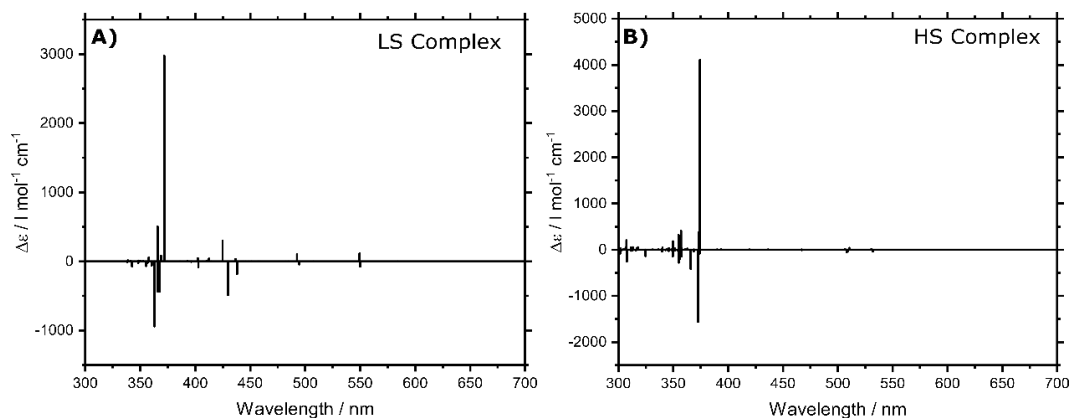


Figure 3.18: Simulated line spectra of A) Low-spin and B) High-spin (all *S*, Λ) - Fe(II) grid complexes.

This is in full agreement with the experimental results and also with the magnetic measurements. The presence of the MLCT bands, therefore, indicates the presence of the LS iron(ii) centers associated with the complex. The comparable nature of the computed CD spectra obtained from TDDFT calculations has validated the enantiomeric purity of the obtained complex.

Temperature and light-induced spin-state switching characteristics of the grid complexes

The detection of thermal and photo-induced SCO was carried out by variable temperature magnetic investigation in the thermal range 5–385 K. The χT vs. T dependencies indicate the presence of gradual and high-temperature SCO behavior in both heating and cooling modes (Figure 3.19). At room temperature (≈ 300 K), the χT value is close to ca. 2.84 ((all S , Λ)-isomer) and 2.92 ((all R , Δ)-isomer) $\text{cm}^3 \text{K mol}^{-1}$, which corresponds to ca. 25% of the complexes is in the HS state. The values of χT product at the maximal temperature of measurement are ca. 5.88 ((all S , Λ), at 385 K) and 6.14 ((all R , Δ), at 385 K) $\text{cm}^3 \text{K mol}^{-1}$ and suggest approximately 50% of Fe(II) metal centers in HS state. Below 180 K, χT value is close to 1.00 $\text{cm}^3 \text{K mol}^{-1}$, which shows most of the metal centers are in diamagnetic LS state, corroborating well with the spin-state information obtained from the crystallographic studies. The measurements for both complexes were performed in several heating and cooling modes. The tiny differences between the curves in corresponding measurement cycles can be tentatively attributed to the partial loss of lattice solvents or adsorbed moisture.

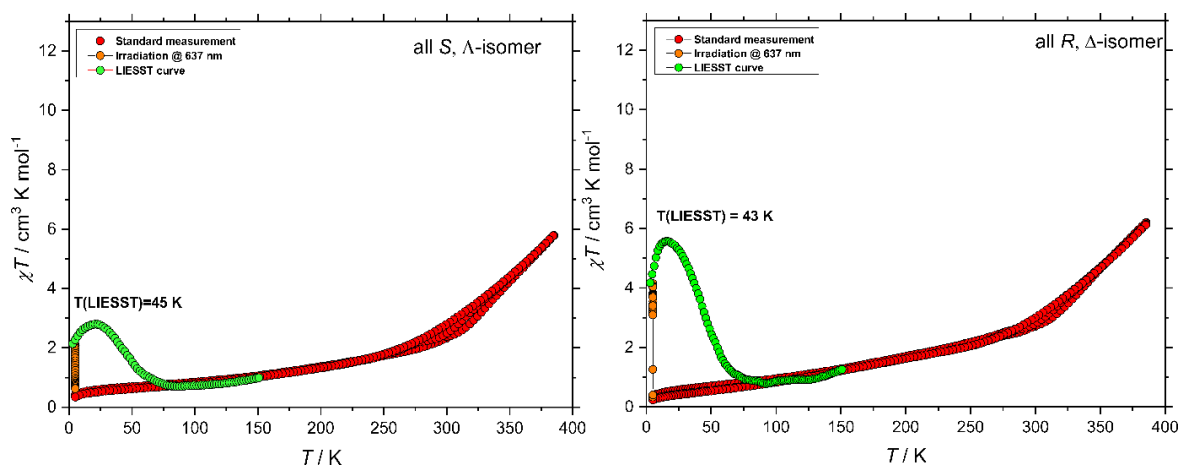


Figure 3.19: χT vs. T plots and photo-magnetic characteristics of (all S , Λ)- and (all R , Δ)-complexes.

For light-induced excited spin-state trapping (LIESST) measurements, both LS samples were irradiated with red light ($\lambda = 637$ nm, power = 10 mW/cm^2) in the dark for ca. 2 h at 5 K. A significant increase of magnetization was observed under the irradiation, which is an indisputable proof for the formation of photo-excited metastable HS state. The progress of the magnetization was followed with time, and when saturation was reached, the light was switched off, and temperature-dependent magnetization was recorded in the dark. Both isomers exhibit similar photo-magnetic properties with partial LS \rightarrow HS photo-conversion ($\approx 23\%$ for (all S , Λ) and $\approx 46\%$ for (all R , Δ)) and gradual thermal relaxation upon the slow

heating. The various amounts of the photo-excited metastable HS state for (all *S*, Λ) and (all *R*, Δ) might be attributed to the different penetration of light through the prepared samples for the irradiation experiments. On the other hand, T(LIESST) temperatures are very similar to each other and correspond to high $T_{1/2}$ temperature of thermal SCO, which agrees with the “inverse energy gap law,” which states that T(LIESST) is inversely proportional to $T_{1/2}$.^{142,143}

⁵⁷Fe Mössbauer spectroscopy is a valuable tool for accessing the spin and charge state of the Fe atoms. To study the spin states at various temperatures, Mössbauer spectra were measured for the ⁵⁷Fe enriched Λ and Δ enantiomeric complexes at 77 K and 300 K temperature. The parameters obtained were compiled in the table below.

<i>T</i> / K	Complex	δ (mm/s)	ΔE_Q (mm/s)	Area (%)
77	(all <i>S</i> , Λ)–isomer (LS)	0.38	0.49	91
	(all <i>S</i> , Λ)–isomer (HS)	1.10	2.54	9
77	(all <i>R</i> , Δ)–isomer (LS)	0.38	0.49	93
	(all <i>R</i> , Δ)–isomer(HS)	1.10	2.54	7
300	(all <i>S</i> , Λ)–isomer (LS)	0.32	0.47	78
	(all <i>S</i> , Λ)–isomer (HS)	0.78	1.80	22
300	(all <i>R</i> , Δ)–isomer (LS)	0.30	0.48	83
	(all <i>R</i> , Δ)–isomer(HS)	0.78	1.82	17

The spectra (Figure 3.20) feature two quadrupole doublets at 77 K for both the isomers (for (all *S*, Λ) and (all *R*, Δ)) with isomer shift (δ) of 0.38 and 1.10 mm/s. The quadrupole splitting parameter obtained was $\Delta E_Q=0.49$ mm/s corresponds to LS-Fe(II) ions and $\Delta E_Q=2.54$ corresponding to HS. The area under the peaks confirms around *ca.* 8% HS content at 77 K and agrees with the SQUID measurements, which showed non-zero χT values. On the other hand, the spectra obtained at RT also features well-separated quadrupole doublets in both the isomers, confirming two types of iron atoms. The figure shows the green doublet at $\delta = 0.32$ mm/s, (with $\Delta E_Q= 0.47$ mm/s for (all *S*, Λ)) and $\delta = 0.30$ mm/s ($\Delta E_Q= 0.48$ mm/s for (all *R*, Δ)) corresponding to LS content in the samples. Whereas, the brown doublet at $\delta = 0.78$ mm/s, (with $\Delta E_Q= 1.80$ mm/s for (all *S*, Λ)) and $\delta = 0.78$ mm/s ($\Delta E_Q= 1.82$ mm/s for (all *R*, Δ)) corresponding to HS (Figure 3.20). The area under the peaks confirms around *ca.* 20% HS content at RT and agrees with the magnetic measurements.

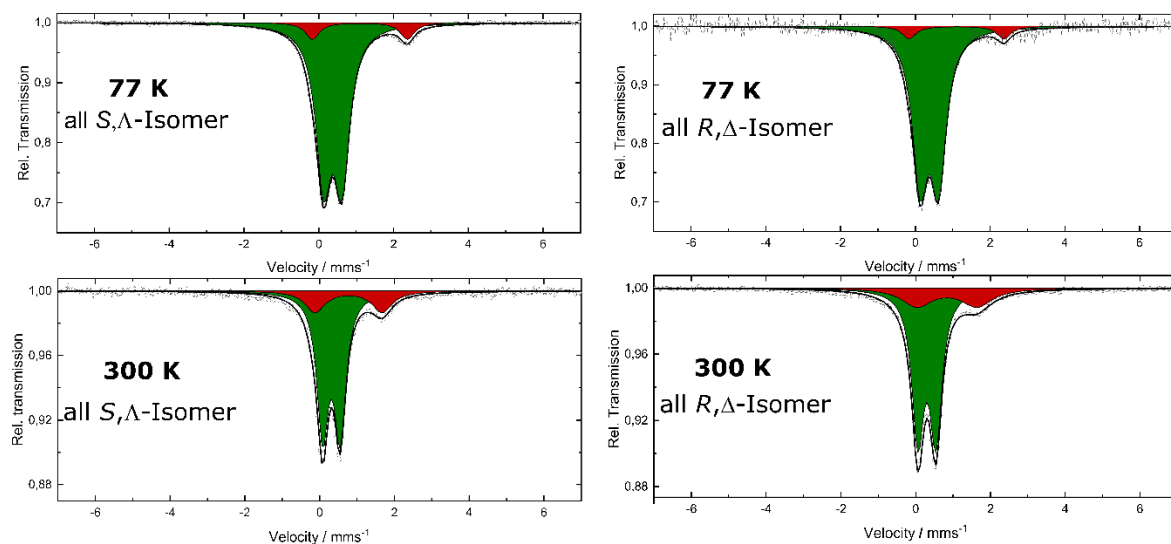


Figure 3.20: Mössbauer spectra for ^{57}Fe enriched (all S, Λ) and (all R, Δ) complexes at 77 K and 300 K, green represents LS, and red represents HS states.

Despite the numerous applications of chiral SCO complexes in optoelectronic devices and magneto-optical memory devices, reported examples of chiral SCO complexes are quite rare. The majority of the chiral SCO complexes in the literature were obtained via spontaneous resolution. While some others are obtained due to just the presence of a chiral solvent or a counter anion,¹⁴⁴ i.e., chirality is absent in the intrinsic coordination environment. In this regard, our complexes resolved and discussed in this chapter stand out as a new example for chiral SCO complexes where chirality is intrinsic in the coordination environment. Previously, Bark and coworkers reported on successful chiral resolution of Fe(II) grid complexes using a chiralized version of the ligand, where the chiral moiety blocks the formation of the other diastereomers with steric hindrance.^{122,145} However, in the present case, the resolution was not achieved in a single step, which could be due to the weak interaction of the chiral unit with the neighboring ligands, resulting in the formation of a product with small diastereomeric excess.

Later, the crucial and surprising step that helped us in the purification of diastereomers was the crystallization steps. Chiral self-sorting effects could have possibly helped during the self-assembly process. Chiral self-sorting is a phenomenon where racemic components are spontaneously sorted into homo- or hetero-chiral molecular assemblies through chiral discrimination between the components.^{146,147,148} The presence of some pure diastereomeric crystals from the first crystallization step could have helped by taking on the role of the seed crystal and undergo preferential crystallization.¹⁴⁹ This helped to improve the diastereoselectivity, as this can be evidenced by CD measurements. In general, preferential crystallization requires the addition of an external seed crystal. However, in the

present case, the in-situ generated crystal has helped as a seed crystal for successive stages of crystallization to produce a pure diastereomeric product.

Till now, several SCO grid complexes were reported, but to the best of our knowledge, this is the first set of chiral SCO grid complexes. Even though the resolved complexes do not show great SCO properties compared to other previously reported grid complexes,^{118,119,150,151} the present strategy of resolution can be applied, and ligands tuning could achieve in better SCO properties.

3.4 Conclusions

In conclusion, by performing the substitution on the ligand backbone, we synthesized a new set of ligands— CIS- and TRANS-type—that cannot be tautomerized, unlike the parent ligand. Moreover, two different conformers (C and S) were synthesized from CIS and TRANS ligand. Thus the difficulty of separation has been avoided, and moreover, the stability of these complexes has increased. Therefore, individual studies can be performed on the complexes without any difficulties. The obtained complexes of C-conformer and S-conformer showed different magnetic properties – S-conformer showed gradual SCO behaviour, whereas the C-form showed complete HS nature. Moreover, the stability of the S-conformer in the solution state was increased, and thus further studies could be performed without any further problem

In addition, we were able to programme the synthesis of the first set of enantiomers of SCO S-grid complexes by tailoring the parent ligand system with chiral centers. Appending the chiral center has resulted in blocking the tautomerism in the ligand, and more importantly, an additional chiral center has been inserted, which should help in formation of diastereomers. As expected, a set of diastereomers were formed during the complexation reaction, for which IMMS experiments were used to confirm the diastereomers. The diastereomers in each case were separated by fractional crystallization to achieve a pair of enantiomers by using the concept of chiral self-sorting and preferential crystallization. The stereochemistry of the complexes was confirmed by XRD and CD measurements. Magnetic measurements have shown the same gradual temperature-induced SCO behavior in both the enantiomeric complexes. Mössbauer measurements at various temperatures have helped to confirm the spin state of the complexes obtained. The complexes were found to be LIESST active at low temperatures. Moreover, TDDFT calculations provided additional evidence not only for chirality but also for magnetic studies. Such multifunctional architectures, possessing chirality and SCO behavior, are of interest for future applications since they can offer magneto-chiral effects.

Chapter 4

Terbium(III) Single-molecule magnets based on tetra-pyrrole ligands

4.1 Introduction

4.1.1 Lanthanide Chemistry

Lanthanides consist of 15 elements with atomic numbers (Z) ranging from 57 to 71 (La – Lu). These 4f elements have numerous applications in various fields because of their catalytic, electronic, optical, and magnetic properties. For example, the optical properties of lanthanide compounds are known to be useful in biomedical fields¹⁵² and non-linear optics.^{153,154} Lanthanides are also used as magnets and are potential candidates for high-density information storage devices¹⁵⁵ and quantum devices.^{156,157}

Lanthanides are also called rare earth elements, with the inclusion of Scandium ($Z=21$) and Yttrium ($Z=39$). Lanthanides have an electronic configuration of $[\text{Xe}] 4f^n 5d^0 6s^2$ and $[\text{Xe}] 4f^{(n-1)} 5d^1 6s^2$ with 4f orbitals shielded by 5s and 5p. Due to this configuration, they exhibit a stable +3 oxidation state, where the electrons are removed from 5d and 6s orbitals. In 4f elements from left to right, the size of the atom reduces with an increase in atomic number, which is called lanthanide contraction. This is due to the poor shielding effect of 4f orbitals.

4.1.2 Magnetism in lanthanides

Lanthanides show a wide range of coordination (≥ 6) and geometries. In lanthanides, the 4f orbitals are well shielded by filled 5s and 5p orbitals. This results in weak-splitting due to the crystal field, which is different from transition elements. Instead, the spin-orbit coupling becomes important for a better description of the electronic structure of lanthanide ions (Figure 4.1). This interaction between S and L is also called as Russel-Saunders coupling, and this results in a multiplet denoted by $^{2S+1}L_J$ ($|L-S| \leq J \leq |L+S|$). Here the total momentum J is derived from the sum of the total orbital momentum $L=\sum_i l_i$ and the total spin momentum $S=\sum_i s_i$ based on the vector model and $L = 0, 1, 2, 3, \dots$ is labeled as S, P, D, F... etc. The lowest-lying J multiplet is called the ground state multiplet. For electronic shells less than half-filled, J takes the values of $L-S$ as the ground state, whereas for more than half-filled, the ground state will have the value of $L+S$.

Since this chapter deals with Tb^{3+} ions, we will consider this as an example to find the ground state. Tb^{3+} ($4f^8$) has 6 unpaired electrons. Thus it gives a total spin quantum number of $S=3$ and a total orbital quantum number of $L=3$. Since Tb^{3+} ion has more than a half-filled f -shell, J takes the value of $L+S = 3+3 = 6$. Therefore, the ground state term is given by 7F_6 .

Except for Lu^{3+} and La^{3+} , all Ln^{3+} ions contain unpaired electrons and thus are paramagnetic. The magnetic moment of the Ln^{3+} ions is given by the equation below

$$\mu_{\text{eff}} = g_J \cdot \sqrt{J(J+1)} \quad (4.1)$$

And the susceptibility is given by

$$\chi = \frac{N_A \mu_B^2}{3k_B T} \mu_{\text{eff}}^2 = \frac{N_A \mu_B^2}{3k_B} g_J^2 J(J+1) \quad (4.2)$$

where J is the total angular momentum quantum number, N_A is the Avogadro's number, k_B is the Bohr magneton, and g_J is the Landé factor, given by

$$g_J = \frac{S(S+1) - L(L+1) + 3J(J+1)}{2J(J+1)} \quad (4.3)$$

Using equation 1.8 and 1.9, for Tb(III) , with $J = 6$, $S = L = 3$, g_J is $3/2$. Thus χT is $11.82 \text{ cm}^3 \text{ mol}^{-1} \text{ K}$.

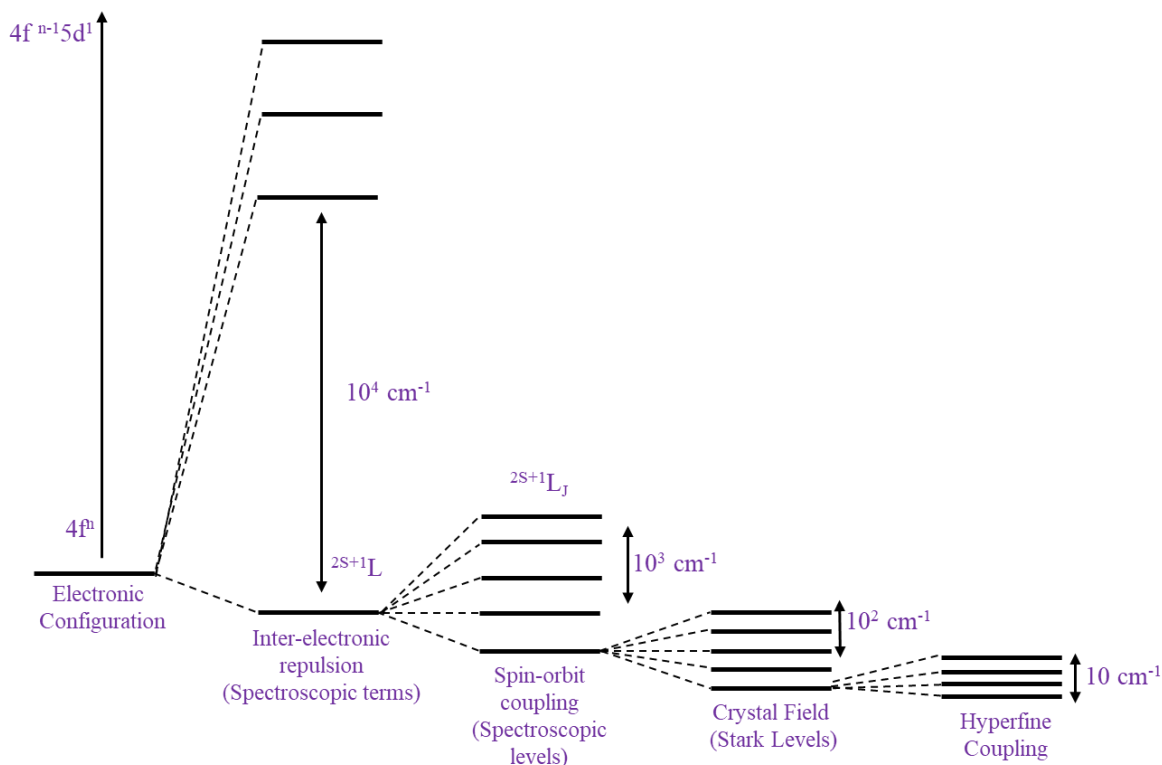


Figure 4.1: Level scheme of the electronic structures of the Ln^{3+} ion obtained after the electronic repulsion, spin-orbit coupling, crystal field splitting, and hyperfine coupling.

4.1.3 Lanthanide based SMMs

As mentioned in the introduction, most of the reported SMMs were based on 3d metal ions, with trails of using large spin ground states (S) and negative ZFS (D). However, later it became apparent that this strategy might not produce the SMM required with high U_{eff} . Also, it became clear that anisotropy plays a key role in preparing a "good" SMM.

In 2003, Ishikawa and coworkers reported the first class of lanthanide-based SMMs with a general formula of $[\text{LnPc}_2]^-$ with a double-decker structure.¹⁵⁸ Among them, $\text{Ln}=\text{Tb}$, i.e., $[\text{TbPc}_2][\text{TBA}]$ showed a high effective barrier of $U_{\text{eff}} = 230 \text{ cm}^{-1}$ (331 K), which is a lot higher than that of Mn_{12} SMM. This high energy barrier arises from single-ion anisotropy due to large unquenched orbital moments and strong spin-orbit coupling. Since then, lots of interest has been put on lanthanide-based SMMs and thus stimulated the design of several classes of Ln SMMs that include lanthanide polyoxometalates (LnPOM),¹⁵⁹ lanthanide β -diketones,¹⁶⁰⁻¹⁶² organometallic double- and triple-decker complexes.^{163,164}

In contrast to transition metal ions, the prominent features in lanthanide ions for designing the SMMs is the anisotropy caused by strong spin-orbit coupling. Even though the crystal field is quite small compared to RS coupling, it plays a vital role in obtaining better SMMs. Thus to obtain SMMs with large magnetic anisotropy, the ligand field must be designed accordingly.¹⁶⁵ For a well-performing SMM, the two main requisites are - (i) a doubly degenerate ground state with high $\pm M_J$. This ensures the high magnetic moment is maintained at low temperatures whereas double degeneracy ensures the bistable magnetic properties, and (ii) the second requirement is a large separation between the bistable ground state and the first excited state. This separation defines the energy required for the spin to relax.

The single-ion anisotropy is mainly derived from the internal nature of lanthanide ions, and the crystal field is an additional perturbation to the spin-orbit coupled state. The charge distribution of free lanthanide ions of lowest J states, which are based on the quadrupole moment of the f-electron charge cloud, helps in quantifying the anisotropy of the lanthanide ions. They are classified into three shapes – spherical (for Gd(III)), equatorially expanded or oblate (Ce(III), Pr(III), Nd(III), Tb(III), Dy(III), and Ho(III)), and axially elongated or prolate (Pm(III), Sm(III), Er(III), Tm(III), and Yb(III)) (Figure 4.2). The isotropic nature of Gd(III) ions partially excludes them for SMM purposes. On the other hand, to maximize the anisotropy, a highly axial ligand field is required for oblate ions, whereas for prolate ions, equatorial ligands fields are favored. This model helps to approach in designing of SMM molecules of f-elements.

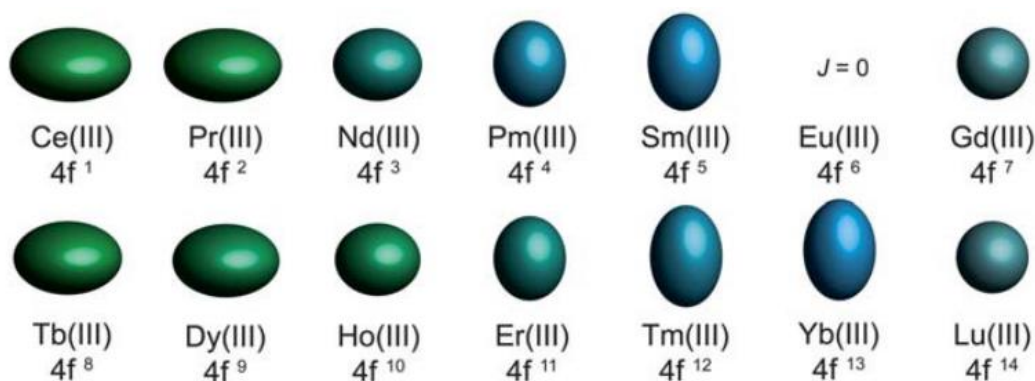


Figure 4.2: Quadrupole approximations of the 4f-shell electron distribution for the Ln(III) ions. (Reproduced from Ref. 165)

4.1.4 Phthalocyanine-type ligands and [LnPc₂] structure

Phthalocyanines (Pc) are one of the most common and important tetrapyrrole derivatives that form complexes with a wide range of metal ions varying from transition metals to lanthanide ions. Pcs form planar molecules with 3d-transition metal ions such as Fe²⁺, Cu²⁺, Ni²⁺, Mn²⁺, whereas it forms sandwich-type complexes with lanthanides. Phthalocyanines form three types of complexes with lanthanides such as lanthanide mono-phthalocyanines, lanthanide bis(phthalocyanines), and di-lanthanide tris(phthalocyanine) complexes. The lanthanide bis(phthalocyanines) are also called double-decker or sandwich complexes with the lanthanide ion in the center. When the two phthalocyanine rings are identical, they are termed as homoleptic, and if they differ, they are called heteroleptic complexes. Similarly, the triple-decker complexes can also be heteroleptic and heteronuclear.

Even though lanthanide phthalocyanine complexes were reported in the 1960s, the SMM studies were first characterized in 2003 by Ishikawa and coworkers.¹⁵⁸ Before that, the same research group has established a new method for the determination of ligand field parameters for a series of lanthanide double deckers¹⁶⁶ and triple deckers¹⁶⁷ by using magnetic susceptibility and ¹H-NMR spectra and thus extracted the ground-state multiplets energy diagram (Figure 4.3).

Figure 4.3 shows that the first excited state is about 440 cm⁻¹ (633 K) above the ground state for Tb³⁺. This high energy of the first excited state helped in the prediction of the SMM behaviour, and as a result, AC magnetic susceptibility was recorded. As expected, the AC magnetic studies showed a maximum at higher temperatures than SMMs reported before. The Mn₁₂ SMM reported in 1993 showed a maximum in out-of-phase susceptibility at 6 K²⁶ (with 100 Hz as oscillating frequency), whereas [TbPc₂][TBA] showed a maximum at 33 K³¹ at the same conditions (Figure 4.4).

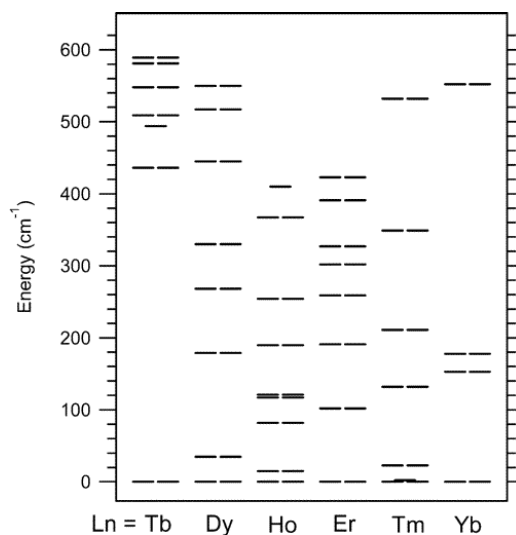


Figure 4.3: Energy diagram for the ground-state multiplets of $[\text{Pc}_2\text{Ln}]^+$ (Ln: Tb, Dy, Ho, Er, Tm, or Yb). (Reproduced from Ref. 166)

In the anionic form of TbPc_2 , the Pc ligands have a formal charge of 2^- with a closed shell π electronic system. This can undergo one- or two-electron oxidation to form neutral or oxidized complexes $[\text{LnPc}_2]^{0/+}$. The removal of the electrons on oxidation can change the coordination environment in the complex and thus tune the SMM properties.¹⁶⁸ Till now, several lanthanide double-decker complexes were reported and studied with changes in the periphery of the Pc ring to form heteroleptic and homoleptic sandwich complexes.

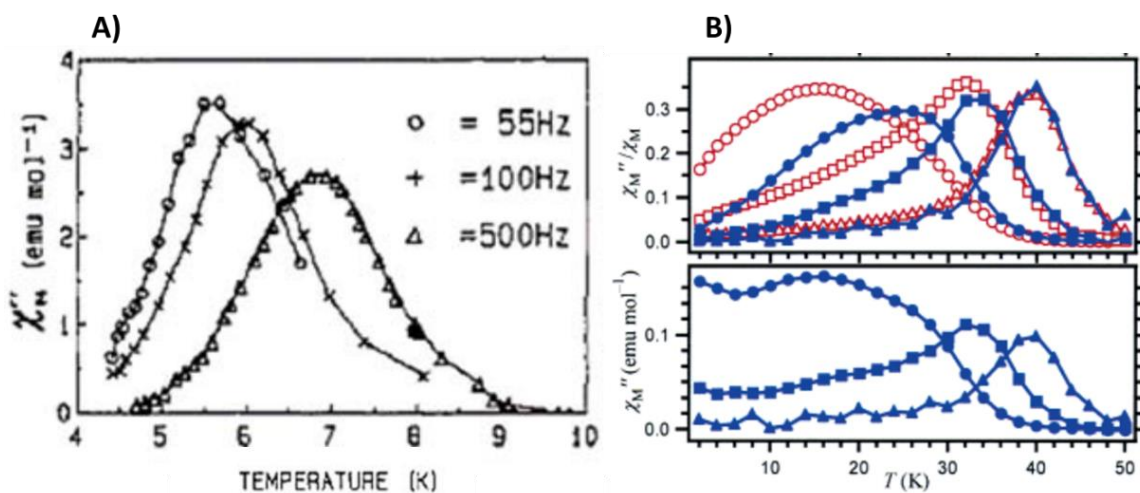


Figure 4.4: AC susceptibility data of A) Mn_{12} complex and B) $[\text{TbPc}_2]^- \text{TBA}^+$. (Reproduced from Ref. 26, 31). Here χ'' represents the out-of-phase magnetic susceptibility.

Porphyrins are macrocyclic compounds constituted by four pyrrole units and are structural analogs to phthalocyanines showing a similar tetra-pyrrolic planar structure. Porphyrins are of wide range with various substituents and are simple to prepare. Compared to phthalocyanines, porphyrins have higher solubility, which could ease the synthesis and increase the yields. The possibility of varying the substituents and high solubility of porphyrins makes them better candidates for preparing SMM double-decker complexes and tuning their magnetic behavior.

Moreover, a lot of interest research has been developed in the field of poly-nuclear Lanthanide based SMMs, since they show suppressed quantum tunneling of magnetization compared with the mononuclear SMMs. So till now, several strategies have been developed in order to couple them – by extending vertically, i.e., by synthesizing triple-decker and quadrupole deckers complexes, or by coupling the mononuclear complexes.^{169,170,171,172} However, to the best of our knowledge, there were no reports in polynuclear complexes of double-decker complexes based on porphyrin and Pc ligands.

4.2 Objectives

Till now, there were many reports on the homoleptic and heteroleptic Tb(III) phthalocyaninato complexes, but complexes using porphyrin were less explored.^{173,174,175} Moreover, by the time we started this work, to the best of our knowledge, there were no reports on SMM properties based on redox behaviour on molecules of mixed porphyrin and phthalocyanine double-deckers complexes.^{176,177} Therefore, the following objectives are pursued in this chapter of this thesis for the exploration of SMM complexes -

Objective 1: To synthesize and perform systematic studies on the heteroleptic Tb(III) porphyrinato phthalocyaninato sandwich complexes by varying the substituents on the porphyrin molecule and oxidation state in order to produce functional magnetic molecules.

Objective 2: To synthesize and study the dimers and trimers of heteroleptic Tb(III) sandwich complexes, where the monomeric double deckers were linked covalently by various linkers.

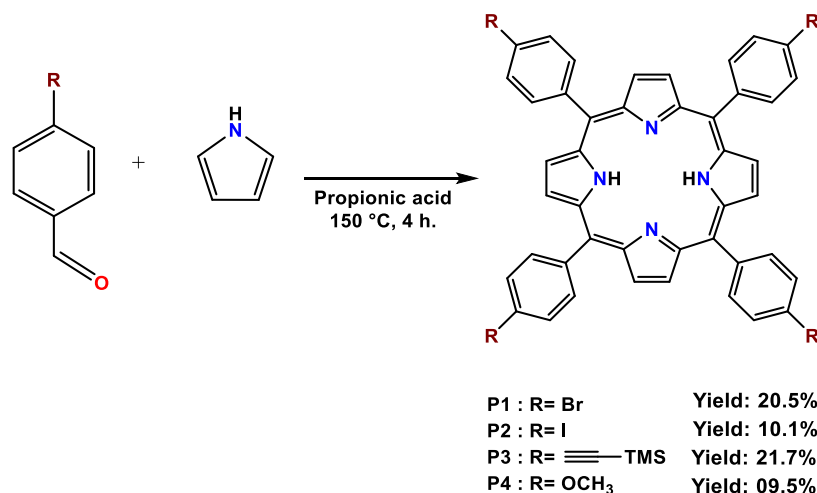
4.2.1 Objective 1: Synthesis and Characterization of Tb (Porphyrinato) (Phthalocyaninato) sandwich complexes

The work presented in this chapter - the synthesis, characterization, and magnetic measurements, were performed at INT, KIT.

Synthesis and characterization of Porphyrins (P1-P4)

Tetraphenylporphyrins are heterocyclic substances formed from pyrrole and benzaldehyde units that resemble naturally occurring porphyrins. These porphyrins are synthesized by using Alder and Longo's method of condensation reaction by treating

equimolar amounts of respective benzaldehydes and pyrrole in refluxing propionic acid.^{178,179} The porphyrins (**P1-P4**) with different substitutions (electron-withdrawing to electron-donating groups) on the periphery were synthesized as depicted in Scheme 4.1. This reaction resulted in purple precipitate with yields of 10-20%. The ¹H-NMR of the obtained porphyrins were accord with those previously reported. The signal for NH protons are characteristic for porphyrins, and they resonate in the shielded region around $\delta = -2.5$ ppm. The upfield shift is due to magnetic anisotropy arising from the ring current in the porphyrin system.



Scheme 4.1: Synthesis of porphyrins **P1-P4** (TMS stands for trimethylsilyl).

The absorption spectra of the porphyrins **P1-P4** measured in CHCl₃ show typical Soret bands centered at 400 - 450 nm and the four Q bands at 500 - 650 nm, which is in agreement with the literature (Figure 4.5).^{178,180} The molecular structures were further confirmed by ESI-MS and ¹³C-NMR spectroscopy.

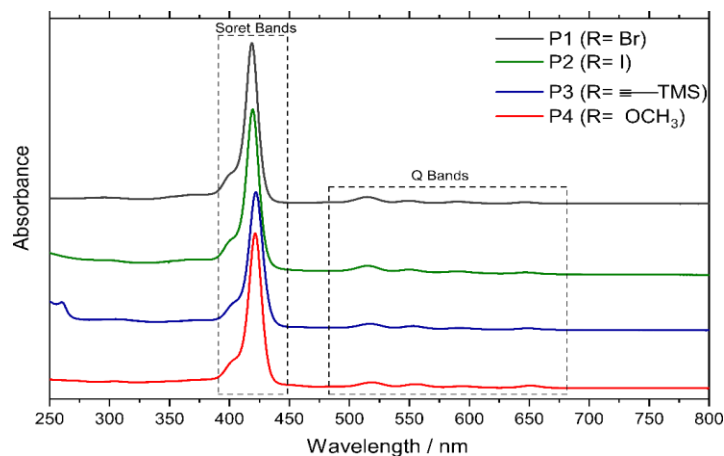
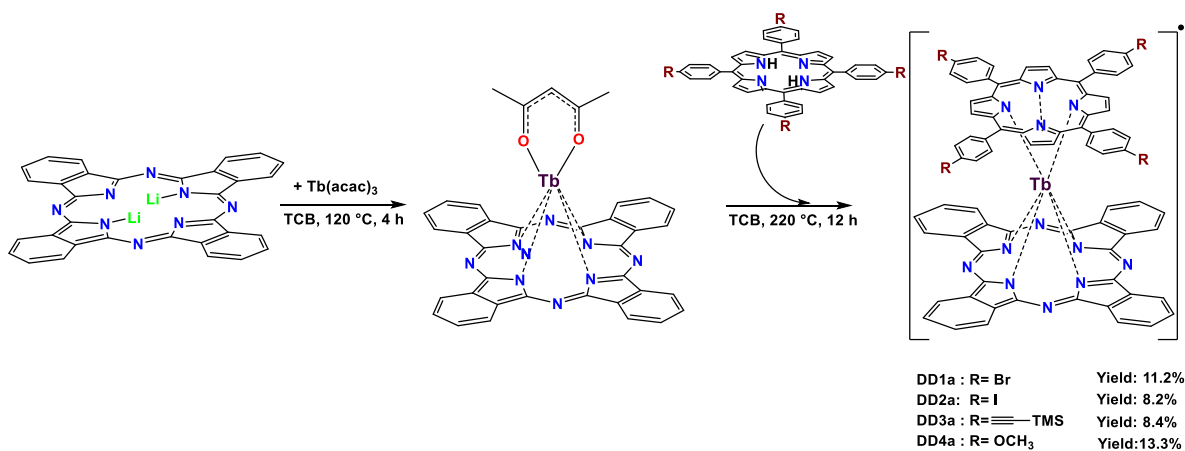


Figure 4.5: UV-Vis spectra of porphyrins **P1-P4** measured in CHCl₃, showing both Soret bands and Q-bands in the 250-800 nm region.

Synthesis and characterization of neutral Tb Double-decker complexes (DD1a-DD4a)

The neutral sandwich complexes (**DD1a-DD4a**) were prepared from equimolar amounts of Li_2Pc , $\text{Tb}(\text{acac})_3$, and the respective porphyrins (**P1-P4**). Several synthetic methods¹⁸¹ were reported for the preparation of double-decker complexes. Unlike homoleptic double-decker complexes, the synthesis of heteroleptic complexes requires two-step synthesis, which involves - synthesis of single-decker compounds and then converting into double-decker complexes. Moreover, this complexation requires very harsh conditions; thus, solvents with higher boiling points like n-octanol or 1,2,5-trichlorobenzene (TCB) should be used. The complexes were labelled in the order of substituents, from electron-withdrawing group (Br and I) to electron-donating group (TMS ¹⁸² and OCH_3).

Here we performed the first step of complexing $\text{Tb}(\text{acac})_3$ with the Pc to form a single-decker complex and further in-situ treatment with free-base porphyrin (**P1-P4**) to form double-decker complexes **DD1a-DD4a** as depicted in Scheme 4.2. The crude reaction mixture was subjected to column chromatography, and the neutral radical species were separated as a brown product along with some other triple-decker complexes as side products. Compared to the Pc analogs of the sandwich complexes, these above complexes are easier to synthesize and have a higher solubility in the common organic solvents.



Scheme 4.2: Synthesis of neutral Tb-double deckers complexes **DD1a-DD4a**.

Electrospray Ionization Mass spectrometry (ESI-MS)

Along with the paramagnetic lanthanide ions, the presence of a radical in the neutral complexes **DD1a-DD4a** produces broad signals in $^1\text{H-NMR}$ with large unconventional shifts. Thus ESI mass spectra come into the picture as a simple tool for confirming the identity of these complexes. Figure 4.6 shows the ESI experimental mass spectrum and simulated mass spectrum for $[\text{M}]^-$ for all the double-decker complexes.

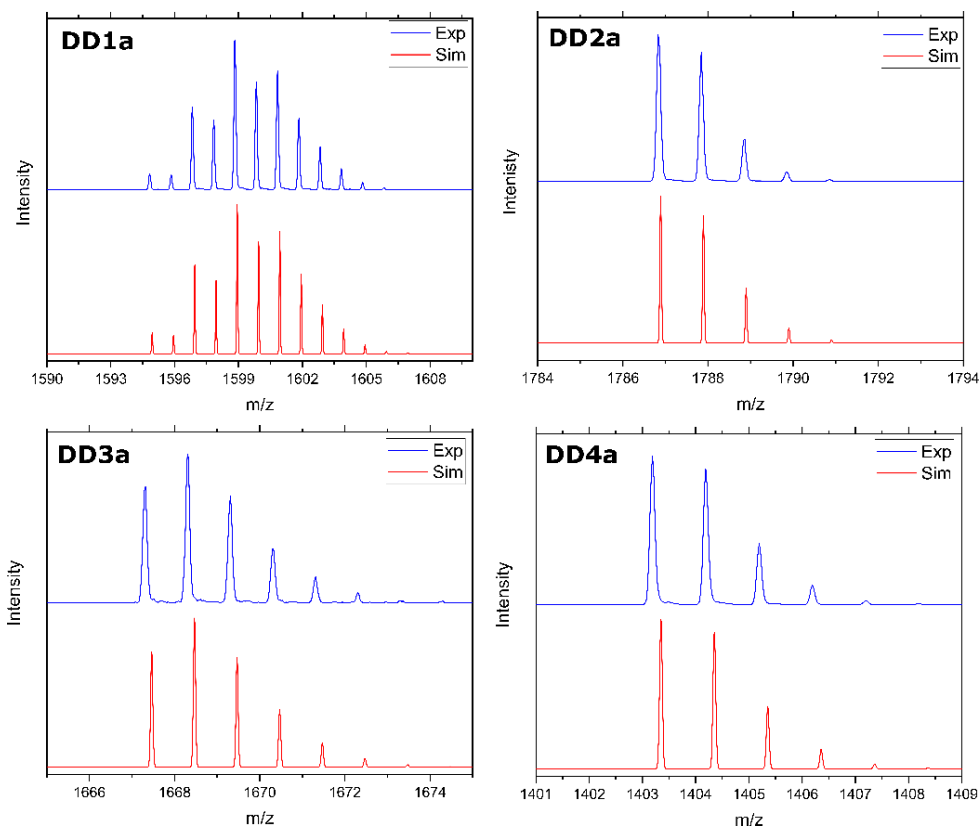


Figure 4.6: ESI-MS characterization of the double-deckers **DD1a-DD4a** in negative mode (experimental data in blue, and simulated in red).

NMR Analysis

The Yttrium analog of **DD1a** was prepared to reduce the paramagnetic contribution from Ln(III), to analyze the structure using NMR studies. However, the presence of the radical makes the peaks broader and challenging to study. In order to quench the effect of the radical, the double-decker complex was reduced in-situ to the anionic species by the addition of hydrazine hydrate. Since the anionic complex does not contain an unpaired electron, the NMR spectra should reveal the chemical shift values in the general range. The ^1H NMR of $[\text{Y}^{\text{III}}(\text{Pc})(\text{P1})]$ (Figure 4.7) was measured in 1:1 CDCl_3 : DMSO-d_6 solution in the presence of 10% (by volume) hydrazine hydrate. With the help of ^1H - ^1H COSY analysis and previous results in the literature on corresponding analogs,¹⁸³ the peaks were assigned. The doublet at $\delta = 9.00 - 9.02$ ppm is attributed to the Pc α -protons, while the doublet signals for correlated β -protons are observed at $\delta = 8.1$ ppm. The tetrabromo-phenyl porphyrin (**P1**) β -protons resonate as a sharp singlet at $\delta = 7.90$, whereas the four doublets between $\delta = 6.3 - 7.7$ ppm correspond to protons of the benzene ring of porphyrin (**P1**).

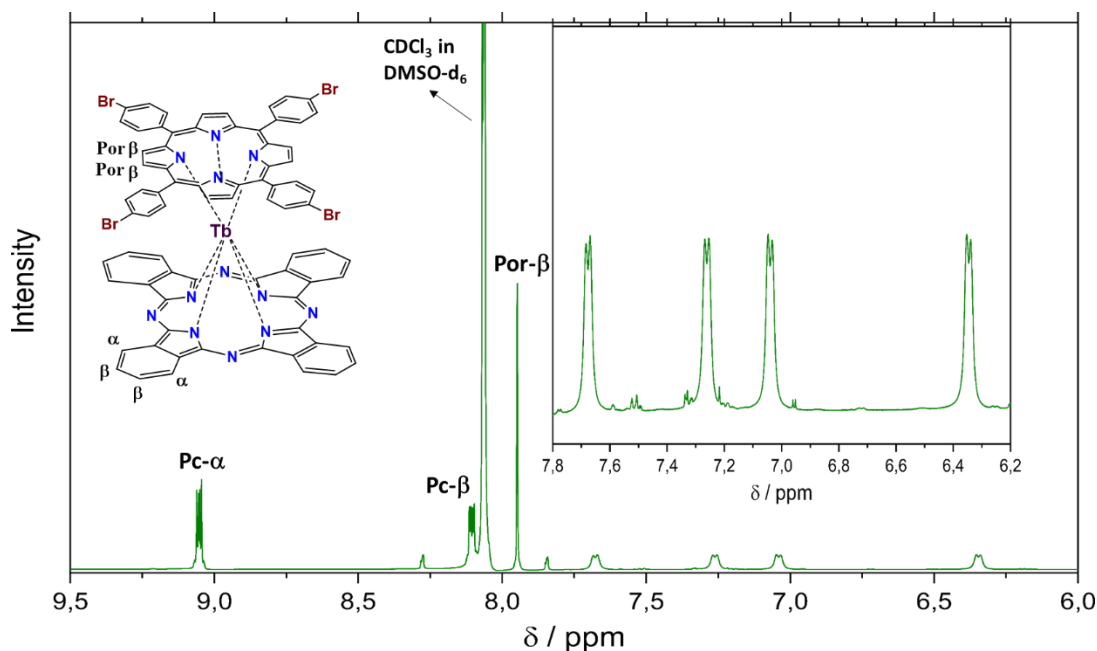


Figure 4.7: ^1H NMR spectrum of $[\text{Y}^{\text{III}}(\text{Pc})(\text{P1})]$ in CDCl_3 : DMSO-d_6 (1:1) in the presence of *ca.* 10% (by volume) hydrazine hydrate.

UV-Vis Studies

Like any other double-deckers complexes, these complexes of Tb^{3+} (**DD1a-DD4a**) on Pc and porphyrins show intense characteristic peaks in electronic absorption spectra. So the UV-Vis-NIR spectroscopic studies for the present series of neutral complexes (**DD1a-DD4a**) were recorded in CHCl_3 , and all the data were compiled in table 4.1. The absorption spectra of the neutral complexes **DD1a-DD4a** show strong bands at 315 - 330 nm, and 400 - 410 nm corresponds to Soret bands of these complexes having predominant Pc and Por character, respectively.¹⁸⁴ The absorption bands at 465 - 475 nm (Blue Valance: BV) and 1015 - 1040 nm (Red Valance: RV) are due to electronic transitions involving the semi occupied orbital that has a higher Pc character. An additional NIR band at 1240 - 1330 nm can also be observed, which are inter-valance (IV) bands. The absorption peak positions are sensitive to the substitution on the porphyrin ring, which plays a major role in bathochromic or hypsochromic shifts, as observed in Table 4.1.

Table 4.1: Electronic absorption data for compounds **DD1a-DD4a** in CHCl_3 .

Complex	$\lambda_{\text{max}} / \text{nm}$				
DD 1a	329.2	402.5	466.3	1021.7	1248.2
DD 2a	325.8	403.8	467.6	1017.1	1252.4
DD 3a	325.7	408.6	467.9	1015.7	1270.4
DD 4a	317.4	406.3	474.2	1036.3	1323.0

Figure 4.8 shows a simplified MO diagram for these complexes, which is adapted from the literature.¹⁸³ Due to ease of oxidation and reduction of Pc compared to porphyrins,¹⁸⁵ the a_{1u} orbital of Pc is higher in energy than that of porphyrins while e_g orbitals are lower than that of porphyrin. So the SOMO and LUMO of **DD1a-DD4a** are mainly due to the Pc ligand, whereas the second HOMO and second LUMO contain a greater amount of porphyrin character. Thus the electronic absorption at 1015–1040 nm can thus be attributed to the electronic transition from the semi-occupied orbital to the degenerated LUMO (RV). The lower energy near-IR absorption at 1240–1330 nm is due to the transition from the second HOMO to the semi-occupied orbital.¹⁸³

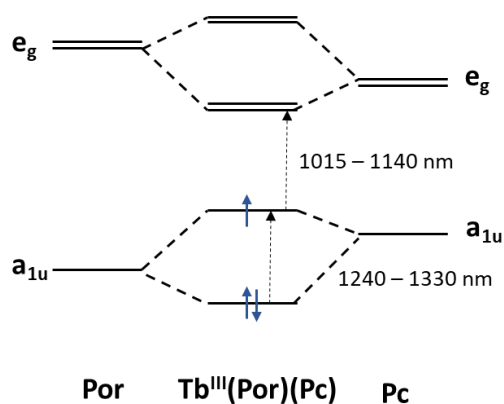


Figure 4.8: Simplified molecular orbital diagram for neutral complex [Tb(Porphyrin)(Pc)] (Reproduced from Ref. ¹⁸³)

So, as the periphery of the porphyrin changes from the electron-donating group (EDG) to the electron-withdrawing group (EWG), the HOMO, which has a higher porphyrin character, gets stabilized, and the 2nd LUMO energy level increases. Thus the energy gap increases and shows a hypsochromic shift (from 474.2 to 466.3 nm). Similarly, the blue-shift in the inter-valence band can be attributed to an increase in the gap between the HOMO and SOMO due to a change in the periphery of the porphyrin moiety from OCH₃ to Br (Figure 4.9 and Table 4.1).

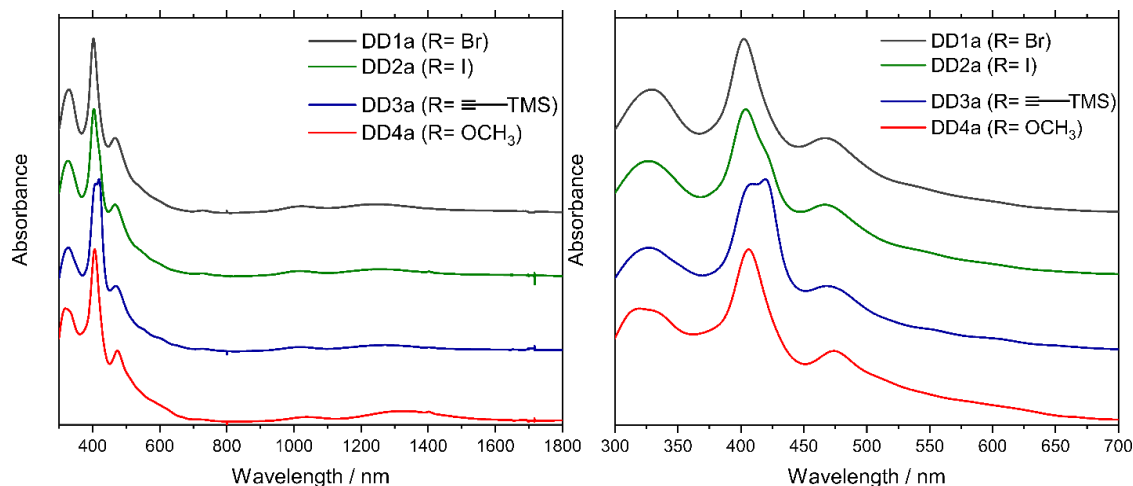


Figure 4.9: UV-Vis-NIR absorption spectra of **DD1a-DD4a** in CHCl_3 . The peak positions from these spectra were presented in Table 4.1 for comparison.

Lanthanide based sandwich complexes show distinctive features in absorption spectra upon oxidation or reduction. The neutral radical complex **DD1a** was in-situ reduced to anionic form by the addition of 1% (by volume) hydrazine hydrate, which resulted in an immediate change in colour from brown to green (Figure 4.10). As a consequence, the spectra (Figure 4.10) shows several changes in peaks, such as the disappearance of bands between 1000 – 1800 nm. This is due to the addition of an electron into the SOMO turning into a new HOMO. Thus the bands (IV, RV, and BV), which are responsible from π -radical, disappear on reduction with hydrazine.

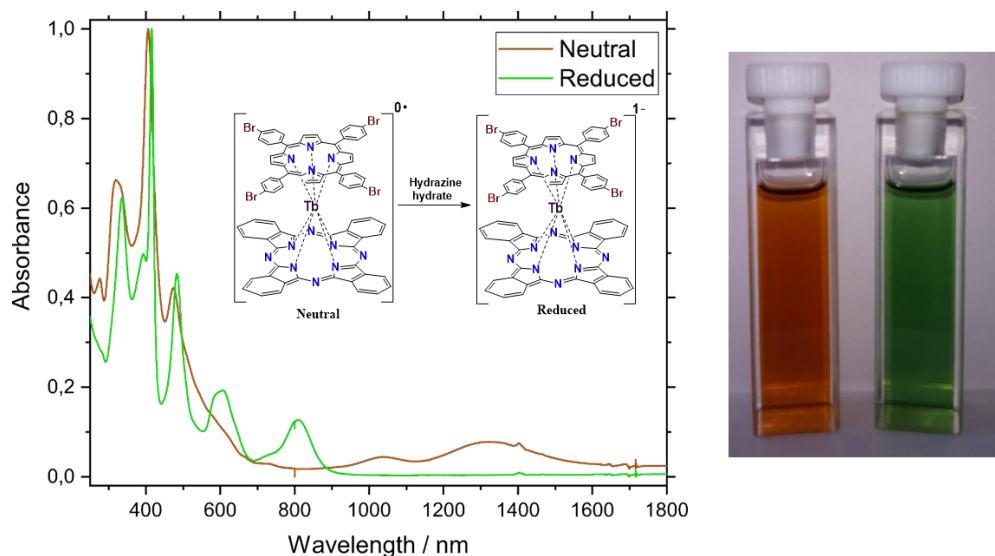


Figure 4.10: UV-Vis-NIR absorption spectra of neutral and anionic forms of **DD1a** in CDCl_3 (on left) The figure in inset represents the scheme for conversion neutral to reduced double-decker complex. Clear visualization of colours difference between neutral (brown) and reduced (green) forms of **DD1a** in CDCl_3 (on the right).

Electrochemical Studies

The redox behaviour of the heteroleptic double-decker complexes **DD1a - DD4a** was studied by cyclic voltammetry (CV) and differential pulse voltammetry (DPV). All these complexes exhibited three quasi reversible one-electron oxidations and three quasi reversible one-electron reduction processes. All the data were compiled in Table 4.2, and Figure 4.11 shows the CV and DPV for the neutral double-decker complexes **DD1a-DD4a**. All the reduction and oxidation processes can be attributed to one electron addition or removal on the ligand-based orbitals of the double-decker complexes.

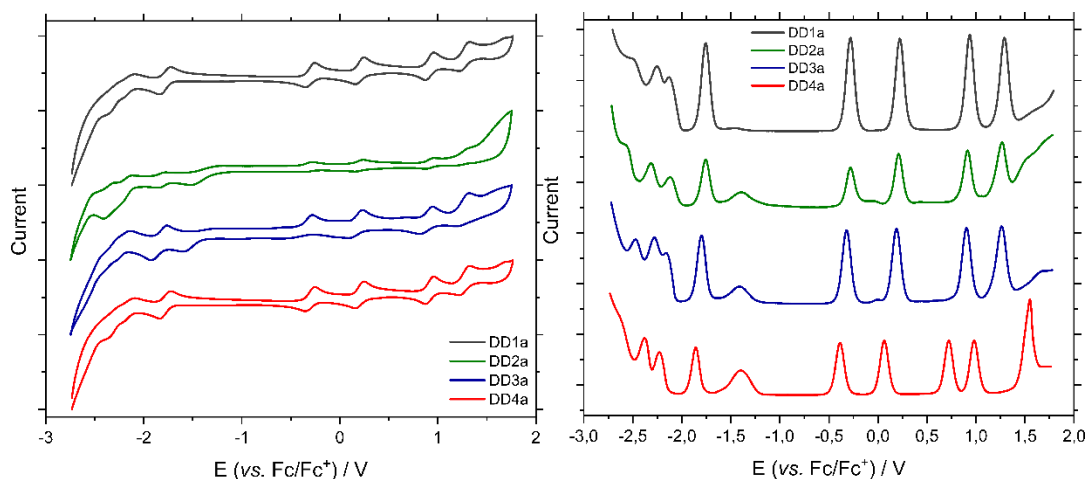


Figure 4.11: Cyclic voltammogram (left) and differential pulse voltammogram (right) of **DD1a-DD4a** in CH_2Cl_2 containing 0.1 M $[\text{Bu}_4\text{N}][\text{PF}_6]$ at a scan rate of 50 and 10 mV/s, respectively.

Table 4.2: Electrochemical data for compounds **DD1a-DD4a**.^a

	O_3	O_2	O_1	R_1	R_2	R_3	$\Delta E_{1/2}^b$	$\Delta E'_{1/2}^c$
DD1a	1.29	0.94	0.22	-0.28	-1.76	-2.13	0.50	0.71
DD2a	1.26	0.91	0.21	-0.28	-1.78	-2.12	0.49	0.70
DD3a	1.26	0.89	0.19	-0.32	-1.80	-2.16	0.51	0.70
DD4a	0.98	0.72	0.06	-0.39	-1.86	-2.23	0.45	0.66

^a Data was obtained using DPV, ^b $\Delta E_{1/2} = O_1 - R_1$ and ^c $\Delta E'_{1/2} = O_2 - O_1$

As shown in Table 4.2, the half-wave potentials of both the first oxidation (O_1) and the first reduction (R_1) processes, which involve the semi-occupied molecular orbital (SOMO), decrease upon moving from EWG to EDG substitution on porphyrin periphery. That is, the incorporation of the EDG onto the porphyrin ring makes the complex easier to oxidize and also harder to reduce. The difference between 1st and 2nd oxidation potentials (which is $\Delta E'_{1/2}$) represents the gap between HOMO and SUMO, and this reduces from 0.71 V to 0.66 V. This is also in agreement with the red-shift occurring in the 1240 – 1330 nm

region, confirming that this is due to electron-donating nature of the substituents on the periphery of the porphyrin.

Structural Analysis of Neutral complexes

The molecular structure of the neutral sandwich complexes (**DD1a**, **DD2a**, **DD4a**) was confirmed using X-ray diffraction analysis. Single crystals for XRD analysis were obtained by slow diffusion of hexane into CH_2Cl_2 solution (CHCl_3 in case of **DD2a**) by layering. Unfortunately, suitable single crystals of **DD3a** were not obtained to determine its structure and packing in the solid. The terbium centers in the obtained structures are octahedrally coordinated by four pyrroles and four isoindole nitrogens from porphyrin and phthalocyanine rings, resulting in square anti-prismatic (SAP) coordination. So the ligands appear in a staggered conformation with a twist angle approximately equal to 45° .

The double-decker complex **DD1a** crystallizes in monoclinic space group $I2/a$ with the unit cell volume of 14741.7 \AA^3 and $Z=8$. The adjacent Tb(III) double-decker molecules in the unit cell form a dimer via the $\pi-\pi$ interaction through phthalocyanine ligands resulting in the nearest Tb-Tb distance of 8.84 \AA . The average Tb-N(pyrrole) and Tb-N(isoindole) distances are $2.464(7)$ and $2.434(7) \text{ \AA}$. The two N_4 planes (porphyrin and Pc) are parallel giving to a ring separation of 2.768 \AA with a twist angle of 44.07° . Figure 4.12 shows two perspective views of the coordination environment of the neutral complex **DD1a**.

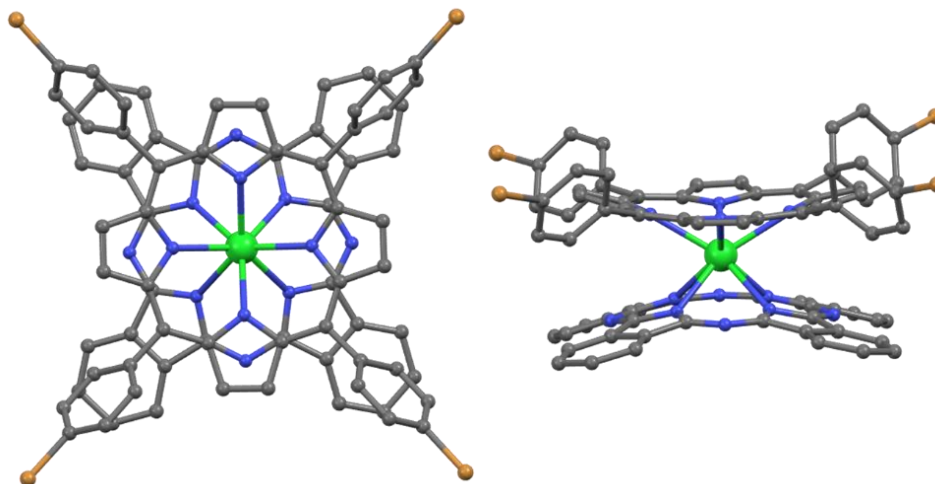


Figure 4.12: Top and side views of the molecular structure of neutral complex **DD1a**, obtained from single crystal showing the SAP coordination, hydrogen atoms are omitted for clarity [Tb(III)-green, C-grey, N-blue, Br-light brown].

The double-decker complex **DD2a** crystallized in monoclinic space group $C2/c$ with the unit cell volume of 32672.3 \AA^3 and $Z=8$. The adjacent Tb(III) double-decker molecules in the unit cell form a dimer via the $\pi-\pi$ interaction of phthalocyanine ligands with the nearest Tb-Tb distance of 9.28 \AA . The average Tb-N(pyrrole) and Tb-N(isoindole) distances

are 2.432(12) and 2.450(12) Å. The two N₄ planes (porphyrin and Pc) are parallel and are separated by 2.783 Å with a twist angle of 44.25°.

Table 4.3: Comparison of angles and distances obtained from crystallographic data of neutral double-decker complexes **DD1a-DD4a**.

	DD1a	DD2a	DD4a
Avg. Tb-N (Por) / Å	2.464 (7)	2.432 (12)	2.434 (5)
Avg. Tb-N (Pc) / Å	2.436 (7)	2.450 (12)	2.477 (6)
Tb-N(Por) plane dist. / Å	1.287	1.297	1.281
Tb-N(Pc) plane dist. / Å	1.481	1.484	1.490
Inter-planar distance / Å	2.768	2.783	2.771
Twist angle* / °	44.07	44.25	43.58

*defined as the angle of rotation of one ring away from the eclipsed conformation of the two rings

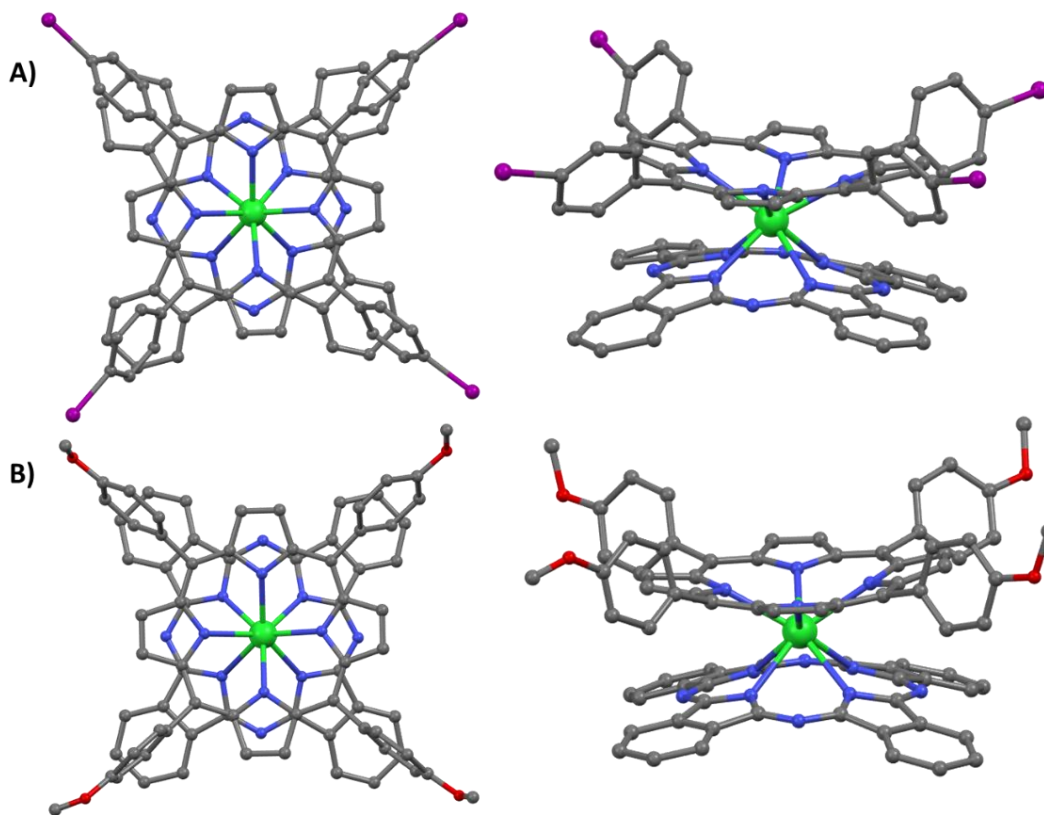


Figure 4.13: Top and side views of the molecular structure of A) **DD2a** and B) **DD4a** complex, obtained from single crystals, showing the SAP coordination, hydrogen atoms are omitted for clarity [Tb(III)-green, C-grey, N-blue, O-red, I-violet].

The double-decker complex **DD4a** crystallized in monoclinic space group $P2_1/c$ with a unit cell volume of 7401.7 Å³ and $Z=4$. The adjacent molecules in a unit cell form a dimer

via the π - π interaction through phthalocyanine ligands resulting in the shortest Tb-Tb distance of 9.55 Å. The average Tb-N(pyrrole) and Tb-N(isoindole) distances are 2.434(5) and 2.477(6) Å. The two N₄ planes (porphyrin and Pc) are parallel giving to a separation of 2.771 Å, with a twist angle of 43.58°.

Magnetic Measurements of Neutral complexes (DD1a-DD4a)

DC magnetic susceptibility measurements were performed for the neutral sandwich complexes **DD1a-DD4a** under an applied field of 0.1 T. At RT, χT value of 10.6 to 11.05 cm³ K mol⁻¹ were observed, which is in agreement to the expected values for single Tb³⁺ ions. The contribution of the radical centered on the organic ligand is negligible to the overall magnetic moment of the complex. Upon cooling of the sample, the χT values slowly decrease until 20 K, and then rapidly decreases (Figure 4.14 A), suggesting crystal field effects such as thermal depopulation of Tb(III) stark sublevels.

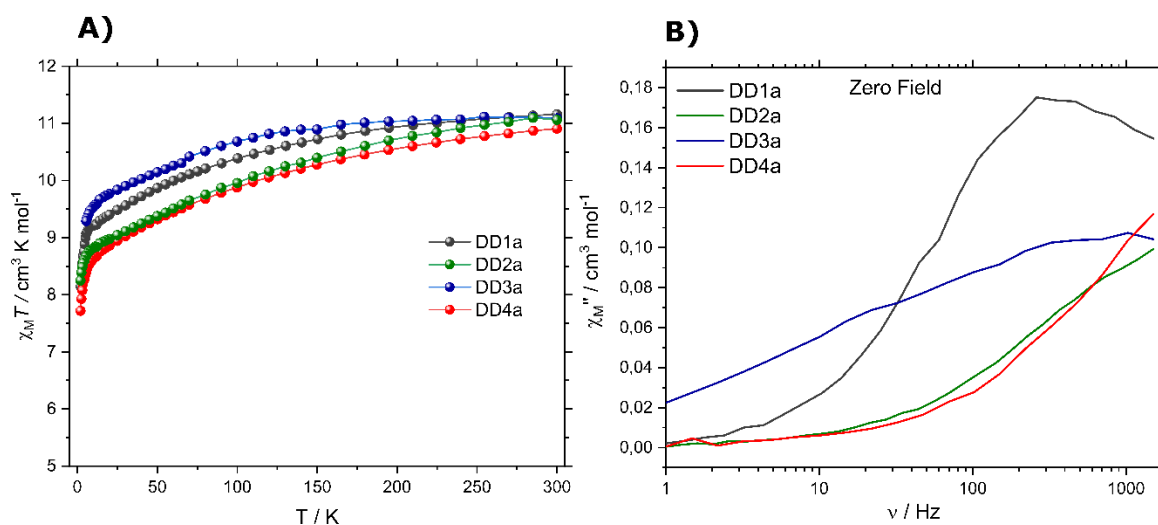


Figure 4.14: A) DC magnetic data for complexes **DD1a-DD4a** and B) frequency dependence of the out-of-phase (χ'') AC susceptibility of **DD1a-DD4a** in zero field at 15 K.

To estimate their magnetization relaxation behaviour at zero field, the ac susceptibility measurements were carried out using 5 Oe ac field in a frequency range of 1-1500 Hz. The frequency-dependent out-of-phase signals (χ'') for neutral complexes **DD1a-DD4a** were not observed, demonstrating that these complexes do not act as SMMs at zero field. For further characterization of the magnetic behaviour, an external magnetic field was applied in order to suppress the possibility of quantum tunneling of the magnetization process. In the presence of an external magnetic field, the neutral complexes **DD1a-DD4a** showed frequency-dependent character in both in-phase (χ') and out-of-phase (χ'') in the 1-1500 Hz region, demonstrating the field-induced SMM nature of the neutral **DD1a-DD4a** complexes. Even though in the case of **DD1a** showed a characteristic maximum in frequency-dependent AC signal, to improve suppress the QTM, the ac susceptibility measurements were performed in OF.

The optimal field (OF) for each neutral complex was obtained and was found to be around 3500-4000 Oe. The application of the OF prevents the quantum tunneling relaxation process. Then magnetic susceptibility measurements were performed for neutral complexes with their respective OFs showing clear frequency dependence up to a temperature region of 29 K (Figure 4.15).

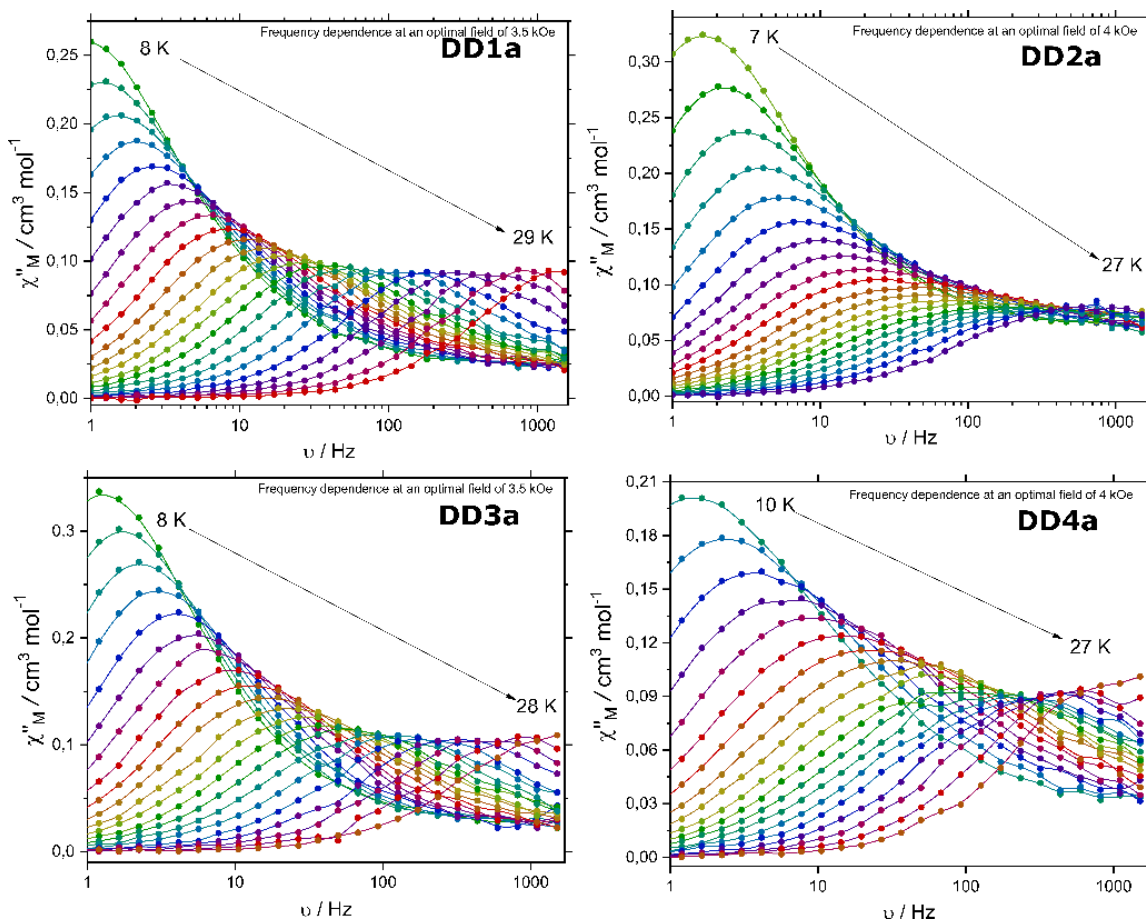


Figure 4.15: Out of phase AC susceptibilities for neutral sandwich complexes **DD1a-DD4a** in respective OFs.

The relaxation time (τ) was extracted for each temperature for every complex from Figure 4.15. With that, the effective energy barrier for reversal of magnetic moment and pre-exponential factors were determined from Arrhenius plots (Figure 4.16) using equations 1.17 and 1.18. As shown in Figure 4.16, the energy barrier for complex **DD1a**, with the EWG is around 231 K, whereas for **DD4a**, with the EDG, the energy barrier U_{eff} is 88 K. So the change in substitution on the phenyl group of the porphyrin ring tunes the ligand field and thus affects the SMM behavior. The difference in optimal fields for each complex makes it difficult to compare their SMM properties.

Table 4.4: Effective energy barriers and pre-exponential factors for neutral double-decker complexes **DD1a-DD4a**.

Neutral Complex	$U_{\text{eff}} / \text{K}$	τ_0 / s	Optimal Field / Oe
DD1a	231	9.03×10^{-8}	3500
DD2a	102	7.50×10^{-6}	4000
DD3a	89.5	3.36×10^{-5}	3500
DD4a	88	1.12×10^{-5}	4000

However, the change in substituent at the *meso*- attached phenyl moieties of the porphyrin ligand in the double-decker molecule from EWG (R=Br) to EDG (R= OCH₃), stronger quantum tunneling of magnetization (QTM) was revealed for **DD4a** in comparison with **DD1a** despite of same coordination behaviour of SAP. The larger perturbation of ligand field strength influences the ground state sublevels of Tb(III) as can be seen from the U_{eff} from Table 4.4.

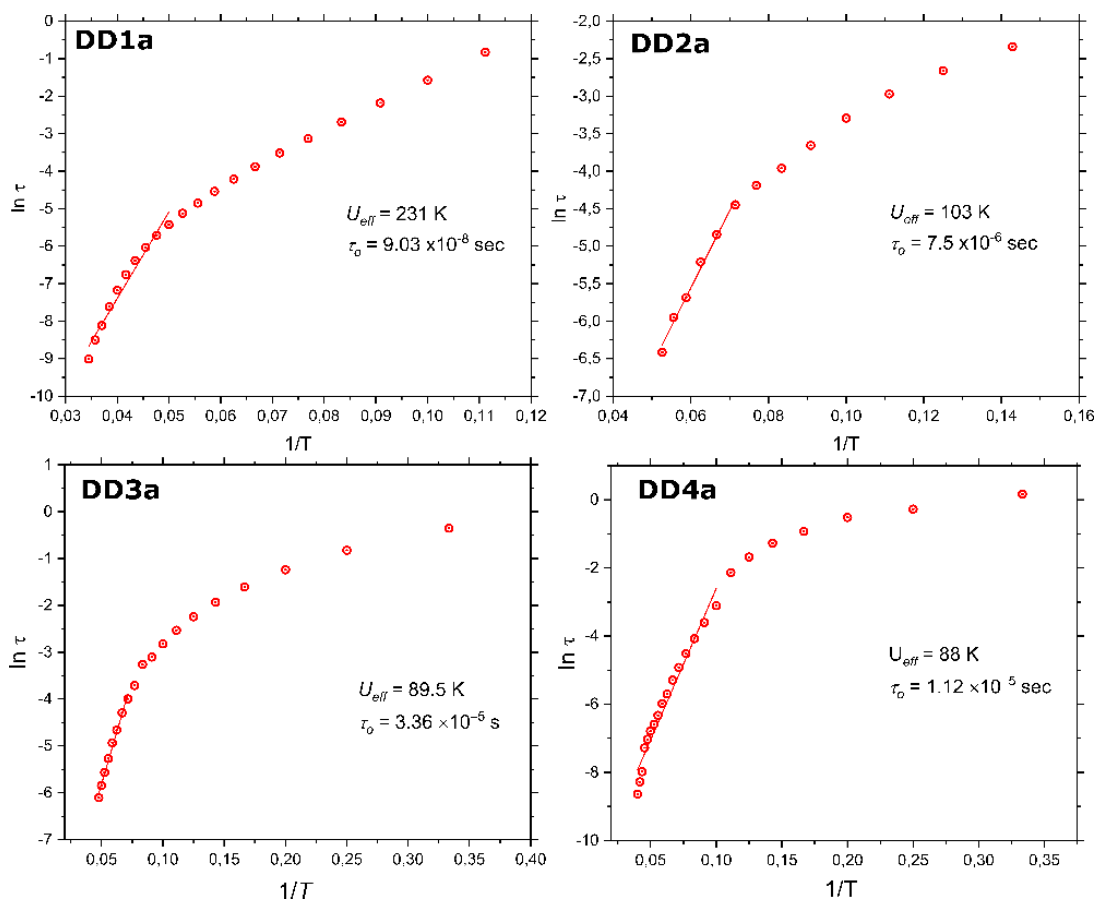
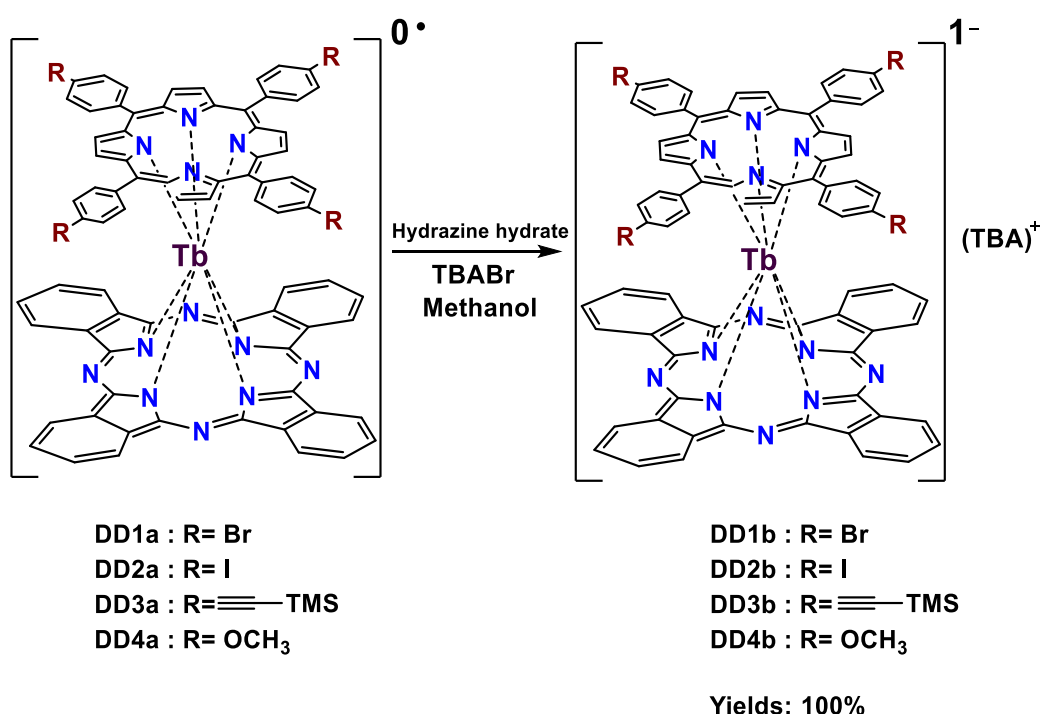


Figure 4.16: $\ln(\tau)$ vs. $1/T$ plots for neutral double-decker complexes **DD1a-DD4a**. The continuous line corresponds to the best fit for the Arrhenius equation to determine the activation energy (U_{eff}) and pre-exponential factor (τ_0).

Structural Analysis of Anionic complexes (DD1b-DD4b)

The reduced complexes **DD1b-DD4b** were prepared by treating the neutral complexes with hydrazine hydrate with TBABr in methanol, as depicted in Scheme 4.3. The complexes were filtered to yield **DD1b-DD4b**. Suitable crystals for single-crystal XRD were obtained by slow evaporation of 1:1 CH₂Cl₂: hexane solution (CHCl₃ in case of **DD2b**). Unfortunately, suitable single crystals of **DD2b** and **DD3b** were not obtained to determine their structure and packing in the solid. Like the neutral complexes, the terbium centers in the obtained anionic structures are octahedrally coordinated by four pyrroles and four isoindole nitrogens from porphyrin phthalocyanine rings, resulting in SAP coordination. So the ligands appear in a staggered position with a twist angle near to 45°.



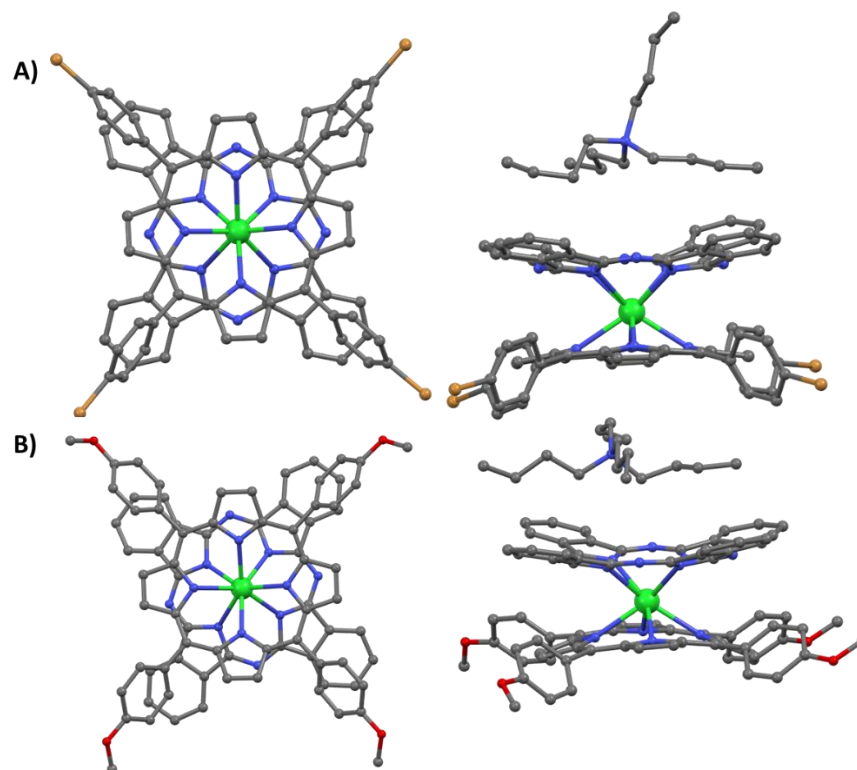
Scheme 4.3: Synthesis of reduced complexes (**DD1b-DD4b**) from neutral complexes (**DD1a-DD4a**).

The anionic double-decker complex **DD1b** crystallized in monoclinic space group *P*2₁/*c* with a unit cell volume of 17704.2 Å³ and *Z*=8. The tetrabutylammonium cation locates on the top of the phthalocyanine ligands and changes the nearest Tb-Tb distance to 12.56 Å (Figure 4.17 A), which has increased compared to that of **DD1a**. The average Tb-N(pyrrole) and Tb-N(isoindole) distances are 2.455(9) and 2.487(9) Å. The two N₄ planes (porphyrin and Pc) are parallel giving a ring separation of 2.822 Å with a twist angle of 42.9°.

Table 4.5: Angles and distances obtained from crystallographic data of anionic double-decker complexes **DD1b** and **DD4b**.

	DD1b	DD4b
Average Tb-N (Por) / Å	2.455 (9)	2.466 (9)
Average Tb-N (Pc) / Å	2.497 (9)	2.484 (8)
Tb-N(Por) plane distance / Å	1.316	1.369
Tb-N(Pc) plane distance / Å	1.506	1.504
Inter-planar distance / Å	2.822	2.873
Twist angle / °	42.90	36.08

The anionic double-decker complex **DD4b** crystallizes in monoclinic space group $P2_1/c$ with a unit cell volume of 4070.6 \AA^3 and $Z=2$. The tetrabutylammonium cation locates on the top of the phthalocyanine ligands and thus increases the nearest Tb-Tb distance to 14.38 \AA (Figure 4.17B) compared to **DD4a**. The average Tb-N(pyrrole) and Tb-N(isoindole) distances are $2.466(9) \text{ \AA}$ and $2.484(9) \text{ \AA}$. The two N_4 planes (porphyrin and Pc) are parallel giving to a ring separation of 2.873 \AA with a twist angle of 36.08° . Because of the presence of the electron-donating group (OCH₃) on the porphyrin ring, the avg. N-Tb(Por) increases from 2.455 \AA (in **DD1b**) to 2.466 \AA (in **DD4b**). Moreover, the Pc rings move closer to the Tb(III) as they were pushed by the porphyrin ring functionalized with EDG.

**Figure 4.17:** Top and side views of the molecular structure of A) **DD1b** and B) **DD4b** complex obtained from single crystals, showing the SAP coordination, hydrogen atoms are omitted for clarity [Tb(III)-green, C-grey, N-blue, O-red, Br-light brown].

Magnetic Measurements of Anionic complexes (DD1b-DD4b)

DC magnetic susceptibility measurements were performed for the anionic sandwich complexes **DD1b-DD4b** under an applied field of 0.1 T. At room temperature, χT value of 10.4 to 11.0 $\text{cm}^3 \text{mol}^{-1} \text{K}$ were observed, which is in agreement to what is expected for single Tb^{3+} ions. The contribution of the radical centered on the organic ligand is negligible to the overall magnetic moment of the complex. As the temperature is lowered, the χT value was lowered (Figure 4.18 A), suggesting crystal field effects such as thermal depopulation of Tb(III) stark sublevels.

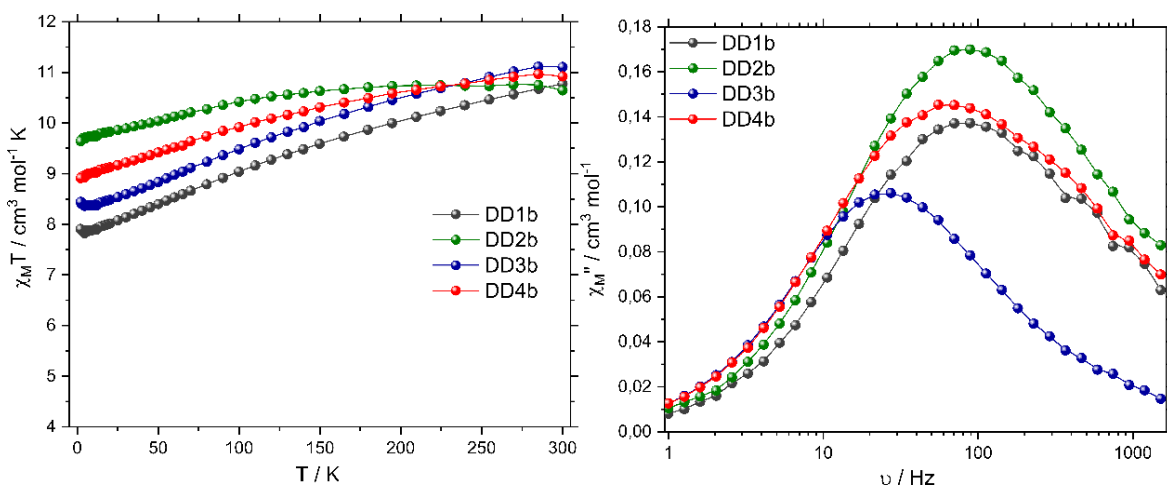


Figure 4.18: A) DC magnetic data for compounds **DD1b-DD4b** and B) frequency-dependent of the out-of-phase (χ'') AC susceptibility of **DD1b-DD4b** in zero field measured at 15 K.

To estimate their magnetization relaxation behaviour at zero field, the ac susceptibility measurements were carried out using 5 Oe ac field in a frequency range of 1-1500 Hz at 15 K. The frequency-dependent out-of-phase signals (χ'') for anionic complexes **DD1b-DD4b** were observed, demonstrating that these complexes do act as SMMs at zero field (Figure 4.18 B). This shows that the anionic complexes are better SMMs at zero fields than the neutral complexes, which is quite unusual in comparison with bis(phthalocyaninato) lanthanide complexes.¹⁸²

For further characterization of the magnetic behaviour of reduced Tb^{3+} complexes **DD1b-DD4b** at zero DC field, they showed frequency-dependent character in both in-phase and out-of-phase in 1-1500 Hz region over a temperature region of 2-30 K. This indicates the SMM nature of the anionic complexes (Figure 4.19).

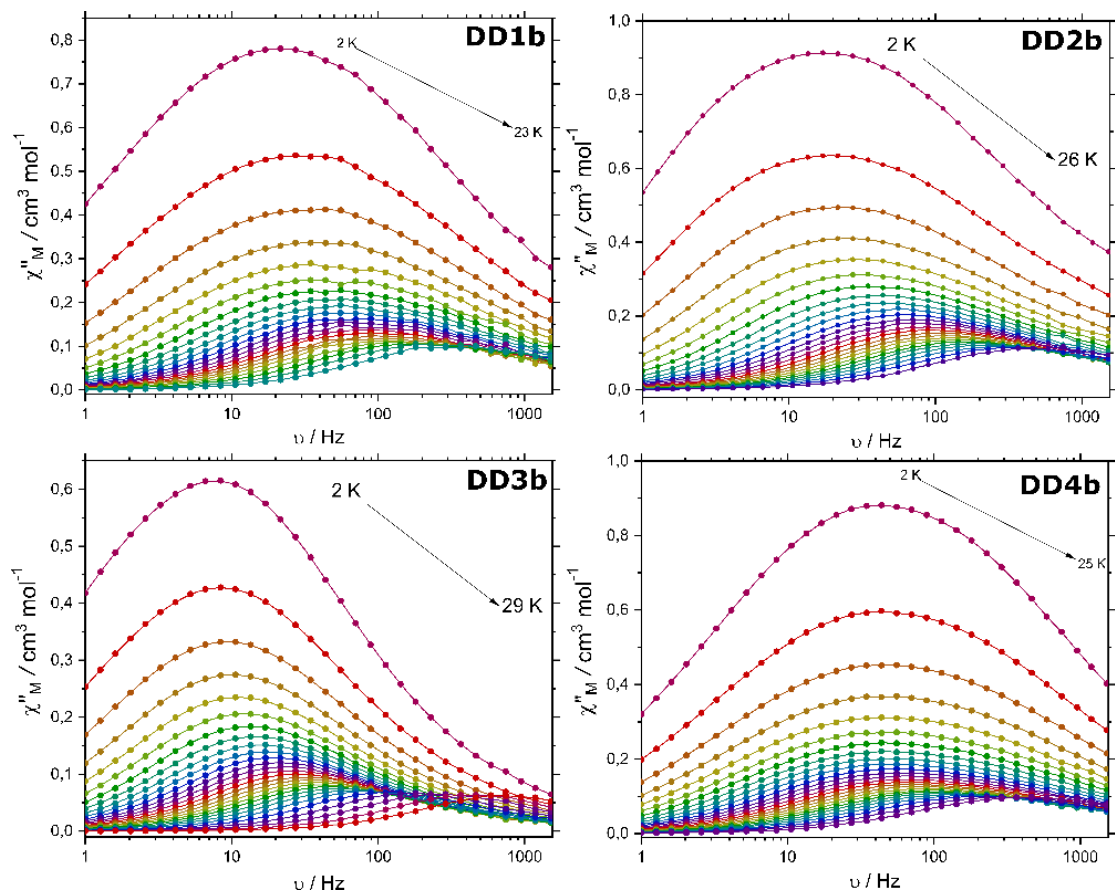


Figure 4.19: Out-of-phase ac susceptibilities for reduced sandwich complexes **DD1b-DD4b** at zero field.

The relaxation time (τ) was determined for each temperature for every complex from Figure 4.19 with the same procedure as performed for neutral complexes. The effective energy barrier for reversal of magnetic moment and pre-exponential factors were determined from Arrhenius plots (Figure 4.20) using equation 1.17 and 1.18. As shown in Figure 4.20, the energy barrier for complex **DD1b**, with the EWG, is around 116 K, whereas for **DD4b**, with the EDG, shows effective energy barrier U_{eff} is 22.3 K. So it is clearly evident that the presence of EDG groups over EWG has shown decrease in SMM properties at zero field. This can be explained using the crystal structure obtained, which showed change in twist angle to 36° showing distorted Square antiprism coordination, thus resulting in reduction symmetry. So this should negative influence on SMM properties and resulted in low U_{eff} of 22.3 K for **DD4b** (R=OCH₃). On the other hand, even though, TMS group shows electron donating behavior, **DD3b** showed better SMM properties in comparison with **DD2b** (R=I). This could be due to presence of long and steric groups on the porphyrin ring, which helped in isolation of the molecule.

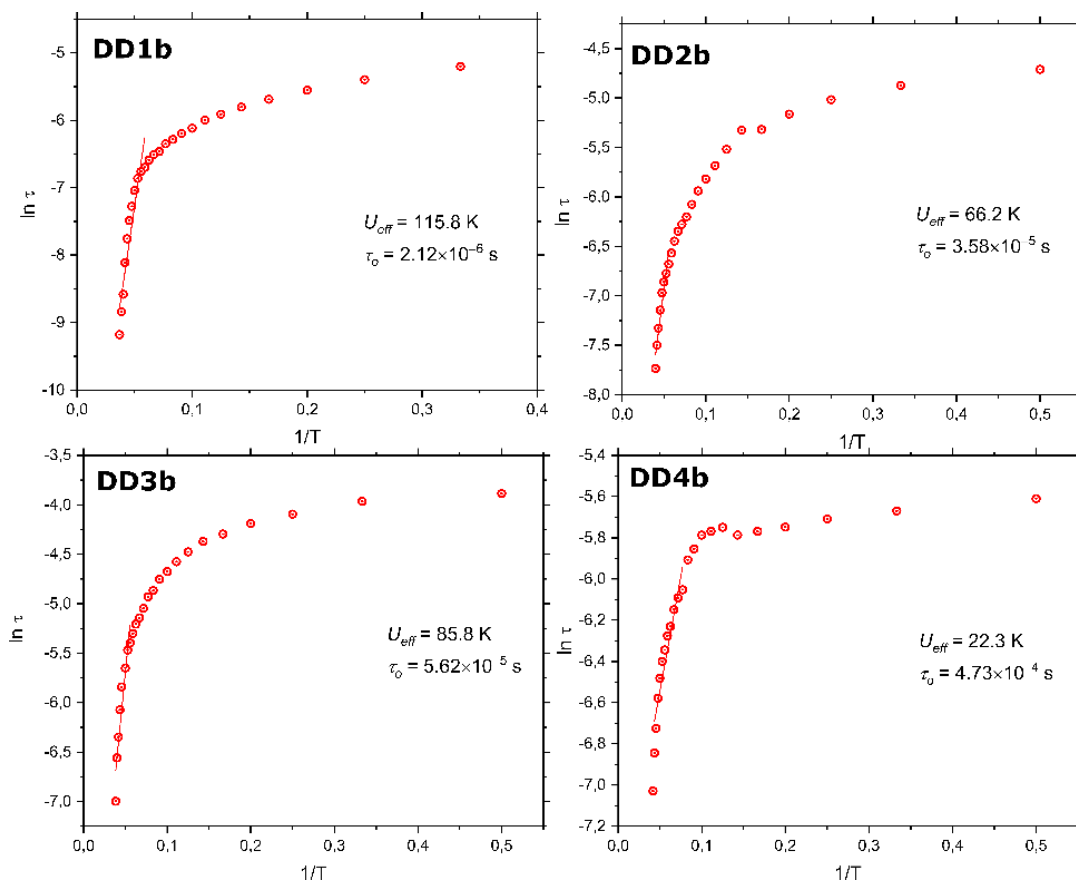


Figure 4.20: $\ln(\tau)$ vs. $1/T$ plots for anionic double-decker complexes **DD1b-DD4b**. The continuous line corresponds to the best fit for the Arrhenius equation to determine the activation energy (U_{eff}) and pre-exponential factor (τ_0).

Table 4.6: Effective energy barriers and pre-exponential factors for the anionic complexes **DD1b-DD4b** at zero field.

Reduced Complex	$U_{\text{eff}} / \text{K}$	τ_0 / s
DD1b	115.8	2.12×10^{-6}
DD2b	66.2	3.58×10^{-5}
DD3b	85.8	5.62×10^{-5}
DD4b	22.3	4.73×10^{-4}

In general, in lanthanide-based double-decker complexes, it was evident that the radical plays a key role in enhancing of SMM performance in comparison with non-radical species, i.e., the radical species show slow magnetic relaxation at higher temperatures in comparison with reduced complexes. This behaviour was observed in both bis(porphyrinato)^{175,174} and bis(phthalocyaninato)¹⁸⁶ based lanthanide double-decker complexes.¹⁷⁵ However, in our present work on mixed porphyrin and phthalocyanine based lanthanide double-deckers, the presence of radical showed a negative impact in enhancing

the SMM properties. All the radical species presented in this chapter (**DD1a-DD4a**) were not SMMs at zero field, whereas the reduced complexes (**DD1b-DD4b**) were SMMs at zero field. That is, the SMM properties of the complexes can be reversibly switched on by reduction or oxidation, which is inverse to that of porphyrin-based Tb(III) double-decker. Later, we found similar results reported by J. Jiang and coworkers showing the negative impact of f-radical interaction in mixed phthalocyanine and porphyrin-based Dy(III) sandwich complexes.¹⁸⁷ This is due to a reduction in electrostatic interaction between the tetra-pyrrole ligands and lanthanide ions in neutral complex, which in turn decreases the uniaxial magnetic anisotropy and thus reduces the SMM properties.

To rationalize the SMM properties showed in this chapter, we need to also consider the other factors that influence the ligand field, other than the oxidation state. Those include the presence of a functional group on the periphery of tetra-pyrrole ligand, which influences the electronic and structural properties of these ligands. The presence of the EDG has induced longer N-Tb distances and thus decreases the twist angle to 36° from 45°, showing distorted SAP coordination in **DD4b**. The distortion might have resulted in symmetry reduction and thus impacted negative influence on SMM properties. Moreover, the steric groups also influence the SMM properties of the complex. The presence of bulky trimethylsilane (TMS) groups on the porphyrin in complex **DD3b** contributed to the dilution of the compound and thus reduced the intermolecular interaction and improved the SMM properties. Unfortunately, the structural features could not be corroborated by X-ray analysis due to failure in obtaining suitable single crystals for **DD3b**.

4.2.2 Objective 2: Synthesis and Characterization of poly-nuclear Tb (Porphyrinato) (Phthalocyaninato) sandwich complexes

Structural optimization was performed by Jorge Enrique Olivares Pena from Prof. Wolfgang Wenzels group from INT, KIT. EPR measurements were performed by Athanassios K. Boudalis from our group.

Synthetic approach

In order to design and build the polynuclear magnetic architectures, we require several elements that include the magnetic building block, the linker, and the mechanism to couple them (Figure 4.21). Here, in our case, we chose the porphyrin and phthalocyanine based double-decker as a magnetic building block and Sonogashira coupling reaction as a linking strategy.

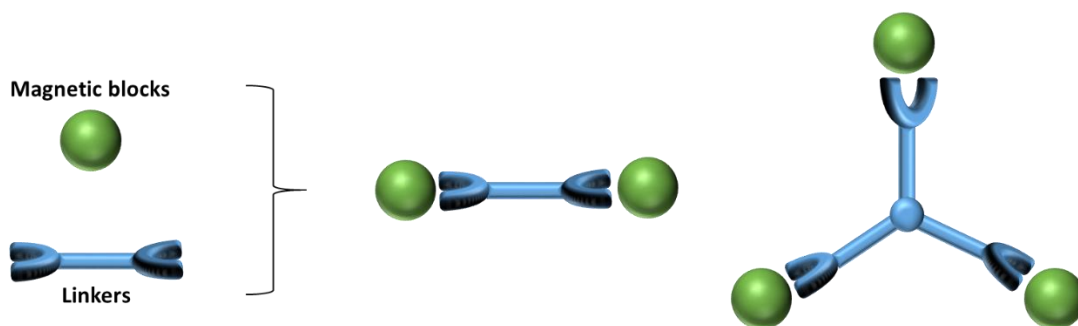


Figure 4.21: Schematic representation of the building blocks and their planned stepwise assembly. The magnetic building blocks are represented in green, and the linking groups in blue.

The retrosynthesis scheme (Figure 4.22) shows a clear view of the synthesis, which requires a single sandwich complex and thus one can synthesize a family of coupled double-decker complexes, just by varying the linkers. The green sphere in Figure 4.22 represents the Tb^{3+} ions, blue circle represents the phthalocyanine and blue square represents the porphyrin. The monomeric units were coupled via porphyrin to form dimeric complexes.

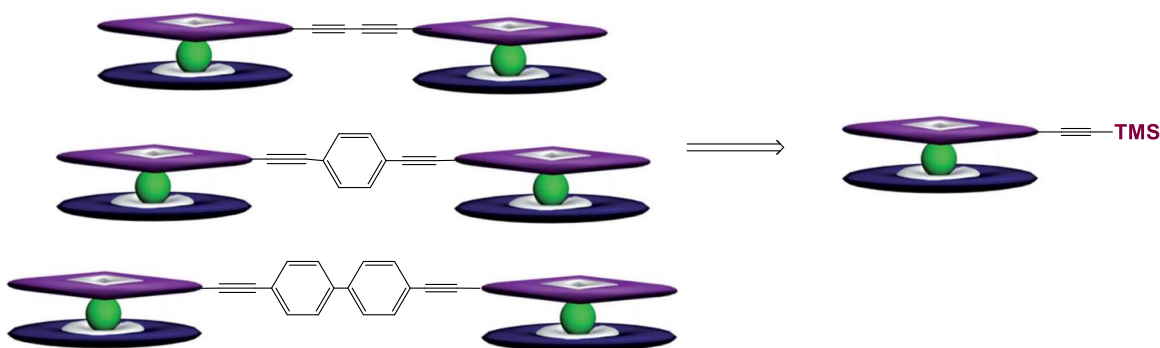
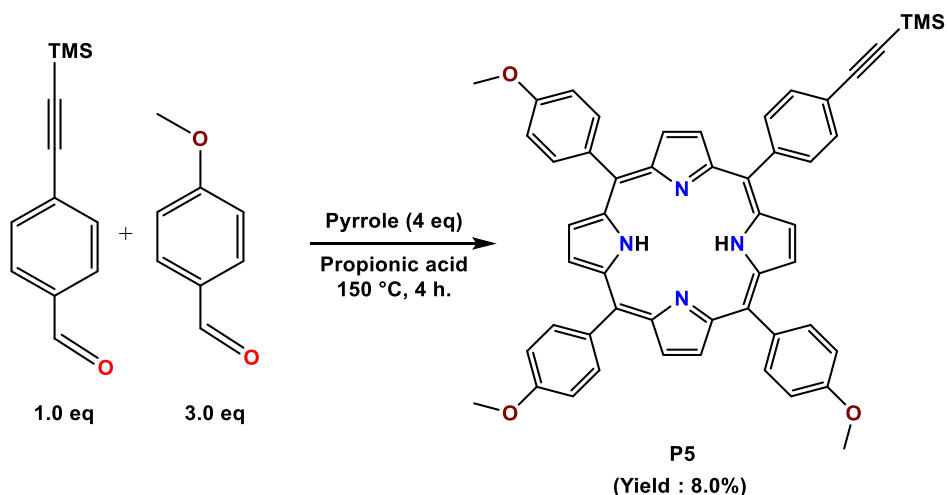


Figure 4.22: Retrosynthesis of heteroleptic binuclear double-decker complexes.

Synthesis and characterization of mono-nuclear double-decker complex as starting material

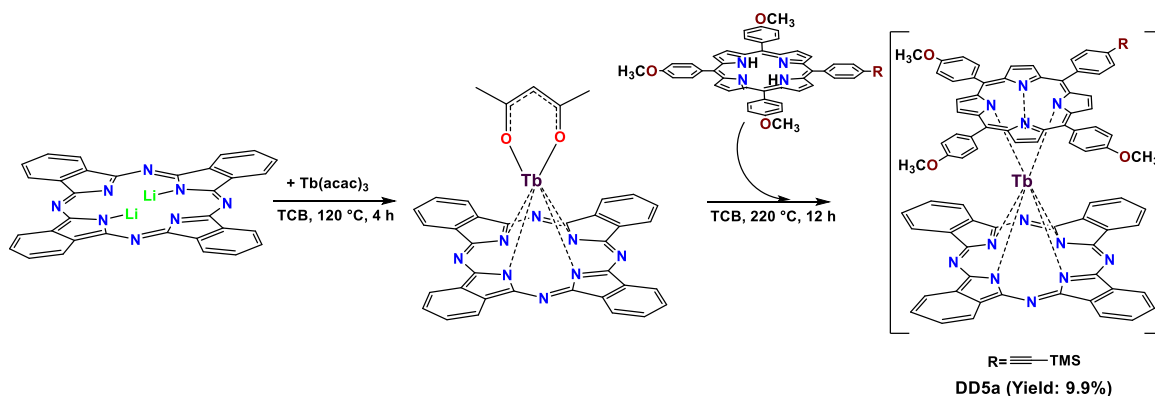
The porphyrin (**P5**) with different substitutions on the periphery were synthesized as depicted in Scheme 4.4. This reaction has obtained in several side products, and the required compound was separated using column chromatography as a purple-colored product with a yield of 10%. The $^1\text{H-NMR}$, $^{13}\text{C-NMR}$ and Mass spectra of the porphyrin obtained were in agreement with the reported data of the complex. Even though the main idea is to prepare the porphyrin with three equivalents of benzaldehyde instead of 4-methoxybenzaldehyde, our trails to separate the required product has failed. To obtain the pure mono substituted

TMS product, we introduced the methoxy group to help in tuning the solubilities of the formed porphyrins.



Scheme 4.4: Synthesis of porphyrin **P5**.

The neutral sandwich complex (**DD5a**) was prepared from equimolar amounts of Li_2Pc , $\text{Tb}(\text{acac})_3$, and the respective porphyrins (**P5**) as depicted in Scheme 4.5. The crude reaction mixture was subjected to column chromatography, and the neutral radical species were separated as a brown solid along with some other triple-decker complexes as side products.



Scheme 4.5: Synthesis of neutral double-decker complex **DD5a**.

Unfortunately, suitable single crystals of **DD5a** were not obtained to determine its structure and packing in the solid. Moreover, the complex was reduced to anionic species **DD5b** with tetrabutylammonium as counter cation following Scheme 4.3. However, the crystals obtained were of poor quality to determine the structure. So, the ESI mass spectra come into the picture as a simple tool for characterizing the complexes. Figure 4.23 A shows the ESI experimental mass spectrum and simulated mass spectrum for $[\text{M}]^-$ confirming the

double-decker complex **DD5a**. Moreover, absorption spectra in the UV-Vis-NIR region (Figure 4.23 B) helps to confirm the presence of π - radical in the neutral complex and differentiate it with the anionic complex. The reduced complexes **DD5b** was prepared by treating the neutral complex **DD5a** with hydrazine hydrate with TBABr in methanol, similar to that of Scheme 4.3.

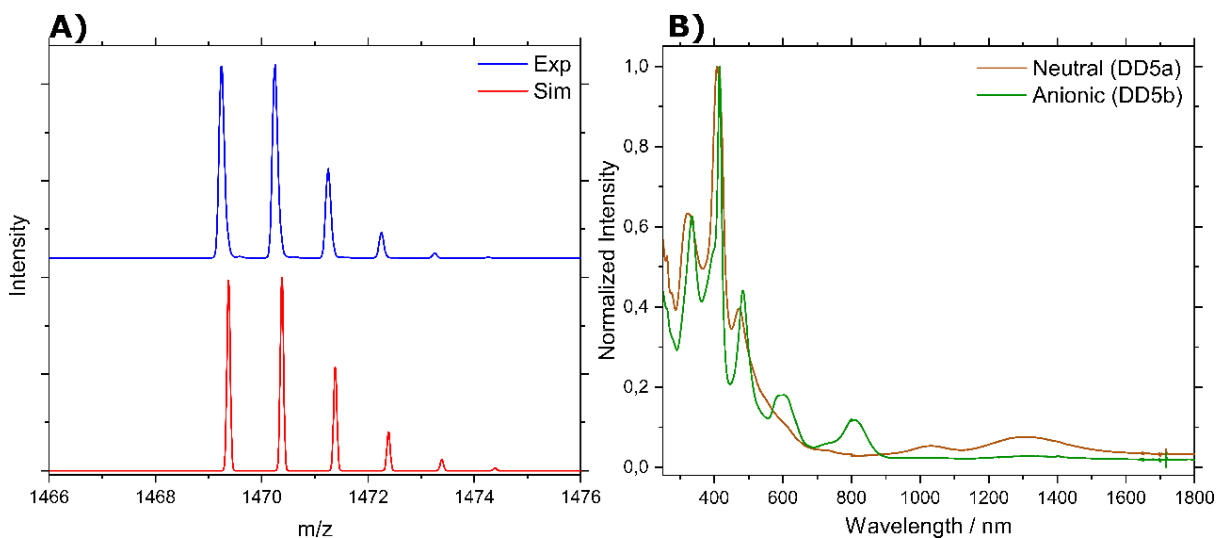


Figure 4.23: A) ESI-MS characterization of the neutral complex **DD5a** in negative mode (experimental data in blue, and simulated in red). B) UV-Vis-NIR absorption spectra of neutral and anionic forms of **DD5** in CDCl_3 .

Magnetic Measurements

DC magnetic susceptibility measurements were performed for both neutral and anionic sandwich complexes **DD5a** and **DD5b** under an applied field of 0.1 T. At RT, χT value of 10.6 to 10.8 $\text{cm}^3 \text{K mol}^{-1}$ were observed (Figure 4.24 A), which is as expected for single Tb^{3+} ions. The contribution of the radical centered on the organic ligand is negligible to the overall magnetic moment of the complex.

To estimate their magnetization relaxation behaviour at zero field, the ac susceptibility measurements were carried out in 5 Oe ac field with a frequency range of 1-1500 Hz. No frequency-dependent out-of-phase signals (χ'') for neutral complexes **DD5a** was observed, demonstrating that the complex does not act as SMM at zero field (Figure 4.24 B). For further characterization of the magnetic behaviour, an external field was applied in order to suppress the possibility of quantum tunneling of the magnetization process. However, even in the presence of an external field, the neutral complex **DD5a** didn't show any clear frequency-dependent character in both in-phase (χ') and out-of-phase (χ'') in the 1-1500 Hz region, demonstrating the poor SMM behaviour of the neutral complex **DD5a**. However in the case of the anionic complex (**DD5b**), similar to that of other anionic

complexes (**DD1b-DD4b**) mentioned in the previous task, this complex showed a clear maximum in zero field, suggesting SMM behaviour.

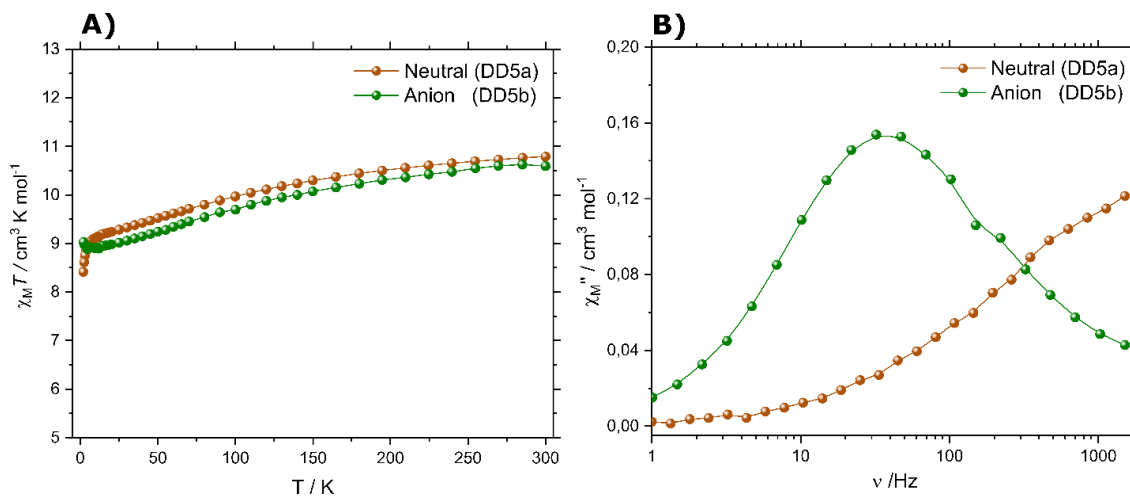


Figure 4.24: A) DC magnetic data for compounds **DD5a** and **DD5b** and B) frequency-dependent of the out-of-phase (χ'') AC susceptibility of **DD5a** and **DD5b** in zero field at 15 K.

For further characterization of the magnetic behaviour of the reduced Tb^{3+} complex **DD5b** at zero field, they showed frequency-dependent character in both in-phase and out-of-phase in 1-1500 Hz region over a temperature region of 2-30 K. This indicates the SMM nature of the anionic complex **DD5b** (Figure 4.25 A). The relaxation time (τ) was extracted for each temperature for every complex from Figure 4.25 A. Using that, the effective energy barrier for reversal of magnetic moment and pre-exponential factors were determined from Arrhenius plots (Figure 4.25 B) using equation 1.17 and 1.18 and found to have $U_{\text{eff}} = 94$ K.

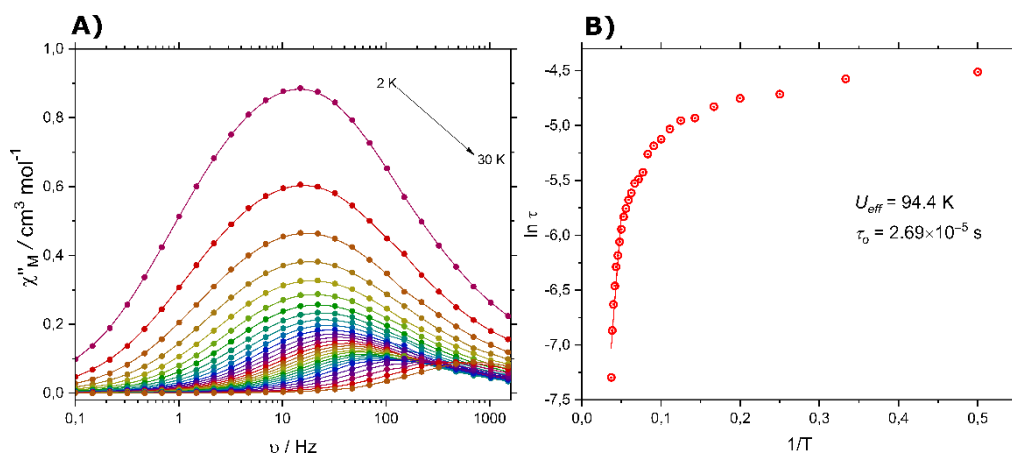


Figure 4.25: A) Out-of-phase ac susceptibilities for reduced sandwich complex **DD5b** at zero field, and B) $\ln(\tau)$ vs. $1/T$ plot for anionic double-decker complexes **DD5b**. The continuous line corresponds to the best fit for the Arrhenius equation to determine the activation energy (U_{eff}) and pre-exponential factor (τ_0).

As mentioned in the previous objective, on mononuclear double-decker complexes (**DD1-DD4**), the starting material (**DD5a** and **DD5b**) are similar to them in terms of structural, spectroscopic, and magnetic properties. The neutral complex (**DD5a**), which is not an SMM, turns into an SMM active complex at zero field upon simple reduction. Moreover, the dimeric complexes obtained upon coupling showed similar behaviour. The magnetic behaviour of the mono-nuclear complex (**DD5a**) and the di-nuclear complexes (**C1b-C3b**) are similar, but extracting a meaningful comparison is difficult due to the lack of crystal structures. Moreover, the periphery of both classes of complexes is different due to the difference in substitutions.

Electron paramagnetic resonance (EPR) studies to study the radical

It is well known that the lanthanide-based sandwich complexes usually exist in several forms; for example, bis(phthalocyaninato) Tb(III) complexes can be isolated as TbPc_2 , $[\text{TbPc}_2]^-$, or $[\text{TbH}(\text{Pc})_2]$.¹⁸⁸ The anionic form (Pc_2Ln) consists of trivalent lanthanide ion with two Pc ligands, each with a formal charge of -2, with a closed shell of π electronic system. But the neutral form Pc_2Ln has an open shell π electronic system i.e., an unpaired electron on the ligands. It was shown that this radical plays an important role, mainly in the case of SMM behaviour.¹⁸⁶ So there were many studies performed on these neutral sandwich complexes in order to locate the radical. Most of these studies include vibrational spectroscopy (IR and Raman),^{189,190} along with a few XRD¹⁹¹ and NMR studies.^{192,193} However, even though EPR is an excellent method for the characterization of radicals, there were only a few reports on the characterization of neutral sandwich complexes.^{194,195,196,197,198} Among them, most of them include homoleptic complexes,^{197,198} which again becomes quite difficult to localize. So, to differentiate the radicals, the present systems of hybrid sandwich complexes become the ideal examples for studying the EPR. Moreover, the EPR studies on the binuclear complexes help in studying the interaction between the radicals.

In general, EPR studies on lanthanide-based radical species are tricky due to their interaction between the paramagnetic lanthanide centers and with the radical in the organic ligand. Keeping this in mind, we began our EPR studies with the Yttrium analog of **DD5a** complex. The spectra collected for the powder sample of **Y-DD5a** at RT is shown in Figure 4.26. The complex **Y-DD5a** showed a sharp $g = 2.002$, which can be ascribed to $S=1/2$ radical delocalized over the ligands.

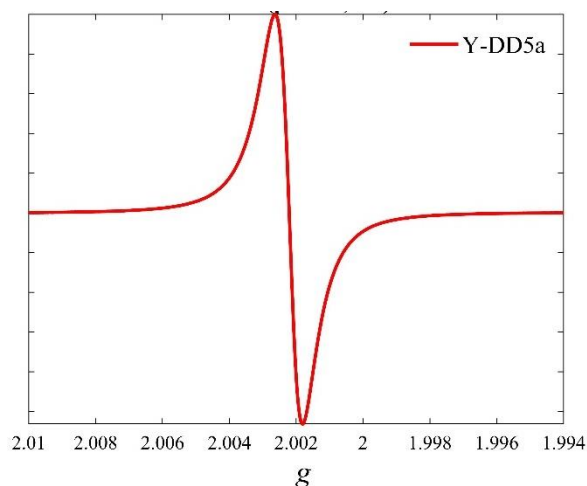


Figure 4.26: EPR spectra of Y analogs of **DD5a** (i.e., **Y- DD5a** complex in red).

The EPR spectra of **Y-DD5a** was obtained at various temperatures in the powder sample and frozen solution are shown in Figure 4.27. The linewidth increases (from 1.3 G at 300 K to 3.8 G at 4 K) gradually upon cooling which could be an indication of inter-cluster interaction between the radicals of the adjacent molecules.¹⁹⁹ Moreover, at very low temperatures (4 K), a small shoulder appears, which was also observed in literature²⁰⁰ of neutral Y^{3+} sandwich complex. On the other hand, Tb^{3+} complex shows even higher broadening on cooling.

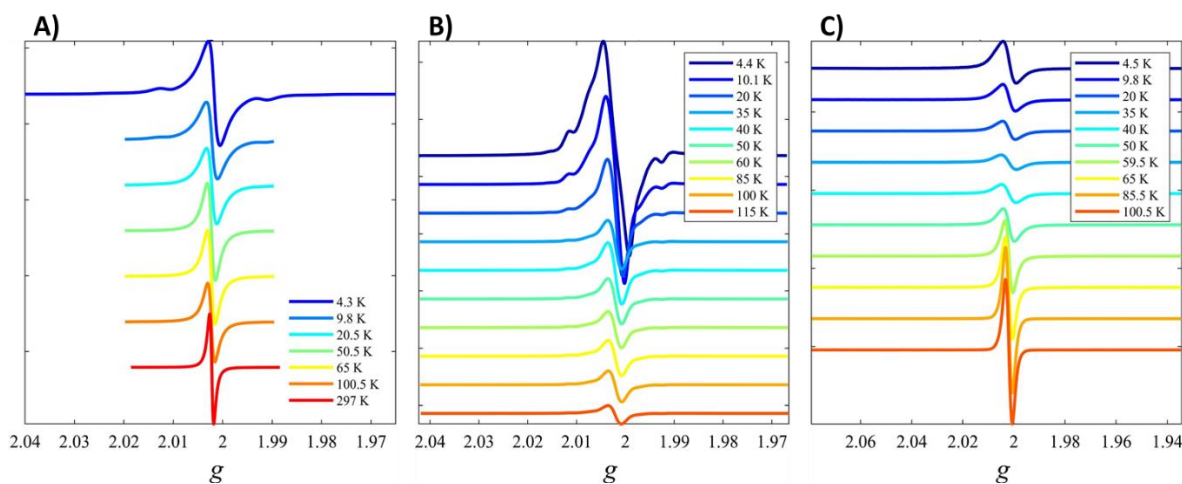


Figure 4.27: Temperature-dependent EPR spectra of A) **Y-DD5a** in solid state. B) **Y-DD5a** in frozen solution ($CD_2Cl_2:CDCl_3$ in 4:1 ratio) and C) **Tb-DD5a** in frozen solution state ($CD_2Cl_2:CDCl_3$ in 4:1 ratio).

EPR measurements on the Tb-monomer (**DD5a**) sample shows the presence of hyperfine features in it. However, due to the high intensity of the peak due to the central

radical, they are challenging to observe. So in order to improve the hyperfine signals, we measured for Tb- monomer complex (**DD5a**) at two different concentrations 5 mM and 28 mM. It is found to be the ratio of the central feature to the hyperfine feature is concentration-dependent. On changing from 5 mM to 28 mM solution, the approximate amplitudes of the resonances jump from ~10:1 to ~70:1, as seen in Figure 4.28.

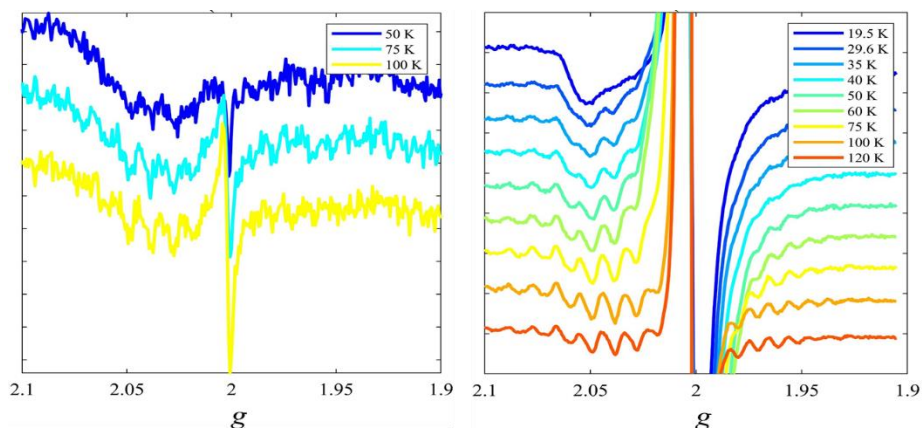


Figure 4.28: Concentration-dependent EPR spectra of Tb- **DD5a** ($c = 5$ mM (on left) and $c = 28$ mM (on right) in 4:1 $\text{CD}_2\text{Cl}_2:\text{CDCl}_3$).

The magnetic properties of the complex **DD5a** can be analyzed from the variation of the intensity of the EPR spectra with temperature. The intensity $I(T)$ obtained by double integration of the experimental EPR spectrum is directly proportional to the magnetic susceptibility χ . So the following figure shows the behaviour of χT vs T , which shows the antiferromagnetic interaction between Tb^{3+} ion and the radical. This anti-ferromagnetic interaction can be deduced from the following figure; as the temperature reduces, the $I \times T$ value reduces, which is an indication of anti-ferromagnetic interaction.

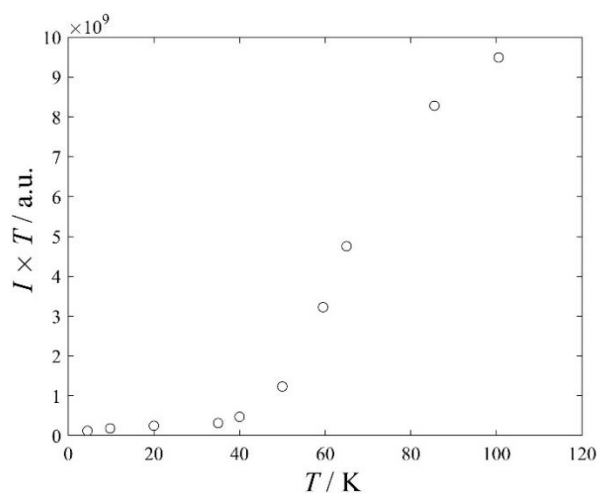


Figure 4.29: Plot of IT vs. T where I is the double integral of EPR signal proportional to magnetic susceptibility.

To obtain further clarity on the Yttrium complexes, the EPR spectra was extracted at different microwave powers and at different temperatures. At low temperatures (below ca. 35 K) we observed two clearly defined resonances at high powers, which seems to merge to single resonance at higher powers and or temperatures as can be observed from Figure 4.30.

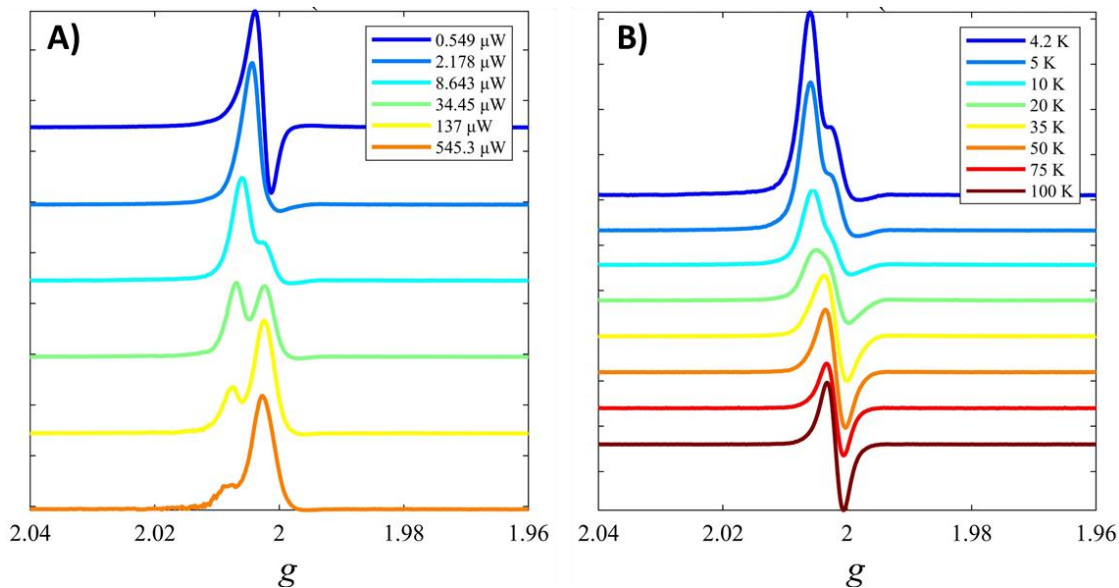


Figure 4.30: A) Power dependent EPR spectra of **Y-DD5a** at constant temperature of 4.2 K. and B) Temperature dependent EPR spectra of **Y-DD5a** at constant power $P = 8.64 \mu\text{W}$ and at concentration $c = 12.7 \text{ mM}$.

These observations might be explained by the presence of two species in solution, each with its saturation behavior. One hypothesis could be that these are $\text{por}^*\text{-Tb-pc}$ and por-Tb-pc^* , with the radical on either of the two ligands. We could further assume that this radical is (i) fixed on either of the two tetrapyrrole rings at lower temperatures, and (ii) the jumping back and forth between the rings could become faster at higher temperatures so that they resonate as one, as observed at 100 K.

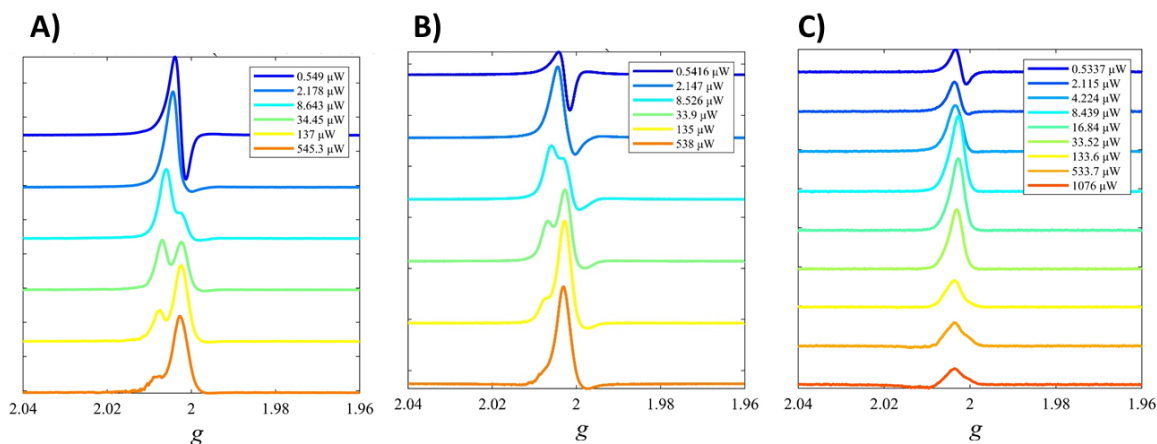
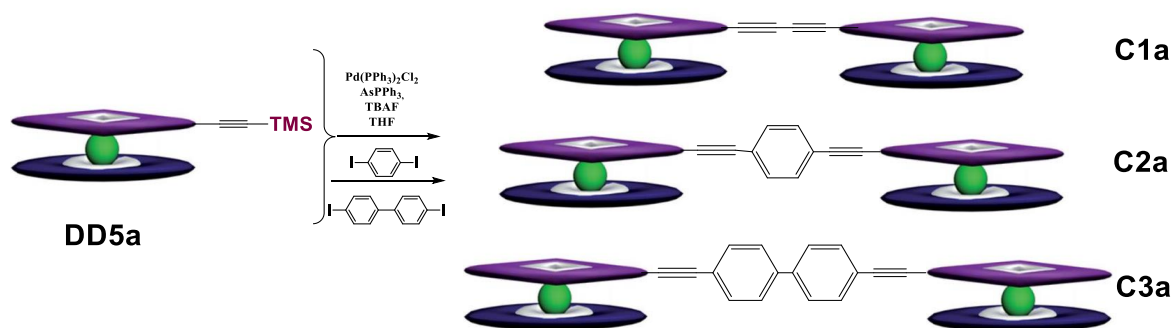


Figure 4.31: Power-dependent EPR spectra of monomeric complex **Y-DD5a** at 4.2 K at various concentrations of A) 12.7 mM, B) 1.0 mM and C) 0.1 mM.

To reduce the effects of aggregation, the spectra was recorded for diluted samples at 1.0 mM and 0.1 mM concentrations. The following Figure 4.31 shows the power-dependent EPR spectra of monomeric sample **Y-DD5a** at various concentrations. The spectra at 12.7 mM and 1.0 mM concentrations show the presence of two peaks but at the lower concentration shows only a single peak. So, the concentration dependence of the spectra has complicated the results, but this could be possibly explained by aggregation effects at higher concentrations, where the complexes dimerize. These have the possibilities: a) por-Y-pc...por-Y-pc, b) por-Y-pc...pc-Y-por, and c) pc-Y-por...por-Y-pc. The radical may presumably be on the external ligand in each case, leading to two distinct signals. Whereas at lower concentrations, there could be no aggregation, hence we observe only the average signal from the delocalized radical. But to confirm this, we would need experiments and simulations furthermore to be performed.

Synthesis and characterization of di-nuclear double-decker complexes

The neutral forms of the couple dimeric sandwich complexes (**C1a-C3a**) were synthesized using homocoupling and Sonogashira coupling from the mono-nuclear complex **DD5a**, as depicted in Scheme 4.6. In order to obtain the dimeric complex **C1a**, the homo-coupling mechanism was involved in the presence of Pd(PPh₃)₂Cl, AsPPh₃ in the presence of atmospheric oxygen. The oxygen favors the mechanism of the homo-coupling reaction. Whereas in the case of synthesis of complexes **C2a** and **C3a**, the mono-nuclear complex **DD5a** was involved in hetero-coupling with a linker, but with inert conditions for Sonogashira reaction.



Scheme 4.6: Synthesis of coupled di-nuclear sandwich complexes **C1a-C3a**.

Due to the presence of TBAF in the reaction mixture, the crude product was obtained as an anionic complex. So, the crude product extracted was oxidized by sodium-periodate (NaIO_4) and was subjected to column chromatography to obtain the pure neutral form of product in yields of 19-24%. The reduced complexes **C1b-C3b** were prepared by treating the neutral complex **C1a-C3a** with hydrazine hydrate with TBABr in methanol, similar to that of Scheme 4.3.

Mass spectrometric analysis

Due to difficulties in analyzing the NMR spectra of the lanthanide complexes, mass spectrometry plays a key role in detecting these coupled complexes during the purification process. The obtained complexes were subjected to ESI-MS analysis in positive mode, which showed peaks corresponding to the $[\text{M}]^{2+}$ cation. It can be observed in Figure 4.32 that the isotopic pattern is in good agreement with the simulated pattern.

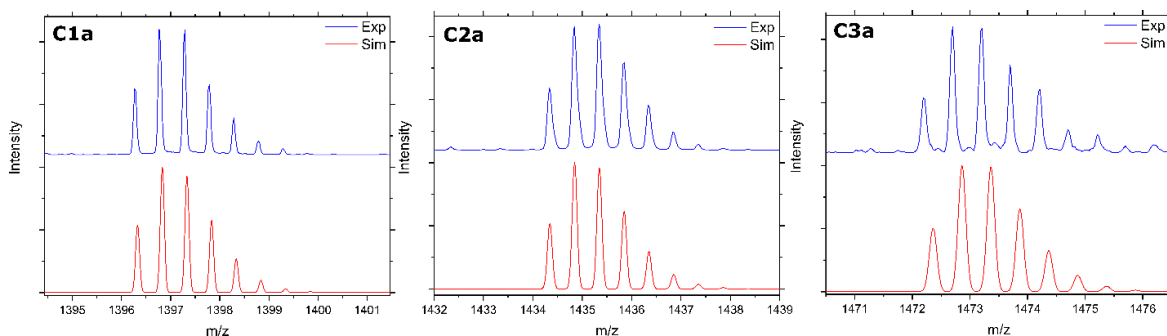


Figure 4.32: ESI-MS of neutral dimeric complexes **C1a-C3a** in positive mode.

In addition, the MALDI-TOF mass spectra of complexes **C1a-C3a** showed an isotopic cluster due to the formation of the cation $[\text{M}^+]$. Moreover, due to the high energy of the laser applied, the molecules undergo fragmentation and fly by losing the methyl group present on the porphyrin ring. Thus several peaks with a difference of *ca.* 15 m/z can be

observed in the MALDI spectra, which corresponds to the successive fragmentation of methyl groups (Figure 4.33).

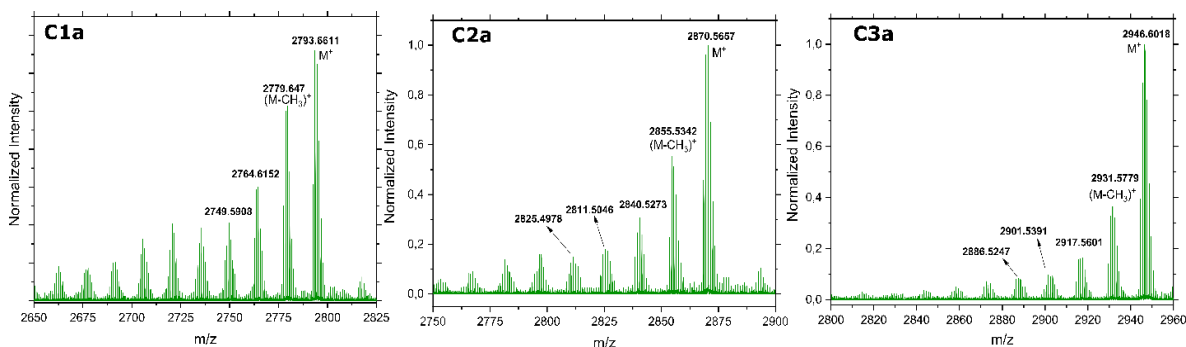


Figure 4.33: MALDI-TOF spectra for neutral dimeric complexes **C1a-C3a** in positive mode.

NMR Analysis

In order to confirm the structure from spectroscopic methods, NMR is one of the best options available. However, due to the presence of radical and paramagnetic contribution from Tb(III) ions, it becomes challenging to analyze the peaks. So, we prepared the yttrium(III) analogs of the neutral dimeric complexes as **Y-C1 to Y-C3**. $^1\text{H-NMR}$ was measured on each sample in 1:1 CDCl_3 : DMSO-d_6 solution in the presence of 10% (by volume) hydrazine hydrate to quench the radical effect. Figure 4.34 shows a clear difference in the spectra in the $\delta=7.75\text{-}8.00$ ppm region (shaded region), which corresponds to the protons on the linker groups (benzene rings). This confirms the coupling of the monomeric complex with the respective linkers.

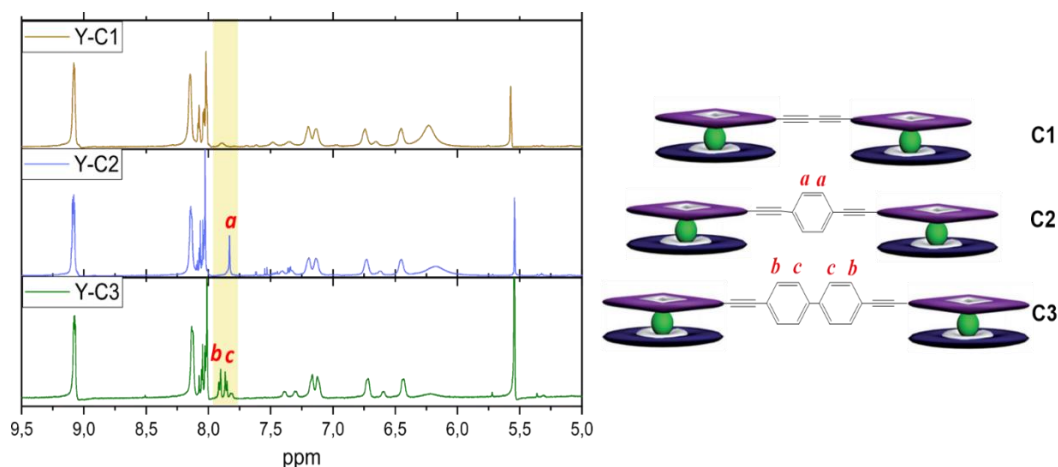


Figure 4.34: $^1\text{H-NMR}$ spectra of Yttrium analogs of dimeric complexes in CDCl_3 : DMSO-d_6 (1:1) in the presence of *ca.* 10% (by volume) hydrazine. The yellow stripe highlights the presence of proton peaks from the linker in the dimers **Y-C2** and **Y-C3** and its absence in dimer **Y-C1**.

UV Studies

Similar to the monomeric double-deckers complexes, these dimeric complexes of Tb (**C1a-C3a**) of Pc and porphyrins show intense characteristic peaks in electronic absorption spectra. The UV-Vis-NIR spectroscopic studies for the present series of neutral complexes (**C1a-C3a**) were recorded in CHCl_3 as shown in Figure 4.35 A. The absorption spectra are similar to that of the monomeric complexes **DD5a**, showing Soret bands with predominant Pc and porphyrin character. Along with that, Figure 4.35 A shows electronic transitions of BV, RV, and IV, involving the π -radical in SOMO.

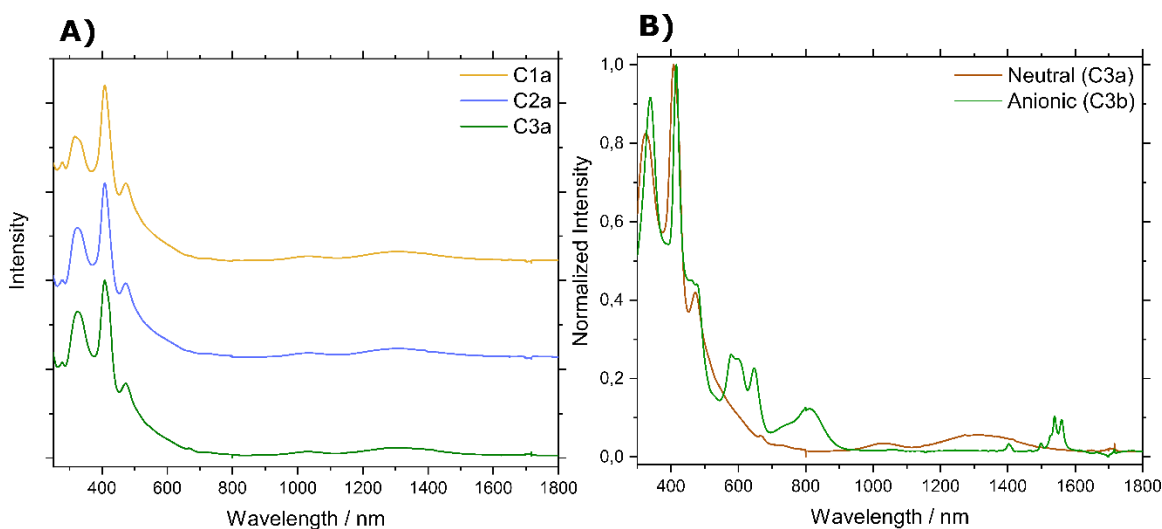


Figure 4.35: A) UV-Vis-NIR absorption spectra of **C1a-C3a** in CHCl_3 , and B) UV-Vis-NIR absorption spectra of neutral and anionic forms of **C3** in CDCl_3 .

Similar to other lanthanide-based sandwich complexes, **C1a-C3a** show distinctive features in absorption spectra on oxidation or reduction. Therefore, the neutral radical dimeric complex **C3a** was in-situ reduced to anionic form by the addition of 1% (by volume) hydrazine hydrate, which resulted in an immediate change in colour from brown to green. As a consequence, the spectra (Figure 4.35 B) shows several changes in peaks, such as the disappearance of bands between 1000 – 1800 nm, which is due to the addition of an electron into SOMO, and it turns into HOMO.

Unfortunately, suitable single crystals of **C1a-C3a** were not obtained to determine their structure and packing in the solid. Moreover, the neutral complexes were reduced to anionic species **C1b-C3b** with tetrabutylammonium as counter cation following Scheme 4.3. However, the crystals obtained after several trials were of poor quality to determine the structure. Instead, structure optimizations were performed to determine the model of the neutral complexes. The distances between the lanthanide centers are found to be 21.38 Å in **C1a**, 25.70 Å in **C2a** and 29.32 Å in complex **C3a**.

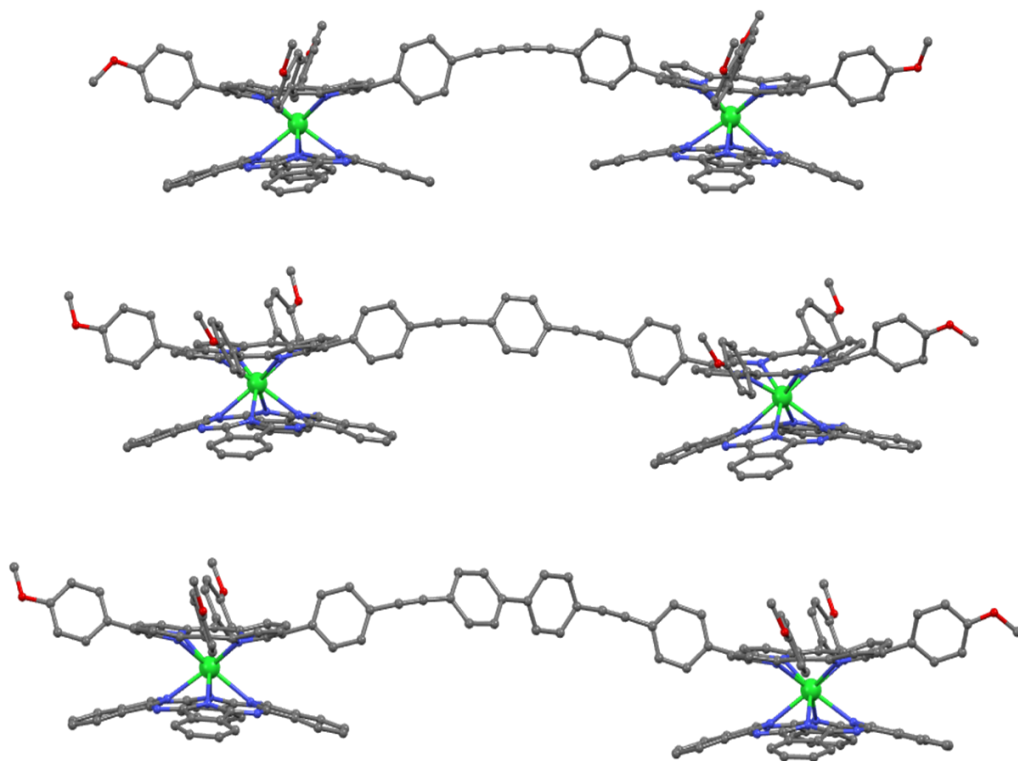


Figure 4.36: Proposed models for neutral dimeric complexes **C1a-C3a**, respectively obtained by structural optimization. Hydrogen atoms are omitted for clarity [Tb(III)-green, C-grey, N-blue, and O-red].

Magnetic Measurements

DC magnetic susceptibility measurements were performed for three anionic sandwich complexes **C1b-C3b** under an applied field of 0.1 T. At RT, χT value of 20.1 to 20.3 cm³ K mol⁻¹ were observed, which is in agreement to the expected value for two Tb³⁺ ions (Figure 4.37 A).

To estimate their magnetization relaxation behaviour at zero field, the ac susceptibility measurements were carried out using 5 Oe ac field in a frequency range of 1-1500 Hz. No frequency-dependent out-of-phase signals (χ'') for neutral complexes **C1a-C3a** was observed, demonstrating that the complex does not act as SMMs at zero field. However, in the case of the anionic complexes (**C1b-C3b**), similar to that of mononuclear anionic complex (**DD5b**) mentioned before, we observed a clear maximum in zero field exhibiting the SMM behaviour (Figure 4.37 B).

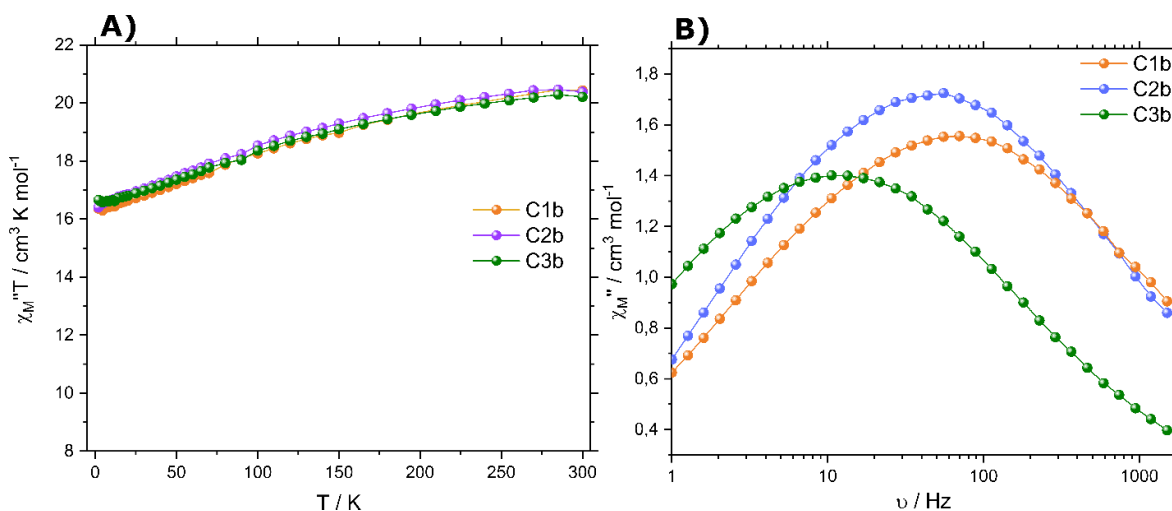


Figure 4.37: A) DC magnetic data for compounds **C1b** – **C3b** and B) frequency-dependent of the out-of-phase (χ'') AC susceptibility of **C1b**, **C2b** and **C3b** in zero field at 2 K.

For further characterization of the magnetic behaviour of the reduced dimeric Tb^{3+} complexes **C1b-C3b** at zero field, they showed frequency-dependent character in both in-phase and out-of-phase in 1-1500 Hz region over a temperature region of 2-30 K. This indicates SMM nature of the anionic dimer complexes **C1b-C3b** (Figure 4.38). The relaxation time (τ) was extracted for each temperature for every complex from Figure 4.38. The effective energy barrier for reversal of magnetic moment and pre-exponential factors were determined from Arrhenius plots (Figure 4.38) using equation 1.17 and 1.18 and found to have effective energy barriers of 77 K, 85 K and 122 K for **C1b**, **C2b**, and **C3b**, respectively.

On the other hand, the anionic dinuclear complexes (**C1b-C3b**) showed the trend in their magnetic behaviour. As the distance between the terbium centers increases, Figure 4.38 shows an increase in the effective energy barrier. Moreover, at 2 K and in zero field, Figure 4.37-B shows that these three anionic dimers showed a clear maximum in their out-of-phase (χ'') susceptibility measurements. The complex with the largest distance between the Tb centers resonates at a lower frequency, suggesting better SMM properties. This increase in intramolecular distance improves magnetic isolation and thus improves the magnetic behaviour.

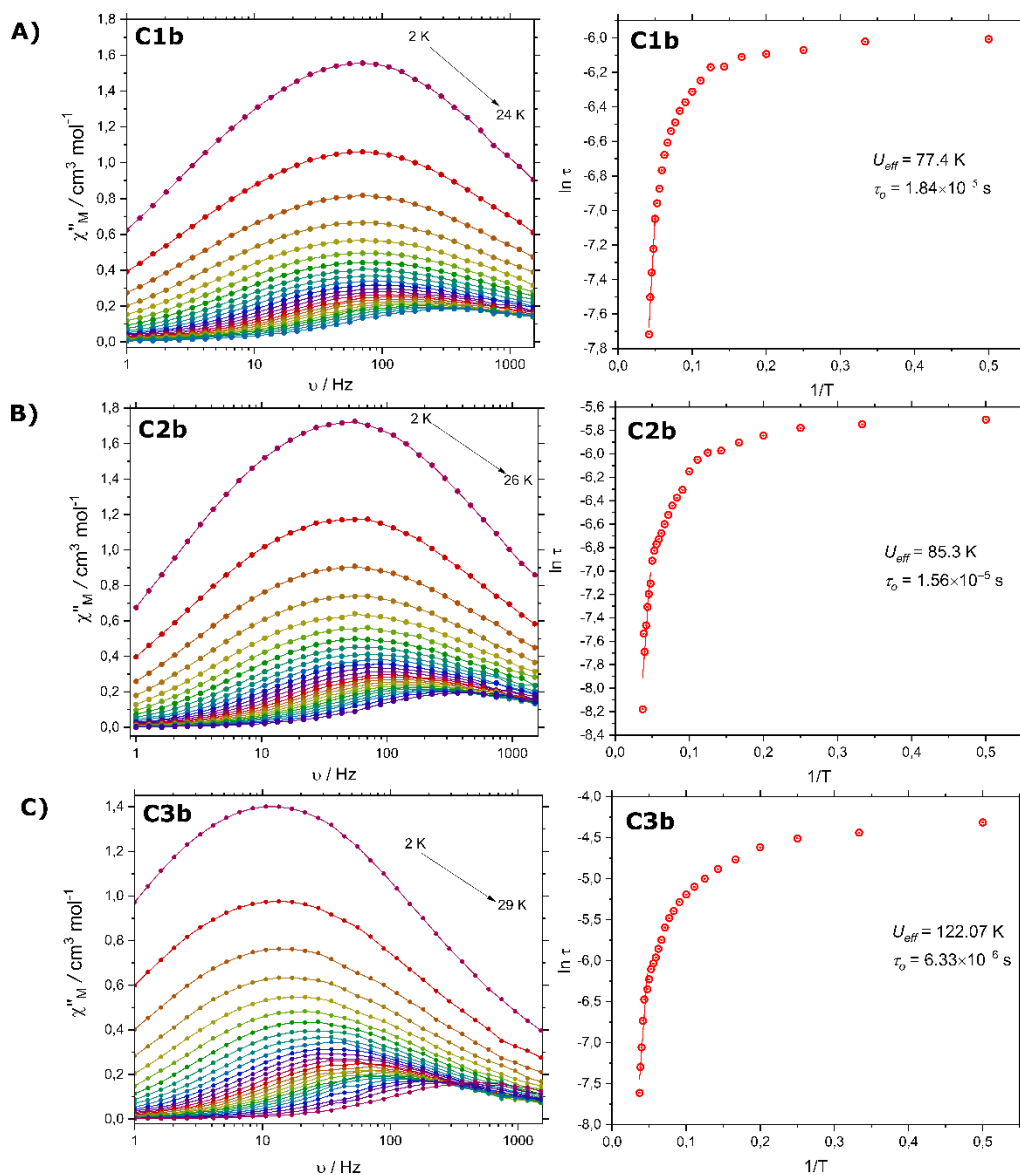
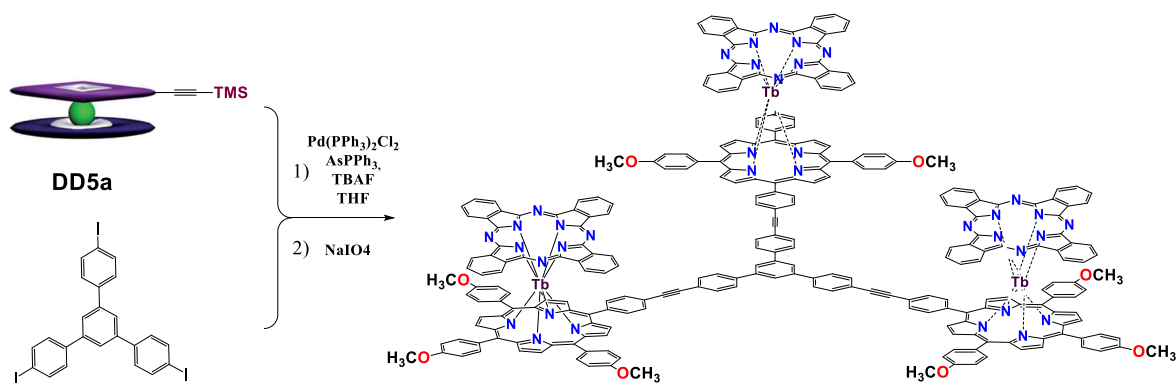


Figure 4.38: Out-of-phase ac susceptibilities plots at zero field (on left), and $\ln(\tau)$ vs. $1/T$ plot (on right) for anionic dimeric complexes A) **C1b**, B) **C2b**, and C) **C3b**.

Synthesis and characterization of tri-nuclear double-decker complexes

The neutral complex **DD5a** was used as a starting material to synthesize trinuclear complex **C4** using the Sonogashira coupling reaction as depicted in Scheme 4.7, with a yield of 2%.



Scheme 4.7: Synthesis of coupled tri-nuclear sandwich complex **C4**.

Mass spectrometry was used to detect the product. The ESI-MS analysis of the product showed that the complex was detected as $[M]^{3+}$ cation in positive mode. It can be observed in Figure 4.39 A that the isotopic pattern is in good agreement with the simulated one.

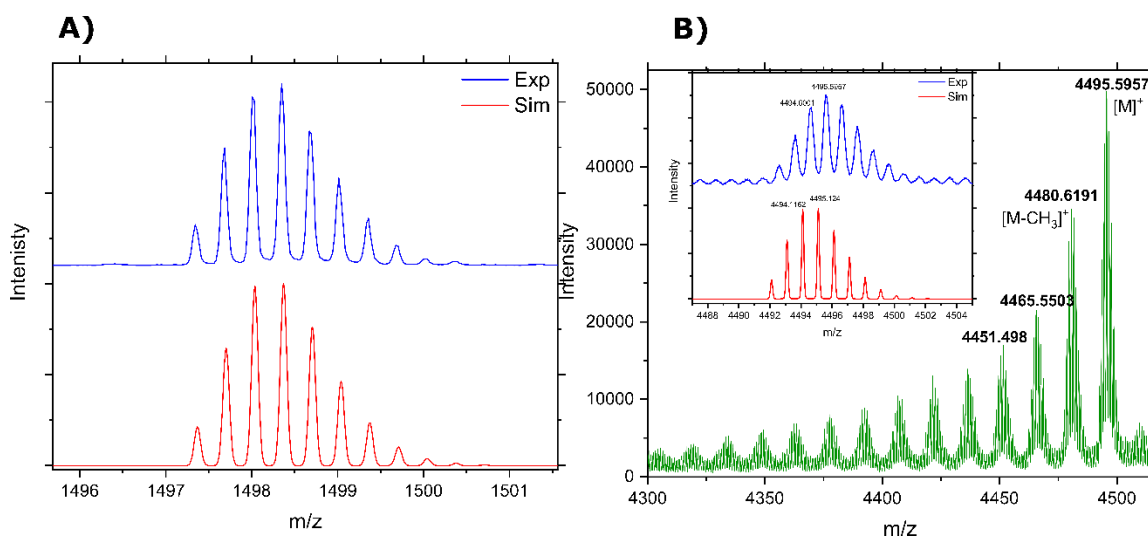


Figure 4.39: A) ESI-MS analysis and B) MALDI-TOF analysis for neutral trimeric complexes **C4** in positive modes.

In addition, the MALDI-TOF mass spectra of complexes **C4** showed an isotopic cluster due to the formation of the radical cation $[M]^+$. Moreover, due to the high energy of the laser applied, the molecules undergo fragmentation and travel by losing the methyl group present on the porphyrin ring. Thus several peaks with a difference of *ca.* 15 m/z can be observed in the MALDI spectra, which corresponds to the successive fragmentation of methyl groups (Figure 4.39 A). Unfortunately, due to significantly lower yields (< 2%) of the complex **C4**, we were unable to perform further studies.

Electron paramagnetic resonance (EPR) studies

Figure 4.40 shows the EPR spectra of Tb^{3+} complex **C3** (blue line) measured at RT. It showed a peak at $g=2.002$ similar to that of mononuclear **Y-DD5a** but with a lower intensity. This EPR signal shows the typical signal for an $S=1/2$ radical species. The lower intensity is could be due to interaction between the radical and the paramagnetic Tb ion.

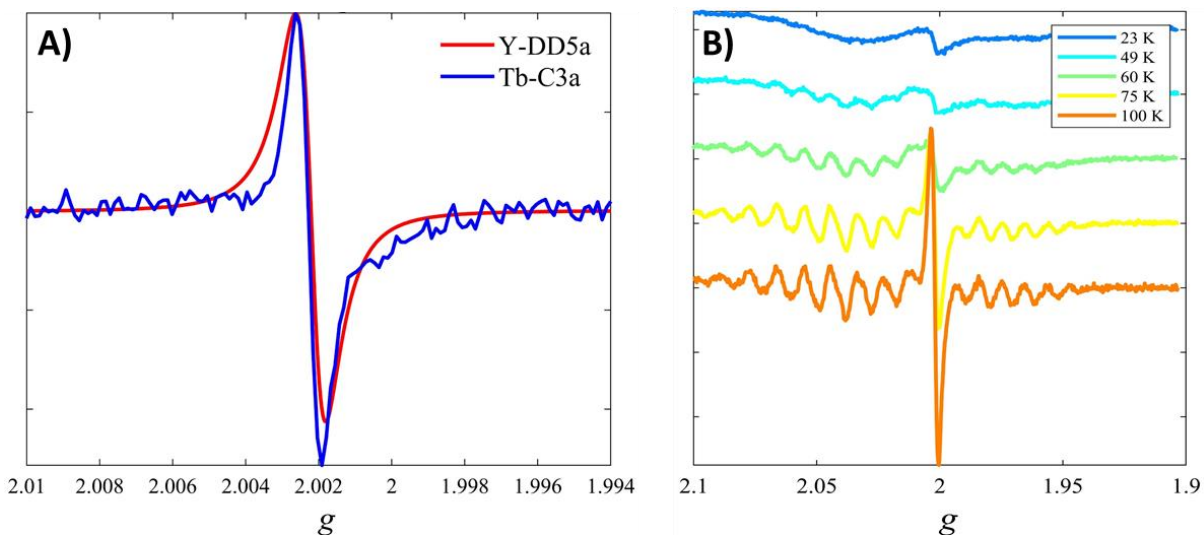


Figure 4.40: A) EPR spectra of Y analog of **DD5a** (i.e., **Y-DD5a** complex in red) and **Tb-C3a** (in blue) and B) the EPR spectra of dimeric complex **Tb-C3a** dissolved in 4:1 $\text{CDCl}_2:\text{CDCl}_3$ (with $c=12$ mM and as frozen sample).

To study the radical behaviour in the dimeric complexes, EPR spectra was recorded for the complex **C3a** at 12 mM. The figure shows nicely resolved hyperfine at 100 K, and they disappear gradually upon cooling (Figure 4.40 B). To further understand coupling or interaction between the radicals in the binuclear complexes, Yttrium analogs should be studied first to study their interaction.

4.3 Conclusion

In conclusion, we have performed a precise structural characterization and systematic analysis of the SMM behavior of a series of heteroleptic, peripherally functionalized terbium(III) (phthalocyaninato)(porphyrinato) complexes with different oxidation states and substitution pattern. Single crystal X-ray diffraction analysis shows a similar coordination geometry for the central Terbium ion, which is sandwiched between the two tetrapyrrole ligands. The electronic absorption spectroscopic and electrochemical studies showed slight differences in the electronic structure which is due to different substituents, varying from electron-withdrawing groups to electron-donating groups, at the *meso*-attached phenyl moieties of the porphyrin ring. The comparative investigation on their magnetic properties shows the SMM and non-SMM nature of the anionic and radical species, respectively, showing the negative impact of the f-radical on the SMM behaviour. Moreover, the influence of the type of substituent on the *meso*-attached phenyl ring on porphyrin on the SMM properties were studied.

Also, we performed the synthesis of dinuclear and trinuclear Tb(III) based sandwich complexes by employing a Sonogashira and Glaser coupling reactions through porphyrin rings by varying the linkers. Even though we failed to obtain the crystal structures of the polynuclear complexes, and these complexes were confirmed using NMR and mass spectrometry. The anionic dinuclear complexes showed SMM behaviour at zero field and showed improved energy barriers for longer linkers. This ability to tune the SMM properties by coupling using various linkers or using various substituents could open new possibilities for the application of SMMs in molecular devices. Moreover, these functionalized double-decker complexes showed higher solubilities than that of bis(phthalocyanine) lanthanide complexes in common organic solvents, which could help in fabrication for device making.

The preliminary results on the mixed porphyrin and phthalocyanine complexes have proved the delocalization of radical at different tetrapyrrole rings. However, we need to perform several other studies to confirm the study and to understand the delocalization of the radical and its behaviour in the polynuclear complexes.

Chapter 5

Experimental Section

5.1 Materials and Equipment

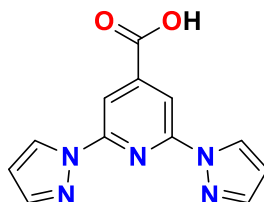
All the commercially available chemicals were used as received without further purification. Thin-layer chromatography (TLC) was performed on aluminum plates precoated with Merck 5735 silica gel 60 F₂₅₄. Column chromatography was performed with Merck silica gel 60 (230-400 mesh). ¹H-NMR and ¹³C-NMR spectra were recorded on a Bruker Ultrashield plus 500 spectrometer employing deuterated solvents. Electrospray ionization mass spectrometry (ESI-MS) data were acquired with a Bruker micrOTOF-Q II spectrometer. Matrix-assisted laser desorption/ionization time-of-flight (MALDI-ToF) mass data were acquired from Voyager-DE PRO Bio spectrometry work station with 2,5-dihydroxybenzoic acid (DHBA) as a matrix. Gas-chromatography mass spectrometry (GCMS) data was acquired from Thermo Scientific Trace 1300 Gas Chromatography equipped with single quadrupole MS. Infrared (IR) spectra were recorded with a MAGNA FTIR, Nicolet spectrometer in the region of 4000-400 cm⁻¹. The samples for IR were prepared by grinding the compounds with dry potassium bromide (KBr), and the mixture was made into pellets for measurements. UV-Visible spectra were recorded on a Cary 500 Scan UV-Vis-NIR Spectrophotometer.

For spin-crossover samples, the standard DC magnetic measurements were performed on an MPMS-XL7 and MPMS-XL5 magnetometers (Quantum Design). For standard magnetic experiments, the temperature-dependent magnetization was recorded at B_{DC} = 0.1 T as an external magnetic field. The general temperature sweeping rate of 3 K min⁻¹ was employed for cooling and heating modes. Gelatin capsules were used as sample holders in the general temperature range (2- 400 K). The very small diamagnetic contribution of the gelatin capsule was negligible to the overall magnetization, which was dominated by the sample. The diamagnetic corrections of the molar magnetic susceptibilities were applied using Pascal's constants.²⁰¹ Alternating-current (AC) measurements were performed with an oscillating magnetic field of 5 Oe at frequencies ranging from 0.1 to 1512 Hz. For AC measurements, the samples were embedded in solid eicosane to prevent the torque.

5.2 Iron(II) bis(pyrazoly)pyridine (*bpp*) based molecules – From surface to bulk

5.2.1 Preparation of ligands and complexes

Synthesis of *bpp*-COOH (**L1**)



Compound **L1** was prepared according to the reported literature²⁰². Freshly distilled DMF (200 mL) was taken in a three-necked round-bottomed flask and was degassed with argon for 1 hour. Pyrazole (5.5 g, 80 mmol, 3 eq) was added and dissolved by stirring at RT. NaH (60 wt% in mineral oil, 6.5 g, 163 mmol, 6 eq) was added in 3 portions (Caution: evolution of H₂ !), which resulted in the formation of a white turbid solution and was stirred for 1 h at 100 °C. 2,6-dichloroisonicotinic acid (5 g, 26 mmol, 1 eq) was added in one portion and was stirred at 130 °C for five days under the Ar atmosphere. The solvent was removed under reduced pressure, and distilled water (100 mL) was added. The mixture was acidified by the addition of conc. HCl. The formed precipitate was filtered and dried in the oven.

Yield: 3.98 g (68.3%)

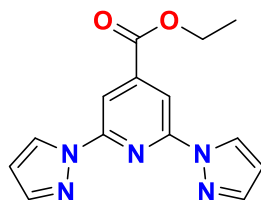
ESI-MS, found (calcd): 254.0695 [M-H]⁻, (254.0673); 210.0805 [M-COOH]⁻, (210.0774).

IR (KBr, cm⁻¹): 3148, 2924, 2854, 2563, 1727, 1619, 1575, 1526, 1471, 1465, 1446, 1402, 1307, 1233, 1211, 1141, 1104, 1045, 990, 972, 946, 900, 858, 786, 766, 746, 683, 646, 604, 504.

¹H NMR (500 MHz, Acetone-d₆) δ/ppm: 8.90 (d, 2H), 8.39 (s, 2H), 7.86 (d, 2H), 6.63 (dd, 2H).

¹³C NMR (126 MHz, Acetone-d₆) δ/ppm: 164.5, 151.06, 144.24, 142.83, 127.67, 108.62, 108.46.

Synthesis of *bpp*-COOC₂H₅ (**L2**)



Compound **L2** was prepared according to the reported literature.²⁰² **L1** (3.98 g, 17.7 mmol)

was taken in ethanol (150 mL) in a round-bottomed flask. Conc. H₂SO₄ (20 mL) was added, and the solution was stirred for 6 h at 85 °C. The solvent was removed under reduced pressure, and distilled water (150 mL) was added. pH was adjusted to 8 by adding aq. Na₂CO₃. The product was extracted using DCM from water, and the organic layers were collected, dried with Na₂SO₄, and the solvent was evaporated to give a precipitate which was dried on the vacuum.

Yield: 4.79 g (95.5%)

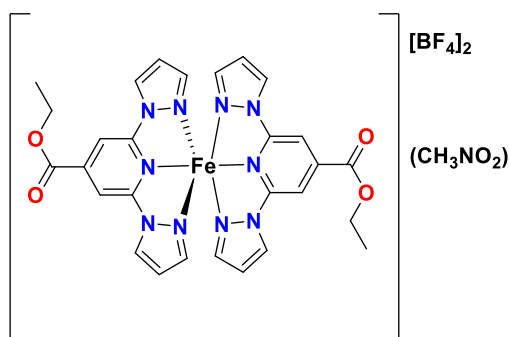
GC-MS, found (calcd): 283.10 [M]⁺, (283.10).

IR (KBr, cm⁻¹): 3427, 3139, 3113, 2980, 2923, 1768, 1722, 1616, 1574, 1523, 1461, 1445, 1398, 1371, 1305, 1285, 1242, 1207, 1143, 1094, 1054, 1020, 949, 917, 887, 787, 771, 730, 648, 608, 490, 420.

¹H NMR (500 MHz, CDCl₃) δ/ppm: 8.60 (d, 2H), 8.42 (s, 2H), 7.83 (d, 2H), 6.55 (dd, 2H), 4.49 (q, 2H), 1.47 (t, 3H).

¹³C NMR (126 MHz, CDCl₃) δ/ppm: 164.03, 150.82, 143.66, 142.84, 127.26, 109.22, 198.44, 62.21, 14.28.

Synthesis of [Fe(*bpp*-COOC₂H₅)₂][BF₄]₂·(CH₃NO₂) = (C1):



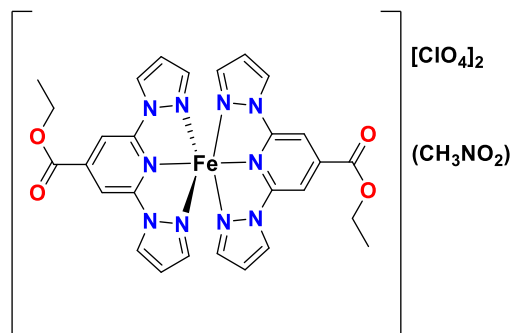
Ligand **L2** (160 mg, 0.565 mmol, 2 eq) was suspended in nitromethane (10 mL). A solution of Fe(BF₄)₂·6H₂O (96 mg, 0.283 mmol, 1 eq) in nitromethane (8 mL) was added drop-wise to the above solution, and the red color solution was formed on addition. The resulting mixture was stirred under argon for 2 h. Solvents were evaporated under reduced pressure. The mixture was dissolved in a minimum amount of nitromethane, and DEE was slowly diffused to obtain a crystalline dark red color complex.

Yield: 62 mg (30.8%)

ESI-MS, found (calcd): 709.1517 [M-BF₄]⁺, (709.1600); 657.1243 [M-2BF₄+Cl]⁺, (657.1172).

IR (KBr, cm⁻¹): 3121, 2985, 1726, 1630, 1573, 1546, 1525, 1498, 1471, 1407, 1378, 1340, 1287, 1253, 1137, 1029, 970, 911, 792, 764, 654, 600, 521.

Elemental Analysis for FeC₂₈H₂₆N₁₀B₂F₈·CH₃NO₂, found (calcd): C: 40.06 (40.64); H: 3.36 (3.41); N: 17.59 (17.98).

Complex [Fe(*bpp*-COOC₂H₅)₂][ClO₄]₂·(CH₃NO₂) = (C2):

Ligand **L2** (160 mg, 0.565 mmol, 2 eq) was suspended in dry nitromethane (10 mL). A solution of Fe(ClO₄)₂·xH₂O (36 mg, 0.282 mmol, 1 eq) in nitromethane (8 mL) was added drop-wise to the above solution, and the red color solution was formed on addition (Caution!: Iron(II) perchlorate is potentially explosive and should be handled with care). The resulting mixture was stirred under argon for 2 h. Solvents were evaporated under reduced pressure. The mixture was dissolved in a minimum amount of nitromethane, and DEE was slowly diffused to obtain a crystalline dark red color complex.

Yield: 80 mg (32.3%)

ESI-MS, found (calcd): 721.1083 [M-ClO₄]⁺, (721.0974).

IR (KBr, cm⁻¹): 3116, 2984, 1729, 1630, 1572, 1546, 1524, 1499, 1459, 1405, 1377, 1338, 1287, 1252, 1137, 1085, 1049, 970, 911, 862, 791, 763, 621, 599.

Elemental Analysis for FeC₂₈H₂₆N₁₀Cl₂O₈·CH₃NO₂, found (calcd): C: 39.16 (39.48); H: 3.03 (3.31); N: 17.17 (17.46).

Elemental Analysis for FeC₂₈H₂₆N₁₀Cl₂O₈·CH₃NO₂ (after SQUID measurements), found (calcd): C: 39.26 (39.48); H: 3.09 (3.31); N: 16.97 (17.46).

5.2.2 Preparation of substrates, samples; STM and XPS studies

The Ag(111) crystal is cleaned by multiple cycles of Ar⁺ sputtering (1 kV, 8 μA sample current, 20 min at SLS; 1 kV, 30 μA sample current, 5 min at TUM) and subsequent annealing (710 K, 5 min). The molecules were out-gassed in vacuum and then evaporated from a quartz crucible at 170°C. Fe was evaporated from a home-built metal-evaporator with Fe wrapped around a tungsten wire, which is heated up by an applied current. The sample was kept at 300 K during evaporation.

An Omicron LT-STM with tungsten etched tips was used running in constant current mode cooled with liquid Helium to 4 K. The tunneling bias was applied to the sample, the base pressure was ≈1.0 × 10⁻¹⁰ mbar.

For the measurements at 300 K images were taken by an Aarhus-STM with tungsten etched tips. The tunneling bias was applied to the sample and the base pressure was $\approx 2.0 \times 10^{-10}$ mbar.

Spectra were recorded with a Scienta EW4000 hemispherical electron analyzer at 300 K. We have used as excitation energies 400 eV for C 1s spectra, 500 eV for N 1s spectra and 640 eV for O 1s spectra. Measurements were performed in normal emission mode and binding energy scales were calibrated by the Ag3d_{5/2} line at 368.27 eV for N 1s and O 1s spectra and by the Fermi edge for C 1s spectra.

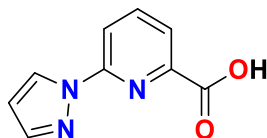
5.2.3 DSC and TGA experiments

DSC measurements were performed with a TA Instruments DSCQ 1000 instrument operated at a scan rate of 2 K/min on heating and on cooling. TGA measurements were performed with a TA Instruments Q50 instrument scanning at rate of 5 K/min.

5.3 Chiral resolution of SCO active Iron(II) Grid complexes

5.3.1 Preparation of ligands for Grid complexes

Synthesis of 6-(pyrazol-1-yl)picolinic acid (A)



Pyrazole (6.2 g, 91.1 mmol, 2.1 eq) was dissolved in 1,4-dioxane (200 mL) in a 500 mL three-necked round-bottomed flask. The mixture was bubbled with argon for 30 min. Later potassium tertiary butoxide (10.7 g, 95.4 mmol, 2.2 eq) was added and stirred at room temperature under argon for 30 min. Later Ethyl 6-bromopyridine-2-carboxylate (10.0 g, 43.5 mmol, 1 eq) was added, and the mixture was stirred for 48 hours at 115 °C under Argon atmosphere. The reaction was stopped and cooled to room temperature. The solvent was evaporated under reduced pressure. The crude product was suspended and refluxed for 3 hours in EtOH (100 mL) and NaOH solution (2M, 50 mL). Ethanol was removed under reduced pressure, and 50 mL water was added to the mixture. The pH was adjusted to 3 with aq. HCl, which resulted in precipitation. The colorless precipitate was collected by filtration and dried at 80 °C in an oven.

Yield: 5.59 g (68.7%)

ESI-MS, found (calcd): 188.0472 [M-H]⁻, (188.0455); 144.0601 [M-COOH]⁻, (144.0556).

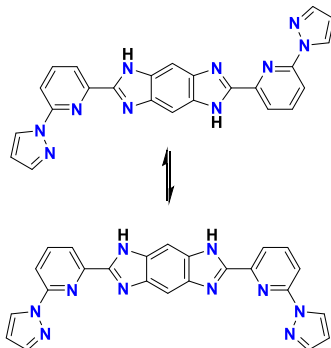
IR (KBr, cm⁻¹): 3435, 3068, 2998, 2581, 1706, 1639, 1593, 1579, 1530, 1484, 1459, 1425, 1398, 1345, 1331, 1315, 1267, 1211, 1162, 1136, 1074, 1055, 993, 948, 847, 836, 774, 761,

724, 651, 611, 589, 483.

^1H NMR (500 MHz, CD_3OD) δ /ppm: 13.03 (b, OH), 8.91 (d, 1H), 8.19 (d, 1H), 8.13 (t, 1H), 8.07 (d, 1H), 7.81 (d, 1H), 6.58 (dd, 1H).

^{13}C NMR (126 MHz, CD_3OD) δ /ppm: 166.48, 151.21, 147.04, 142.34, 140.23, 127.90, 122.50, 115.51, 107.93.

Synthesis of 2,6-bis(6-(pyrazol-1-yl)pyridin-2-yl)-1,5-dihydrobenzo[1,2-d:4,5-d']diimidazole (L)



A (6-(pyrazol-1-yl)picolinic acid, 2.41 g, 12.75 mmol, 2.1 eq), 1,2,4,5-benzenetetramine tetra hydrochloride (1.72 g, 6.05 mmol, 1 eq) and polyphosphoric acid (20 mL) were taken in a 50 mL round-bottomed flask. The reaction mixture was gently heated at 130 °C until the polyphosphoric acid got viscous enough to allow the stirring with a magnetic stirrer bar. Then the temperature was set to 200 °C and stirred for 4 hours. The reaction was cooled to 100 °C and was added into crushed ice. The aqueous suspensions were combined, and the precipitate was filtered off. The solid obtained was suspended in water, and the pH was adjusted to 10 using 2 M aq. Na_2CO_3 solution. Later the suspension was stirred for 2 hours and was collected by filtration. The precipitate was re-suspended in water, pH was set to 4 using 1 M HCl solution, and was stirred overnight. The precipitate was filtered off by washing with water (250 mL), and the light brown color product obtained was dried in the oven at 120 °C.

Yield: 2.25 g (79.1%)

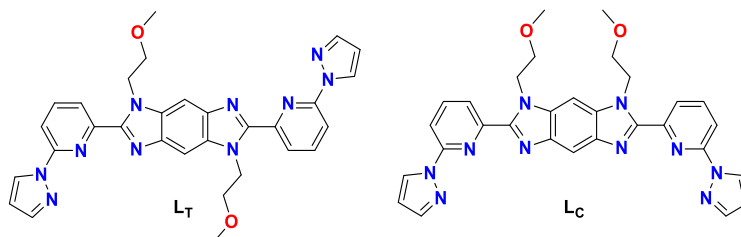
ESI-MS, found (calcd): 445.1607 $[\text{M}+\text{H}]^+$, (445.1632); 467.1421 $[\text{M}+\text{Na}]^+$, (467.1452); 889.3089 $[2\text{M}+\text{H}]^+$, (889.3192).

IR (KBr, cm^{-1}): 3295, 3099, 1601, 1579, 1522, 1474, 1456, 1394, 1341, 1291, 1237, 1204, 1155, 1060, 1038, 993, 938, 885, 834, 807, 752. 702, 651, 591, 418.

^1H NMR (500 MHz, DMSO-d_6) δ /ppm: 13.04 (s, 2H, NH-S), 12.97 (s, 2H, NH-C), 9.32 (d, 2H), 9.29 (d, 2H), 8.26 (d, 4H), 8.19 (dt, 4H), 8.07 (s, 1H, H_β), 8.02 (dd, 4H), 7.92 (s, 4H), 7.88 (s, 2H, H_\square), 7.73 (s, 1H, H_γ), 6.74 (dd, 4H).

^{13}C NMR (126 MHz DMSO-d_6) δ /ppm: 151.46, 150.99, 147.49, 143.12, 143.10, 142.20, 141.33, 134.04, 133.14, 128.72, 128.64, 119.22, 119.14, 112.59, 108.72, 108.63, 100.22, 92.40.

Synthesis of Ligand **L_T** and **L_C**



L (0.895 g, 2.0 mmol, 1 eq) and Cs_2CO_3 (2.64 g, 8 mmol, 4 eq) were taken in a three-necked round-bottomed flask and dried under vacuum at 100 °C for three hours. The flask was flushed with argon, and DMSO (30 mL) was added. After 30 min, the suspension was allowed to cool to ambient temperature. The 1-bromo-2-methoxyethane (0.838 g, 6 mmol, 3 eq, $V=0.566$ mL) was added using a syringe and continued to stir at 80 °C under Argon. The reaction was stopped after 24 h. The reaction mixture was taken into a mixture of $\text{CHCl}_3/\text{EtOAc}$ and H_2O . After phase separation, the aqueous layer was extracted twice with CHCl_3 . The organic layer was dried over Na_2SO_4 , filtered, and evaporated under reduced pressure. Then the products were purified by column chromatography on silica as a stationary phase and a gradient of CHCl_3 and MeOH as a liquid phase.

L_T

Yield: 0.37 g (33.6%)

ESI-MS, found (calcd): 561.2464 $[\text{M}+\text{H}]^+$, (561.2469); 1121.4873 $[2\text{M}+\text{H}]^+$, (1121.4866).
 IR (KBr, cm^{-1}): 3422, 3140, 3108, 2956, 2924, 2815, 1078, 1742, 1594, 1574, 1510, 1471, 1395, 1279, 1248, 1200, 1150, 1118, 1074, 1040, 969, 948, 906, 886, 812, 790, 754, 656, 626.

^1H NMR (500 MHz, CDCl_3) δ/ppm : 8.63 (d, 2H), 8.42 (d, 2H), 8.10 (d, 2H), 8.02 (dd, 2H), 7.94 (s, 2H, H_α), 7.80 (d, 2H), 6.55 (dd, 2H), 5.12 (t, 4H), 3.99 (t, 4H), 3.37 (s, 6H).

^{13}C NMR (126 MHz, CDCl_3) δ/ppm : 150.86, 150.26, 148.40, 142.38, 140.63, 139.83, 135.46, 127.02, 122.50, 112.95, 108.36, 99.33, 71.13, 59.15, 45.44.

Elemental Analysis for $\text{C}_{30}\text{H}_{28}\text{N}_{10}\text{O}_2 \cdot 0.3(\text{EtOAc})$, found (calcd): C: 64.02 (63.79); H: 5.62 (5.24); N: 23.34 (23.74).

L_C

Yield: 0.33 g (29.3%)

ESI-MS, found (calcd): 561.2469 $[\text{M}+\text{H}]^+$, (561.2469)

IR (KBr, cm^{-1}): 3375, 3143, 3104, 2936, 2815, 2720, 1729, 1595, 1573, 1520, 1470, 1395, 1374, 1338, 1277, 1202, 1150, 1114, 1077, 1042, 994, 966, 946, 905, 869, 812, 754, 660, 622.

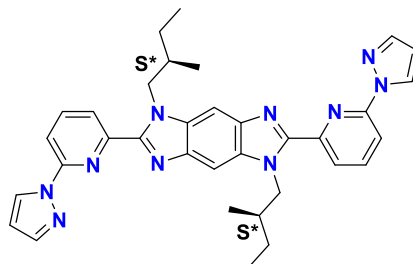
^1H NMR (500 MHz, CDCl_3) δ/ppm : 8.56 (d, 2H), 8.40 (d, 2H), 8.22 (s, 1H, H_β), 8.02 (d, 2H), 7.92 (dd, 2H), 7.79 (d, 2H), 7.48 (s, 1H, γ), 6.54 (dd, 2H), 5.05 (t, 4H), 3.96 (t, 4H), 3.38.

^{13}C NMR (126 MHz, CDCl_3) δ/ppm : 150.79, 149.65, 148.61, 142.41, 140.32, 139.80,

136.15, 126.99, 122.43, 112.81, 109.48, 108.39, 89.91, 71.53, 59.27, 45.59.

Elemental Analysis for $C_{30}H_{28}N_{10}O_2 \cdot 0.3(EtOAc)$, found (calcd): C: 63.97 (63.79); H: 5.63 (5.24); N: 23.44 (23.74).

Synthesis of Ligand L_d



L (0.40 g, 0.9 mmol, 1 eq) and Cs_2CO_3 (1.31 g, 3.6 mmol, 4 eq) were taken in a three-necked round-bottomed flask and dried under vacuum at 100 °C for three hours. The flask was flushed with argon, and DMSO (16 mL) was added. After 30 min, the suspension was allowed to cool to ambient temperature. The (S)-1-bromo-2-methylbutane (0.36 mL, 2.7 mmol, 3 eq) was added using a syringe and continued to stir at 80 °C under Argon. The reaction was stopped after 24 h. The reaction mixture was taken into a mixture of $CHCl_3/EtOAc$ and H_2O . After phase separation, the aqueous layer was extracted twice with $CHCl_3$. The organic layer was dried over Na_2SO_4 , filtered, and evaporated under reduced pressure. Then the crude product was subjected to column chromatography on silica as a stationary phase and a gradient of $CHCl_3$ and MeOH as a liquid phase yielding the yellow-colored product (L_d) along with a side product.

Yield: 0.16 g (30.7%)

ESI-MS, found (calcd): 585.3195 $[M+H]^+$, (585.3197).

IR (KBr, cm^{-1}): 3434, 2959, 2930, 2870, 1593, 1575, 1508, 1470, 1397, 1373, 1340, 1275, 1248, 1201, 1182, 1152, 1076, 1040, 996, 951, 879, 813, 764, 738.

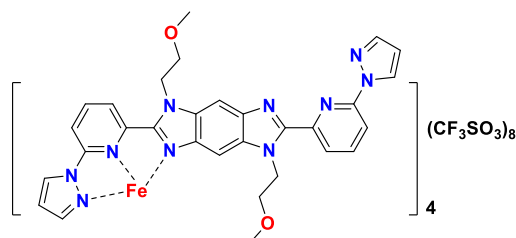
1H NMR (500 MHz, CD_2Cl_2) δ/ppm : 8.63 (d, 2H), 8.39 (d, 2H), 8.11 (d, 2H), 8.06 (t, 2H), 7.86 (s, 2H), 7.83 (d, 2H), 6.60 (dd, 2H), 4.95 (d, 4H), 2.20 (m, 2H), 1.46 (m, 2H), 1.26 (m, 2H), 0.88 (m, 12H)

^{13}C NMR (126 MHz, CD_2Cl_2) δ/ppm : 150.71, 150.65, 149.51, 146.16, 140.92, 139.65, 135.55, 126.78, 122.61, 112.56, 108.03, 99.53, 51.21, 35.60, 27.18, 16.61, 11.14.

Elemental Analysis for $C_{34}H_{26}N_{10}$, found (calcd): C: 69.42 (69.84); H: 6.10 (6.21); N: 23.61 (23.95).

5.3.2 Preparation of Fe(II) Grid complexes

Synthesis of $[\text{Fe}_4(\text{L}_T)_4]\text{Tf}_8$:



The ligand L_T (0.112 g, 0.2 mmol, 1 eq) was suspended in dry acetonitrile (30 mL) in a single necked round-bottomed flask and was degassed with argon for 45 minutes. Later, $\text{Fe}(\text{CF}_3\text{SO}_3)_2$ (0.071 g, 0.2 mmol, 1 eq) was added and stirred at 50 °C overnight under argon atmosphere. An immediate change in color to deep red was observed after addition. The mixture was cooled to room temperature and filtered. The filtrate was reduced to about 5 mL under reduced pressure. DEE (50 mL) was added to produce precipitate and collected by centrifugation (4000 rpm, 30 min). DEE was decanted, and the precipitate was dried under vacuum to yield a dark red color product.

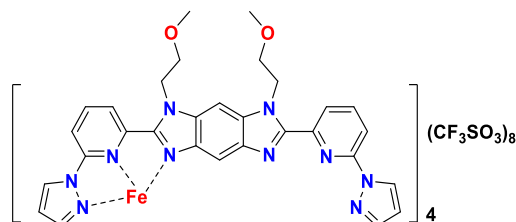
Yield: 0.157 g (86.0%)

ESI MS: 1679.2896 $[\text{M}-2\text{Tf}]^{+2}$, (1679.7066).

IR (KBr, cm^{-1}): 3111, 2938, 1609, 1569, 1518, 1494, 1448, 1425, 1375, 1356, 1250, 1151, 1117, 1050, 1027, 961, 921, 905, 796, 755, 634, 572, 516, 460.

Elemental Analysis for $\text{Fe}_4\text{C}_{128}\text{H}_{112}\text{N}_{40}\text{F}_{24}\text{O}_{32}\text{S}_8$, found (calcd): C: 42.15 (42.35); H: 2.44 (2.33); N: 15.02 (15.43); S: 6.95 (7.07).

Synthesis of $[\text{Fe}_4(\text{L}_C)_4]\text{Tf}_8$:



The ligand L_C (0.112 g, 0.2 mmol, 1 eq) was suspended in dry acetonitrile (30 mL) in a single necked round-bottomed flask and was degassed with argon for 45 minutes. Later, $\text{Fe}(\text{CF}_3\text{SO}_3)_2$ (0.071 g, 0.2 mmol, 1 eq) was added and stirred at 50 °C overnight under argon atmosphere. An immediate change in color to deep red was observed after addition. The mixture was cooled to room temperature and filtered. The filtrate was reduced to about 5 mL under reduced pressure. DEE (50 mL) was added to produce precipitate and collected by centrifugation (4000 rpm, 30 min). DEE was decanted, and the precipitate was dried under vacuum to yield a dark red color product.

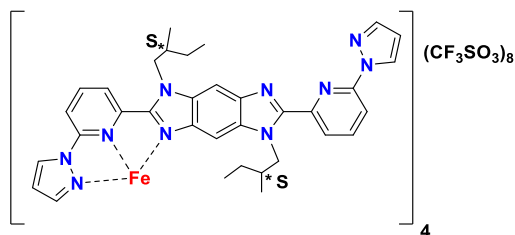
Yield: 0.142 g (78.2%)

ESI MS: 1679.2885 [M-2Tf]⁺, (1679.7066).

IR(KBr, cm⁻¹): 3111, 2938, 1609, 1569, 1518, 1494, 1448, 1425, 1375, 1356, 1250, 1151, 1117, 1050, 1027, 961, 921, 905, 796, 755, 634, 572, 516, 460.

Elemental Analysis for Fe₄C₁₂₈H₁₁₂N₄₀F₂₄O₃₂S₈, found (calcd): C: 42.02 (42.35); H: 2.12 (2.33); N: 15.11 (15.43); S: 7.22 (7.07).

Synthesis of [Fe₄(L_d)₄]Tf₈ = P_d

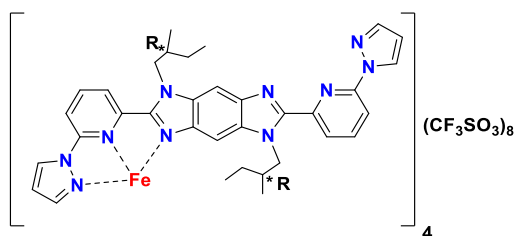


The ligand **L_d** (0.20 g, 0.365 mmol, 1 eq) was suspended in dry acetonitrile (60 mL) in a single necked round-bottomed flask and was degassed with Ar for 45 minutes. Later, Fe(CF₃SO₃)₂ (0.12 g, 0.365 mmol, 1 eq) was added and stirred at 50 °C overnight under argon atmosphere. An immediate change in color to deep red was observed after addition. The mixture was cooled to room temperature and filtered. The filtrate was reduced to about 5 mL under reduced pressure. DEE (50 mL) was added to produce precipitate and collected by centrifugation (4000 rpm, 30 min). Ether was decanted, and the precipitate was dried under vacuum to yield a dark red color product.

Yield: 0.305 g (95.0%)

ESI MS: 3605.6034 [M-Tf]⁺, (3605.6578); 1814.3118 [M-Tf+Na]⁺, (1814.3234); 1728.3341 [M-2Tf]⁺, (1728.3526).

Synthesis of [Fe₄(L_l)₄]Tf₈ = P_l



The ligand **L_l** (0.20 g, 0.365 mmol, 1 eq) was suspended in dry acetonitrile (60 mL) in a single necked round-bottomed flask and was degassed with argon for 45 minutes. Later, Fe(CF₃SO₃)₂ (0.12 g, 0.365 mmol, 1 eq) was added and stirred at 50 °C for overnight under argon atmosphere. An immediate change in color to deep red was observed after addition. The mixture was cooled to room temperature and filtered. The filtrate was reduced to about

5 mL under reduced pressure. DEE (50 mL) was added to produce precipitate and collected by centrifugation (4000 rpm, 30 min). Ether was decanted and the precipitate was dried under vacuum to yield a dark red color product.

Yield: 0.29 g (91.2%)

ESI MS: 3605.6284 [M-Tf]⁺, (3605.6578); 1814.3056 [M-Tf+Na]⁺², (1814.3234); 1728.1473 [M-2Tf]⁺²(1728.3526).

Deconvolution of Diastereomeric grid complexes

Diastereomers in each sample were separated by performing recrystallization several times. In the first step of crystallization, 150 mg of sample was dissolved in ca. 15 mL of acetonitrile, and THF was added slowly via vapor diffusion. This yielded in the crystalline sample. The crystals were dried, powdered, and again dissolved in acetonitrile. THF was slowly diffused again to yield the second recrystallized sample. In each step, the finely powdered sample was used for measuring CD. The powder sample was used instead of crystals to maintain the uniformity. After four steps, the saturation of the CD signal in each case was observed.

Yield for Λ -isomer after four recrystallizations: 30% (with respect to the weight of crude sample used for recrystallization)

IR (KBr, cm⁻¹): 3494, 3107, 2966, 2879, 1608, 1568, 1517, 1493, 1472, 1447, 1422, 1408, 1374, 1357, 1252, 1221, 1197, 1142, 1093, 1050, 1027, 965, 933, 901, 796, 754, 634, 572, 516.

Elemental Analysis for Fe₄C₁₄₄H₁₄₄N₄₀F₂₄O₂₄S₈, found (calcd): C: 45.73 (46.06); H: 3.67 (3.87); N: 14.50 (14.92); S: 6.14 (6.83).

Yield for Δ -isomer after four recrystallizations: 45% (with respect to the weight of crude sample used for recrystallization)

IR (KBr, cm⁻¹): 3495, 3107, 2966, 2879, 1608, 1568, 1517, 1493, 1472, 1447, 1422, 1408, 1374, 1357, 1251, 1221, 1197, 1141, 1093, 1050, 1026, 965, 934, 901, 796, 754, 634, 572, 515.

Elemental Analysis for Fe₄C₁₄₄H₁₄₄N₄₀F₂₄O₂₄S₈, found (calcd): C: 45.69 (46.06); H: 3.90 (3.87); N: 14.43 (14.92); S: 6.04 (6.83).

Synthesis of ⁵⁷FeTf₂:

⁵⁷Fe powder (200 mg, 3.51 mmol) was taken in dry acetonitrile (3 mL) in a 10 mL round bottomed flask. Triflic acid (0.7 mL) was added slowly dropwise, as the reaction is highly exothermic. After the initial effervescence subsided, the mixture was heated to 60 °C and maintained under Ar. Once the effervescence had stopped, the mixture was cooled to RT and unreacted Fe powder was filtered through celite pad. The filtrate was concentrated under reduced pressure and stored at -20 °C over night which resulted in colourless crystals. The

crystals were filtered and by washing with DEE and dried under vacuum overnight to remove solvent.

Yield: 550 mg (43%)

Elemental Analysis for $\text{FeC}_2\text{F}_6\text{O}_6\text{S}_2$ found (calcd): C: 6.39 (6.79); S: 18.44 (18.12).

5.3.3 Other Techniques

a) Ion mobility mass spectrometry

About 10 $\mu\text{g/mL}$ concentrated solution in acetonitrile was directly electro sprayed. A Waters Synapt G2S HDMS high-resolution mass spectrometer coupled with ion mobility separation cell was used for this purpose. The optimized parameters are as follows:

Polarity: ES+, Capillary voltage: 1.5 kV, Source Temperature: 50°C, Sampling Cone: 20 V, Source Offset: 30 V, Source Gas Flow: 0 mL/min, Desolvation Temperature: 120 °C, Cone Gas Flow: 0 L/h, Desolvation Gas Flow: 650.0 L/h, Nebulizer Gas Flow: 2.5 bar, Trap Gas Flow: 10.00 mL/min, Helium Gas Flow: 200 mL/min, IMS Gas Flow: 60 mL/min, IMS Wave Velocity: 500 m/s, IMS Wave Height: 35 V

b) Circular Dichroism

A Jasco J-815 CD Spectrometer (Jasco, Inc.) was used with Spectra Manager software (Jasco Inc.) to record CD spectra. Solutions were prepared by dissolving the samples in acetonitrile to a concentration of 10^{-6} M. All spectra were recorded at 25 °C between 700 and 200 nm at a rate of 50 nm/min and were averaged to 2 accumulations. A 1.0 mm path length cuvette was used to hold solutions, and all spectra were background-subtracted from those of the mobile phases.

c) LIESST

For photo-magnetic experiments, the temperature-dependent magnetization was recorded at $B_{\text{DC}} = 0.1$ T as an external magnetic field. The temperature sweep rate of 0.3 K min^{-1} was used. Each temperature data point was stabilized for 1 minute before the measurement. Gelatin capsule (standard measurements in the dark) was used as sample holders. The very small diamagnetic contribution of the gelatin capsule was negligible to the overall magnetization, which was dominated by the sample. The photo-magnetic measurements were performed by using a diode-pumped solid-state lasers (DPSS) Kvant ($\lambda = 637 \text{ nm}$, 300 mW) coupled through an optical fiber to the cavity of an MPMS SQUID XL7 and the power on the sample surface was adjusted to 10 mW cm^{-1} . The small amount of sample ($\approx 1 \text{ mg}$) was dispersed in melted eicosane, introduced into the plastic straw, and congealed. The exact weight of samples was obtained by weighting and verified by comparison of the thermal χT vs. T curve with a more accurately weighed sample of the same compound. After the cooling

to 5 K, the sample was irradiated, and the change in magnetization was followed. When the saturation point had been reached, the light was switched off, the temperature was increased at a rate of 0.3 K min⁻¹, and the magnetization was measured at 1 K intervals. We observed the most intense increase of magnetic moment under the red light irradiation (637 nm). T(LIESST) value was determined from the minimum of the $\partial(\chi T)/\partial T$ vs. T curve for the relaxation process.

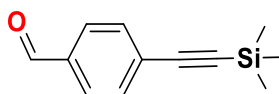
d) TDDFT

TDDFT calculations were performed on the Λ -complex in order to study its CD spectrum using the ESCF module^{131,203,204} of the TURBOMOLE package (Version 7.4.1)²⁰⁵. For this, PBE0 functional^{206,207} together with the def2-SV(P)²⁰⁸ basis set used for all atoms except for iron for which the def2-TZVP²⁰⁸ basis set was chosen. The exchange-correlation functional was evaluated using a gridsize of 5, as implemented in TURBOMOLE.¹³⁸

5.4 Mononuclear and polynuclear SMM complexes

5.4.1 Synthesis of Porphyrin Ligands

Synthesis of 4-((trimethylsilyl)ethynyl)benzaldehyde



The compound was prepared according to the reported literature²⁰⁹. A two necked 250 mL round-bottomed flask was dried under vacuum for 1 hour and filled with dry THF (60 mL) and freshly distilled Et₃N (12 mL, 80.3 mmol). 4-bromobenzaldehyde (3.70 g, 20.0 mmol) and CuI (380 mg, 2.00 mmol) were added to the mixture and was bubbled with argon for 45 min. Later, Pd(PPh₃)₄ (924 mg, 800 μ mol) and trimethylsilylacetylene (4.24 mL, 30.0 mmol) were added stirred overnight under dark at room temperature. The mixture was filtered, and the solids were washed with EtOAc. The filtrate was concentrated under reduced pressure and was purified by column chromatography with silica gel as stationary phase and 5% EtOAc: Hexane as a liquid phase to yield 4-((trimethylsilyl)ethynyl)benzaldehyde as a pale brown solid.

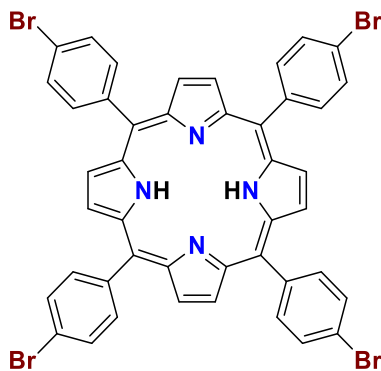
Yield: (4.04 g, 100%).

GC MS found (calcd): 202.08 [M+Na]⁺, (202.08); 187.04 [M-CH₃+Na]⁺, (187.04).

IR (KBr, cm⁻¹): 3382, 2961, 2898, 2830, 2737, 2156, 1702, 1600, 1562, 1455, 1413, 1382, 1300, 1250, 1205, 1162, 1099, 955, 867, 841, 761, 704, 660, 637, 536, 471.

¹H NMR (500 MHz, CDCl₃) δ /ppm: 10.02 (s, 1H), 7.84 (d, 2H), 7.62 (d, 2H), 0.29 (s, 9H)

¹³C NMR (126 MHz, CDCl₃) δ /ppm: 191.47, 135.58, 132.49, 129.45, 103.84, 99.04, -0.19.

Synthesis of 5,10,15,20-tetrakis(4-bromophenyl)porphyrin (P1)

Porphyrin **P1** was prepared according to the reported literature.¹⁷⁸ 4-bromobenzaldehyde (11.1 g, 60 mmol) was dissolved in propionic acid (300 mL) and was heated to 140 °C. Pyrrole (4.14 ml, 60 mmol) was added slowly into the solution and continued to stir at reflux temperature for 1 h. The reaction was cooled to room temperature and stored in the freezer at 4 °C overnight. The blue precipitate was filtered by washing with a little amount of methanol and dried in an oven.

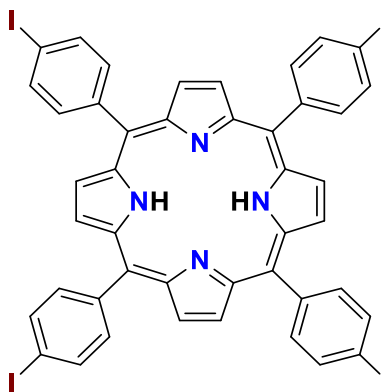
Yield: 2.78 g (20.5%)

ESI-MS, found (calcd): 930.8904 [M+H]⁺, (930.8929).

IR (KBr, cm⁻¹): 3430, 2921, 1624, 1558, 1470, 1390, 1344, 1212, 1173, 1096, 1068, 994, 964, 845, 825, 799, 779, 665, 521, 451, 418.

¹H NMR (500 MHz, CDCl₃) δ/ppm: 8.87 (s, 8H), 8.10 (d, 8H), 7.93 (d, 8H), -2.85 (s, 2H, NH).

¹³C NMR (126 MHz, CDCl₃) δ/ppm: 140.86, 135.86, 130.03, 122.68, 119.04.

Synthesis of 5,10,15,20-tetrakis(4-iodophenyl)porphyrin (P2)

Following the same synthetic procedure of **P1**, from 4-iodobenzaldehyde (4.64 g, 20 mmol) a solid blue precipitate as a product **P2** was obtained.

Yield: 0.56 g (10.1%)

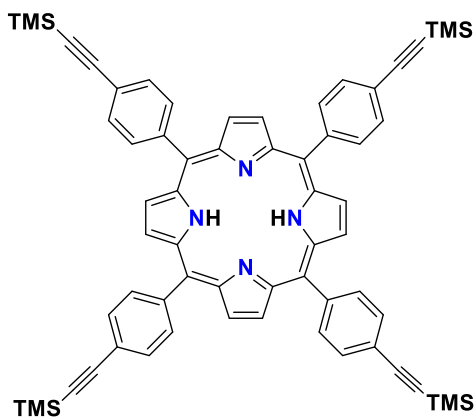
ESI-MS, found (calcd): 1118.8444 [M+H]⁺, (1118.8409).

IR(KBr, cm⁻¹): 3422, 2919, 2233, 1904, 1557, 1554, 1473, 1386, 1342, 1182m 1058, 1006, 963, 876, 823, 797, 726, 670, 516.

¹H NMR (500 MHz, CDCl₃) δ/ppm: 8.87 (s, 8H), 8.14 (d, 8H), 7.96 (d, 8H), -2.86 (s, 2H, NH)

¹³C NMR (126 MHz, CDCl₃) δ/ppm: 146.30, 141.21, 135.85, 135.67.

Synthesis of 5,10,15,20-tetrakis(4-((trimethylsilyl)ethynyl)phenyl)porphyrin (**P3**)



Following the same synthetic procedure of **P1**, from 4-((trimethylsilyl)ethynyl)benzaldehyde (1.14 g, 5.64 mmol), a solid blue precipitate as a product **P3** was obtained.

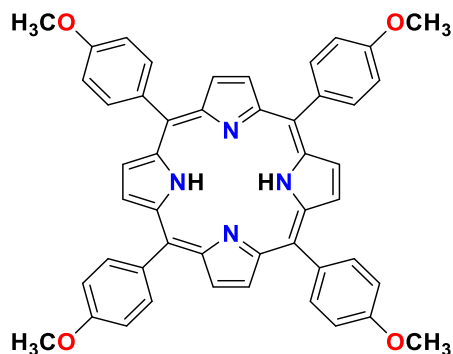
Yield: 0.30 g (21.7%)

ESI-MS, found (calcd): 999.4038 [M+H]⁺, (999.4124).

IR (KBr, cm⁻¹): 3437, 2956, 2860, 2156, 1624, 1495, 1401, 1350, 1250, 1223, 1180, 1050, 964, 864, 849, 805, 762, 654, 419.

¹H NMR (500 MHz, CDCl₃) δ/ppm: 8.84 (s, 8H), 8.17 (d, 8H), 7.90 (d, 8H), 0.41 (s, 36H), -2.82 (s, 2H, NH)

¹³C NMR (126 MHz, CDCl₃) δ/ppm: 142.30, 134.41, 130.41, 122.77, 119.67, 95.69, 0.08.

Synthesis of 5,10,15,20-tetrakis(4-methoxyphenyl)porphyrin (P4)

Following the same synthetic procedure of **P1**, from 4-methoxybenzaldehyde (3.65 mL, 30 mmol) a solid blue precipitate as a product **P4** was obtained.

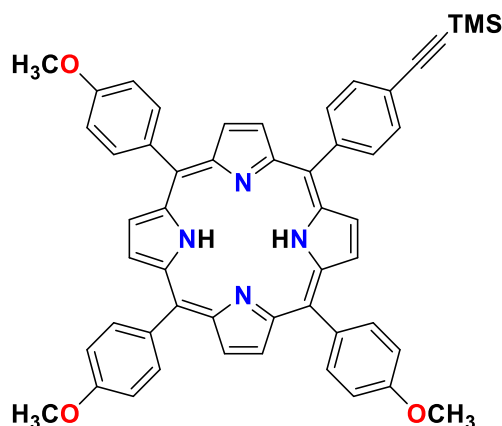
Yield: 0.51 g (9.5%)

ESI-MS, found (calcd): 735.2841 [M+H]⁺, (735.2966).

IR (KBr, cm⁻¹): 3425, 2927, 2831, 1606, 1508, 1468, 1441, 1350, 1289, 1253, 1174, 1106, 1035, 963, 838, 804, 738, 667, 597, 533, 419.

¹H NMR (500 MHz, CDCl₃) δ/ppm: 8.89 (s, 8H), 8.15 (d, 8H), 7.32 (d, 8H), 4.13 (s, 12H), -2.72 (s, 2H, NH).

¹³C NMR (126 MHz, CDCl₃) δ/ppm: 159.4, 135.63, 119.76, 112.22, 55.62.

Synthesis of 5,10,15-tris(4-methoxyphenyl)-20-(4-((trimethylsilyl)ethynyl)phenyl)porphyrin (P5)

4-((trimethylsilyl)ethynyl)benzaldehyde (2.04 g, 10.07 mmol, 1eq) and 4-methoxybenzaldehyde (3.67 mL, 30.21 mmol, 3 eq) were dissolved in propionic acid (100 mL) and was heated to 140 °C. Pyrrole (2.8 mL, 40.28 mmol, 4 eq) was added slowly into the solution and continue to stir at reflux temperature for 4 h. The reaction was cooled to room temperature, and stored in the freezer at 4 °C overnight. The solvent was removed under reduced pressure, and the traces of the solvent was removed by washing with water

and extracted with DCM. Organic layers were collected, dried over anhydrous Na_2SO_4 , and concentrated. TLC in DCM/Hexane shows the presence of 5 products. The product was obtained by column chromatography on silica gel as the stationary phase and gradient of DCM in hexane as mobile phase.

Yield: 0.65 g (8%)

ESI-MS, found (calcd): 801.3212 $[\text{M}+\text{H}]^+$, (801.3255).

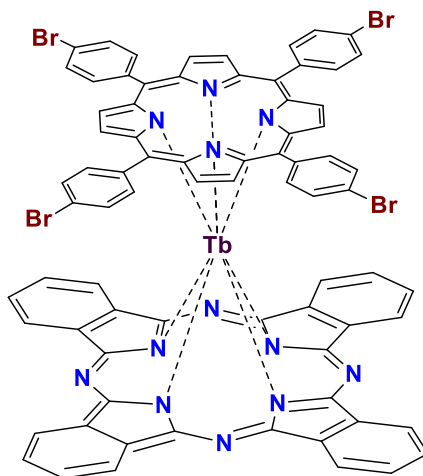
IR(KBr, cm^{-1}): 3382, 2958, 2898, 2831, 2737m 2156, 1701, 1601, 1562, 1413, 1382, 1300, 1250, 1205, 1162, 1099, 1012, 955, 867, 843, 761, 704, 660, 638, 536, 472.

^1H NMR (500 MHz, CDCl_3) δ /ppm: 8.90 (d, 6H), 8.82 (d, 2H), 8.19 (d, 2H), 8.15 (m, 6H), 7.90 (d, 2H), 7.32 (d, 6H), 4.13 (s, 9H), 0.41 (s, 9H), -2.74 (s, 2H, NH).

^{13}C NMR (126 MHz, CDCl_3) δ /ppm: 159.46, 135.59, 134.54, 134.44, 130.35, 119.96, 112.25, 55.61, 31.61, 22.67, 14.15, 0.10.

5.4.2 Synthesis of Tb Phtalocyanato Porphinato double deckers

Synthesis of DD1a



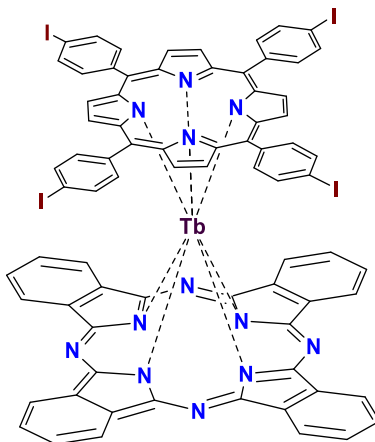
$\text{Tb}(\text{acac})_3 \cdot 3\text{H}_2\text{O}$ (210 mg, 0.46 mmol, 1 eq) and Li_2Pc (250 mg, 0.48 mmol, 1 eq) were taken in a two necked round-bottomed flask with 16 mL dry 1,2,4-trichlorobenzene (TCB). The mixture was stirred at 120 °C under Argon atmosphere for 5 hours. Later, the mixture was cooled to room temperature. Then, **P1** (440 mg, 0.48 mmol, 1 eq) was added and stirred at 220 °C for overnight under Ar. The crude mixture was cooled to room temperature and was subjected to flash column chromatography with hexane to remove TCB and then DCM to obtain the crude material. This crude material was subjected to column chromatography with silica gel as a stationary phase and DCM as an eluent to yield brown-colored product along with other side products, which include triple-decker complexes.

Yield: 80% (11.2%)

ESI-MS, found (calcd): 1598.8354 [M]⁻, (1598.9456).

IR(KBr, cm⁻¹): 3445, 3064, 2923, 2848, 2114, 1741, 1602, 1470, 1451, 1389, 1314, 1259, 1195, 1115, 1070, 1000, 979, 841, 798, 733, 459.

Synthesis of DD2a



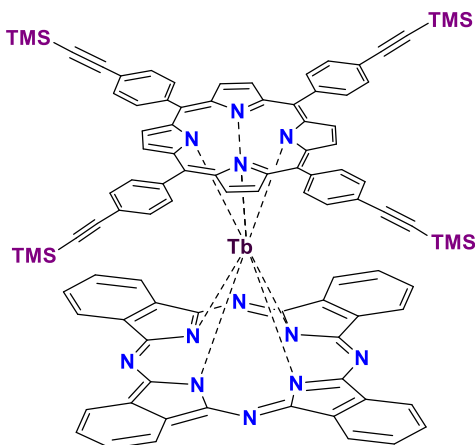
Following the same synthetic procedure of **DD1a**, from porphyrin **P2** (0.54 g, 0.48 mmol) a solid brown precipitate as a product **DD2a** was obtained.

Yield: 68 mg (8.2%)

ESI-MS, found (calcd): 1786.8420 [M]⁻, (1786.8926).

IR (KBr, cm⁻¹): 3440, 2924, 2915, 1650, 1457, 1329, 1280, 1110, 1058, 980, 858, 794, 732, 652.

Synthesis of DD3a



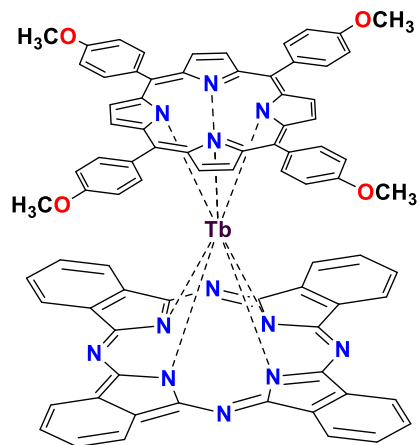
Following the same synthetic procedure of **DD1a**, from porphyrin **P3** (0.48 g, 0.48 mmol) a solid brown precipitate as a product **DD3a** was obtained.

Yield: 62 mg (8.4%)

ESI-MS, found (calcd): 1668.3110 [M]⁻, (1668.4667).

IR (KBr, cm⁻¹): 3438, 2955, 2923, 2856, 2157, 1600, 1453, 1384, 1316, 1249, 1194, 1114, 1075, 980, 863, 808, 735, 658, 566, 473.

Synthesis of DD4a



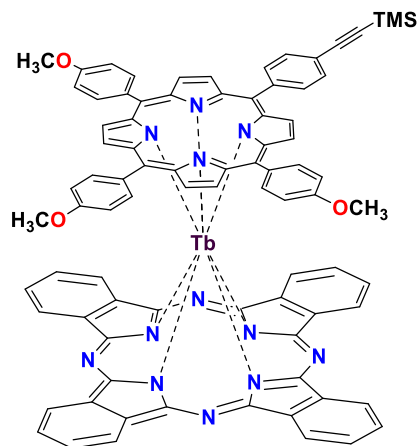
Following the same synthetic procedure of **DD1a**, from porphyrin **P4** (0.32 g, 0.48 mmol) a solid brown precipitate as a product **DD4a** was obtained.

Yield: 87.5 mg (13.3%)

ESI-MS, found (calcd): 1403.1878 [M]⁻, (1403.3482).

IR (KBr, cm⁻¹): 3443, 2926, 2853, 2589, 2453, 1636, 1574, 1508, 1435, 1316, 1281, 1245, 1174, 1114, 1032, 977, 882, 806, 732, 644, 597, 532.

Synthesis of DD5a



Following the same synthetic procedure of **DD1a**, from porphyrin **P5** (0.385 g, 0.48 mmol) a solid brown precipitate as a product **DD5aa** was obtained with slight modification in the workup. The crude material obtained was subjected to column chromatography with silica gel as a stationary phase and DCM as an eluent to yield a brown and green colored product. Due to equal polarity with triple-decker complexes, the separation was not possible by simple column chromatography. To yield the pure product, the material was dissolved in a minimum amount of DCM and added 1000 mL of hexane. After two days, the triple-decker (impurities) was crystallized, and a pure double-decker sandwich complex was obtained by evaporating hexane under reduced pressure.

Yield: 70 mg (9.9%)

ESI-MS, found (calcd): 1470.2468 [M]⁻, (1470.3804).

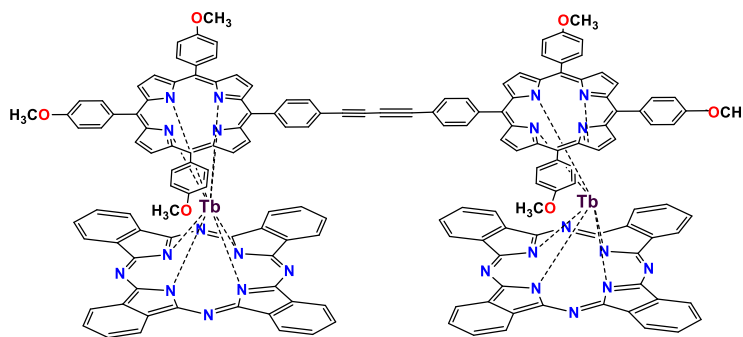
IR (KBr, cm⁻¹): 3443, 2953, 2855, 2154, 1728, 1605, 1509, 1461, 1379, 1316, 1286, 1246, 1174, 1114, 1035, 978, 842, 801, 733.

Synthesis of reduced DD complexes

The brown coloured neutral double-decker complex (**DDn-a**; n=1-5), (~50 mg, 1 eq) was suspended in methanol (6 mL) with tetrabutylammonium bromide (TBABr), (25 mg, 2 eq). Hydrazine hydrate (50 μ L) was added slowly into the mixture and stirred under argon overnight. Immediate color change from brown to green indicated a reduction of the complex. The reaction mixture was filtered, and the product filtered was dried. The product was dissolved in DCM/CHCl₃ and allowed to crystallize from either by slow evaporation or by vapor diffusion to yield green coloured reduced complex **DDn-b** (n=1-5).

5.4.3 Polynuclear Double-decker complexes

Synthesis of Dimer1 (C1a)



The dimeric complex **C1a** was prepared by modifying the homo-coupling reaction. The double-decker complex **DD5a** (100 mg, 0.068 mmol), AsPh₃ (2 mg, 1 mol%), were taken in the round-bottomed flask and dried under vacuum for 2 h. 1M TBAF solution (5 mL) in 5% H₂O in THF was prepared and added into the reaction mixture. Pd(PPh₃)₂Cl₂ (1 mg, 2 mol%) was added and stirred at 60 °C under atmosphere air for 16 h (O₂ in the atmosphere assists

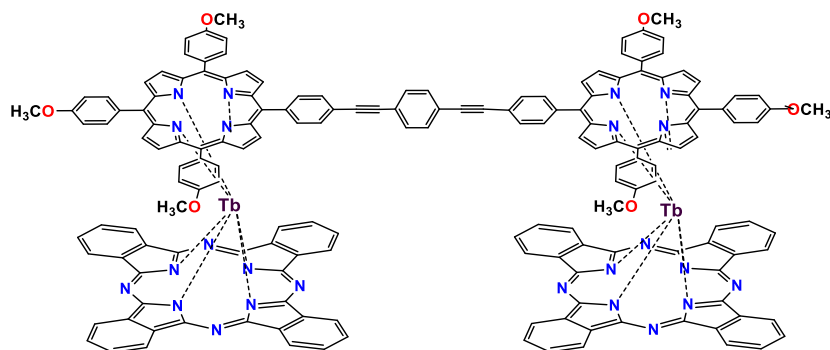
the homo-coupling reaction). Later, the reaction was cooled to room temperature and quenched by the addition of DCM. The reaction mixture was washed with water and extracted with DCM and dried over Na_2SO_4 . The reaction mixture was dried under reduced pressure. The mixture was dissolved in 1:1 DCM/Methanol (50 mL) mixture, and NaIO_4 (50 mg) was added and stirred overnight. Again the complex was extracted by washing with water and extracted with CHCl_3 and dried over Na_2SO_4 . The reaction mixture was dried under reduced pressure. The crude product was subject to column chromatography with silica gel as a stationary phase and CHCl_3 as an eluent to yield a brown-colored product **C1a**.

Yield: 20 mg (21.6%)

ESI-MS, found (calcd): 1396.7789 $[\text{M}]^{2+}$, (1396.8314).

IR (KBr, cm^{-1}): 3442, 2963, 2924, 2853, 1605, 1509, 1453, 1318, 1261, 1174, 1097, 1030, 979, 838, 733, 420.

Synthesis of Dimer2 (C2a)



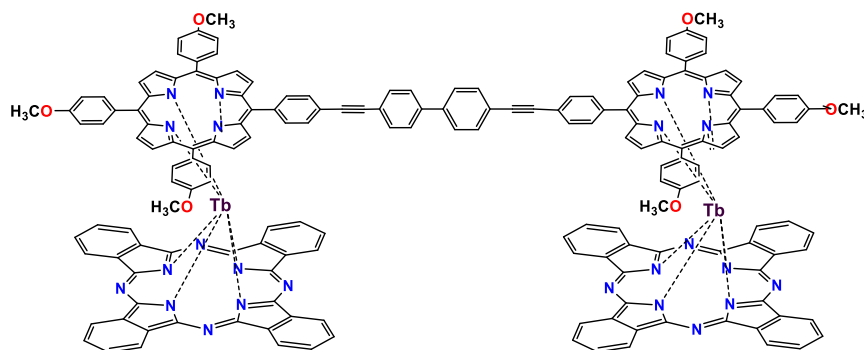
Sonogashira coupling reaction was employed in this reaction to obtain the **C2a**. Following the same synthetic and workup procedure of **C1a**, from **DD5a** (100 mg, 0.068 mmol) along with the addition of a linker 1,4-diiodobenzene (13 mg, 0.034 mmol, 0.5 eq), brown solid precipitate as a product **C2a** was obtained. Here, the reaction was maintained under argon to avoid homo-coupling.

Yield: 21 mg (19.4%)

ESI-MS, found (calcd): 1435.3414 $[\text{M}]^{2+}$, (1435.3470); 2870.6674 $[\text{M}]^+$, (2870.6946)

IR (KBr, cm^{-1}): 3388, 2967, 2923, 2853, 2593, 2470, 1725, 1605, 1509, 1453, 1380, 1318, 1285, 1247, 1174, 1101, 1034, 978, 880, 803, 733, 599, 540, 496.

Synthesis of Dimer3 (C3a)



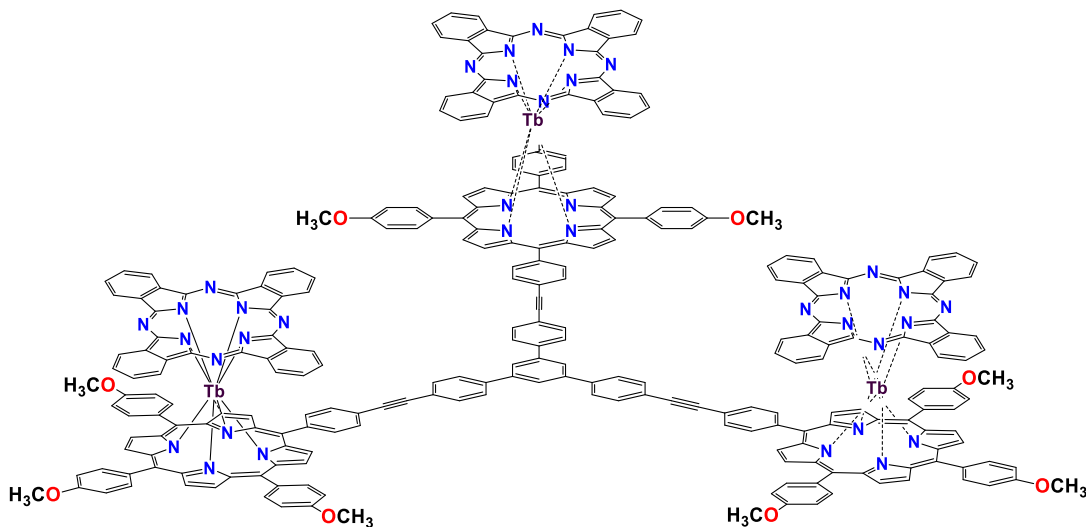
Sonogashira coupling reaction was employed in this reaction to obtain the **C3a**. Following the same synthetic and workup procedure of **C1a**, from **DD5a** (100 mg, 0.068 mmol) along with the addition of a linker 4,4'-diiodobiphenyl (10.7 mg, 0.034 mmol, 0.5 eq), brown solid precipitate as a product **C3a** was obtained. Here, the reaction was maintained under argon to avoid homo-coupling.

Yield: 25 mg (24%)

ESI-MS, found (calcd): 1472.6956 [M]²⁺, (1472.8627); 2946.7053 [M]⁺, (2946.7259)

IR (KBr, cm⁻¹): 3416, 2924, 2853, 2598, 1724, 1604, 1508, 1451, 1316, 1285, 1261, 1246, 1174, 1103, 1051, 978, 880, 803, 734, 599.

Synthesis of Trimer (C4a)



Sonogashira coupling reaction was employed in this reaction to obtain the **C4a**. Following the same synthetic and workup procedure of **C1a**, from **DD5a** (100 mg, 0.068 mmol) along with the addition of a linker 1,3,5-tris(4-iodophenyl)benzene (14 mg, 0.022 mmol, 0.33 eq),

brown solid precipitate as a product **C4a** was obtained. Here, the reaction was maintained under argon to avoid homo-coupling.

Yield: 7 mg (7%)

ESI-MS, found (calcd): 1498.3511 [M]³⁺, (1498.3723) (MW of M = 4492.11).

IR (KBr, cm⁻¹): 3438, 2923, 2585, 2453, 1726, 1643, 1603, 1508, 1451, 1384, 1315, 1222, 1174, 1114, 977, 876, 805, 732, 597.

Synthesis of Yttrium analogs of double-decker complexes

The Yttrium analogs of **DD5** was prepared by following the same synthetic procedure of **DD5a**, from porphyrin **P5** with Y(acac)₃·6H₂O instead of Tb(acac)₃·6H₂O.

Yield: 0.14 g (10.4 %)

ESI-MS, found (calcd): 1470.2468 [M]⁻, (1400.3358).

Similarly, Yttrium analogs of **C1a**, **C2a** and **C3a** were prepared by using Yttrium analog of **DD5a** as per the synthetic procedures employed above for Tb polynuclear complexes.

Y-Dimer1: ESI-MS found (calcd): 1327.3033 [M]⁻, (1327.3136).

Y-Dimer2: ESI-MS found (calcd): 1364.8118 [M]⁻, (1364.8275).

Y-Dimer3: ESI-MS found (calcd): 1403.3348 [M]⁻, (1402.8432).

5.4.4 Other Techniques

Cyclic Voltammetry

Cyclic voltammetry (CV) experiments and Differential potential voltammetry (DPV) electrolysis were performed using a Gamry potentiostat connected to a C3 standard electrochemical cell that consisted of a glassy carbon as working electrode, a Pt wire as counter electrode, and a Ag/AgCl reference electrode

EPR

X-band (9.311 GHz) EPR spectra were collected on an EMXplus spectrometer fitted with an EMX microX bridge. For Tb samples the spectrometer was fitted with a high-sensitivity Bruker ER4122SHQE cavity operating in the TE₀₁₁ mode. As this cavity saturates from low powers, for Yttrium samples which were characterized by very intense signals, the spectrometer was fitted with a Bruker 4102ST rectangular cavity operating in the TE₁₀₂ mode. For low temperature experiments, the cavities were fitted with an ESR900 dynamic continuous flow cryostat controlled with an Oxford ITC503S Intelligent Temperature Controller.

All samples were deoxygenated to remove eventual interactions with paramagnetic O₂ molecules. Solution samples were prepared in CD₂Cl₂/CD₃Cl 4:1 mixtures, which form

homogeneous glasses upon freezing. The solutions were deoxygenated by freeze-pump-thaw cycles and flame-sealed in the EPR tubes.

5.5 Crystal Structures

The single-crystal X-ray diffraction data of the complexes **C1**, **C2**, **DD1a**, **DD4a** and **DD1b** were collected using STOE Stadi Vari 25 diffractometer with graphite monochromated Mo-K α radiation ($\lambda = 0.71073 \text{ \AA}$). The single-crystal X-ray diffraction data of the complexes **A**, **A**, **DD2a** and **DD4b** were collected using STOE Stadi Vari 25 diffractometer with graded multilayer mirrored monochromatic Ga-K α radiation ($\lambda = 1.34143 \text{ \AA}$).

The structures were solved using direct methods and were refined by full-matrix least square methods and using SHELX-2014 inbuilt in Olex2. Data were collected using ϕ and Ω scans chosen to complete the asymmetric unit. All non-hydrogen atoms were refined anisotropically, whereas the hydrogen atoms were calculated geometrically, riding on their parent atoms.

Complex C1

Formula	C ₂₉ H ₂₉ B ₂ F ₈ Fe ₁ N ₁₁ O ₆
Formula weight / g mol ⁻¹	857.10
Temperature / K	150
Crystal dimensions / mm ³	0.33 × 0.13 × 0.10
System	Monoclinic
Space group	<i>P</i> 2 ₁ / <i>n</i> (#14)
<i>a</i> / Å	10.63453(16)
<i>b</i> / Å	23.6122(4)
<i>c</i> / Å	14.5050(2)
β °	99.2978(14)
<i>V</i> / Å ³	3594.42(10)
<i>Z</i>	4
ρ_{calcd} / g cm ⁻³	1.584
μ (MoK α) / mm ⁻¹	0.521
λ / Å	0.71073
$2\theta_{\text{max}}$ / °	54.2
Reflections collected	42670
Unique reflections (<i>R</i> _{int})	7931 (0.0680)
Number of parameters	620
Number of restraints	74
Final <i>R</i> ₁ [<i>I</i> > 2 σ (<i>I</i>)]	0.0469
<i>wR</i> ₂ (all data)	0.1175
Goodness of fit	1.024
Largest diff. peak/ hole / e ⁻ Å ⁻³	0.52 / -0.35

Complex C2:

	HS (335 K)^a	HS (300 K)^a	LS(300 K)^b	LS (150 K)^c
Formula	C ₂₉ H ₂₉ Cl ₂ FeN ₁₁ O ₁₄	C ₂₉ H ₂₉ Cl ₂ FeN ₁₁ O ₁₄	C ₂₉ H ₂₉ Cl ₂ FeN ₁₁ O ₁₄	C ₂₉ H ₂₉ Cl ₂ FeN ₁₁ O ₁₄
FW / g mol ⁻¹	882.38	882.45	882.38	882.48
Temperature / K	335	300	300	150
Crystal dimensions / mm ³	0.35 × 0.20 × 0.13	0.35 × 0.20 × 0.13	0.32 × 0.16 × 0.16	0.23 × 0.19 × 0.17
System	Monoclinic	Monoclinic	Monoclinic	Monoclinic
Space group	<i>P</i> 2 ₁ / <i>c</i> (#14)			
<i>a</i> / Å	9.7805(2)	9.7181(2)	10.7048(2)	10.5596(1)
<i>b</i> / Å	25.8234(5)	25.7973(4)	24.2312(4)	23.9540(3)
<i>c</i> / Å	15.2337(2)	15.1984(2)	14.7020(3)	14.6037(2)
β / °	96.159(2)	95.980(2)	98.509(2)	98.774(1)
<i>V</i> / Å ³	3825.30(12)	3789.52	3771.58(12)	3650.70(8)
<i>Z</i>	4	4	4	4
ρ_{calcd} / g cm ⁻³	1.532	1.547	1.554	1.606
μ (MoK α) / mm ⁻¹	0.614	0.619	0.622	0.643
λ / Å	0.71073	0.71073	0.71073	0.71073
$2\theta_{\text{max}}$ / °	50.7	54.2	54.2	56.6
Reflections collected	25145	29798	29604	31895
Unique reflections (<i>R</i> _{int})	6990 (0.0396)	6161(0.0414)	8307 (0.0489)	9040 (0.0477)
Number of parameters	548	592	590	603
Number of restraints	12	28	14	83
Final <i>R</i> ₁ [<i>I</i> > 2 σ (<i>I</i>)] ^d	0.0552	0.0491	0.0546	0.0419
<i>wR</i> ₂ (all data) ^e	0.1678	0.1452	0.1574	0.1089
Goodness of fit	1.027	1.034	1.036	1.024
Largest diff. peak/ hole / e ⁻ Å ⁻³	0.40 / -0.35	0.37 / -0.37	0.71 / -0.31	0.46 / -0.38
^a Orange block crystal (crystal 1). ^b black block crystal (crystal 2). ^c black block crystal (crystal 3). ^d $R_1 = \sum F_o - F_c / \sum F_o $. ^e $wR_2 = [\sum \{w(F_o^2 - F_c^2)^2\} / \sum w(F_o^2)^2]^{1/2}$.				

S- Complex

Formula	$C_{144}H_{141}F_{24}Fe_4N_{45}O_{33.5}S_8$
Formula weight / $g\ mol^{-1}$	3973.89
Temperature / K	220.15
System	orthorhombic
Space group	$P2_12_12$
$a / \text{\AA}$	32.5873(10)
$b / \text{\AA}$	23.6689(10)
$c / \text{\AA}$	24.8187(7)
$\beta / ^\circ$	90
$V / \text{\AA}^3$	19142.8(11)
Z	4
$\rho_{\text{calcd}} / g\ cm^{-3}$	1.379
$\mu\ (MoK\alpha) / mm^{-1}$	0.484
$\lambda / \text{\AA}$	0.71073
$2\theta_{\text{max}} / ^\circ$	52.33
Reflections collected	78686
Unique reflections (R_{int})	36812 (0.0449)
Number of parameters	2222
Number of restraints	888
Final $R_1 [I > 2\sigma(I)]$	0.0871
wR_2 (all data)	0.2353
Goodness of fit	1.034
Largest diff. peak/ hole / $e^- \text{\AA}^{-3}$	1.23 / -1.17

Complex (all *S*, Δ) and (all *R*, Δ):

	(all <i>S</i> , Δ)	(all <i>R</i> , Δ)
Formula	C140H144F12Fe4N40O12S4	C140H144F12Fe4N40O12S4
Formula weight / g mol ⁻¹	3158.59	3158.59
Temperature / K	180	180
Crystal dimensions / mm ³	0.15 × 0.06 × 0.04	0.1 × 0.07 × 0.07
System	Tetragonal	Tetragonal
Space group	<i>I</i> 4 (#79)	<i>I</i> 4 (#79)
<i>a</i> / Å	20.0596(6)	20.1380(5)
<i>b</i> / Å	20.0596(6)	20.1380(5)
<i>c</i> / Å	24.4391(9)	24.8755(7)
<i>V</i> / Å ³	9834.0(7)	10088.0(6)
<i>Z</i>	2	2
ρ_{calcd} / g cm ⁻³	1.067	1.040
μ (GaK α) / mm ⁻¹	2.181	2.126
λ / Å	1.34143	1.34143
$2\theta_{\text{max}}$ / °	118.27	116.98
Reflections collected	18746	26886
Unique reflections (<i>R</i> _{int})	9873 (0.0430)	10325 (0.0356)
Number of parameters	523	536
Number of restraints	58	90
Final <i>R</i> ₁ [<i>I</i> > 2 σ (<i>I</i>)] ^d	0.0685	0.0770
<i>wR</i> ₂ (all data) ^e	0.2151	0.2562
Goodness of fit	0.995	1.090
Largest diff. peak/ hole / e ⁻ Å ⁻³	0.50/-0.36	0.62/-0.60
Flack parameter	0.12(2)	0.056(17)
Void volume	36.7%	36.7%

Complex DD1a, DD2a, DD4a:

	DD1a	DD2a	DD4a
Formula	C ₇₇ H ₄₁ Br ₄ Cl ₃ N ₁₂ Tb	C _{154.5} H _{82.5} Cl _{7.5} I ₈ N ₂₄ Tb ₂	C ₈₁ H ₅₄ Cl ₂ N ₁₂ O ₄ Tb
FW/ g mol ⁻¹	1719.13	3871.84	1489.18
Temperature / K	300	150.0	180
Crystal dimensions / mm ³	0.559 × 0.167 × 0.165	0.08 × 0.06 × 0.02	0.248 x 0.233 x 0.106
System	Monoclinic	Monoclinic	Monoclinic
Space group	<i>I</i> 2/ <i>a</i>	<i>C</i> 2/ <i>c</i>	<i>P</i> 2 ₁ / <i>c</i>
<i>a</i> / Å	26.2771(3)	52.4893(9)	16.3585(5)
<i>b</i> / Å	18.7924(2)	27.5959(5)	32.1528(6)
<i>c</i> / Å	30.0263(4)	24.7713(4)	16.1628(5)
β °	96.1580(10)	114.4150(10)	119.464(4)
<i>V</i> / Å ³	14741.7(3)	32672.3(10)	7401.7(4)
<i>Z</i>	8	8	4
ρ_{calcd} / g cm ⁻³	1.549	1.574	1.336
μ / mm ⁻¹	3.288	13.744	1.086
λ / Å	0.71073	1.34143	0.71073
$2\theta_{\text{max}}$ / °	54.206	113.942	52.742
Reflections collected	96221	112164	53397
Unique reflections (<i>R</i> _{int})	16268 (0.0514)	31025 (0.0813)	15128 (0.0495)
Number of parameters	874	1826	971
Number of restraints	20	211	122
Final <i>R</i> ₁ [<i>I</i> > 2σ(<i>I</i>)] ^a	0.0535	0.0588	0.0370
<i>wR</i> ₂ (all data) ^b	0.1488	0.1376	0.0905
Goodness of fit	1.074	0.993	1.033
Largest diff. peak/hole / e ⁻ Å ⁻³	2.69/-2.19	1.44/-0.96	1.07/-1.02

Complex DD1b and DD4b:

	DD1b	DD4b
Formula	C186H157Br8Cl6N26Tb2	C96H88N13O4Tb
Formula weight / g mol ⁻¹	3926.19	1646.71
Temperature / K	150	150
Crystal dimensions / mm ³	0.386 × 0.083 × 0.067	0.08 × 0.08 × 0.03
System	Monoclinic	Triclinic
Space group	<i>P</i> 2 ₁ / <i>c</i>	<i>P</i> -1
<i>a</i> / Å	24.4778(4)	11.4100(3)
<i>b</i> / Å	27.1118(4)	16.5959(4)
<i>c</i> / Å	27.9709(5)	22.0716(5)
β / °	107.492	81.599(2)
<i>V</i> / Å ³	17704.2(5)	4070.57(18)
<i>Z</i>	4	2
ρ_{calcd} / g cm ⁻³	1.473	1.344
μ (MoK α) / mm ⁻¹	2.748	4.915
λ / Å	0.71073	1.34143
$2\theta_{\text{max}}$ / °	50.056	113.94
Reflections collected	149325	43279
Unique reflections (<i>R</i> _{int})	31255 (0.0963)	16269 (0.0478)
Number of parameters	2041	1035
Number of restraints	0	0
Final <i>R</i> ₁ [<i>I</i> > 2σ(<i>I</i>)] ^d	0.0546	0.0708
<i>wR</i> ₂ (all data) ^e	0.1284	0.1834
Goodness of fit	1.027	1.010
Largest diff. peak/ hole / e ⁻ Å ⁻³	2.41/-1.55	5.45/-2.48

Conclusion and Outlook

In this thesis, we successfully synthesized and studied different types of molecular magnetic architectures such as – mononuclear and polynuclear SCO and SMM complexes. The molecules obtained were structurally characterized by various spectroscopic techniques, and magnetic properties were obtained. Below are the summarized conclusions for the research conducted in various topics-

Iron(II) bis(pyrazolyl)pyridine (*bpp*)-based molecules – From surface to bulk: We successfully deposited the ligand **L1** and studied the self-assembled metal-organic networks at surfaces. Our finding shows the formation of a Kagome lattice by deprotonation of the **L1** ligand. Whereas, sublimation of the ligand **L1** with Fe subsequently resulted in surface confined coordination oligomers, exhibiting two different binding modes – which tuned them to form 1D chains and 2D knots. These results in surface-confined self-assembled architectures could help to engineer the complex nano-architectures as they could exhibit electronic, catalytic, magnetic, and other properties.

On the other hand, we synthesized new *bpp* based SCO complexes employing nitromethane as a solvent. For the first time, we structurally characterized the SCO complexes of the *bpp* family in LS and HS at room temperature. Moreover, our results on magnetic measurements on complex **C2** showed ST with stable hysteresis of 60 K around room temperature satisfying the requirements for device applications. The simple synthesis of the complex and the stable RT hysteresis makes this complex suitable for further investigations on future applications.

Chiral Resolution of SCO active Iron(II) Grid complexes: In this work, the family of [2 x 2] grid complexes was studied. These complexes showed multifunctional features, which include – i) divergent coordination, ii) molecular chirality, iii) thermally-induced, and iv) light-induced SCO behaviour.

By performing the ligand substitution on the backbone, we synthesized a new set of ligands– CIS- and TRANS-type—and, thus, two different conformers (C and S) were synthesized by treating the respective ligands with Fe(II). Moreover, we separated the first set of enantiomeric SCO grid complexes by tailoring the parent ligand system with chiral centers. IMMS experiments helped in confirming the formation of diastereomers during the reaction. The stereochemistry of the complexes was confirmed by XRD and CD measurements. Magnetic measurements and Mössbauer experiments helped in determining the spin state of the grid complexes at different temperatures, and along with that, these enantiomers were shown to be LIESST active and also exhibited gradual thermal SCO behaviour. These results obtained in preparing the multifunctional architectures with chirality and SCO behaviour are important for future applications, since they can offer

magneto-chiral effects. Thus, it also represents the promising model for the development of future memory devices. Moreover, this study has opened the path for preparing other functional molecules by tuning the ligand and the metal center. Thus, by tuning the metal centers, we could design hetero-metallic chiral grid-like architectures with SMM properties or other photo-physical properties.

So far, in our study, the attempts to separate the diastereomers using chiral counter anion have failed. Later, the IMMS and CD studies have shown the clear presence of diastereomers, but we could not achieve their separation in bulk quantities. So the separation of diastereomers has remained a challenge for future work, as the diastereomers could prove the expected difference in SCO properties.

Terbium(III) Single-molecule magnets based on tetra-pyrrole ligands: In this work, we prepared a series of mononuclear, dinuclear and trinuclear Tb SMM complexes. We performed a structural characterization and SMM studies for a series of heteroleptic, peripherally functionalized terbium(III) (phthalocyaninato)(porphyrinato) complexes with different oxidation states and substitution pattern. These studies on their magnetic properties showed the SMM and non-SMM nature of the anionic and radical species, respectively. Also, electron-donating substitution on the periphery of the porphyrin ligand has shown to tend to decrease in anisotropy barrier.

Moreover, we synthesized polynuclear Tb(III) based double-decker complexes by employing a coupling reaction through the porphyrin rings and characterized their magnetic properties. We employed different linkers to tune the distance between the Tb centers and thus tuning the magnetic properties. These classes of SMM complexes shown an increased anisotropy barrier. These results could open new possibilities for applying SMMs in molecular devices. Moreover, these functionalized double-decker complexes showed higher solubilities than that of bis(phthalocyanine) lanthanide complexes in common organic solvents, which could help in fabrication for device making.

The preliminary studies of EPR studies on these complex **Y-DD5a** have shown the presence of two peaks in the spectra at 20 K, which could correspond to the presence of radical in the porphyrin ring and phthalocyanine ring. These interesting results may open the path for further studies on EPR studies on these classes of complexes.

In conclusion, various kinds of molecular magnetic architectures were studied - (i) *bpp* based Fe(II) complexes, (ii) tetranuclear enantiomeric Fe(II) SCO grid complexes, and (iii) mononuclear, binuclear and trinuclear Tb- SMM complexes based on porphyrins and phthalocyanine. Such design and studies of these magnetic materials are key for future devices based on a bottom-up approach.

Bibliography

- 1 C. Tannous and R. L. Comstock, in *Springer Handbooks*, Springer, 2017, p. 1.
- 2 G. E. Moore, *IEEE Solid-State Circuits Soc. Newsl.*, 2009, **11**, 33–35.
- 3 M. Fondo, A. Escuer and J. M. Herrera, *Front. Chem.*, 2019, **7**, 229.
- 4 M. A. Halcrow, *Spin-Crossover Materials: Properties and Applications*, John Wiley & Sons Ltd, Oxford, UK, 2013.
- 5 P. Gütllich and H. A. Goodwin, in *Spin Crossover in Transition Metal Compounds I*, 2012, pp. 1–47.
- 6 P. Gütllich, Y. Garcia and H. A. Goodwin, *Chem. Soc. Rev.*, 2000, **29**, 419–427.
- 7 K. Senthil Kumar and M. Ruben, *Coord. Chem. Rev.*, 2017, **346**, 176–205.
- 8 P. Gütllich, A. B. Gaspar and Y. Garcia, *Beilstein J. Org. Chem.*, 2013, **9**, 342–391.
- 9 L. Cambi and L. Szegö, *Berichte der Dtsch. Chem. Gesellschaft (A B Ser.)*, 1931, **64**, 2591–2598.
- 10 A. H. White, R. Roper, E. Kokot, H. Waterman and R. L. Martin, *Aust. J. Chem.*, 1964, **17**, 294–303.
- 11 K. Senthil Kumar, I. Šalitraš, B. Heinrich, O. Fuhr and M. Ruben, *J. Mater. Chem. C*, 2015, **3**, 11635–11644.
- 12 K. S. Murray, *Eur. J. Inorg. Chem.*, 2008, 3101–3121.
- 13 D. J. Harding, P. Harding and W. Phonsri, *Coord. Chem. Rev.*, 2016, **313**, 38–61.
- 14 Y. Garcia and P. Gütllich, in *Spin Crossover in Transition Metal Compounds II*, 2012, pp. 49–62.
- 15 P. Gütllich and H. A. Goodwin, *Top Curr Chem*, 2012, **1**, 1–47.
- 16 S. Brooker, *Chem. Soc. Rev.*, 2015, **44**, 2880–2892.
- 17 J. A. Real, A. B. Gaspar and M. Carmen Muñoz, *Dalt. Trans.*, 2005, 2062–2079.
- 18 S. Decurtins, P. Gütllich, C. P. Köhler, H. Spiering and A. Hauser, *Chem. Phys. Lett.*, 1984, **105**, 1–4.
- 19 E. W. Müller, J. Ensling, H. Spiering and P. Gütllich, *Inorg. Chem.*, 1983, **22**, 2074–2078.
- 20 A. Hauser, *Chem. Phys. Lett.*, 1986, **124**, 543–548.
- 21 O. Kahn, J. Kröber and C. Jay, *Adv. Mater.*, 1992, **4**, 718–728.
- 22 O. Kahn and C. J. Martinez, *Science*, 1998, 279, 44–48.
- 23 J. M. Frost, K. L. M. Harriman and M. Murugesu, *Chem. Sci.*, 2016, **7**, 2470–2491.

-
- 24 G. A. Craig and M. Murrie, *Chem. Soc. Rev.*, 2015, **44**, 2135–2147.
- 25 T. Lis, *Acta Crystallogr. Sect. B Struct. Crystallogr. Cryst. Chem.*, 1980, **36**, 2042–2046.
- 26 R. Sessoli, D. Gatteschi, A. Caneschi and M. A. Novak, *Nature*, 1993, **365**, 141–143.
- 27 A. J. Tasiopoulos, A. Vinslava, W. Wernsdorfer, K. A. Abboud and G. Christou, *Angew. Chemie*, 2004, **116**, 2169–2173.
- 28 A. M. Ako, I. J. Hewitt, V. Mereacre, R. Clérac, W. Wernsdorfer, C. E. Anson and A. K. Powell, *Angew. Chemie*, 2006, **118**, 5048–5051.
- 29 C. J. Milios, A. Vinslava, W. Wernsdorfer, S. Moggach, S. Parsons, S. P. Perlepes, G. Christou and E. K. Brechin, *J. Am. Chem. Soc.*, 2007, **129**, 2754–2755.
- 30 R. Bagai and G. Christou, *Chem. Soc. Rev.*, 2009, **38**, 1011–1026.
- 31 N. Ishikawa, M. Sugita, T. Ishikawa, S. Y. Koshihara and Y. Kaizu, *J. Am. Chem. Soc.*, 2003, **125**, 8694–8695.
- 32 K. S. Cole and R. H. Cole, *J. Chem. Phys.*, 1941, **9**, 341–351.
- 33 J. An, Z.-D. Chen, X.-X. Zhang, H. G. Raubenheimer, C. Esterhuysen, S. Gao and G.-X. Xu, *J. Chem. Soc. Dalton Trans.*, 2001, 3352.
- 34 E. Moreno-Pineda, C. Godfrin, F. Balestro, W. Wernsdorfer and M. Ruben, *Chem. Soc. Rev.*, 2018, **47**, 501–513.
- 35 W. Wernsdorfer and M. Ruben, *Adv. Mater.*, 2019, **31**, 1806687.
- 36 B. Weber, W. Bauer and J. Obel, *Angew. Chemie - Int. Ed.*, 2008, **47**, 10098–10101.
- 37 E. Tailleur, M. Marchivie, N. Daro, G. Chastanet and P. Guionneau, *Chem. Commun.*, 2017, **53**, 4763–4766.
- 38 J.-F. Létard, P. Guionneau, E. Codjovi, O. Lavastre, G. Bravic, D. Chasseau, O. Kahn and H. A. Coord, *J. Am. Chem. Soc.*, 1997, **119**, 10861–10862.
- 39 E. Coronado, J. R. Galán-Mascarós, M. Monrabal-Capilla, J. García-Martínez and P. Pardo-Ibáñez, *Adv. Mater.*, 2007, **19**, 1359–1361.
- 40 A. Michalowicz, J. Moscovici, B. Ducourant, D. Cracco and O. Kahn, *Chem. Mater.*, 1995, **7**, 1833–1842.
- 41 P. J. Van Koningsbruggen, Y. Garcia, E. Codjovi, R. Lapouyade, O. Kahn, L. Fournè and L. Rabardel, *J. Mater. Chem.*, 1997, 2069–2075.
- 42 K. Jonas, A. Jean-Paul, C. Renée, C. Epiphane, K. Olivier, J. G. Haasnoot, G. Françoise, J. Charlotte, A. Bousseksou, L. Jorge, V. François and G. V. Anne, *Chem. Mater.*, 1994, **6**, 1404–1412.
- 43 A. Sugahara, H. Kamebuchi, A. Okazawa, M. Enomoto and N. Kojima, *Inorganics*, 2017, **5**, 1–23.
- 44 V. Gómez, J. Benet-Buchholz, E. Martin and J. R. Galán-Mascarós, *Chem. - A Eur. J.*,
-

-
- 2014, **20**, 5369–5379.
- 45 K. Hosoya, S. Nishikiori, M. Takahashi and T. Kitazawa, *Magnetochemistry*, 2016, **2**, 8.
- 46 S. Cobo, G. Molnár, J. A. Real and A. Bousseksou, *Angew. Chemie - Int. Ed.*, 2006, **45**, 5786–5789.
- 47 V. Niel, J. M. Martinez-Agudo, M. C. Muñoz, A. B. Gaspar and J. A. Real, *Inorg. Chem.*, 2001, **40**, 3838–3839.
- 48 S. Bonhommeau, G. Molnár, A. Galet, A. Zwick, J. A. Real, J. J. McGarvey and A. Bousseksou, *Angew. Chemie - Int. Ed.*, 2005, **44**, 4069–4073.
- 49 V. M. Hiiuk, S. Shova, A. Rotaru, V. Ksenofontov, I. O. Fritsky and I. A. Gural'skiy, *Chem. Commun.*, 2019, **55**, 3359–3362.
- 50 J. M. Holland, J. A. Mcallister, Z. Lu, C. A. Kilner, M. Thornton-Pett and M. A. Halcrow, *Chem. Commun.*, 2001, 577–578.
- 51 M. A. Halcrow, *Coord. Chem. Rev.*, 2009, **253**, 2493–2514.
- 52 N. T. Madhu, I. Salitros, F. Schramm, S. Klyatskaya, O. Fuhr and M. Ruben, *Comptes Rendus Chim.*, 2008, **11**, 1166–1174.
- 53 R. Pritchard, H. Lazar, S. A. Barrett, C. A. Kilner, S. Asthana, C. Carbonera, J. F. Létard and M. A. Halcrow, *J. Chem. Soc. Dalt. Trans.*, 2009, 6656–6666.
- 54 K. S. Kumar, I. Šalitroš, E. Moreno-Pineda and M. Ruben, *Dalt. Trans.*, 2017, **46**, 9765–9768.
- 55 R. González-Prieto, B. Fleury, F. Schramm, G. Zoppellaro, R. Chandrasekar, O. Fuhr, S. Lebedkin, M. Kappes and M. Ruben, *Dalt. Trans.*, 2011, **40**, 7564–7570.
- 56 A. Abhervé, M. Clemente-León, E. Coronado, C. J. Gómez-García and M. López-Jordà, *Dalt. Trans.*, 2014, **43**, 9406–9409.
- 57 V. Garcíá-López, M. Palacios-Corella, A. Abhervé, I. Pellicer-Carrenõ, C. Desplanches, M. Clemente-León and E. Coronado, *Dalt. Trans.*, 2018, **47**, 16958–16968.
- 58 I. Šalitroš, N. T. Madhu, R. Boča, J. Pavlik and M. Ruben, *Monatshefte fur Chemie*, 2009, **140**, 695–733.
- 59 N. Bridonneau, L. Rigamonti, G. Poneti, D. Pinkowicz, A. Forni and A. Cornia, *Dalt. Trans.*, 2017, **46**, 4075–4085.
- 60 M. A. Halcrow, *Chem. Soc. Rev.*, 2011, **40**, 4119–4142.
- 61 I. Šalitroš, O. Fuhr, A. Eichhöfer, R. Kruk, J. Pavlik, L. Dlhá, R. Boa and M. Ruben, *Dalt. Trans.*, 2012, **41**, 5163–5171.
- 62 R. Chandrasekar, F. Schramm, O. Fuhr and M. Ruben, *Eur. J. Inorg. Chem.*, 2008, 2649–2653.
- 63 K. Senthil Kumar, I. Šalitroš, N. Suryadevara, E. Moreno-Pineda and M. Ruben, *Eur. J.*
-

-
- Inorg. Chem.*, 2018, 5091–5097.
- 64 L. J. Kershaw Cook, R. Kulmaczewski, R. Mohammed, S. Dudley, S. A. Barrett, M. A. Little, R. J. Deeth and M. A. Halcrow, *Angew. Chemie - Int. Ed.*, 2016, **55**, 4327–4331.
- 65 K. V. Barth, Johannes, Costantini, Giovanni and Kern, *Nature*, 2005, **437**, 671–679.
- 66 R. Thiruvengadathan, V. Korampally, A. Ghosh, N. Chanda, K. Gangopadhyay and S. Gangopadhyay, *Reports Prog. Phys.*, 2013, **76**, 1–57.
- 67 L. E. C. Van De Leemput and H. Van Kempen, *Reports Prog. Phys.*, 1992, **55**, 1165–1240.
- 68 K. Senthil Kumar, B. Heinrich, S. Vela, E. Moreno-Pineda, C. Bailly and M. Ruben, *Dalt. Trans.*, 2019, **48**, 3825–3830.
- 69 W. Zhang, A. Nefedov, M. Naboka, L. Cao and C. Wöll, *Phys. Chem. Chem. Phys.*, 2012, **14**, 10125–10131.
- 70 S. Stepanow, T. Strunskus, M. Lingenfelder, A. Dmitriev, H. Spillmann, N. Lin, J. V Barth, C. Wöll and K. Kern, *J. Phys. Chem. B*, 2004, **108**, 19392–19397.
- 71 S. L. Tait, Y. Wang, G. Costantini, N. Lin, A. Baraldi, F. Esch, L. Petaccia, S. Lizzit and K. Kern, *J. Am. Chem. Soc.*, 2008, **130**, 2108–2113.
- 72 A. Schiffrin, M. Capsoni, G. Farahi, C. G. Wang, C. Krull, M. Castelli, T. Roussy, K. A. Cochrane, Y. Yin, N. V Medhekar, M. Fuhrer, A. Q. Shaw, W. Ji and S. A. Burke, *ACS Nano*, 2018, **12**, 6545–6553.
- 73 W. Wang, X. Shi, C. Lin, R. Q. Zhang, C. Minot, M. A. Van Hove, Y. Hong, B. Z. Tang and N. Lin, *Phys. Rev. Lett.*, 2010, **105**, 126801.
- 74 C. S. Kley, J. Čechal, T. Kumagai, F. Schramm, M. Ruben, S. Stepanow and K. Kern, *J. Am. Chem. Soc.*, 2012, **134**, 6072–6075.
- 75 S. Bommakanti, U. Venkataramudu and S. K. Das, *Cryst. Growth Des.*, 2019, **19**, 1155–1166.
- 76 V. Garcíá-López, M. Palacios-Corella, A. Abhervé, I. Pellicer-Carrenõ, C. Desplanches, M. Clemente-León and E. Coronado, *Dalt. Trans.*, 2018, **47**, 16958–16968.
- 77 S. A. Barrett and M. A. Halcrow, *RSC Adv.*, 2014, **4**, 11240–11243.
- 78 I. Galadzhun, R. Kulmaczewski, O. Cespedes, M. Yamada, N. Yoshinari, T. Konno and M. A. Halcrow, *Inorg. Chem.*, 2018, **57**, 13761–13771.
- 79 I. Galadzhun, R. Kulmaczewski and M. A. Halcrow, *Magnetochemistry*, 2019, **5**, 9.
- 80 K. S. Kumar, I. Šalitroš, E. Moreno-Pineda and M. Ruben, *Dalt. Trans.*, 2017, **46**, 9765–9768.
- 81 S. Basak, P. Hui and R. Chandrasekar, *Synthesis (Stuttg.)*, 2009, 4042–4048.
- 82 M. Sorai, Y. Nakazawa, M. Nakano and Y. Miyazaki, *Chem. Rev.*, 2013, **113**, PR-41-
-

-
- PR122.
- 83 A. Bousseksou, J. J. McGarvey, F. Varret, J. A. Real, J. P. Tuchagues, A. C. Dennis and M. L. Boillot, *Chem. Phys. Lett.*, 2000, **318**, 409–416.
- 84 J. M. Holland, J. A. McAllister, C. A. Kilner, M. Thornton-Pett, A. J. Bridgeman and M. A. Halcrow, *J. Chem. Soc. Dalton Trans.*, 2002, 548–554.
- 85 J. Elhaik, C. A. Kilner and M. A. Halcrow, *Dalt. Trans.*, 2006, 823–830.
- 86 M. Nihei, L. Han, H. Tahira and H. Oshio, *Inorganica Chim. Acta*, 2008, **361**, 3926–3930.
- 87 L. J. Kershaw Cook, F. L. Thorp-Greenwood, T. P. Comyn, O. Cespedes, G. Chastanet and M. A. Halcrow, *Inorg. Chem.*, 2015, **54**, 6319–6330.
- 88 R. A. Hegstrom and D. K. Kondepudi, 1990, **262**, 108–115.
- 89 S. J. Mohan, E. C. Mohan and M. R. Yamsani, *Int. J. Pharm. Sci. Nanotechnol.*, 2009, **1**, 309–316.
- 90 Y. Wang, J. Xu, Y. Wang and H. Chen, *Chem. Soc. Rev.*, 2013, **42**, 2930–2962.
- 91 Y. Xia, Y. Zhou and Z. Tang, *Nanoscale*, 2011, **3**, 1374–1382.
- 92 V. Prelog and G. Helmchen, *Angew. Chemie Int. Ed. English*, 1982, **21**, 567–583.
- 93 R. S. Cahn, C. Ingold and V. Prelog, *Angew. Chemie Int. Ed. English*, 1966, **5**, 385–415.
- 94 N. Berova, L. Di Bari and G. Pescitelli, *Chem. Soc. Rev.*, 2007, **36**, 914–931.
- 95 G. Pescitelli, L. Di Bari and N. Berova, *Chem. Soc. Rev.*, 2011, **40**, 4603–4625.
- 96 H. Amouri and M. Gruselle, *Chirality in Transition Metal Chemistry*, 2008.
- 97 D. B. Amabilino, *Chirality at the Nanoscale: Nanoparticles, Surfaces, Materials and more*, John Wiley and Sons, 2009.
- 98 G. L. J. A. Rikken and E. Raupach, *Nature*, 1997, **390**, 493–494.
- 99 K. Ishii, S. Hattori and Y. Kitagawa, *Photochem. Photobiol. Sci.*, 2020, **19**, 8–19.
- 100 C. Train, T. Nuida, R. Gheorghe, M. Gruselle and S.-I. Ohkoshi, *J. Am. Chem. Soc.*, 2009, **131**, 16838–16843.
- 101 R. Naaman, *Isr. J. Chem.*, 2016, **56**, 1010–1015.
- 102 J. -M Lehn, *Angew. Chemie Int. Ed. English*, 1988, **27**, 89–112.
- 103 F. Biedermann and H.-J. J. Schneider, *Chem. Rev.*, 2016, **116**, 5216–5300.
- 104 M. Ruben, J. M. Lehn and G. Vaughan, *Chem. Commun.*, 2003, **3**, 1338–1339.
- 105 M. Ruben, E. Breuning, M. Barboiu, J. P. Gisselbrecht and J. M. Lehn, *Chem. - A Eur. J.*, 2003, **9**, 291–299.
- 106 I. V Kolesnichenko and E. V Anslyn, *Chem. Soc. Rev.*, 2017, **46**, 2385.
-

-
- 107 M. J. Webber, E. A. Appel, E. W. Meijer and R. Langer, *Nat. Publ. Gr.*, 2016, **15**, 13–26.
- 108 L. F. L. and I. M. A. J. Fraser Stoddart, in *Self Assembly in Supramolecular Systems*, 2007, pp. 1–6.
- 109 G. M. Whitesides and M. Boncheva, *Proc. Natl. Acad. Sci. U. S. A.*, 2002, **99**, 4769–4774.
- 110 A. Klug, *Angew. Chemie Int. Ed. English*, 1983, **22**, 565–582.
- 111 A. C. Mendes, E. T. Baran, R. L. Reis and H. S. Azevedo, *Wiley Interdiscip. Rev. Nanomedicine Nanobiotechnology*, 2013, **5**, 582–612.
- 112 G. F. Swiegers and T. J. Malefetse, *Chem. Rev.*, 2000, **100**, 3483–3537.
- 113 F. Puntoriero, S. Campagna, A. M. Stadler and J. M. Lehn, *Coord. Chem. Rev.*, 2008, **252**, 2480–2492.
- 114 M. Ruben, J. Rojo, F. J. Romero-Salguero, L. H. Uppadine and J. M. Lehn, *Angew. Chemie - Int. Ed.*, 2004, **43**, 3644–3662.
- 115 C. Piguet, G. Bernardinelli and G. Hopfgartner, *Chem. Rev.*, 1997, **97**, 2005–2062.
- 116 V. Patroniak, P. N. W. Baxter, J. M. Lehn, M. Kubicki, M. Nissinen and K. Rissanen, *Eur. J. Inorg. Chem.*, 2003, 4001–4009.
- 117 J. Rojo, F. J. Romero-Salguero, J.-M. Lehn, G. Baum and D. Fenske, *Eur. J. Inorg. Chem.*, 1999, **1999**, 1421–1428.
- 118 J.-M. Lehn, K. Näntinen, L. H. Uppadine, J.-P. Gisselbrecht, K. Rissanen and N. Kyritsakas, *Chem. - A Eur. J.*, 2005, **11**, 2549–2565.
- 119 T. Matsumoto, G. N. Newton, T. Shiga, S. Hayami, Y. Matsui, H. Okamoto, R. Kumai, Y. Murakami and H. Oshio, *Nat. Commun.*, 2014, **5**, 3865.
- 120 B. Schäfer, J.-F. Greisch, I. Faus, T. Bodenstein, I. Šalitroš, O. Fuhr, K. Fink, V. Schünemann, M. M. Kappes and M. Ruben, *Angew. Chemie*, 2016, **55**, 11040–11044.
- 121 X. Hua and A. von Zelewsky, *Inorg. Chem.*, 1995, **34**, 5791–5797.
- 122 T. Bark, M. Düggele, H. Stoeckli-Evans and A. von Zelewsky, *Angew. Chem. Int. Ed. Engl.*, 2001, **40**, 2848–2851.
- 123 E. König, in *Progress in Inorganic Chemistry*, Wiley, 2007, vol. 35, pp. 527–622.
- 124 Q. Wang, S. Venneri, N. Zarrabi, H. Wang, C. Desplanches, J. F. Létard, T. Seda and M. Pilkington, *Dalt. Trans.*, 2015, **44**, 6711–6714.
- 125 I. Šalitroš, O. Fuhr, R. Kruk, J. Pavlik, L. Pogány, B. Schäfer, M. Tatarko, R. Boča, W. Linert and M. Ruben, *Eur. J. Inorg. Chem.*, 2013, 1049–1057.
- 126 Z.-G. Gu, J. Bürck, A. Bihlmeier, J. Liu, O. Shekhah, P. G. Weidler, C. Azucena, Z. Wang, S. Heissler, H. Gliemann, W. Kloppe, A. S. Ulrich and C. Wöll, *Chem. - A Eur. J.*, 2014, **20**, 9879–9882.
- 127 J. Podlech, S. C. Fleck, M. Metzler, J. Bürck and A. S. Ulrich, *Chem. - A Eur. J.*, 2014,
-

-
- 20**, 11463–11470.
- 128 A. Hauser, *J. Chem. Phys.*, 1991, **94**, 2741–2748.
- 129 E. Runge and E. K. U. Gross, *Phys. Rev. Lett.*, 1984, **52**, 997–1000.
- 130 M. E. Casida and D. P. Chong, *Recent Adv. Density Funct. Methods, Part I*, 1995, **1**, 155.
- 131 E. K. U. Gross and W. Kohn, *Adv. Quantum Chem.*, 1990, **21**, 255–291.
- 132 E. K. U. Gross, J. F. Dobson and M. Petersilka, in *Density Functional Theory II*, Springer-Verlag, 2005, pp. 81–172.
- 133 C. Diedrich and S. Grimme, *J. Phys. Chem. A*, 2003, **107**, 2524–2539.
- 134 J. Autschbach, F. E. Jorge and T. Ziegler, *Inorg. Chem.*, 2003, **42**, 2867–2877.
- 135 S. Grimme, *Chem. Phys. Lett.*, 1996, **259**, 128–137.
- 136 R. Bauernschmitt, R. Ahlrichs, F. H. Hennrich and M. M. Kappes, *J. Am. Chem. Soc.*, 1998, **120**, 5052–5059.
- 137 C. Bannwarth and S. Grimme, *Comput. Theor. Chem.*, 2014, **1040–1041**, 45–53.
- 138 O. Treutler and R. Ahlrichs, *J. Chem. Phys.*, 1995, **102**, 346–354.
- 139 M. Von Arnim and R. Ahlrichs, *J. Comput. Chem.*, 1998, **19**, 1746–1757.
- 140 M. Von Arnim and R. Ahlrichs, *J. Chem. Phys.*, 1999, **111**, 9183–9190.
- 141 T. Yanai, D. P. Tew and N. C. Handy, *Chem. Phys. Lett.*, 2004, **393**, 51–57.
- 142 I. Šalitroš, L. Pogány, M. Ruben, R. Boča and W. Linert, *Dalt. Trans.*, 2014, **43**, 16584–16587.
- 143 A. Hauser, *Coord. Chem. Rev.*, 1991, **111**, 275–290.
- 144 I. O. Fritsky, I. A. Gural'skiy, V. Ksenofontov, O. I. Kucheriv, S. I. Shylin and R. A. Polunin, *Chem. - A Eur. J.*, 2015, **21**, 18076–18079.
- 145 T. Bark, A. Von Zelewsky, D. Rappoport, M. Neuburger, S. Schaffner, J. Lacour and J. Jodry, *Chem. - A Eur. J.*, 2004, **10**, 4839–4845.
- 146 L. J. Chen, H. B. Yang and M. Shionoya, *Chem. Soc. Rev.*, 2017, **46**, 2555–2576.
- 147 C. Gütz, R. Hovorka, G. Schnakenburg and A. Lützen, *Chem. - A Eur. J.*, 2013, **19**, 10890–10894.
- 148 T. Tateishi, T. Kojima and S. Hiraoka, *Commun. Chem.*, 2018, **1**, 1–12.
- 149 L. F. Qin, C. Y. Pang, W. K. Han, F. L. Zhang, L. Tian, Z. G. Gu, X. Ren and Z. Li, *CrystEngComm*, 2015, **17**, 7956–7963.
- 150 B. Schneider, S. Demeshko, S. Dechert and F. Meyer, *Angew. Chemie - Int. Ed.*, 2010, **49**, 9274–9277.
- 151 B. Schneider, S. Demeshko, S. Neudeck, S. Dechert and F. Meyer, *Inorg. Chem.*, 2013,
-

-
- 52**, 13230–13237.
- 152 P. Escribano, B. Julián-López, J. Planelles-Aragó, E. Cordoncillo, B. Viana and C. Sanchez, *J. Mater. Chem.*, 2008, **18**, 23–40.
- 153 C. Andraud and O. Maury, *Eur. J. Inorg. Chem.*, 2009, 4357–4371.
- 154 G. Wang, Q. Peng and Y. Li, *Acc. Chem. Res.*, 2011, **44**, 322–332.
- 155 S. T. Liddle and J. Van Slageren, *Chem. Soc. Rev.*, 2015, **44**, 6655–6669.
- 156 R. Vincent, S. Klyatskaya, M. Ruben, W. Wernsdorfer and F. Balestro, *Nature*, 2012, **488**, 357–360.
- 157 S. Thiele, F. Balestro, R. Ballou, S. Klyatskaya, M. Ruben and W. Wernsdorfer, *Science*, 2014, **344**, 1135–1138.
- 158 N. Ishikawa, M. Sugita, T. Ishikawa, S. Y. Koshihara and Y. Kaizu, *J. Am. Chem. Soc.*, 2003, **125**, 8694–8695.
- 159 M. A. AlDamen, J. M. Clemente-Juan, E. Coronado, C. Martí-Gastaldo and A. Gaita-Ariño, *J. Am. Chem. Soc.*, 2008, **130**, 8874–8875.
- 160 N. F. Chilton, S. K. Langley, B. Moubaraki, A. Soncini, S. R. Batten and K. S. Murray, *Chem. Sci.*, 2013, **4**, 1719–1730.
- 161 G. J. Chen, Y. N. Guo, J. L. Tian, J. Tang, W. Gu, X. Liu, S. P. Yan, P. Cheng and D. Z. Liao, *Chem. - A Eur. J.*, 2012, **18**, 2484–2487.
- 162 S. Da Jiang, B. W. Wang, G. Su, Z. M. Wang and S. Gao, *Angew. Chemie - Int. Ed.*, 2010, **49**, 7448–7451.
- 163 F. S. Guo, B. M. Day, Y. C. Chen, M. L. Tong, A. Mansikkamäki and R. A. Layfield, *Angew. Chemie - Int. Ed.*, 2017, **56**, 11445–11449.
- 164 S. Da Jiang, B. W. Wang, H. L. Sun, Z. M. Wang and S. Gao, *J. Am. Chem. Soc.*, 2011, **133**, 4730–4733.
- 165 J. D. Rinehart and J. R. Long, *Chem. Sci.*, 2011, **2**, 2078–2085.
- 166 N. Ishikawa, M. Sugita, T. Okubo, N. Tanaka, T. Iino and Y. Kaizu, *Inorg. Chem.*, 2003, **42**, 2440–2446.
- 167 N. Ishikawa, T. Iino and Y. Kaizu, *J. Phys. Chem. A*, 2002, **106**, 9543–9550.
- 168 N. Ishikawa, M. Sugita, N. Tanaka, T. Ishikawa, S. Y. Koshihara and Y. Kaizu, *Inorg. Chem.*, 2004, **43**, 5498–5500.
- 169 Y. Horii, K. Katoh, B. K. Breedlove and M. Yamashita, *Chem. Commun.*, 2017, **53**, 8561–8564.
- 170 K. Wang, D. Qi, H. Wang, W. Cao, W. Li, T. Liu, C. Duan and J. Jiang, *Chem. - A Eur. J.*, 2013, **19**, 11162–11166.
- 171 T. Morita, M. Damjanović, K. Katoh, Y. Kitagawa, N. Yasuda, Y. Lan, W. Wernsdorfer,
-

-
- B. K. Breedlove, M. Enders and M. Yamashita, *J. Am. Chem. Soc.*, 2018, **140**, 2995–3007.
- 172 Y. Horii, K. Katoh, N. Yasuda, B. K. Breedlove and M. Yamashita, *Inorg. Chem*, 2015, **54**, 19.
- 173 K. Yamashita, T. Yamanaka, N. Sakata and T. Ogawa, *Chem. - An Asian J.*, 2018, **13**, 1692–1698.
- 174 T. Inose, D. Tanaka, H. Tanaka, O. Ivasenko, T. Nagata, Y. Ohta, S. De Feyter, N. Ishikawa and T. Ogawa, *Chem. - A Eur. J.*, 2014, **20**, 11362–11369.
- 175 D. Tanaka, T. Inose, H. Tanaka, S. Lee, N. Ishikawa and T. Ogawa, *Chem. Commun.*, 2012, **48**, 7796–7798.
- 176 H. Wang, K. Wang, J. Tao and J. Jiang, *Chem. Commun.*, 2012, **48**, 2973–2975.
- 177 W. Cao, Y. Zhang, H. Wang, K. Wang and J. Jiang, *RSC Adv.*, 2015, **5**, 17732–17737.
- 178 E. Önal, V. Ahsen, J. Pécaut, D. Luneau and C. Hirel, *Tetrahedron Lett.*, 2015, **56**, 5157–5160.
- 179 A. D. Adleb, F. R. Longo, J. D. Finarelli, J. Goldmacher, J. Assour and L. Korsakoff, *J. Org. Chem.*, 1967, **32**, 476.
- 180 A. G. Mojarrad and S. Zakavi, *New J. Chem.*, 2020, **44**, 3028–3037.
- 181 V. E. Pushkarev, L. G. Tomilova and V. N. Nemykin, *Coord. Chem. Rev.*, 2016, **319**, 110–179.
- 182 R. A. Benkeser and H. R. Krysiak, *J. Am. Chem. Soc.*, 1953, **75**, 2421–2425.
- 183 F. Lu, X. Sun, R. Li, D. Liang, P. Zhu, C.-F. Choi, D. K. P. Ng, T. Fukuda, N. Kobayashi, M. Bai, C. Ma and J. Jiang, *New J. Chem.*, 2004, **28**, 1116–1122.
- 184 D. Chabach, M. Tahiri, A. De Cian, J. Fischer, R. Weiss and M. El Malouli Bibout, *J. Am. Chem. Soc.*, 1995, **117**, 8548–8556.
- 185 G. Hariprasad, S. Dahal and B. G. Maiya, *J. Chem. Soc. - Dalt. Trans.*, 1996, 3429–3436.
- 186 N. Ishikawa, M. Sugita, N. Tanaka, T. Ishikawa, S. Y. Koshihara and Y. Kaizu, *Inorg. Chem.*, 2004, **43**, 5498–5500.
- 187 N. Sun, H. Wang, T. Liu, D. Qi and J. Jiang, *Dalt. Trans.*, 2019, **48**, 1586–1590.
- 188 Y. Lan, S. Klyatskaya and M. Ruben, in *Lanthanides and Actinides in Molecular Magnetism*, Wiley-VCH Verlag GmbH & Co. KGaA, Weinheim, Germany, 2015, pp. 223–292.
- 189 T. H. Tran-Thi, T. A. Mattioli, D. Chabach, A. D. Cian and R. Weiss, *J. Phys. Chem.*, 1994, **98**, 8279–8288.
- 190 R. J. Donohoe, J. K. Duchowski and D. F. Bocian, *J. Am. Chem. Soc.*, 1988, **110**, 6119–6124.
- 191 D. Markovitsi, T. H. Tran-Thi, R. Even and J. Simon, *Chem. Phys. Lett.*, 1987, **137**, 107–
-

-
- 112.
- 192 N. Ishikawa, O. Ohno and Y. Kaizu, *Chem. Phys. Lett.*, 1991, **180**, 51–56.
- 193 J. W. Buchler, J. Hüttermann and J. Löffler, *Bull. Chem. Soc. Jpn.*, 1988, **61**, 71–77.
- 194 D. Komijani, A. Ghirri, C. Bonizzoni, S. Klyatskaya, E. Moreno-Pineda, M. Ruben, A. Soncini, M. Affronte and S. Hill, *Phys. Rev. Mater.*, 2018, **2**, 1–9.
- 195 D. V Konarev, S. S. Khasanov, M. S. Batov, A. G. Martynov, I. V Nefedova, Y. G. Gorbunova, A. Otsuka, H. Yamochi, H. Kitagawa and R. N. Lyubovskaya, *Inorg. Chem.*, 2019, **58**, 5058–5068.
- 196 T. V Dubinina, A. D. Kosov, E. F. Petrusevich, N. E. Borisova, A. L. Trigub, G. V Mamin, I. F. Gilmutdinov, A. A. Masitov, S. V Tokarev, V. E. Pushkarev and L. G. Tomilova, *Dalt. Trans.*, 2019, **48**, 13413–13422.
- 197 G. A. Spyroulias, A. G. Coutsolelos, C. P. Raptopoulou and A. Terzis, *Inorg. Chem.*, 1995, **34**, 2476–2479.
- 198 K. Wang, D. Qi, H. Wang, W. Cao, W. Li, T. Liu, C. Duan and J. Jiang, *Chem. - A Eur. J.*, 2013, **19**, 11162–11166.
- 199 K. L. Trojan, W. E. Hatfield, K. D. Kepler and M. L. Kirk, *J. Appl. Phys.*, 1991, **69**, 6007–6009.
- 200 J. W. B. Jürgen Hüttermann, Jürgen Löffler, *Bull. Chem. Soc. Jpn.*, 1988, **61**, 71–77.
- 201 G. A. Bain and J. F. Berry, *J. Chem. Educ.*, 2008, **85**, 532–536.
- 202 C. Klein, E. Baranoff, M. Grätzel and M. K. Nazeeruddin, *Tetrahedron Lett.*, 2011, **52**, 584–587.
- 203 R. Bauernschmitt and R. Ahlrichs, *Chem. Phys. Lett.*, 1996, **256**, 454–464.
- 204 R. Bauernschmitt and R. Ahlrichs, *J. Chem. Phys.*, 1996, **104**, 9047–9052.
- 205 R. Ahlrichs, M. Bär, M. Häser, H. Horn and C. Kölmel, *Chem. Phys. Lett.*, 1989, **162**, 165–169.
- 206 J. P. Perdew, K. Burke and M. Ernzerhof, *Phys. Rev. Lett.*, 1996, **77**, 3865–3868.
- 207 J. P. Perdew, M. Ernzerhof and K. Burke, *J. Chem. Phys.*, 1996, **105**, 9982–9985.
- 208 F. Weigend and R. Ahlrichs, *Phys. Chem. Chem. Phys.*, 2005, **7**, 3297–3305.
- 209 M. Yu, J. K. H. Wong, C. Tang, P. Turner, M. H. Todd and P. J. Rutledge, *Beilstein J. Org. Chem.*, 2015, **11**, 37–41.
-

Appendix

Abbreviations

General

AC	Alternating Current
BE	Binding energy
BV	Blue Valance
CCS	Collison Cross section
CD	Circular Dichroism
CIP	Cahn-Ingold-Prelog
CISS	Chiral Induced Spin selectivity
CT	Charge Transfer
CV	Cyclic Voltammetry
DC	Direct Current
DPV	Differential Pulse Voltammetry
DSC	Differential Scanning Calorimetry
EDG	Electron donating group
EPR	Electron Paramagnetic Resonance
ESCA	Electron spectroscopy for chemical analysis
ESI	Electron Spray Ionization
EWG	Electron Withdrawing group
FC	Field Cooling
HOMO	Highest Occupied Molecular Orbital
HPLC	High Performance Liquid Chromatography
HS	High Spin
IMMS	Ion Mobility Mass Spectrometry
IR	Infra-Red
ISC	Inter System Crossing
IV	Inter Valance
JT	Jahn Teller
KE	Kinetic Energy
LC	Ligand Center
LCP	Left Circularly Polarized
LIESST	Light Induced Excited Spin State Trapping
LS	Low Spin
LUMO	Lowest Unoccupied Molecular Orbital
MALDI	Matrix Assisted Laser Desorption Ionization
MChD	Magneto-Chiral Dichroism
MLCT	Metal to Ligand Centered Transfer
MO	Molecular Orbital
MOA	Magnetically Induced optical activity
NLO	Non-linear Optics

NMR	Nuclear Magnetic Resonance
NOA	Natural Optical Activity
OF	Optimal Field
PBE	Perdew–Burke-Ernzerhof
PES	Photo electron Spectroscopy
QTM	Quantum Tunneling of Magnetization
RCP	Right Circularly Polarized
ROA	Raman Optical Activity
RT	Room Temperature
RV	Red Valance
SAP	Square Antiprism
SCO	Spin-Crossover
SHG	Second Harmonic Generation
SMM	Single Molecule Magnet
SOMO	Single Occupied Molecular Orbital
SQUID	Super Conducting Quantum Interference Device
ST	Spin Transition
STM	Scanning Tunneling Microscope
TDDFT	Time dependent Density Functional Theory
TGA	Thermo Gravimetric analysis
TS	Tanabe Sugano
VCD	Vibrational Circular Dichroism
XPS	X-ray Photoelectron Spectroscopy
XRD	X-ray Diffraction
ZFC	Zero Field Cooling
ZFS	Zero Field Splitting
ZPE	Zero Potential Energy

Chemicals

DMF	Dimethyl Formamide
<i>bpp</i>	Bis(pyrazolyl) pyridine
DCM	Dichloromethane
DEE	Diethyl ether
DMSO	Dimethyl sulfoxide
NME	Nitromethane
Pc	Phthalocyanine
TBA	Tetra-butyl Ammonium
TCB	1,2,5-Trichlorobenzene
THF	Tetrahydrofuran
TMS	Trimethyl silyl
